LIBRARY COPY

FEB 1 1965

LANGLEY RESEARCH CENTER
LIBRARY, NASA
LANGLEY STATION

JET PROPULSION LABORATORY
CALIFORNIA INSTITUTE OF TECHNOLOGY
PASADENA, CALIFORNIA

FACILITY FORM 602

N65-88243
(ACCESSION NUMBER)

276
(PAGES)

CR-68876
(NASA CR OR TMX OR AD NUMBER)

(THRU)

None
(CODE)

(CATEGORY)

VENUS-MARS CAPSULE STUDY

MID-TERM REPORT

May 18, 1962

JPL Contract Number 950250

GENERAL ELECTRIC COMPANY

Missile & Space Vehicle Department

TABLE OF CONTENTS

1.0 Summary

2.0 Theoretical Vehicle-Environment Interactions

3.0 Experimental Vehicle-Enviroment Interactions

4.0 Mission Instrumentation

5.0 Telemetry and Power Supply

6.0 Capsule Parametric Analysis

TABLE OF CONTENTS

1.0 Summary

2.0 Theoretical Vehicle-Environment Interactions

3.0 Experimental Vehicle-Enviroment Interactions

4.0 Mission Instrumentation

5.0 Telemetry and Power Supply

6.0 Capsule Parametric Analysis

1.0 SUMMARY

This report is a discussion of the work that has been accomplished during the first half of the Venus-Mars Capsule Study and an outline of the work planned for the second half.

Since this is for the most part a parametric study to define the problems that will be encountered in designing entry capsules for Venus and Mars, the study is divided into two general plases. During the first phase or the first half of the study, the emphasis has been on developing the relationship among the variables within each of the areas of study, e.g. telemetry, instrumentation, capsule design, etc. In the main, the study of the relationship between the various study areas and hence the performance that may be expected of typical capsule designs will be the subject of the second half of the study.

The Venus-Mars Capsule Study is divided into five areas:

- Theoretical Vehicle-Environment Interactions
- Experimental Vehicle-Environment Interactions
- Mission Instrumentation
- Telemetry and Power Supply
- Capsule Parametric Analysis

A summary of the activity in each area is given below.

Theoretical Vehicle-Environment Interactions

- A series of reports have been issued on the thermodynamic properties, enthalpy, free energy and specific heat, of species of interest in the high temperature air system and the carbon enriched air system.

- Approximate flow fields at two Venusian flight conditions (40,000 ft/sec - 255,000 ft and 30,000 ft/sec - 208,000 ft) have been calculated by simplified methods for a capsule employing a 10 degree sphere-cone shape. Electron density profiles for one axial position have been prepared.

- The normal shock equations are being used to calculate the thermodynamic properties along several entry trajectories.

- The radiation for fourteen species (considered to be the important radiators in the Venusian atmosphere) has been computed for temperatures between 3000°K and 24000°K.

- Graphs of the variation of aerodynamic heat transfer with time are now being prepared for each of the entry trajectories of interest.

- A chemical system for the determination of the kinetics has been developed and rate constant for the reactions have been found or estimated.

Experimental Vehicle-Environment Interactions

- The tandem-Gerdien arc heater has been modified and is now being calibrated prior to the conduction of the ablation experiments in gases representative of the Martian and Venusian atmospheres.

- The experimental studies of the stagnation point heat transfer in pure CO_2 and N_2 gases have been completed.

- The experiments in the hypervelocity shock tube with the 9% CO_2 gas mixture are in progress.

Mission Instrumentation

- No fundamental difficulties are envisioned in measuring temperature, pressure, total density, and carbon dioxide density at Venusian altitudes below 80 KM in the subsonic regime.

- Investigations are now underway to establish the feasibility of measuring oxygen concentration.

- A satisfactory radar altimeter design is evolving.

Telemetry and Power Supply

- For post-entry communications over a capsule-to-spacecraft relay link, two general approaches are being considered 1) the use of a spacecraft receiver with an IF bandwidth sufficiently wide to include the doppler shift and oscillator instability inherent in the signal and 2) a phase-lock loop to track the frequency of the received signal.

- The study of error correction coding is nearly completed.

- Antennas are being studies for both a capsule-to-spacecraft relay link (100 to 500 MC) and a direct capsule to earth link (2.3 KMC).

- Initial investigations of the Venusian model atmospheres have shown that the post-entry propagation effects are comparable to those of the Earth.

- Power supply studies to date have been directed toward defining the requirements.

- A study has been completed on the attenuation effects resulting from entry induced plasma for Martian entry.

Capsule Parametric Analysis

- Three general types of configurations have been selected for more detailed analysis: Discoverer type, Apollo type and a Cone-Flared type.

- Utilizing a large number of point mass trajectories the effect of atmospheric model, initial velocity, entry angle and ballistic coefficient on entry design have been considered for Venusian entry.

- An analysis has been conducted to determine if the maximum capsule to bus communication time after capsule entry is sufficient to permit the bus to be used as an information relay link.

- Several methods of entry trajectory modulation have been considered for the purpose of reducing the peak capsule deceleration during Venusian entry.

- A study of the variation of heat shield requirements with ballistic coefficient and entry angle for each of the three configurations and model atmospheres under consideration is in progress.

- Heat shield temperatures during Earth-Venus transit have been calculated.

- A survey is being made of bonding materials and techniques to determine their applicability to a Venusian entry capsule.

2.0 THEORETICAL VEHICLE ENVIRONMENT INTERACTIONS

2.1 THERMOCHEMISTRY

A series of reports have been recently issued on the thermodynamic properties, enthalpy, free energy and specific heat, of species of interest in the high temperature air system and the carbon-enriched air system. (1-6) The thermodynamic properties of the atoms of oxygen, nitrogen, argon and carbon, their singly, doubly and triply positive charged ions, the negative oxygen and carbon ions and the free electron have been computed by evaluating the translational and electronic partition function (1,5). Energy levels up to the ionization potential were summed in the electronic partition function. The thermodynamic properties of the diatomic species oxygen, nitrogen, nitric oxide, carbon monoxide, their respective singly positive charged ions, the negative ion of oxygen, the dimer of carbon and the cyanide radical have been calculated at low temperatures based on the rigid rotator-harmonic oscillator approximation with certrifugal stretching and anharmonicity corrections included. (2,5)

At high temperatures, the virial formalism has been utilized to ascertain the thermodynamic properties of the diatomic species (4). The classical second virial coefficient and its first and second temperature derivatives based on the Morse potential has been related through the usual partition function to the enthalpy, free energy and specific heat at constant pressure. The low and high temperature results have been joined in the overlap region by graphical smoothing. The linear polyatomic molecules of interest, namely, carbon dioxide, nitrous oxide, the trimer of carbon and cyanogen along with the nonlinear polyatomic molecule nitrogen dioxide have been treated by recourse to the rigid rotator-harmonic oscillator approximation (2,3). A comparison of the results of thermodynamic property calculations (1-4) with values reported in the literature is given in reference (6).

The thermodynamic properties of the species of interest in the high temperature air system and the carbonaceous species CN, C_2, C_3, C_2N_2 and C^- have been utilized in evaluating the equilibrium composition and thermodynamic properties of the 9 and 25% CO_2 Venusian atmospheres. The calculation procedure is the well known Brinkley method in which the mixture is considered to be composed of ideal gases without charge interaction. The system of algebraic equations expressing the free energy constraints

are solved in conjunction with the atomic conservation statements by use of the Newton-Rhapson technique. The program is capable of handling thirty species in the mixture. The computations are performed on an IBM 7090 computing machine.

The independent variables for the calculation of the thermodynamic properties of the Venusian environment are the temperature T in ^{o}K and the logarithm to the base 10 of the density ratio ρ / ρ_o where ρ_o refers to a reference density in g/cm^3. In these calculations, all reference parameters were taken to be the standard values for the earth's atmosphere. The Venusian atmosphere calculations have been performed at $200^{o}K$ and 0.4 intervals of temperature and $\log_{10} \rho / \rho_o$ respectively. The calculations cover the range of temperature $200^{o} \div 15,000^{o}K$ and were run in four separate sections as depicted in Table 2.1. The thermodynamic properties of the mixture calculated are listed in Table 2.2.

With regard to suggestions that one should include the Debye-Huckel approximation, the conclusions drawn by Duclos (7) are here reproduced.

"In general, electrostatic corrections to the equation of state of an ionized gas can be neglected for electron densities below about 10^{16} per cm^3. Depending on the temperature and composition of the gas and the amount of error which is acceptable, they may be neglected at even higher densities. The perfect gas pressure of a gas at $10,000^{o}K$ and having a density of 10^{16} particles per cm^3 is about one-tenth of an atmosphere. Therefore, electrostatic corrections can usually be considered negligible for pressures below one atmosphere."

Table 2.1

VENUS ENVIRONMENT CALCULATIONS

Temperature Range	$\log_{10} \rho/\rho_o$ Range	Species Considered
200°-800^oK	-7.0 -3.0	N_2, A, CO_2
1000°-3000^oK	-7.0 -3.0	O_2, N_2, A, CO_2, O, CO, NO, N
3200°-7800^oK	-7.0 -3.0	O, N_2, A, CO, E^-, CO_2, NO_2, N_2O, C_3, C_2N_2, CO^+, N_2^+, NO, NO^+, O_2^-, O_2, O_2^+, C_2, CN, C, N, O^-, C^+, O^+, N^+, A^+, C^{++}, O^{++}, N^{++}, C^-
8000°-$15,000^oK$	-7.0 -1.8	O, N, A, C, E^-, CO, CO^+, N_2, N_2^+, NO, NO^+, O_2^-, O_2, O_2^+, C_2, CN, O^-, C^+, O^+, N^+, A^+, C^{++}, O^{++}, N^{++}, A^{++}, C^{+++}, O^{+++}, N^{+++}, A^{+++}, C^-

Table 2.2

Thermodynamic Properties	List of Thermodynamic Designations	Units
Composition	Concentrations	Particles/cm^3
Molecular Weight	Z^*	Dimensionless
Enthalpy	H^*/RT_o	Dimensionless
Entropy	S^*/R	Dimensionless
Enthalpy/Internal Energy	H^*/E^*	Dimensionless
Eq. Isentropic Coefficient	γ	Dimensionless
Pressure	p	Atmospheres

Notes

$Z^* = M_o/M$ $\quad$ M = g/gmol mixture

$H^* = h\ M_o$ $\quad$ h = cal/g mixture

$S^* = s\ M_o$ $\quad$ s = cal/g mixture ^oK

$E^* = e\ M_o$ $\quad$ e = cal/g mixture

Mo = 28.966 g/gmol

R = 1.98726 cal/gmol ^oK

$T_o = 273.15^oK$

REFERENCES

1. William G. Browne, "Thermodynamic Properties of Some Atoms and Atomic Ions", Engineering Physics Technical Memo #2 (A, O, N, C, Ne, A^+, O^+, N^+, C^+, Ne^+, A^{++}, O^{++}, N^{++}, C^{++}, Ne^{++}, A^{+++}, O^{+++}, N^{+++}, C^{+++}, Ne^{+++}, e^-, O^-) 50°-$60,000^oK$.

2. William G. Brown "Thermodynamic Properties of Some Diatomic and Linear Polyatomic Molecules", Engineering Physics Technical Memo. #3. (O_2, N_2, NO, CO, O_2^+, N_2^+, NO^+, CO^+, O_2^-, CO_2 and N_2O) 50°-$10,000^oK$.

3. William G. Browne, "Thermodynamic Properties of Some Non-Linear Polyatomic Molecules", Engineering Physics Technical Memo #4 (NO_2 and O_3) 50°-$10,000^oK$.

4. William G. Browne, "thermodynamic Properties of Some Diatoms at High Temperature", In Preparation (O_2, N_2, NO, CO, O_2^+, N_2^+, NO^+, CO^+, O_2^-) 50°-$60,000^oK$.

5. William G. Browne, "Thermodynamic Properties of the Species CN, C_2, C_3, C_2N_2 and C^-" In Preparation 50°-$60,000^oK$.

6. William G. Browne, "A Comparison of Some Recently Generated Thermodynamic Properties with Reported Values From Literature", In Preparation.

7. Donald P. Duclos, "The Equation of State of an Ionized Gas", Arnold Engineering Development Center Technical Note 60-192, October 1960, p. 121.

2.2 FLOW FIELDS

The thermodynamic data for the 9% CO_2 Venusian atmosphere are being cross-plotted to obtain the isentropic "a" and "b" functions required in flow field calculations for an equilibrium gas. Other tables and least-squares curve fits for the computer program are also being prepared. The cross plots of thermodynamic data will also speed up and improve accuracy of the simplified calculations.

Data Processing and Computations [redacted] are assisting in check-out of the subsonic compressible flow program.

Work on the simplified calculations is on schedule. The first set of results has been published as PIR 8152-193.

Approximate flow fields at two flight conditions (40,000 ft/sec, 255,000 ft. and 30,000 ft/sec, 208,000 ft.) have been calculated by simplified methods. The capsule shape used was a 10 degree sphere cone. Electron density profiles at an axial position of $\frac{x}{D_N} = 0.9$ (approximate antenna location) have been prepared. A plot of these profiles is attached, Fig. 2.1. Maximum electron density encountered to date is approximately 2.3×10^{15} particles/cc.

Since the basic thermodynamic data were received during May 1 to May 11, initiation of the flow field work was somewhat behind schedule. In order to complete the work within the schedule, it will be necessary to limit the accuracy of the data representation to approximately 5%, rather than the hoped for 1%.

Curve fitting of the thermodynamic properties of the Venusian atmosphere will continue. These curves will be used in the digital hypersonic flow field calculation. A subsonic incompressible run, will also be made.

Several more simplified flow fields will be calculated at pertinent flight conditions as more trajectory information becomes available. Effort will also be directed toward using the simplified flow field methods to extend the results of computer flow field calculations to flight conditions other than those for which computer calculations will be carried out. More accurate methods will be used as additional data (e.g. normal shock tables) becomes available.

FIGURE 2.1

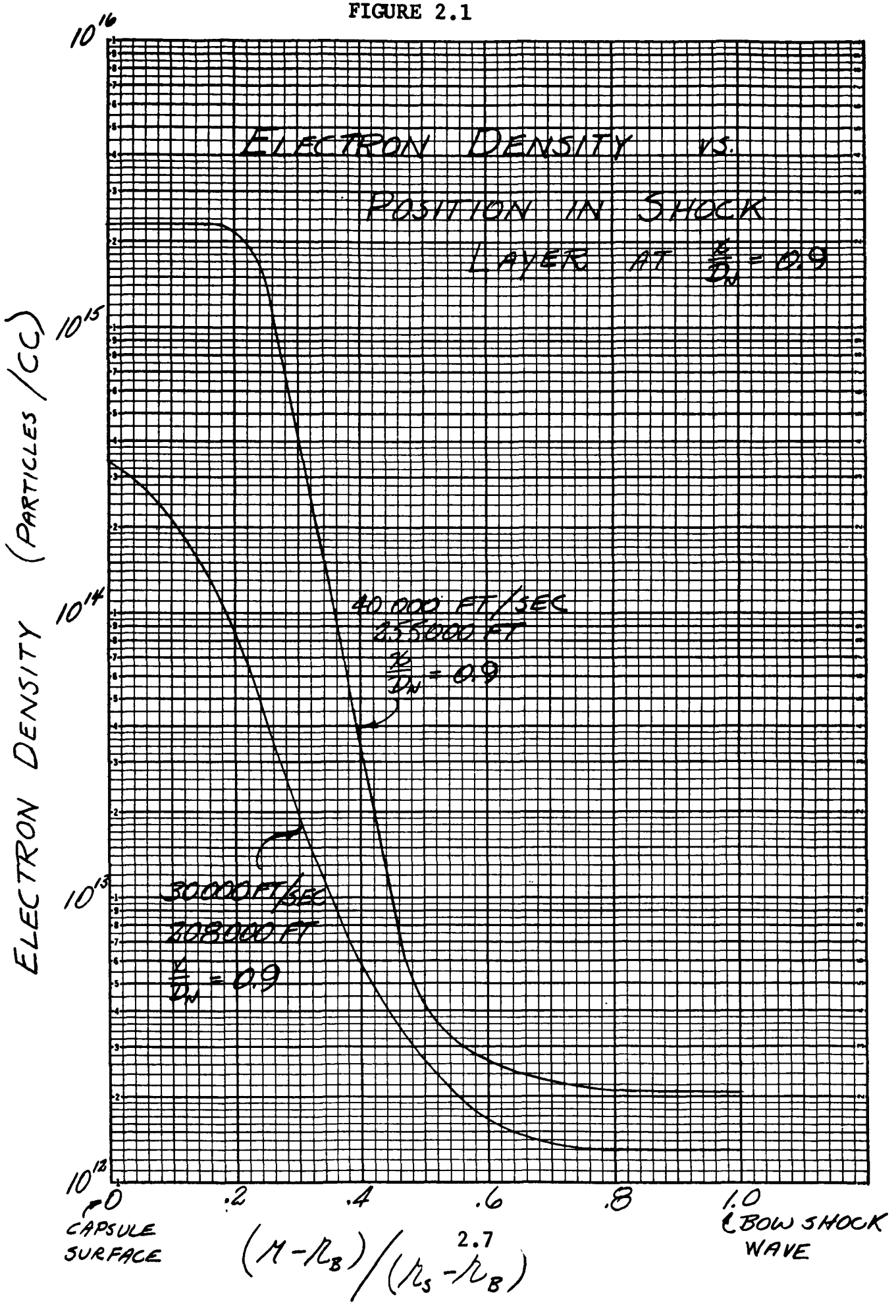
ELECTRON DENSITY VS.
POSITION IN SHOCK
LAYER AT $\frac{r}{D_N} = 0.9$
ELECTRON DENSITY (PARTICLES/CC)
10^{16}
10^{15}
10^{14}
10^{13}
10^{12}
40 000 FT/SEC
255000 FT
$\frac{r}{D_N} = 0.9$
30000 FT/SEC
208000 FT
$\frac{r}{D_N} = 0.9$
0
.2
.4
.6
.8
1.0
CAPSULE SURFACE
℄ BOW SHOCK WAVE
$(r - r_B)/(r_s - r_B)$

2.3 NORMAL SHOCK TABLES

A program to solve the normal shock equations is now being used on the IBM 7090 computer. The chemical composition used in the program is a thirteen component carbon-oxygen-argon partially ionized mixture, including O, O_2, N, N_2, N^+, O^+, C, C^+, CO, CO_2, A, A^+, e^-. These thirteen species were chosen because of their major contribution to the enthalpy of the mixture. The remaining species in the system contribute little to the enthalpy of the mixture, hence they can be neglected as far as determining the thermodynamic properties behind the shock and at the stagnation point.

The main objective is to calculate the thermodynamic properties along any given trajectory using at the present two different chemical models for the ambient conditions recommended by JPL. One mixture consists of 9% CO_2, 1% A, and 90% N_2; the other mixture consists of 74% N_2, 25% CO_2, and 1% A. For each trajectory, we are utilizing both the "best" model atmosphere and extreme model I for the ambient conditions.

When the calculations are completed graphs of P, T, ρ, Re, Q_{aero}, Q_{rad} versus time for each trajectory considered are being prepared.

Some typical results are given in Figures 2.2 and 2.3.

TEMPERATURE VS. TIME FOR

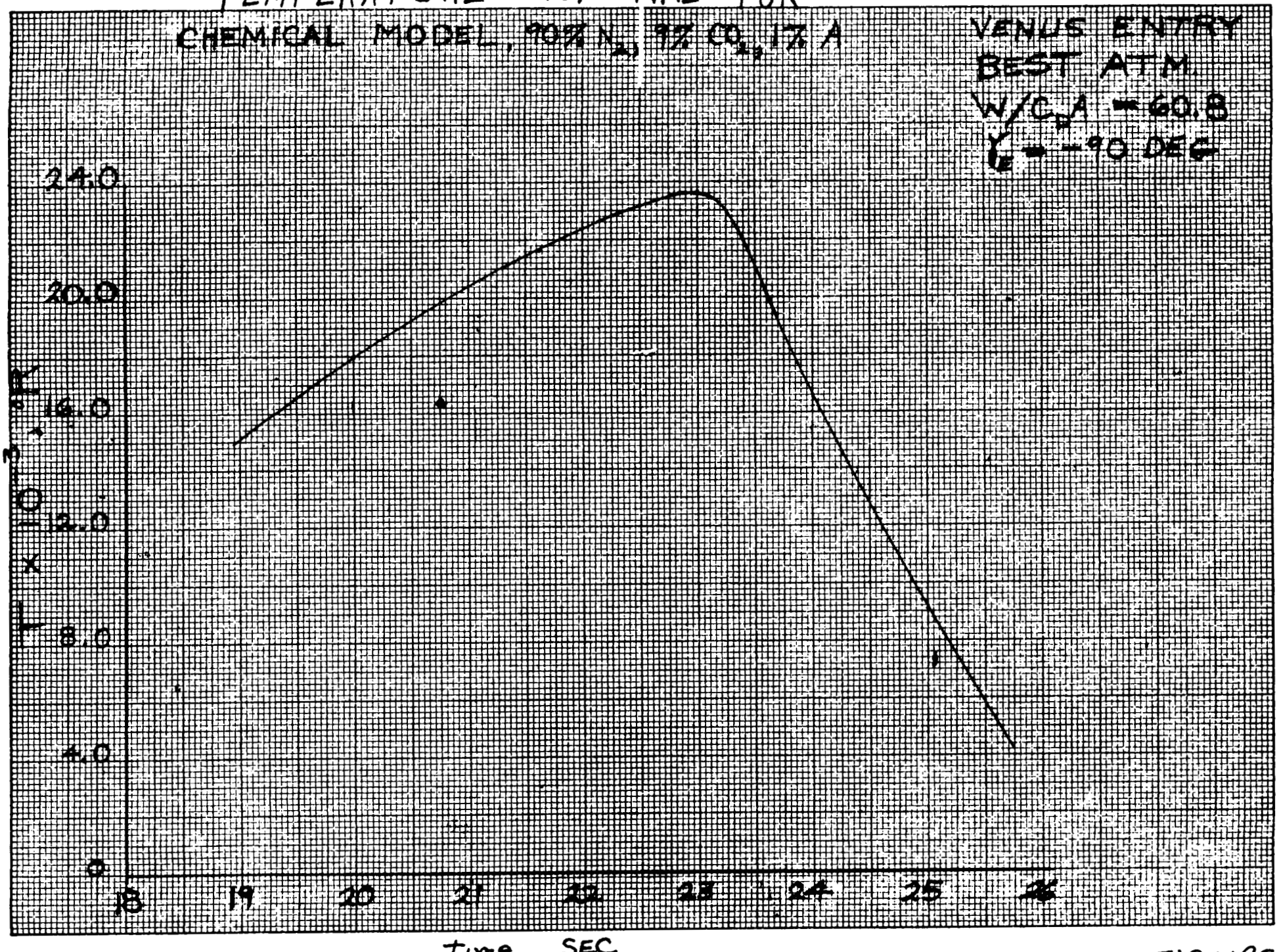

FIGURE 22

PRESSURE, DENSITY AND ELECTRON DENSITY VS TIME FOR CHEMICAL MODEL, 90% N_2, 9% CO_2, 1% A

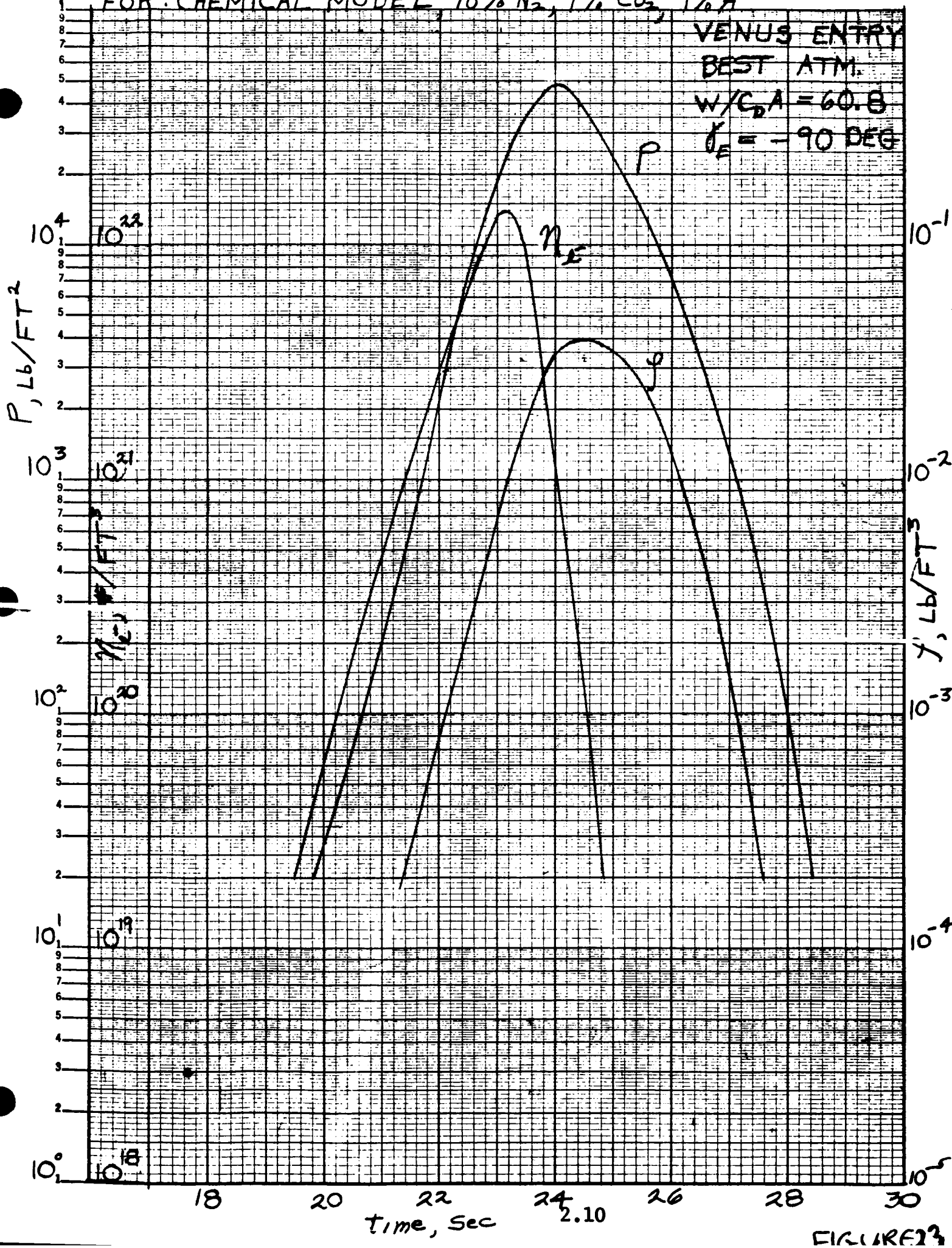

FIGURE 23

2.4 THEORETICAL RADIENT HEAT TRANSFER

The radiation for the following species has been computed for temperatures between 3000°K and 24000°K and are considered to be the important radiators in the Venus atmosphere:

1. C_2 band systems
2. CO band systems
3. N_2 band systems
4. N_2^+ band systems
5. NO band systems
6. O_2 band systems
7. CN band systems
8. O^- free bound continua
9. C^- free bound continua
10. O^+ free free continua
11. N^+ free free continua
12. C^+ free free continua
13. N deionization continua
14. O deionization continua

In addition to these, the deionization continua for carbon is to be included in the total radiance for the Venus atmosphere.

The radiance of the individual species has been plotted vs. temperature for various values of concentration. Typical results for cyanogen are given in the figure 2.4. The total radiance including all species is also being computed as a function of density,temperature and chemical composition.

Figure 2.4

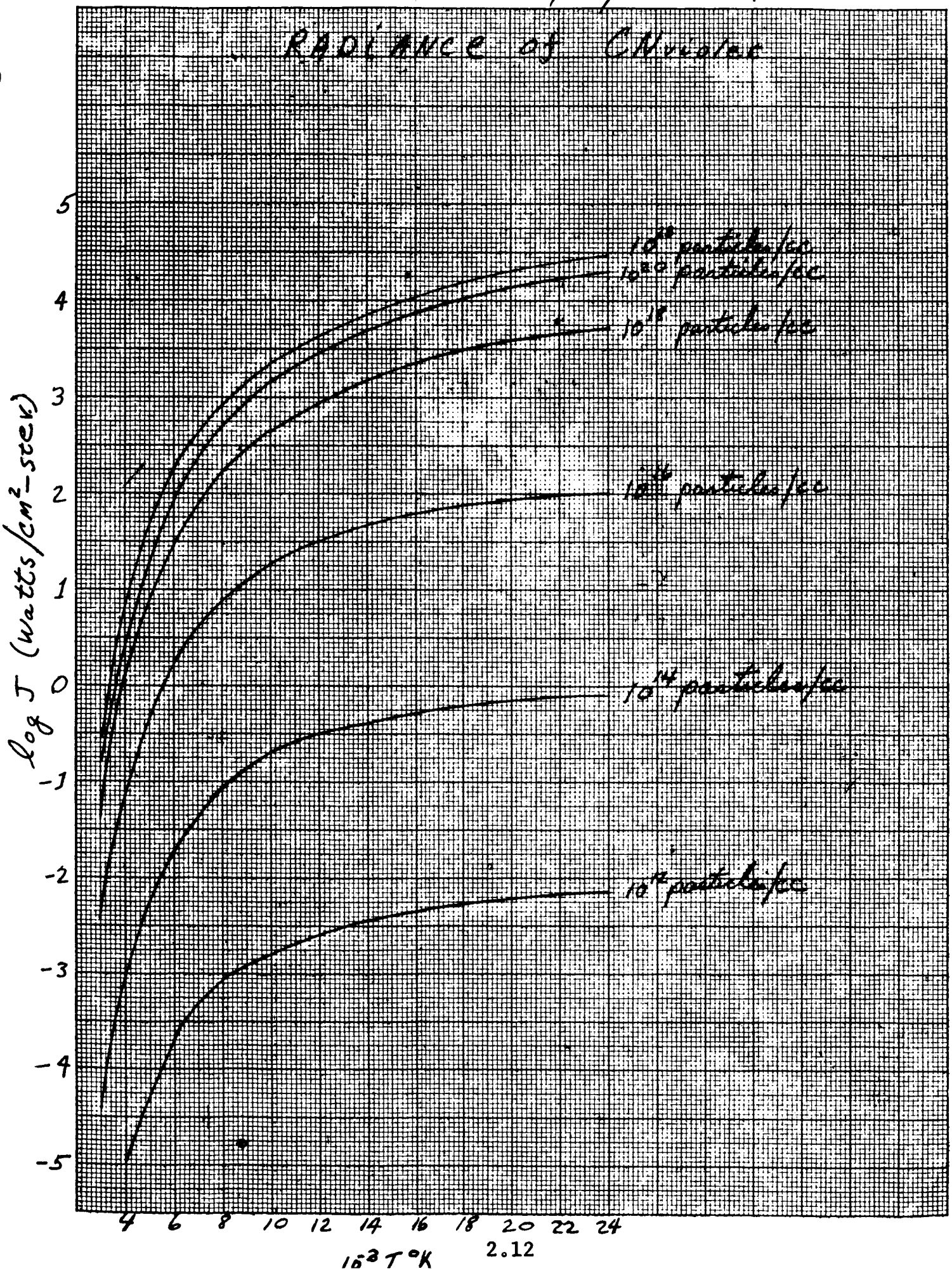
RADIANCE of CAVITY
10^{22} particles/cc
10^{20} particles/cc
10^{18} particles/cc
10^{16} particles/cc
10^{14} particles/cc
10^{12} particles/cc
log J (watts/cm²-steradian)
5
4
3
2
1
0
-1
-2
-3
-4
-5
4
6
8
10
12
14
16
18
20
22
24
10^{-3} T °K

2.5 THEORETICAL AERODYNAMIC HEAT

Work has been initiated on developing a theoretical relationship for the dependence of aerodynamic heat transfer on the level of ionization in a high temperature gas. A correlation has been found which relates the heat transfer rate and the number density of free electrons which can be obtained from the normal shock solutions.

Graphs of the variation of aerodynamic heat transfer with time are now being prepared for each of the trajectories of interest. A wide range of values of ballistic coefficient W/C_DA, entry angle γ_e, model atmosphere and chemical composition is being considered.

2.6 CHEMICAL KINETICS

During entry into the atmosphere of Venus or Mars, the gas in the flow field can be expected to have a composition appreciably different from that which equilibrium would predict. The composition must therefore be determined by the chemical kinetics of the gas. A chemical system for the determination of the kinetics has been developed and rate constants for the reactions have been found or estimated.

A system of severteen reversible reactions is being used to describe the kinetics. The system may be described by the following features:

1. The direct dissociation of the major constituents CO_2 and N_2.

2. The decomposition of N_2 by reaction with O atoms. This is, in general, a faster reaction than direct dissociation.

3. The decomposition of CO_2 by reaction with O atoms. This reaction, together with the comparatively easy O_2 dissociation, forms a chain equivalent to but faster than CO_2 dissociation.

4. The decomposition of CO_2 by reaction with H atoms. This reaction, together with OH dissociation, forms another chain equivalent to and also faster than direct CO_2 dissociation. This introduces the very important effect of water on CO_2-CO kinetics. The supplying of H atoms is represented here by H_2O decomposition, although it is really a very complex system in itself.

5. The direct ionization of various constituents, N_2, CO_2, N, CO, and O.

6. Associative ionization reactions forming N_2^+, O_2^+ and NO^+. These reactions are extremely fast once appreciable numbers of atoms are formed.

The seventeen reactions, together with the rate constants presently being used, are listed in Table 2.3. This system is being programmed for the 7090 computer. The program will iteratively calculate the reaction rates and concentrations of all species (including electron density) as a function of time.

Following the development of this program, representative calculations will be made for conditions of interest to the problem.

TABLE 2.3

	k (forward)	k (reverse)
$CO_2 + M \rightleftharpoons CO + O + M$	$1 \times 10^{8}\ e^{-86,400/T}$	1×10^{-34}
$N_2 + M \rightleftharpoons N + N + M$	$5.17 \times 10^{-6}\ T^{-1/2}\ e^{-113,000/T}$	$3.37 \times 10^{-31}\ T^{-1/2}$
$O + N_2 \rightleftharpoons N + NO$	$1.17 \times 10^{-12}\ T^{1/2}\ e^{-38,500/T}$	$2.22 \times 10^{-13}\ T^{1/2}$
$CO + M \rightleftharpoons C + O + M$	$1 \times 10^{-8}\ e^{-125,000/T}$	1×10^{-35}
$H_2O + M \rightleftharpoons H + OH + M$	$1 \times 10^{-11}\ e^{-50,300/T}$	1×10^{-31}
$CO_2 + H \rightleftharpoons CO + OH$	$5 \times 10^{-12}\ e^{-16,780/T}$	$3.83 \times 10^{-14}\ e^{-5,190/T}$
$N_2 + M \rightleftharpoons N_2 + e + M$	$2 \times 10^{-20}\ T^{3/2}\ (1 + 2 \times 10^{5}\ \frac{n_e}{n})\ e^{-181,000/T}$	5×10^{-26}
$N + M \rightleftharpoons N^{+} + e + M$	$2 \times 10^{-20} T^{3/2}\ (1 + 2 \times 10^{5}\ \frac{n_e}{n})\ e^{-158,000/T}$	1×10^{-27}
$CO_2 + M \rightleftharpoons CO_2^{+} + e + M$	$2 \times 10^{-20}\ T^{3/2}\ (1 + 2 \times 10^{5}\ \frac{n_e}{n})\ e^{-160,000/T}$	5×10^{-26}
$CO + M \rightleftharpoons CO^{+} + e + M$	$2 \times 10^{-20}\ T^{3/2} (1 + 2 \times 10^{5}\ \frac{n_e}{n})\ e^{-169,500/T}$	5×10^{-26}
$O + M \rightleftharpoons O^{+} + e + M$	$2 \times 10^{-20}\ T^{3/2} (1 + 2 \times 10^{5}\ \frac{n_e}{n})\ e^{-140,000/T}$	1×10^{-27}
$N + O \rightleftharpoons NO^{+} + e$	$1.2 \times 10^{-12}\ e^{-32,100/T}$	1×10^{-8}
$N + N \rightleftharpoons N_2^{+} + e$	$1.87 \times 10^{-14}\ T\ e^{-67,700/T}$	$1 \times 10^{-5}\ T^{-1/2}$
$O + O \rightleftharpoons O_2^{+} + e$	$2.79 \times 10^{-15}\ T^{0.65}\ e^{-80,800/T}$	$9 \times 10^{-5}\ T^{-1}$
$O + CO_2 \rightleftharpoons CO + O_2$	$1 \times 10^{-12}\ e^{-29,000/T}$	$1 \times 10^{-15}\ e^{-25,000/T}$
$O_2 + M \rightleftharpoons O + O + M$	$9.18 \times 10^{-7}\ T^{-1/2}\ e^{-59,800/T}$	$6.09 \times 10^{-32}\ T^{-1/2}$
$OH + M \rightleftharpoons O + H + M$	$1 \times 10^{-8}\ e^{-50,000/T}$	1×10^{-32}

3.0 EXPERIMENTAL VEHICLE ENVIRONMENT INTERACTIONS

3.1 HEAT PROTECTION STUDIES

3.1.1 Introduction

A considerable amount of experimental data has been generated over the past few years in connection with the behavior of ablation materials in terrestial re-entry environments. While these data have been very useful in the design of many re-entry packages, consideration of environments of different gaseous species, other than air, requires additional experimental study. In this phase of the study an investigation is being conducted to examine ablation material performance over a range of gas mixture appropriate for interpretation of behavior in environments typical of Venus and Mars.

3.1.2 Technical Approach

Ablation materials evaluation in ground based test facilities is generally conducted with rocket motors or electric arcs; however, because of the low enthalpy and uncharacterized test flow of the rocket motor, the electric arc is emerging as the better environmental test facility. Although earlier arc heater designs suffered from flow contamination from the electrode materials and were limited in the attainment of high stagnation enthalpy flows, the state of the art has greatly improved. The tandem-Gerdien arc heater, for example, developed at the MSVD's Space Sciences Laboratory (1) operates with various test configurations at stagnation air enthalpy values (h_s/RT_o) in excess of 400 with less than 100 parts per million of electrode contaminant in the flow. One such facility is a hypersonic arc wind tunnel (2) shown in Figure 3.1 with which thermal environments typical of satellite re-entry can be simulated for extremely long periods of time (in excess of 15 minutes). Another is the atmospheric free jet unit shown in Figure 3.2 which is being used to study combined radiation and convective heat transfer effects on various ablators in air environments. For this study the free jet arc stand shown in Figure 3.3 is being used.

Thermal shield materials currently used for earth re-entry vehicle designs will be investigated in the test flow of the arc facility when it is operated with gas mixtures representative of the current estimates of the Venusian and Martian atmospheres.

The specific mixtures selected for the test program are N_2; the "best" Venus model of 90% N_2, 9% CO_2 and 1% A; and the extreme model of 74% N_2, 25% CO_2, and 1% A. Tests in these three model atmospheres will provide sufficient data on the performance of the selected ablation materials over a broad range of CO_2 content from which general trends can be established. Material behavior in the pure nitrogen would be typical of that in the Martian atmosphere.

The ablation materials selected for study are well characterized both experimentally and analytically as a result of their application to earth re-entry projects. They are phenolic nylon -- a charring material, teflon -- a subliming material, and ATJ graphite -- a material whose degredation is by oxidization. The performance of these three in the various gas mixtures will provide data to judge the severity of the entry problem for Mars and Venus and will form the basis for the specification of future materials studies. Existing knowledge of the ablation characteristics in air environments will serve as a reference for evaluating re-entry performance in the selected environments.

Model tests are performed at given stagnation pressure and enthalpy values, the latter being established experimentally by means of a total calorimeter in which the energy in the test gas is extracted and determined. Exposure of the specimens to the test flow for different time intervals results in an ablation rate history from which, along with a knowledge of the heat transfer environment and the model surface temperature values, design parameters such as heat of ablation can be computed. Surface temperature is measured with a two color optical pyrometer (red tube peaks at 7500 A^o and blue tube at 4000 A^o) while the model heat transfer environment is obtained with a heat sink calorimeter slug mounted in a typical model body.

3.1.3 Status

The tandem-Gerdien arc heater as developed required modification in order to make it operational for these studies. Modifications included improved arrangement of gas, water and electrical systems to make the plasma more accessible for diagnostic and material testing. The newly installed 500 kw rectified power supply (operational 5-4-62) is being utilized in the arc heater operation and is a distinct improvement over the 200 kw bank of

of welding generators previously used. An added feature of the new arc facility is a set of argon sheathed electrodes which help reduce the electrode consumption rate. Other minor modifications and improvements were made as the facility was being assembled. Presently the unit is being calibrated after which the model testing program will begin. A photograph of the arc in operation is shown in Figure 3.4.

3.1.4 Accomplishments

To date the emphasis has been on modifying, fabricating and assembling the various arc heater units preparatory to conducting the test program. Some facility calibration has been conducted although additional runs are being made. Test gas mixtures of the desired species are now available with analyses which have been received from the supplier. A few spectral measurements have also been made of the test jet. All ablation models and calorimeters have been fabricated and instrumented and are on hand for testing.

3.1.5 Major Difficulties

The primary obstacle during the course of this program has been the delay in arriving at facility operational status. Although modifications to the arc heater were involved, the menial electrical and plumbing tasks necessary for the assembly of a new piece of test equipment have taken longer than expected.

3.1.6 Future Plans

Calibration of the facility will be completed. Ablation experiments will be conducted on the three test materials for the three test gases to the maximum test gas enthalpy level. This is expected to be approximately 400 RT_o.

The planned test program in the free jet facility will provide material performance in high enthalpy high heat transfer environments which are associated with "hard" re-entry. A logical extension to this program would be the consideration of the same materials in a test environment associated with "soft" re-entry as is the case of the many objects returned from earth orbit. Such a program can be conducted in the hypersonic arc tunnel of the Space Sciences Laboratory (see Figure 3.1) in which hot gases generated by the

tandem-Gerdien arc heater are expanded through a large ratio nozzle to low pressures to provide the above mentioned satellite type heat transfer conditions. That facility has been in operation over a sufficient time period whereby the test flows are well characterized and no delay in program initiation would ensue. All necessary total calorimeters and spectrographic and optical techniques required for flow analysis and model performance are presently available.

3.2 HEAT TRANSFER STUDIES

3.2.1 Introduction

This experimental study is concerned with the measurement of heat transfer rates to the stagnation point of a blunt body. For this purpose the existing high enthalpy shock tube facility, which is shown in Figure 3.5 is used. The tests are performed over a range of incident shock velocities and initial driven shock tube pressures simulating various flight conditions with regard to the flight velocity and the altitude. The measurements are taken in two different gas mixtures corresponding to the "best" and the extreme compositions of the atmosphere of Venus.

In order to interpret the heat transfer measurements the flow parameters have to be known. The calculation of these are completed for the case of 9% CO_2 mixture and are presented herein. The computations for the 25% CO_2 mixture are partially finished.

The experiments in the hypervelocity shock tube with the 9% CO_2 gas mixture are in progress but no results are as yet available for presentation. The tests with the extreme composition will follow.

3.2.2 Experimental Equipment

An electrically heated hypervelocity shock tube is utilized for this stagnation point heat transfer investigation as shown in Figure 3.6. The internal diameter of the driver section is 2 in. and it is 135.5 in. in length. The driver itself is 18 in. inside length with 2 1/4 in. diameter. A Lexan cylindrical sleeve with 1/4 in. wall thickness fits inside the driver tube. It is used to provide electrical insulation of the driver walls and prevent the arc from short-circuiting across to the wall.

The high voltage electrode which is insulated from the driver end flange by a Lexan bushing is a hollow copper cylinder with 3/8 in. diameter. A 1/8 in. diameter Lexan rod insulated by teflon tubing and held in position by a tapered steel washer and a nut is inserted through the center of the main electrode. A tungsten 5 mil wire is attached to the spider electrode at the

diaphragm end of the driver and by about 1 in. cotton thread to the copper main electrode. The position of the brass rod relative to the main electrode determines the breakdown voltage. This adjustment is made with the main capacitors bank disconnected using a small capacitor to prevent breaking of the wire.

The electrical circuit for the driver heating system is shown in Figure 3.7a. The energy for the arc discharge is stored in forty-seven capacitors, each rated at 5 microfarads and 20,000 volts.

Figure 3.7b shows a typical current wave form. It indicates that the circuit is critically damped and that the energy is completely dissipated in fifty microseconds. Full description of the consideration entering into the design of this test facility is presented by Warren, et al,.(3)

Helium is used as the gas heated in the driver. The diaphragm separating the driver and the driven section of the shock tube is made of stainless steel. It is scribed along two diametrical cross lines to a controlled depth (generally 20%-40% of the thickness). The required conditions of a given test run dictate the proper selection of the diaphragm. The diaphragm is found to open cleanly with a negligible loss of material.

As indicated (3) an extensive research program was necessary before a satisfactory operation of this facility was achieved. The model configuration used for the present test is a hemisphere-cylinder as shown in Figure 3.9. Its diameter is 1/2 inch and it is mounted at the end of a sting which forms integral part with the aft flange of the driven tube.

The heat transfer rate is determined by a calorimeter (thick film) gage mounted at the stagnation point of the model. The dimensions of the gage are 1/16 in. wide by 3/16 in. long. The gage is made of 0.004 in. thick hytemco alloy. The leads are brought out from the gage through the internal cavity of the model and its supporting sting and are connected in a circuit shown schematically in Figure 3.10. One of the features of the circuit is the grounding of the instrument circuit in common with the driver circuit and the connection of the gage leads across a balanced differential amplifier. These steps allow extraneous electrical effects observed earlier in the experiments (3) to be

reduced to such a level that they do not interfere with the readings of the heat transfer rate.

The driven section of the shock tube is equipped with several pressure gages equally spaced 11 in. apart along the section just ahead of the model. The signal due to the passage of the shock front is displayed on the oscilloscopes and hence the shock front velocity is determined. In addition an optical pyrometer as shown in Figure 3.8 is used. It views the stagnation region between the bow shock and the model. The relative steadiness of the luminosity generated there by the hot gas cap is interpreted as an indication of the uniformity of the flow around the model.

3.2.3 Experimental Technique

To ensure low degree of contamination the driven tube after each test is thoroughly wiped with alcohol and all traces of materials originating in the driver are removed. The tube is then evacuated to about 5 microns. The leak rate normally does not exceed 10 microns per minute. At this point the tube is filled with the test gas to the required pressure P1 (normally 1, 5 or 25 mm). To minimize the impurities due to outgasing of the walls the test gas mixture is allowed to flow through the tube at a rate of approximately 20 tube volumes per minute for about 30 minutes. The initial pressure is measured with a McLeod gage.

The output of the heat transfer gage is displayed on an oscilloscope and photographed using Polaroid camera. The relation between the heat transfer rate $\dot{q}$ and the change of the voltage with time across the gage is expressed by the simple expression:

$$\dot{q} = K \frac{1}{E_o} \frac{dE}{d\tau}$$

and

$$K = \frac{\rho c L}{\alpha}$$

where

ρ = density of gage material
c = specific heat of gage material
L = gage thickness
α = temperature coefficient of resistivity
E_o = initial voltage across the gage

Since the bulk properties of the gage material are well known the coefficient K can be easily calculated and the gage response established without an extensive calibration procedure.

3.2.4 Shock Tube Parameters

Using the equilibrium thermodynamic properties computed by the Thermochemistry Unit for the established two gas mixtures, one with the nominal content of 9% CO_2, 90% N_2 and 1% A and the other with 25% CO_2, 74% N_2 and 1% A, various gas dynamic properties associated with traveling and stationary shock fronts are calculated and charted as functions of shock velocity and the driven tube initial pressures.

The tabulated values of the equilibrium thermodynamic properties were cross-plotted and the solution of the Rankine-Hugoniot shock relations obtained employing iterative hand computations. All calculations were made for three initial driven tube pressures of P_1 = 1 mm, 5 mm and 25 mm of Hg. The initial driven tube temperature, T_1, was always taken to be 294°K. The range of shock velocities, U_s, between 10,000 ft/sec. and 30,000 ft/sec. was covered. At present only the charts for 9% CO_2 mixture are available. Similar calculations for the 25% CO_2 mixture are in progress.

3.2.4.1 Incident Shock

The state of the gas on both sides of a normal shock is related by three basic equations corresponsing to the physical principles of the conservation of mass, momentum and energy. These are:

$$u_2 = u_s \left(1 - \frac{\rho_1}{\rho_2}\right)$$

$$p_2 - p_1 = \rho_1 u_s^2 \left(1 - \frac{\rho_1}{\rho_2}\right)$$

$$h_2 - h_1 = \frac{1}{2} u_s^2 \left[1 - \left(\frac{\rho_1}{\rho_2}\right)^2\right]$$

where
- h = enthalpy
- p = pressure
- u = velocity
- ρ = density

and subscripts 1 and 2 refer to regions ahead and behind the incident shock. The simultaneous solution of these equations together with the available plots of the equilibrium state produces results which are plotted in Figures 3.15, 3.18, 3.21, 3.24 and 3.26.

3.2.4.2 Stationary Normal Shock

After the passing of the incident shock the model finds itself in a supersonic quasi-steady flow with the properties of region 2. A bow shock is formed ahead of the model. The flow close to the axis of symmetry is decelerated to subsonic velocity. The state of the gas on both sides is governed by the same three conservation laws.

$$\rho_2 u_2 = \rho_3 u_3$$

$$P_3 - P_2 = \rho_2 u_2^2 \left(1 - \frac{\rho_2}{\rho_3}\right)$$

$$h_3 - h_2 = \frac{1}{2} u_s^2 \left[1 - \left(\frac{\rho_2}{\rho_3}\right)^2\right]$$

where subscript 3 refers to region behind the bow shock. The calculation produced the results which are presented in Figures 3.16, 3.19, 3.22 and 3.25.

3.2.4.3 Stagnation Region

The flow along the stagnation streamline in region 3 is decelerated to a stop at the body surface. The stagnation conditions are found as follows. The enthlpy is given directly by $h_s = h_3 + 1/2\ U_3^2$. The stagnation pressure is computed approximately by assuming incompressible flow $P_s = P_3 + 1/2\ P_3\ U_3^2$. Both the stagnation temperature and the corresponding density are read off directly from the thermodynamic state charts and plotted in Figures 3.17, 3.20 and 3.23.

3.2.5 Related Studies

A brief outline of related heat transfer investigations which were done under a different contract will be presented here.

Stagnation point heat transfer measurements were conducted in air using the present 2" diameter hypervelocity shock tube over a relatively wide range of stagnation enthalpy levels. The experimental results shown in Figure 3.11 were obtained for an incident shock Mach number range of 13 to about 25. This corresponds to re-entry velocity enthalpy simulation of approximately 20,000 to 40,000 ft/sec. The driver tube initial pressure levels were 1, 5 and 25 mm of Hg so that stagnation point pressure levels simulation corresponds to approximately 55,000 to 120,000 ft altitude. These initial pressures assured test time for the heat transfer measurements.

The scatter of the preliminary data as shown in the figure is attributed to extraneous electrical effects. These were reduced to the level shown by the modification of the gage circuitry.

The comparison of the test data with Scala's theory (4) which includes specific contributions of atoms, molecules, ions and electrons in the hypersonic laminar boundary layer indicates good agreement over the whole range of simulated flight conditions. Using the emissivities of the radiating species in hot gas cap around the front part of the model the radiant contribution to the measured heat transfer was evaluated (see Figure 3.12) and found that at the conditions of the tests in the hypervelocity shock tube this heat flux is relatively small compared to the convective heat flow. At low shock Mach numbers the results of Rose and Stark (5) agree with the present data. At higher enthalpy levels the data of Reference 6 indicate much lower heat transfer rates than the results of experiments at GE MSVD. At the same time the analysis of Adams indicates that the effects of ionization would increase the stagnation point heat transfer by no more than thirty percent above that obtained from the extrapolation of results obtained for dissociated air.

It was noted by Warren et. al. (3) that the heat transfer measurements in a straight shock tube can be effected by the insufficient test time. This is the time between the beginning of the steady flow established around the test model after the passing of the incident shock wave and the arrival of the diffusing contact discontinuity. It is found to be dependent on the initial pressure in the driven tube and its diameter. Low initial pressure and small diameter can reduce this time to

almost nil. The test results of Offenhartz (5) were obtained in a combustion driven 1-1/2" diameter shock tube and according to Camm (7) the steady flow was of insufficient duration to permit obtaining valid heat transfer data. Further explanation of possible sources of error is elaborated by Warren and Harris (8).

In the course of the experimental studies of the stagnation point heat transfer some tests were also conducted in pure CO_2 and N_2 gases. The results of these tests are shown in Figures 3.13 and 3.14 respectively. Included also are the only other experimental results in CO_2 (9, 10) and in N_2 (9). All of them, however, were obtained at relatively low shock velocities. The new theroretical results obtained by Scala for heat transfer in dissociated carbon dioxide, based on five component mixtures of gaseous species including CO_2, CO, $C_{(g)}$, O and O_2 are also shown in Figure 11. It should be noted here that the experimental points generally lie close to the estimated curve of Scala and disagree significantly with the theoretical results of Hoshizaki (11). It has been pointed out by Scala that the general difference between his results and the lower heat transfer estimates in the ionization regime of several other investigators is caused by his more exact treatment of the transport properties (4 component system , with all diffusion coefficients included, for example, compared to a 2 component system for each of the other studies).

3.2.6 Future Plans

With all the necessary input information now available, the following is the program for the second half of the study period.

a. Complete the computation of the shock tube parameters for the 25% CO_2 gas mixture.

b. Continue the experimental phase by obtaining data to evaluate theoretical calculations of the flow parameters and heat transfer rates.

c. Correlate the data with flight conditions as determined by the trajectories envelope.

d. Using the equilibrium compositions and available emissivity data synthetize the contribution of radiant heat transfer to the measured quantities in the shock tube.

e. Using the newly developed total radiation cavity gage an attempt will be made to measure the radiation from the hot gas cap around the model.

REFERENCES

1. McGinn, J.; Arc Development; GE TIS R61SD201

2. Warren, W. R., and Diaconis, N. S.; Air Arc Simulation of Hypersonic Environments; GE TIS R62SD25; (Pres. Int. Hypersonics Conf., M.I.T. Cambridge, Mass, Aug. 16-18, 1961).

3. Warren, W. R., Rogers, D. A., and Harris, C. J.; The Development of an Electrically Heated Shock Driven Test Facility; TIS R62SD37, GE MSVD.

4. Scala, S. M.; Heating Problems of Entry into Planetary Atmospheres from Supercircular Orbiting Velocities; Proceedings of the USAF ASD Symposium on Aerothermoelasticity, Dayton, Ohio, October 1961.

5. Rose, P. H., and Stark, W. I.; Stagnation Point Heat Transfer Measurements in Dissociated Air; JAS, Vol. 25, No. 2, February, 1958.

6. Offenhartz, E., Weisblatt, H., and Flagg, R. F.; Stagnation Point Heat Transfer Measurements at Super-Satellite Speeds; Journal of the Royal Aeronautical Society; January 1962.

7. Camm, J.; Escape Velocity Shock Tube with Arc-Heated Driver; Avco-Everett Research Laboratory Research Report presented a 2nd Hypervelocity Symposium, Denver, 1962.

8. Warren, W. R., Harris, C. J.; Experimental Measurement of Hypervelocity Stagnation Point Heat Transfer; GE MSVD, Advanced Aerodynamics TM 146, 1962.

9. Rutowski, R. W., and Chan, K. K.; Shock Tube Experiments Simulating Entry into Planetary Atmospheres; LSMD-288139, January 1960.

10. Yee, Layton et al; Ballistic Range Measurement of Stagnation Point Heat Transfer in Air and CO_2 at Velocity up to 18,000 ft/sec; TN-D777, March 1961.

11. Hoshizaki, H.; Heat Transfer in Planetary Atmospheres at Super-Satellite Speeds; ARS Preprint 2173-61, October, 1961.

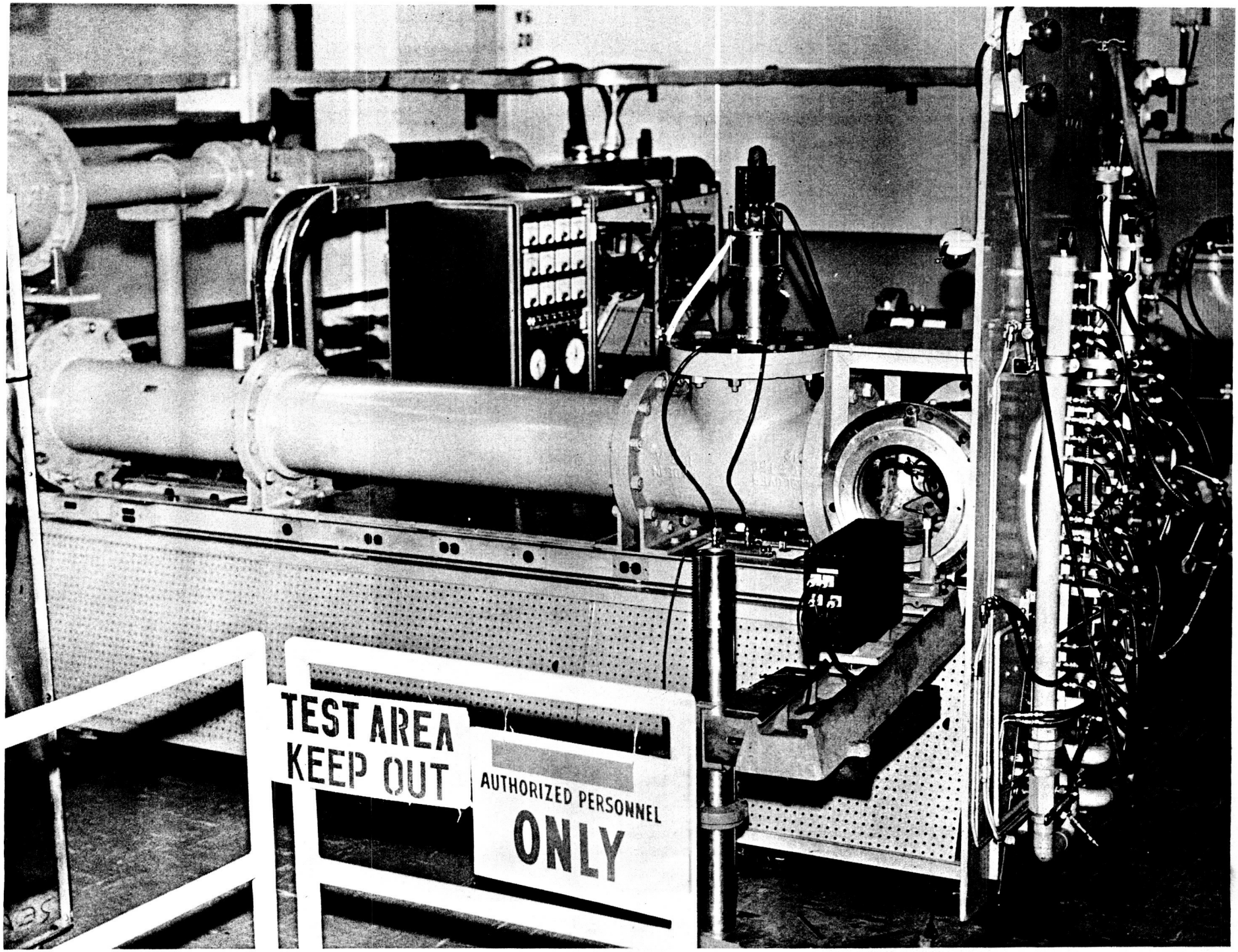

Figure 3.1 Hypersonic Arc Wind Tunnel

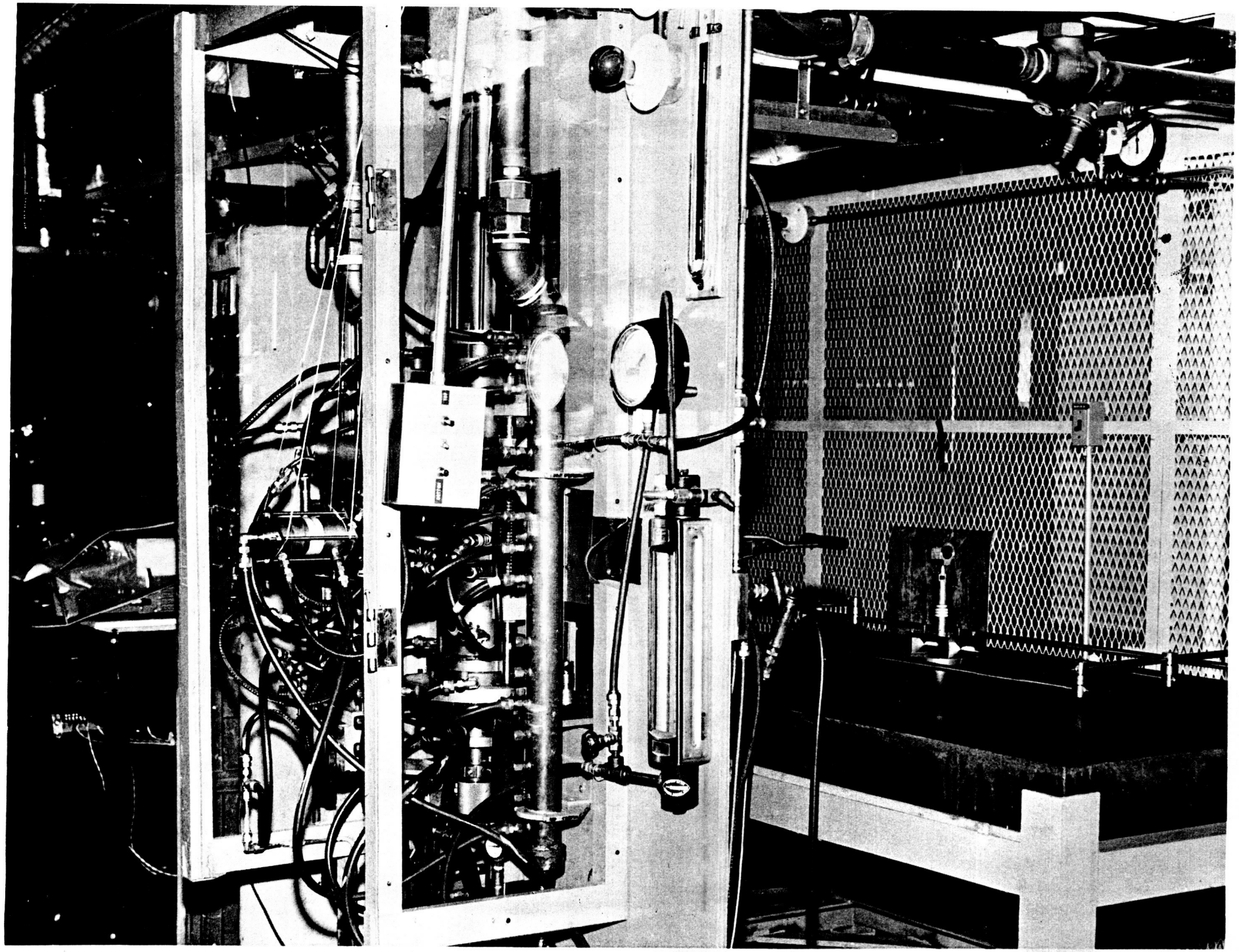

Figure 3.2 - Atmospheric Free Jets are radiative and convective heat transfer studies

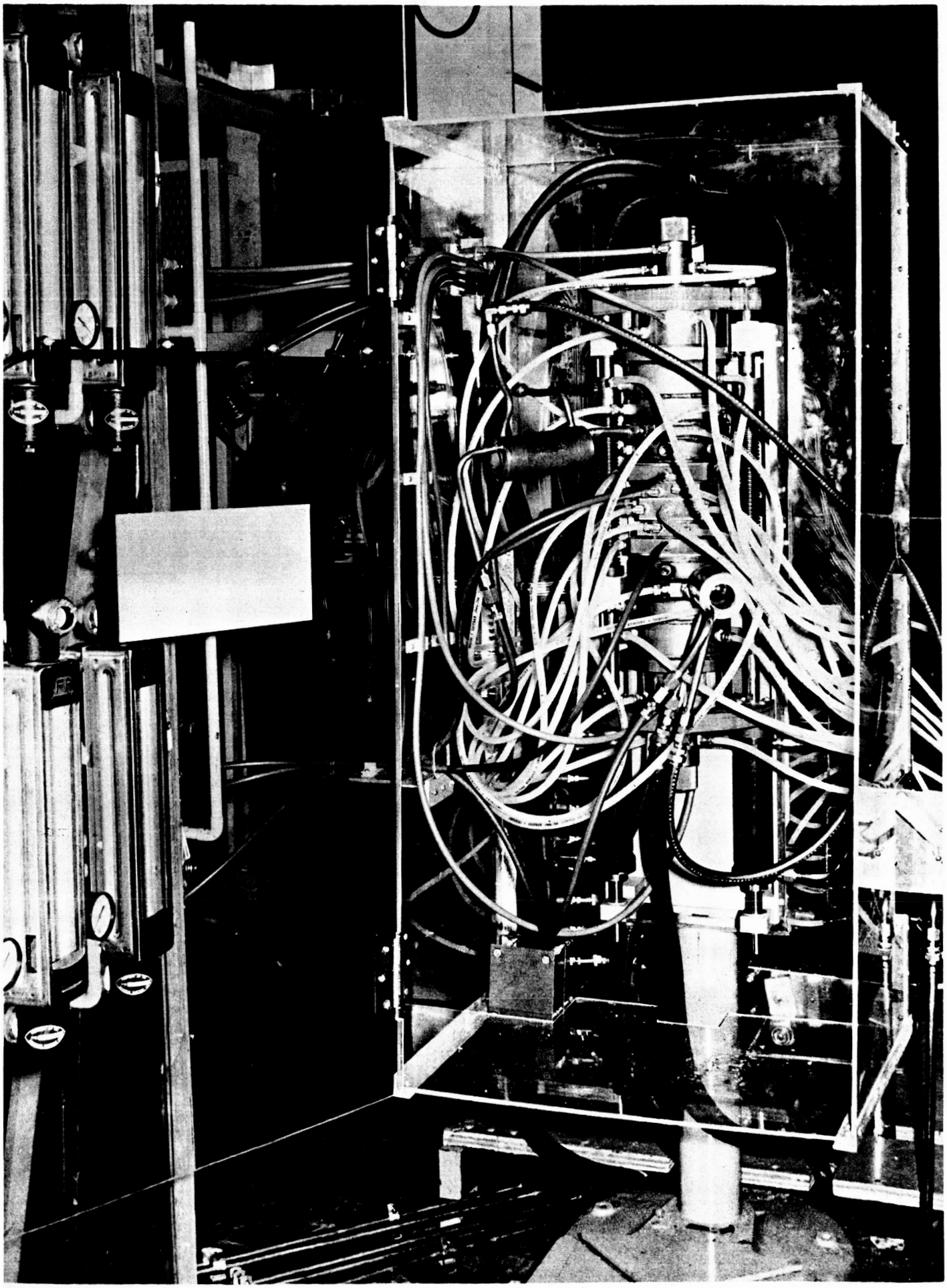

Figure 3.3 - Atmospheric Free Jet Arc (Venus-Mars Capsule Study)

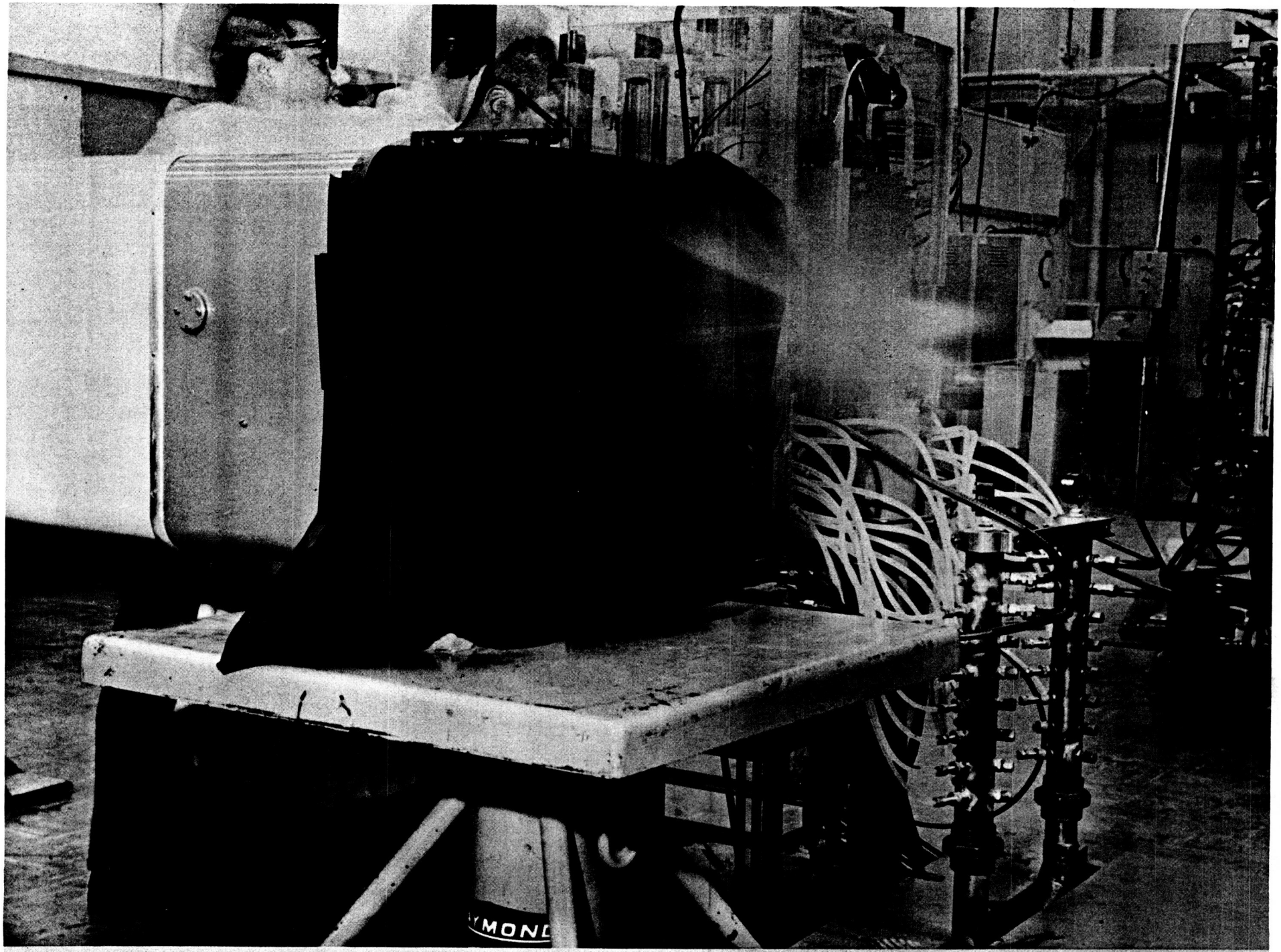

Figure 3.4 - Venus-Mars Free Jet Arc Calibration Run

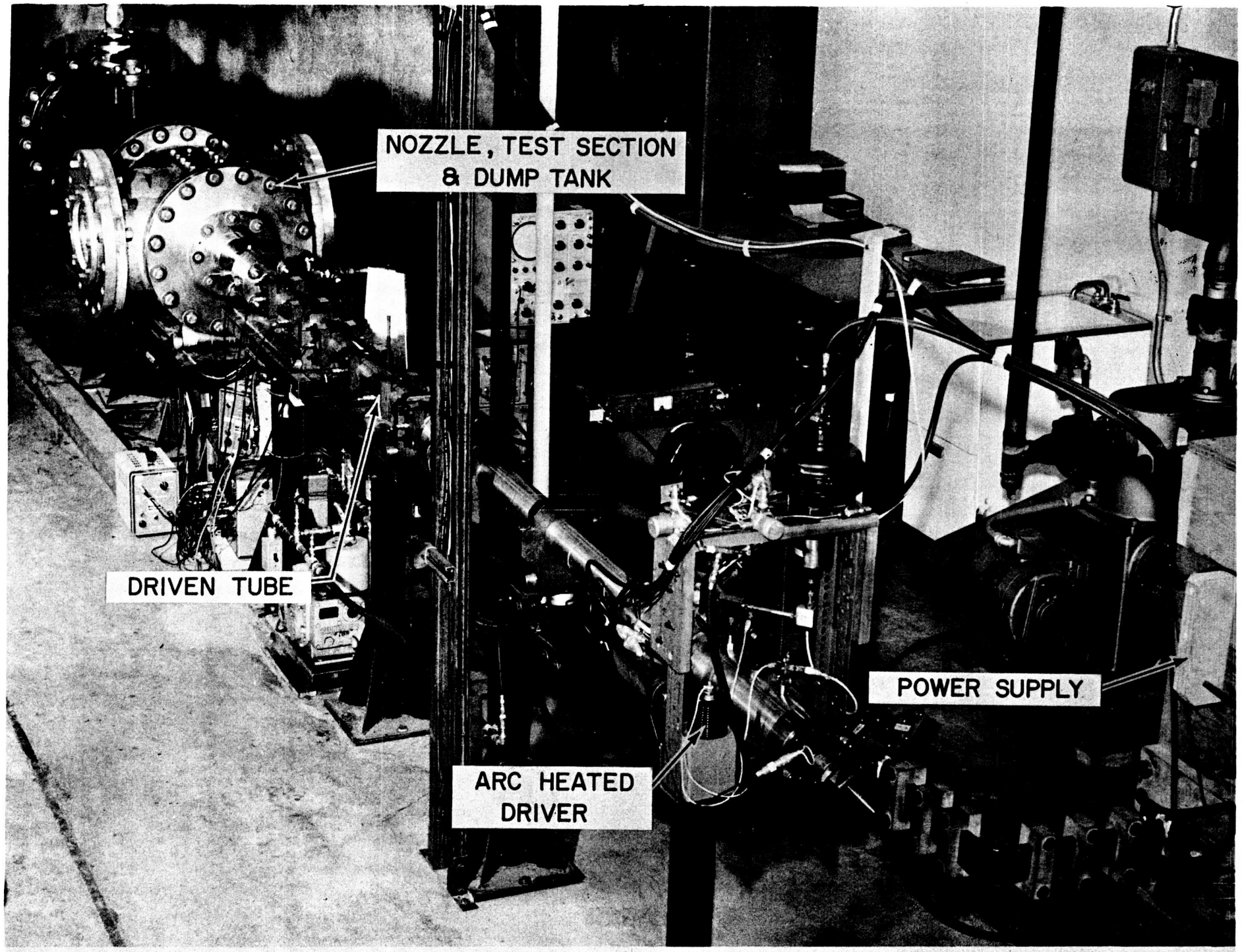

Figure 3.5 - High Enthalpy Shock Tube Facility

DESIGN OF ARC HEATED SHOCK TUBE

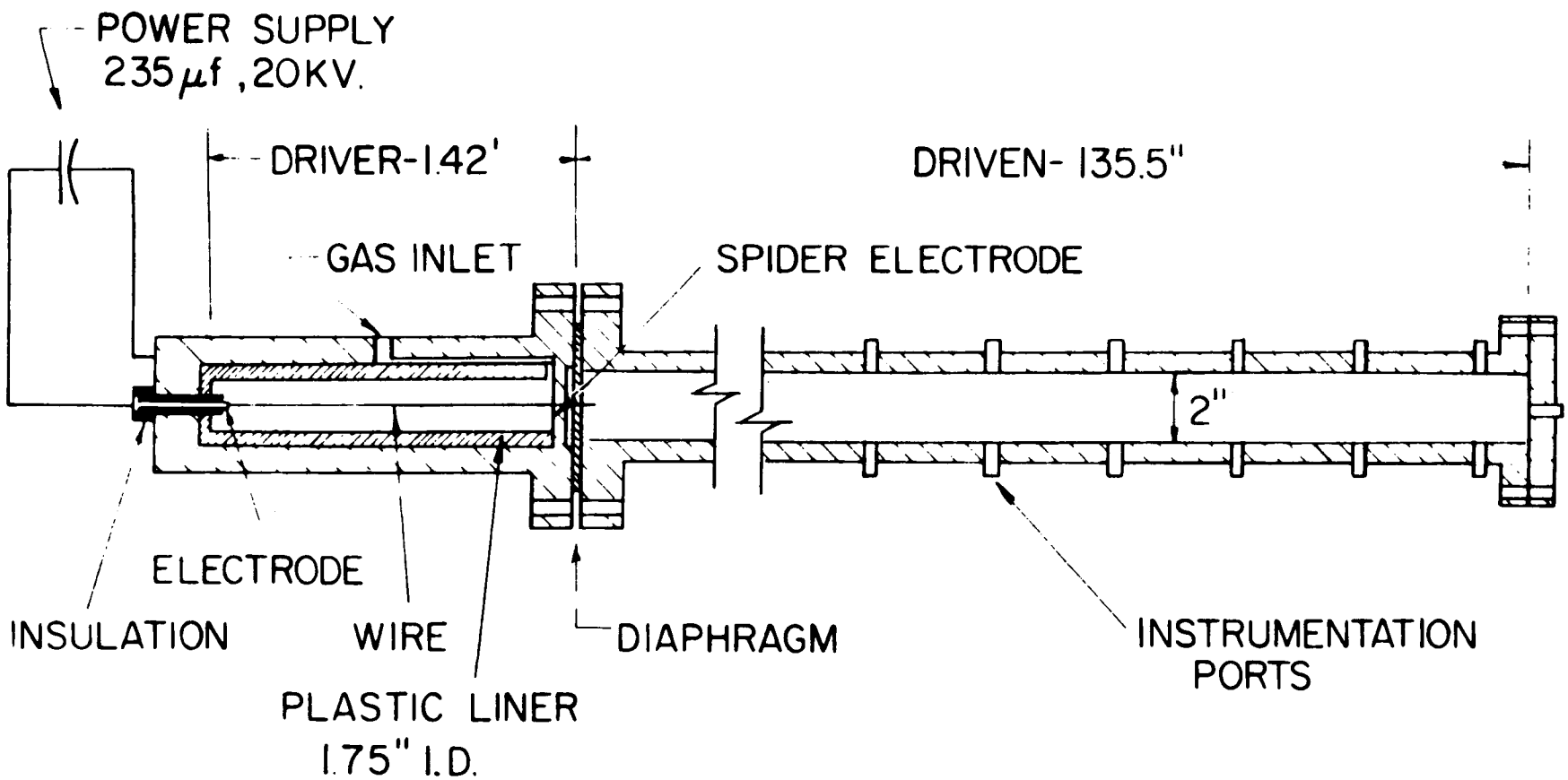

FIG. 3.6

TYPICAL ELECTRICAL CHARACTERISTICS PROTOTYPE SHOCK TUBE

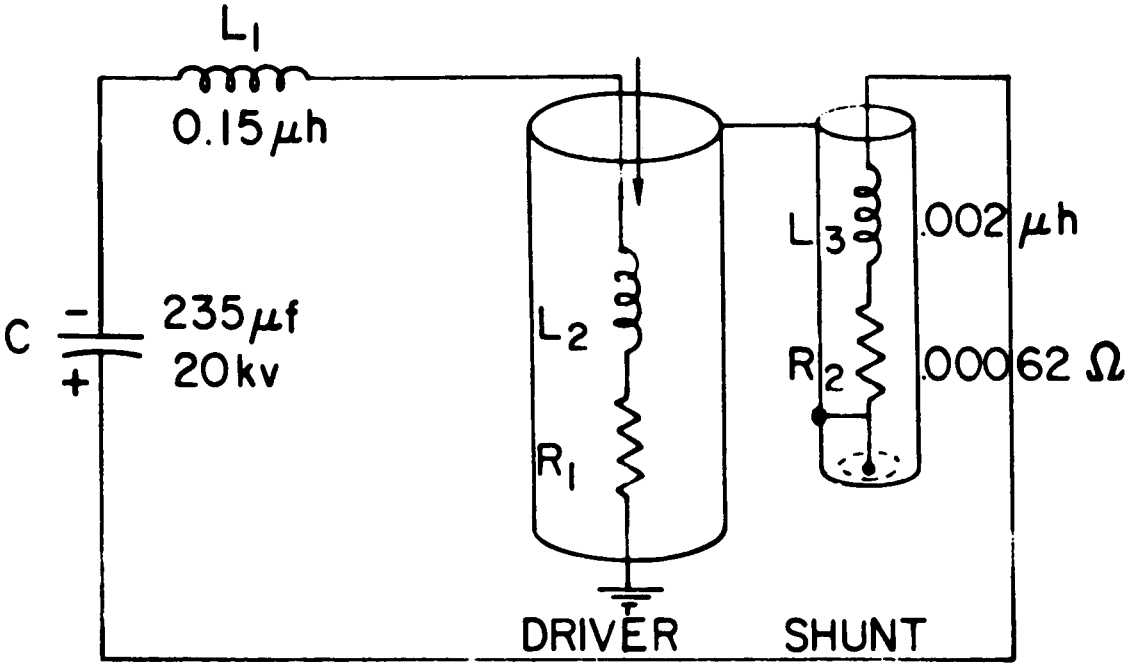

a. CIRCUIT DIAGRAM

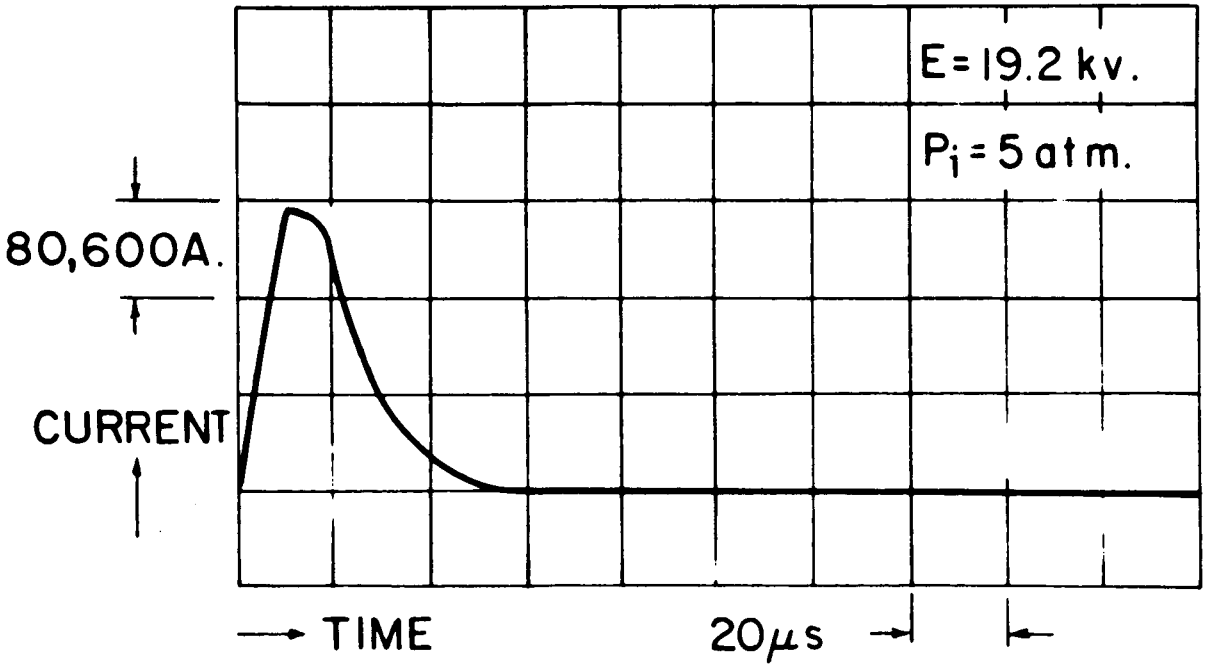

b. CURRENT WAVEFORM

FIG. 3.7

A101A064

STRAIGHT TUBE TEST CONFIGURATION
MODEL HEAT TRANSFER MEASUREMENTS

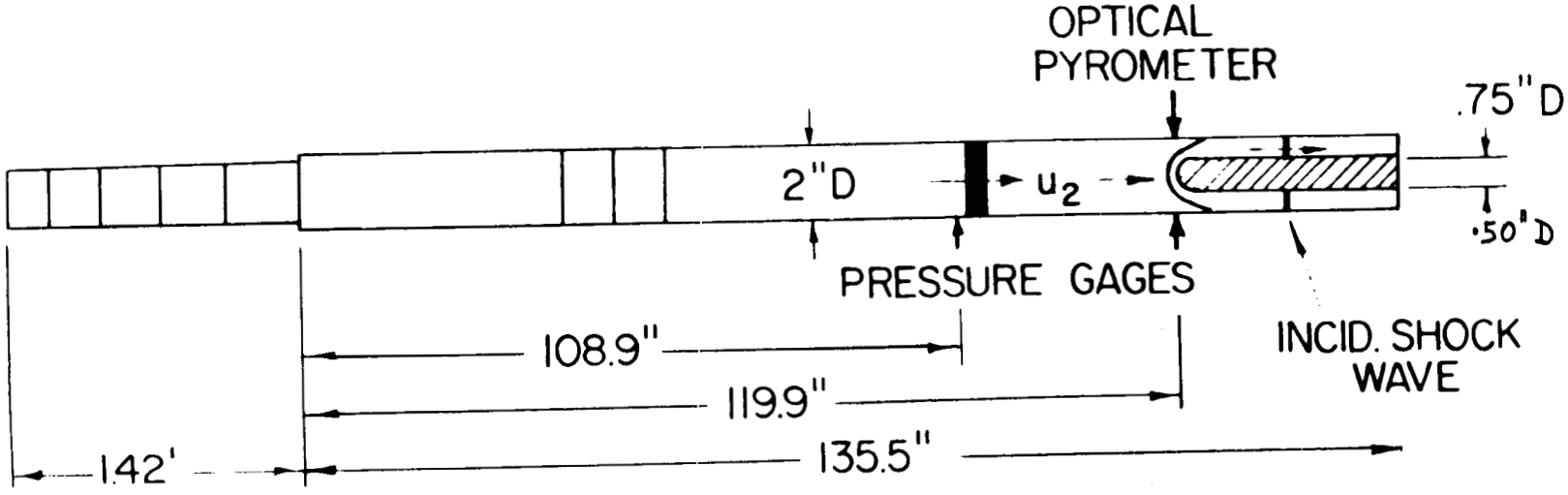

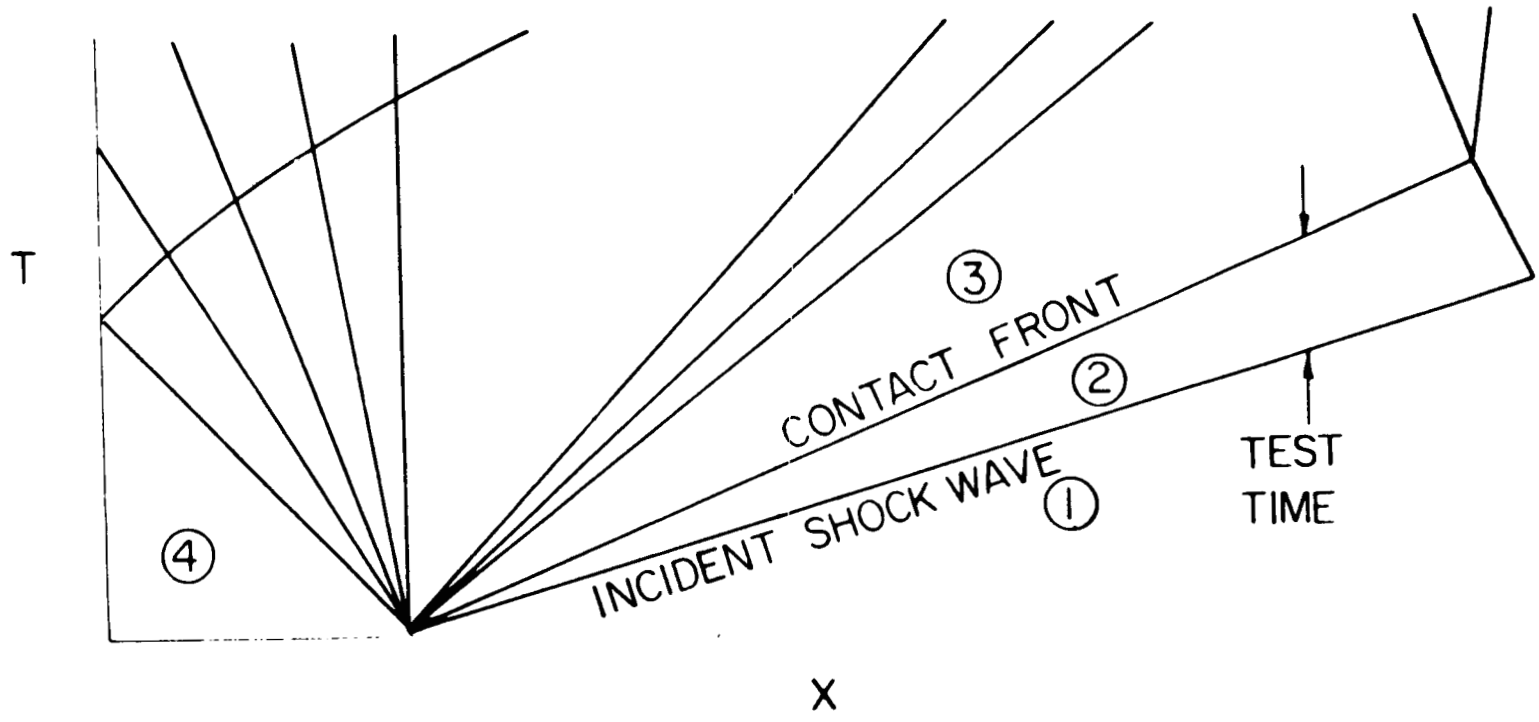

FIG 3.8

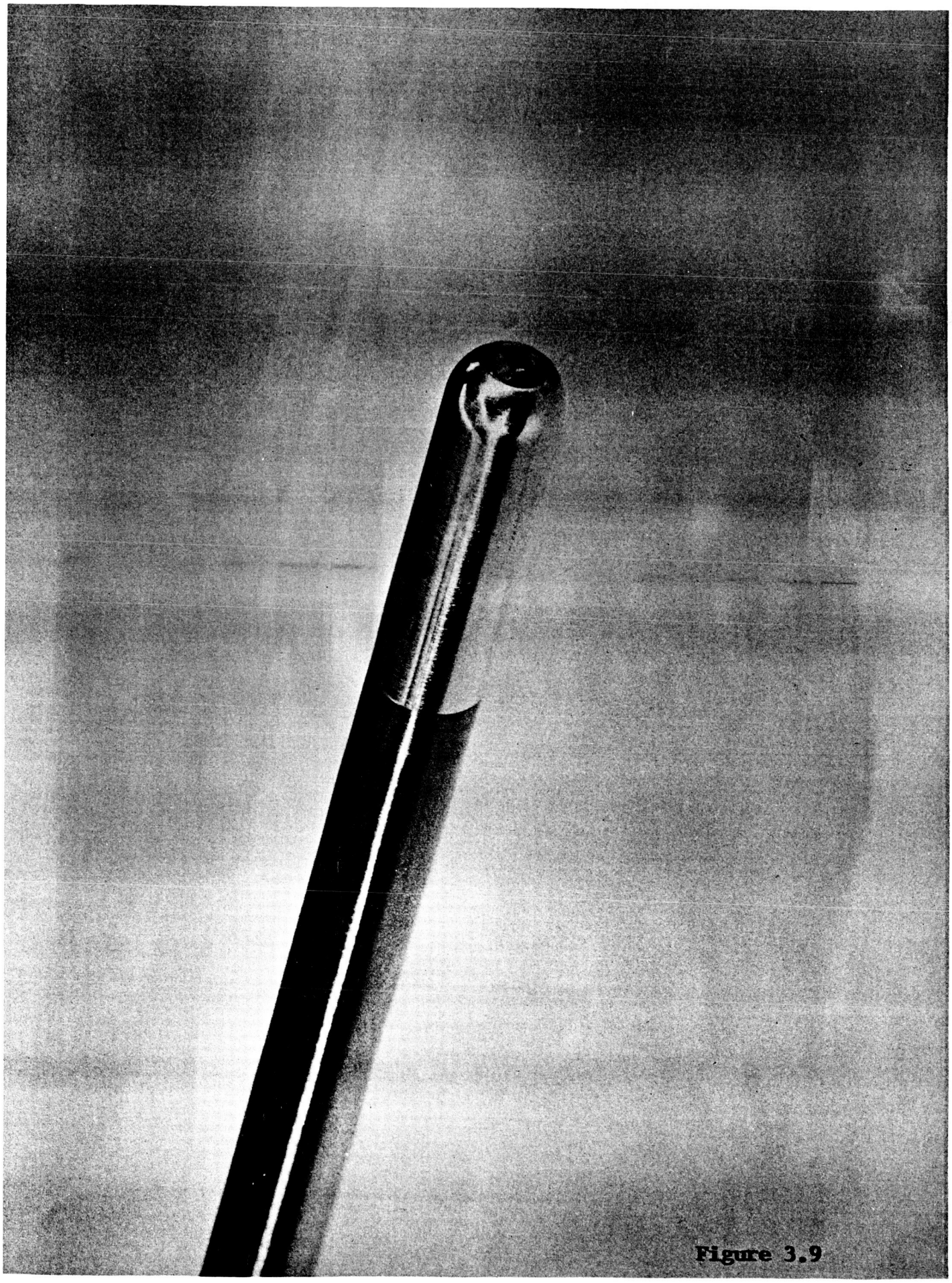

Figure 3.9

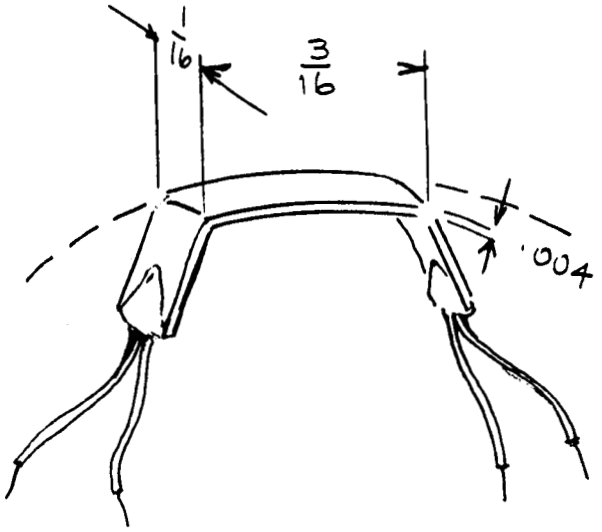

a. CALORIMETER GAUGE

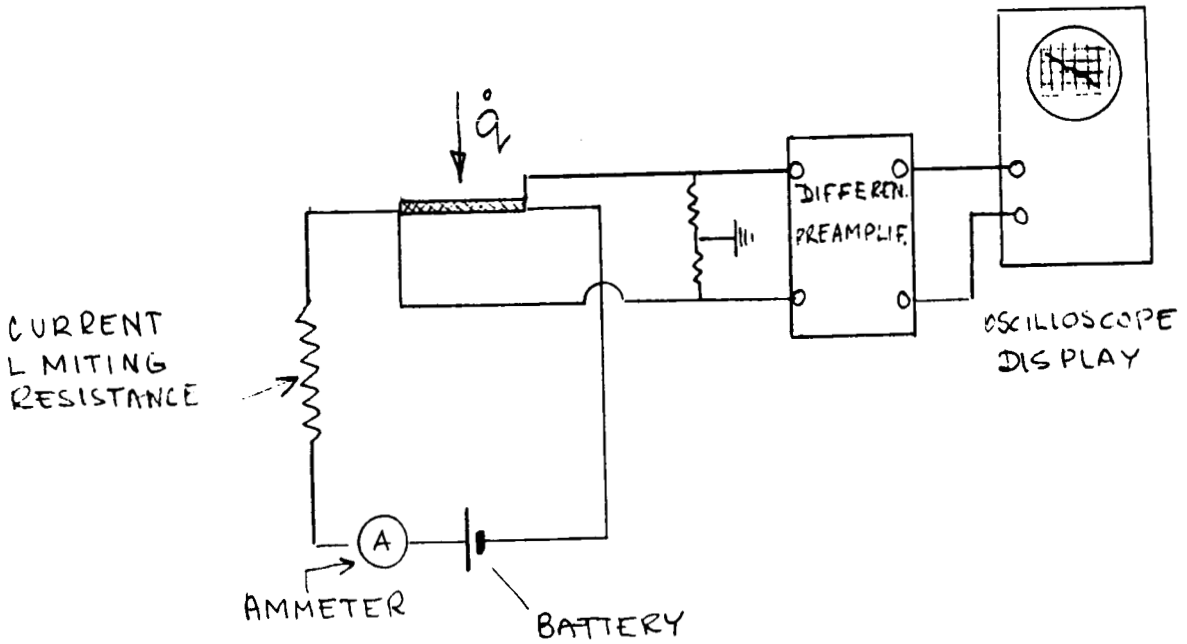

b. SCHEMATIC OF GAUGE CIRCUIT

FIG 3.10

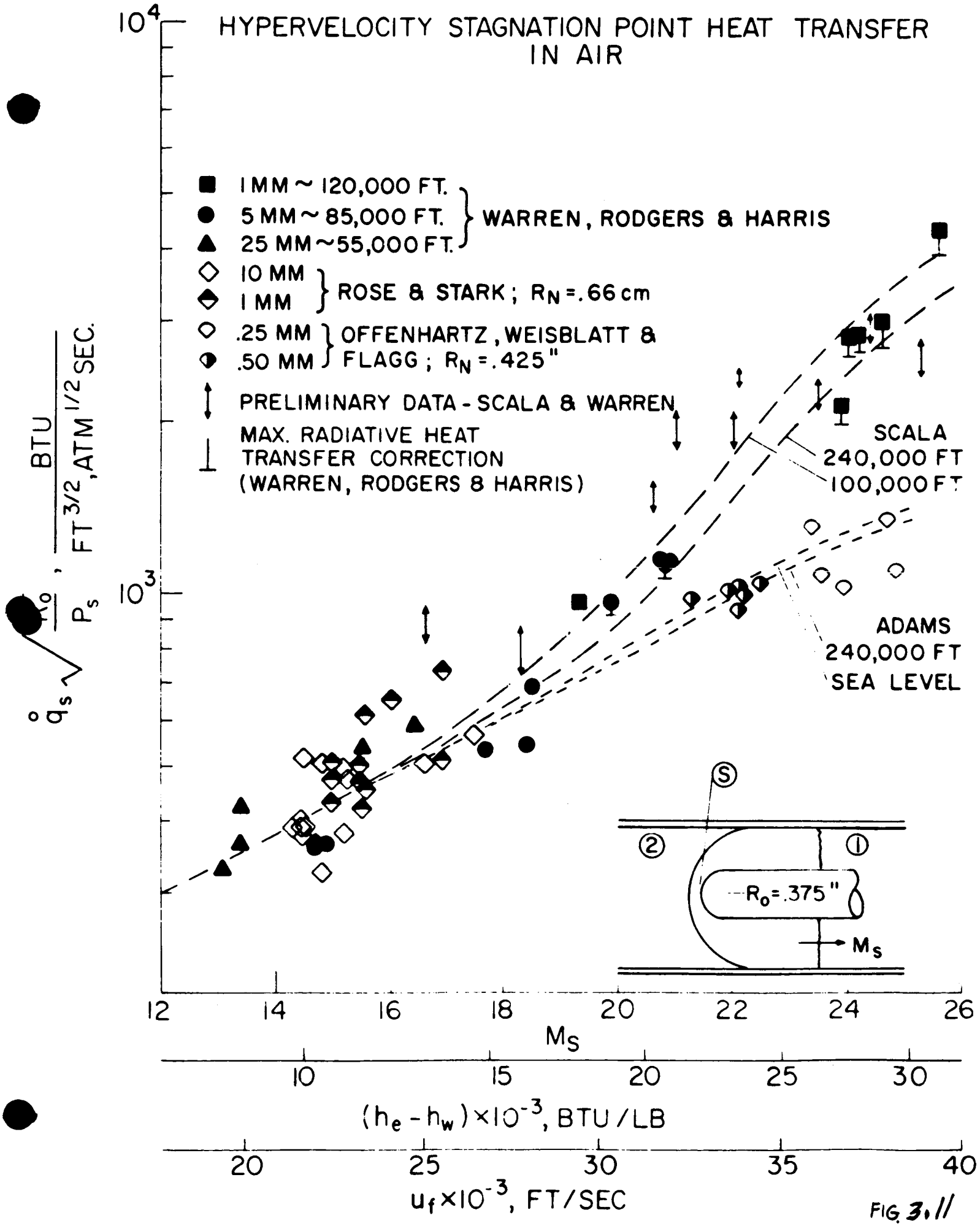
HYPERVELOCITY STAGNATION POINT HEAT TRANSFER IN AIR
1 MM ~ 120,000 FT.
5 MM ~ 85,000 FT.
25 MM ~ 55,000 FT.
WARREN, RODGERS & HARRIS
10 MM
1 MM
ROSE & STARK; R_N = .66 cm
.25 MM
.50 MM
OFFENHARTZ, WEISBLATT & FLAGG; R_N = .425"
PRELIMINARY DATA - SCALA & WARREN
MAX. RADIATIVE HEAT TRANSFER CORRECTION (WARREN, RODGERS & HARRIS)
SCALA
240,000 FT
100,000 FT
ADAMS
240,000 FT
SEA LEVEL
R_o = .375"
M_s
$\dot{q}_s \sqrt{\frac{R_o}{P_s}}$, $\frac{BTU}{FT^{3/2}, ATM^{1/2} SEC.}$
10^4
10^3
12 14 16 18 20 22 24 26
M_S
10 15 20 25 30
$(h_e - h_w) \times 10^{-3}$, BTU/LB
20 25 30 35 40
$u_f \times 10^{-3}$, FT/SEC

FIG. 3.11

EQUILIBRIUM RADIATIVE HEAT TRANSFER AT THE STAGNATION POINT OF THE MODEL

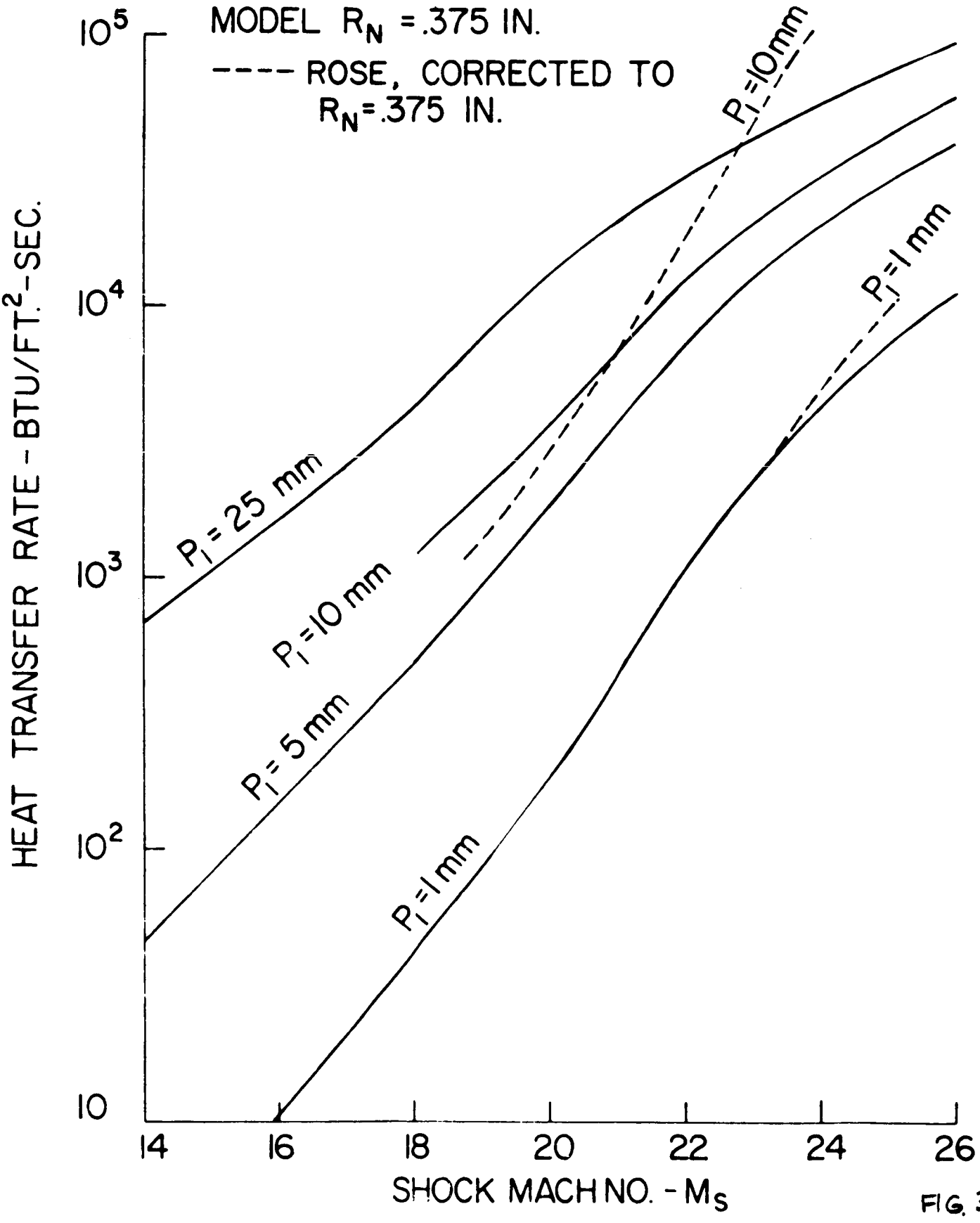

FIG. 3.12

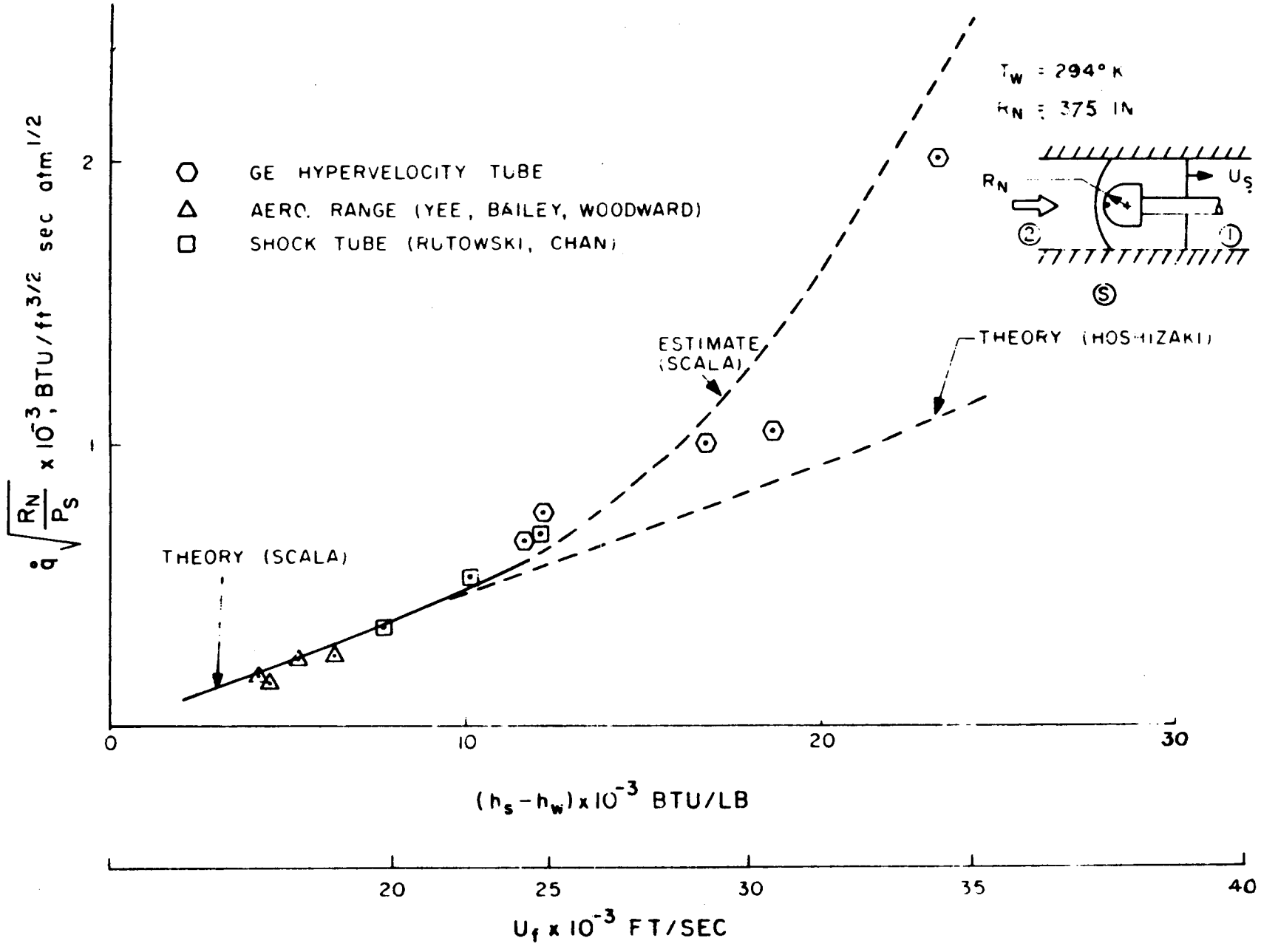

STAGNATION POINT HEAT TRANSFER IN CARBON DIOXIDE

FIG. 3.13

A101A

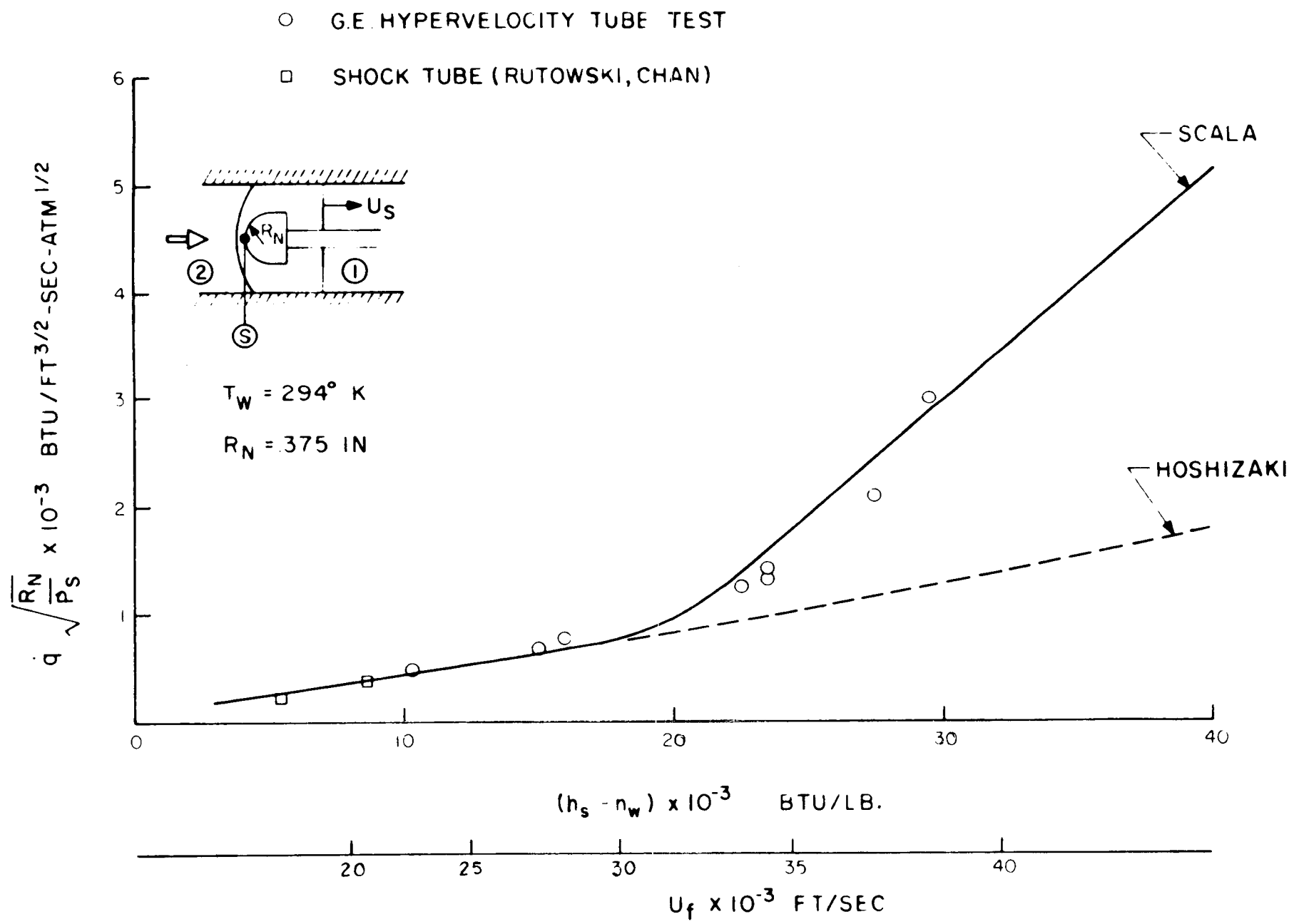

STAGNATION POINT HEAT TRANSFER IN NITROGEN

FIG. 3.14

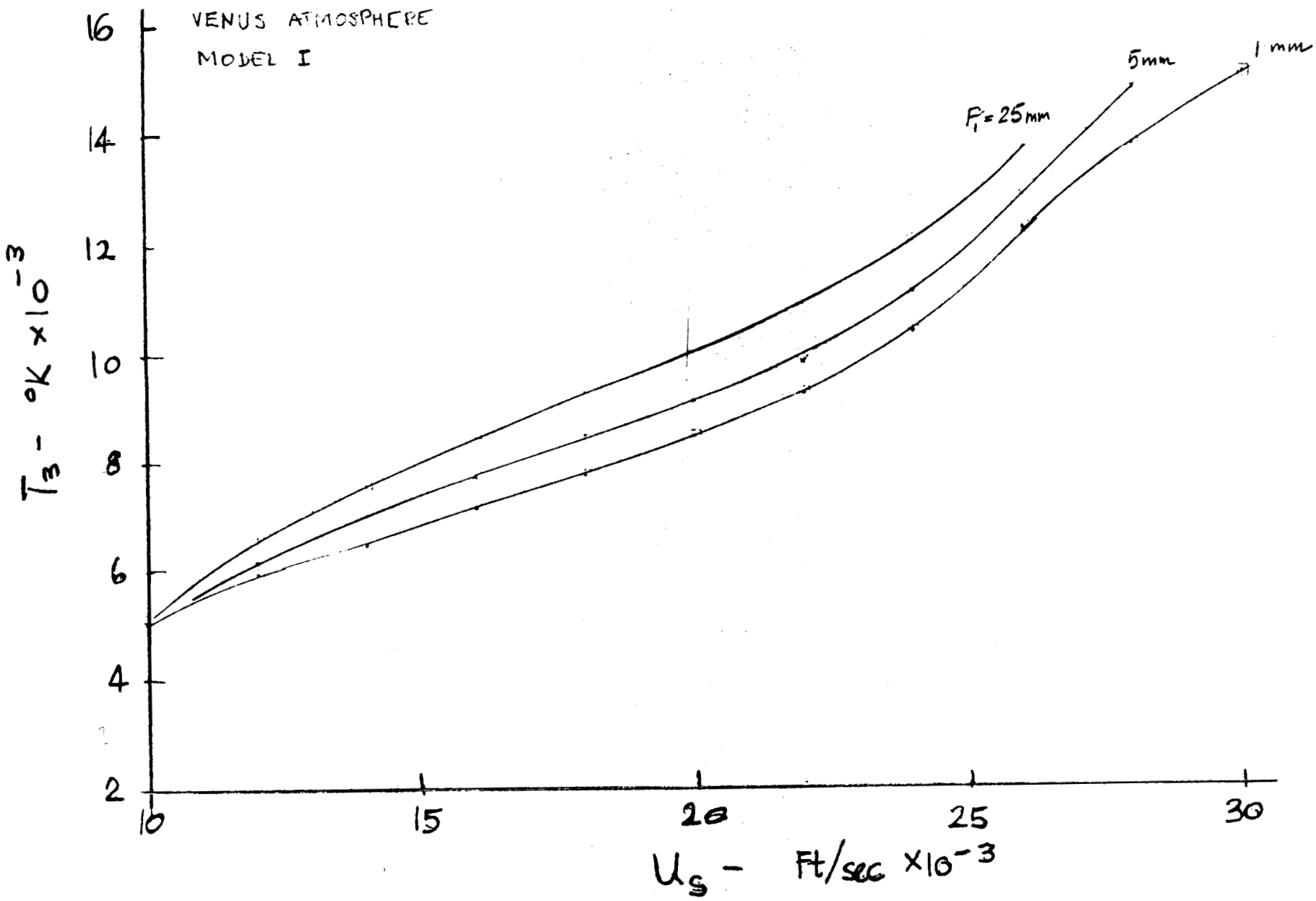
VENUS ATMOSPHERE
MODEL I
$P_1 = 25$ mm
5 mm
1 mm
T_3 - °K $\times 10^{-3}$
16
14
12
10
8
6
4
2
10
15
20
25
30
U_s - Ft/sec $\times 10^{-3}$

Fig 3.16

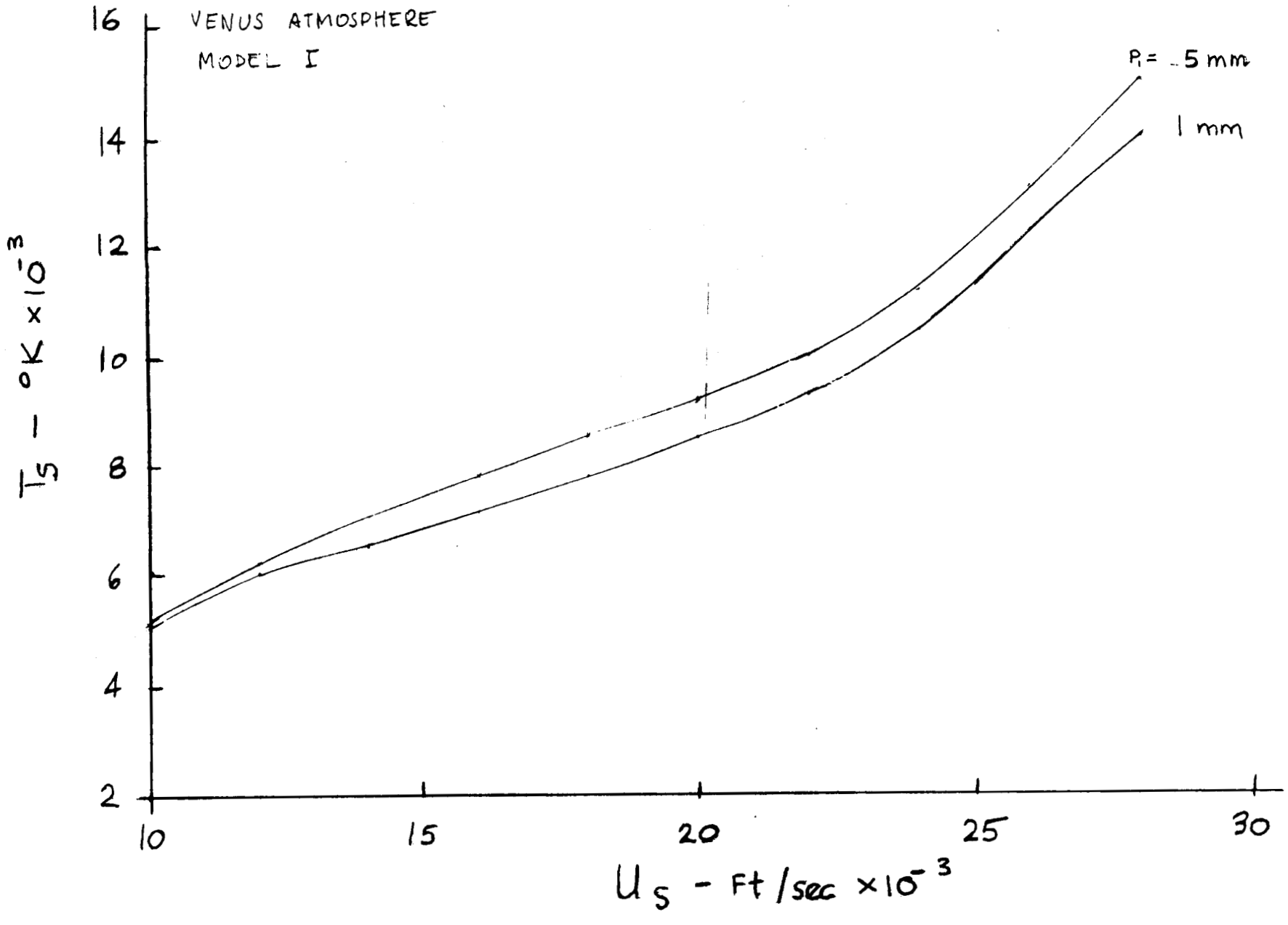
VENUS ATMOSPHERE
MODEL I
R_1 = .5 mm
1 mm
T_S - °K × 10^{-3}
16
14
12
10
8
6
4
2
10
15
20
25
30
U_S - Ft/sec × 10^{-3}

FIG. 3.17

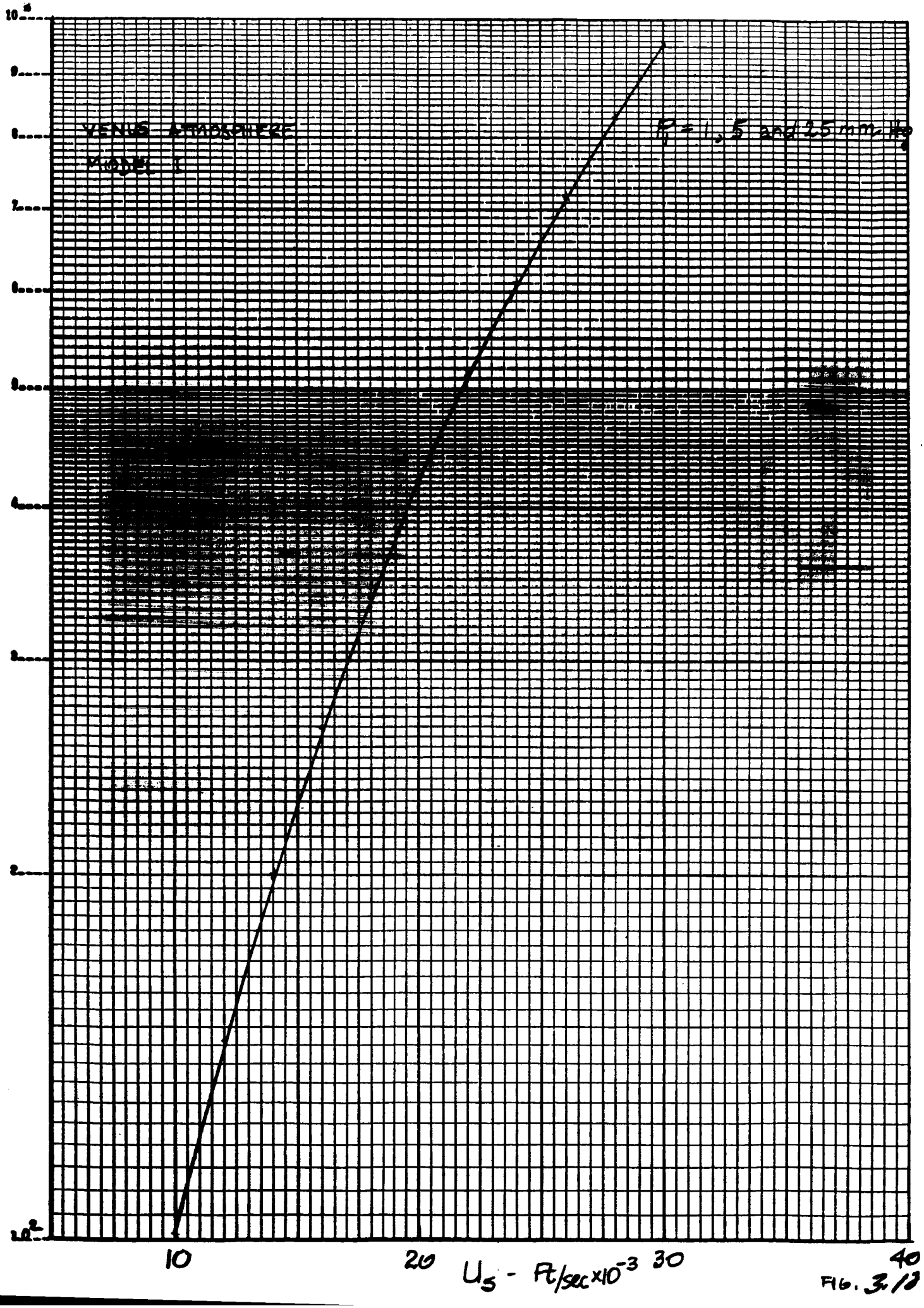
VENUS ATMOSPHERE
MODEL I
P_1 = 1, 5 and 25 mm Hg
P_2/P_1
10^2
10
20
30
40
U_s - Ft/sec x 10^{-3}

FIG. 3.12

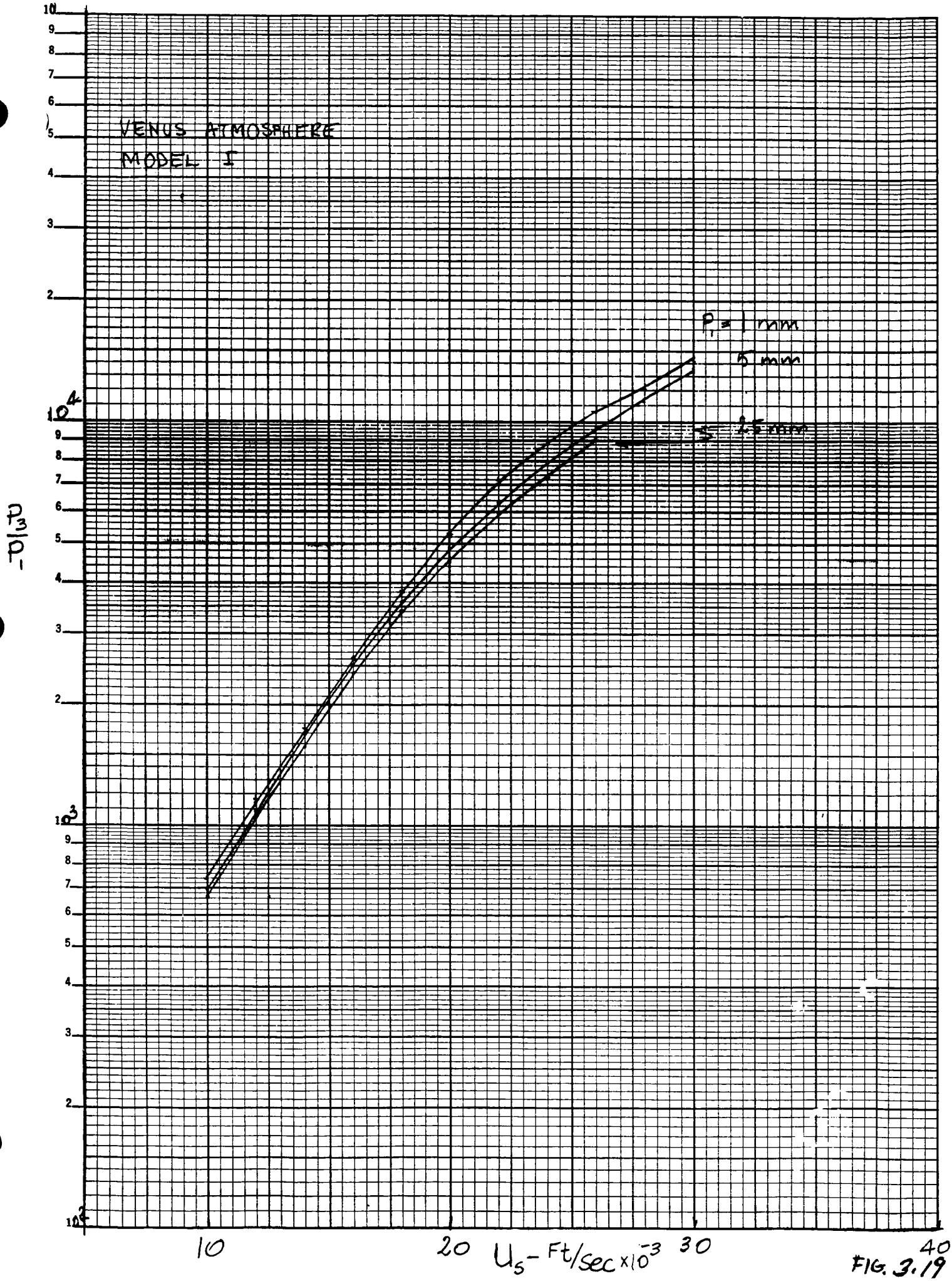
VENUS ATMOSPHERE
MODEL I
$P_1 = 1$ mm
5 mm
2.5 mm
P_3/P_1
10^4
10^3
10^2
10
20
30
40
U_s - Ft/sec $\times 10^{-3}$

FIG. 3.19

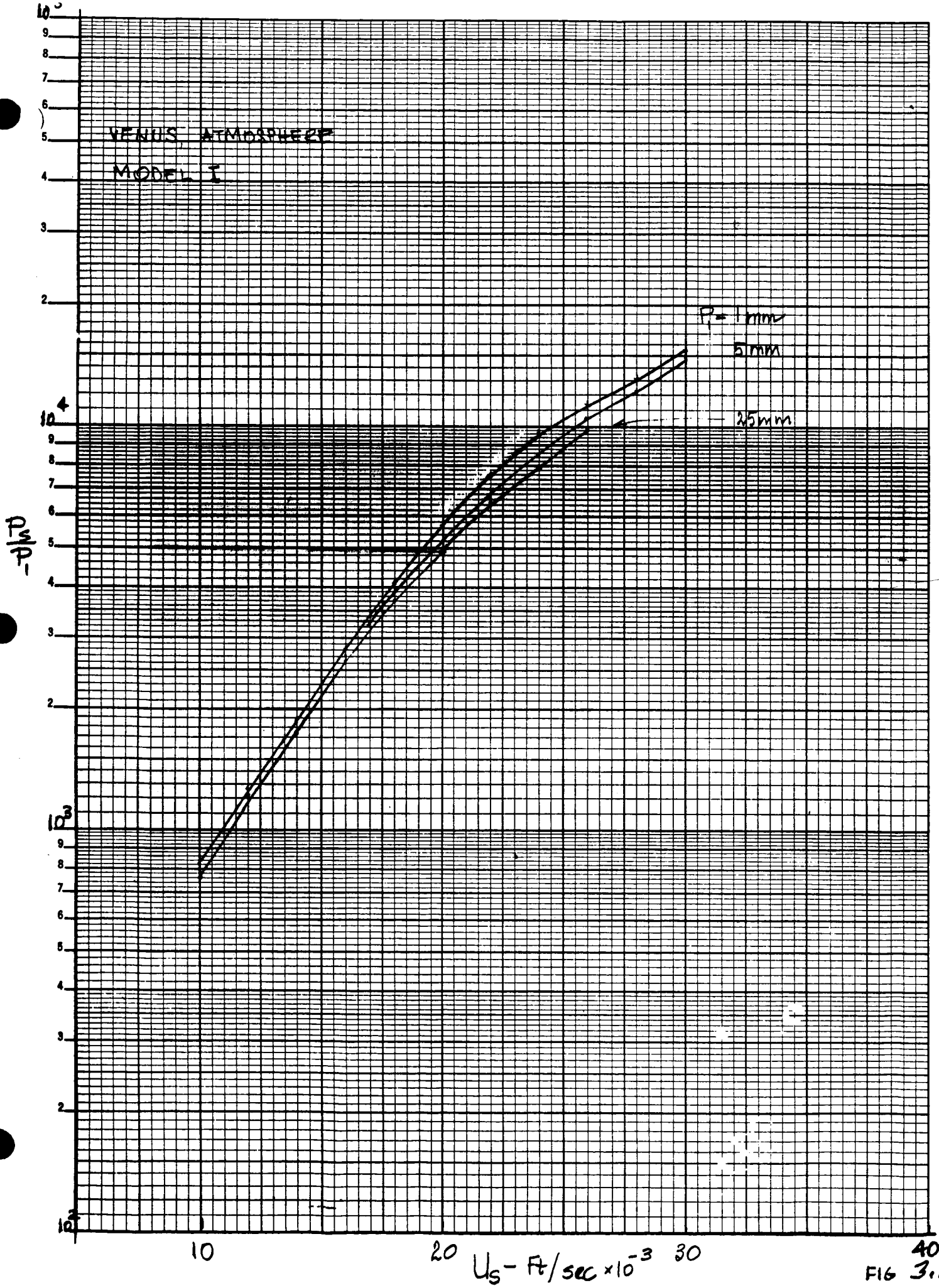
VENUS ATMOSPHERE
MODEL I
P_1 = 1mm
5mm
25mm
P_s/P_1
10^5
10^4
10^3
10^2
10
20
30
40
U_s - Ft/sec $\times 10^{-3}$

FIG 3.20

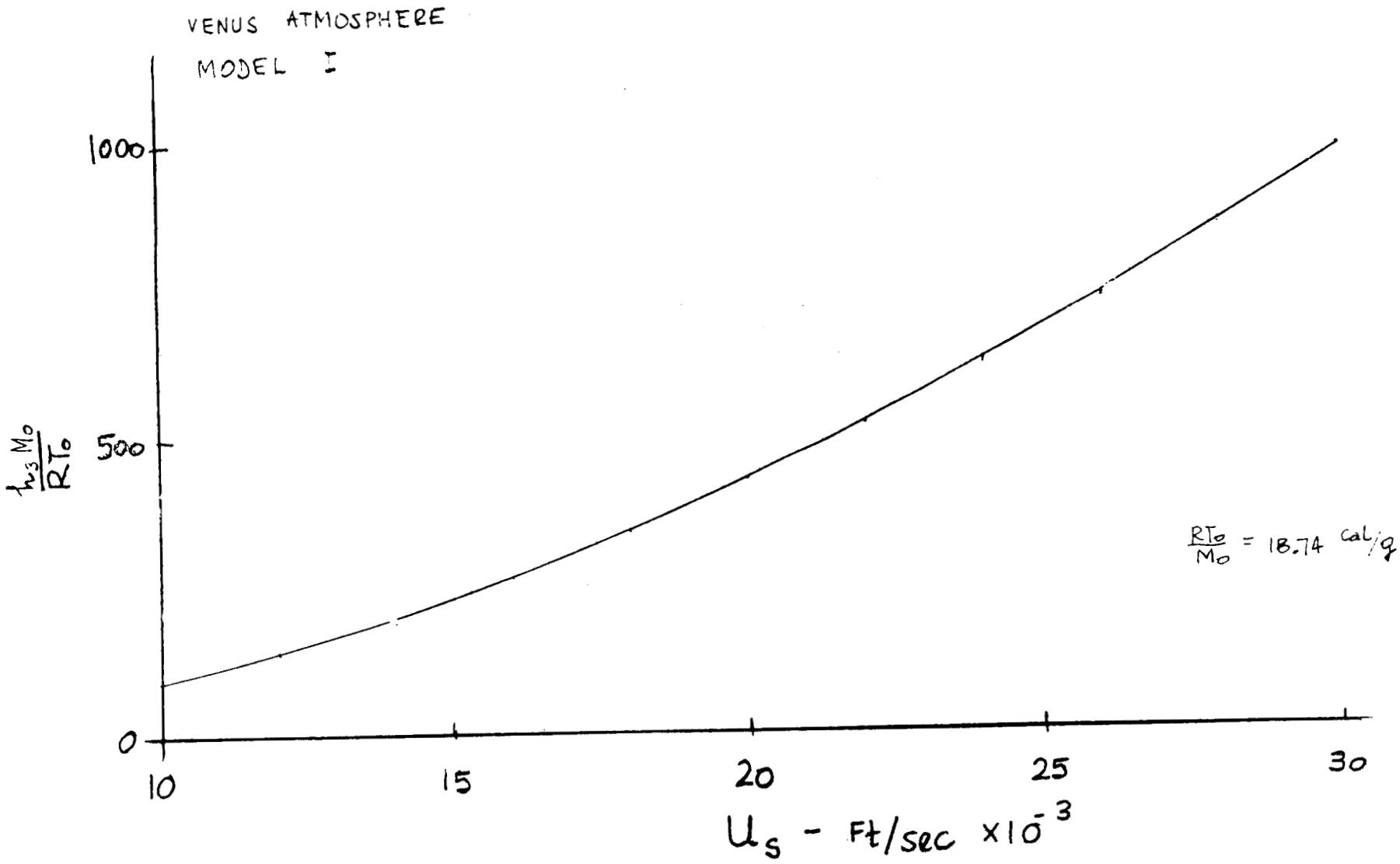
VENUS ATMOSPHERE
MODEL I
1000
500
0
$h_s \frac{M_o}{RT_o}$
10
15
20
25
30
U_s - Ft/sec $\times 10^{-3}$
$\frac{RT_o}{M_o}$ = 18.74 cal/g

FIG. 3.22

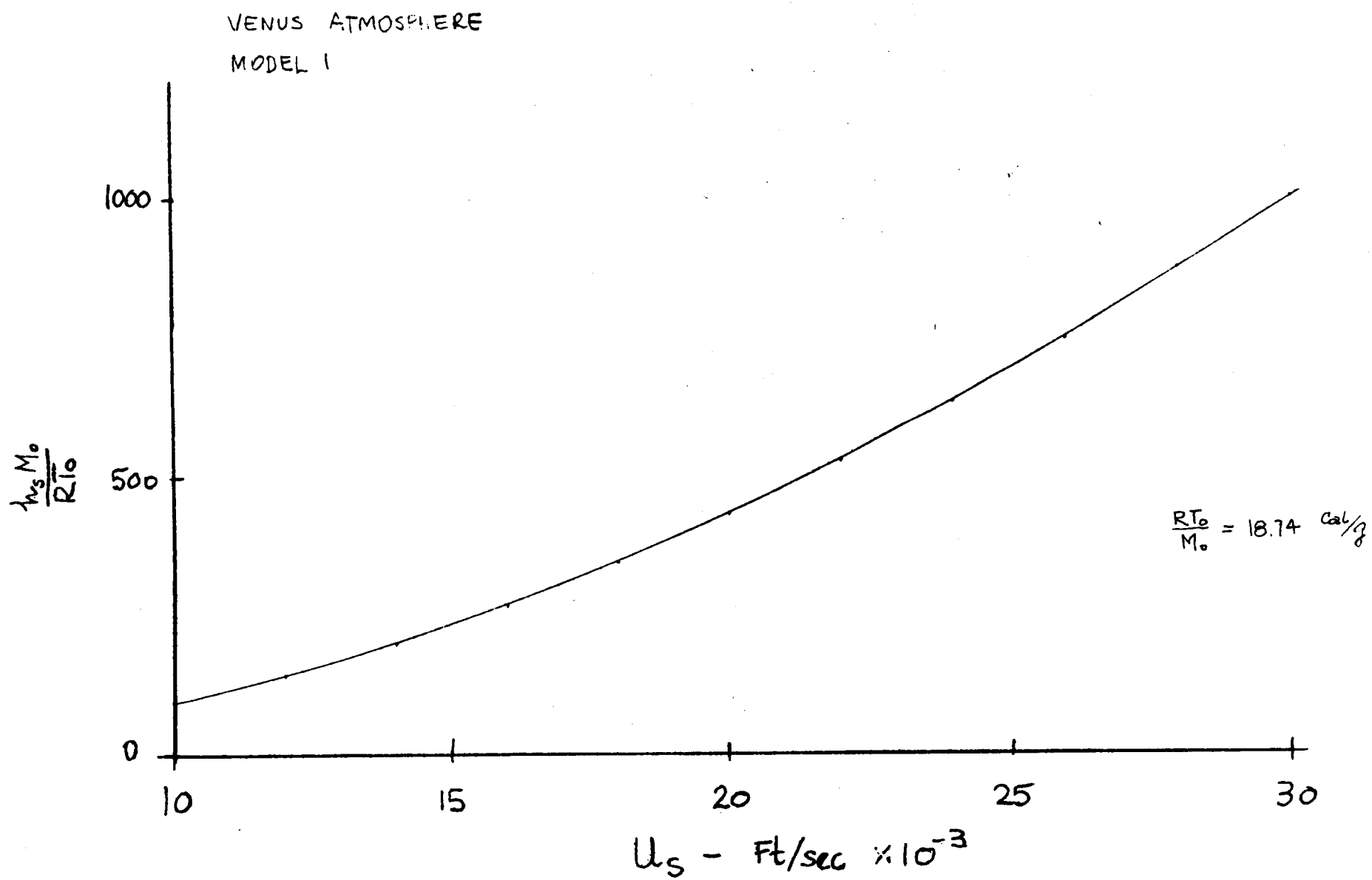
VENUS ATMOSPHERE
MODEL I
1000
500
0
$\frac{\lambda_{w_s} M_o}{R T_o}$
$\frac{R T_o}{M_o} = 18.74$ cal/g
10
15
20
25
30
U_s - Ft/sec $\times 10^{-3}$

FIG. 3d3

VENUS ATMOSPHERE

MODEL 1

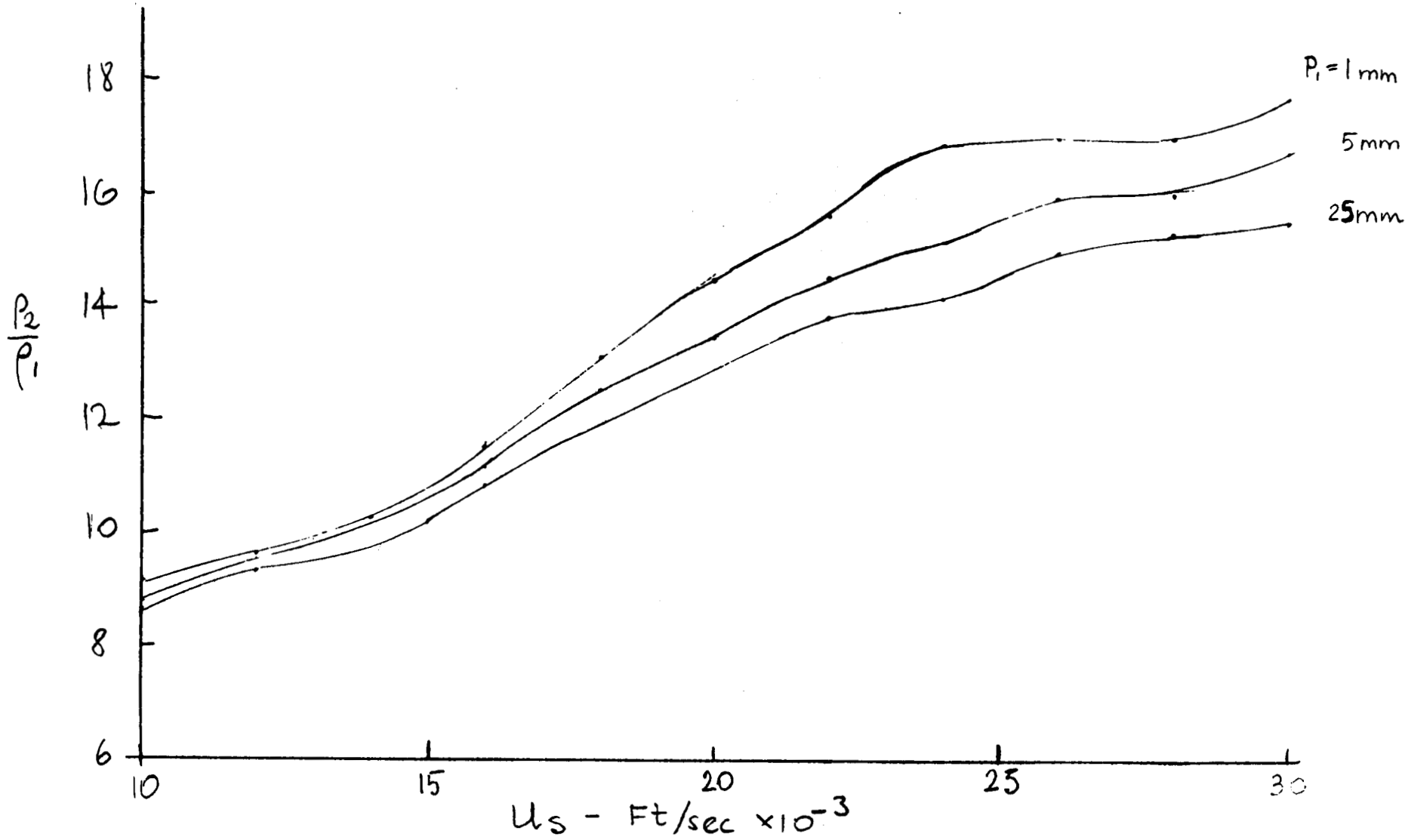

FIG. 3.24

VENUS ATMOSPHERE

MODEL I

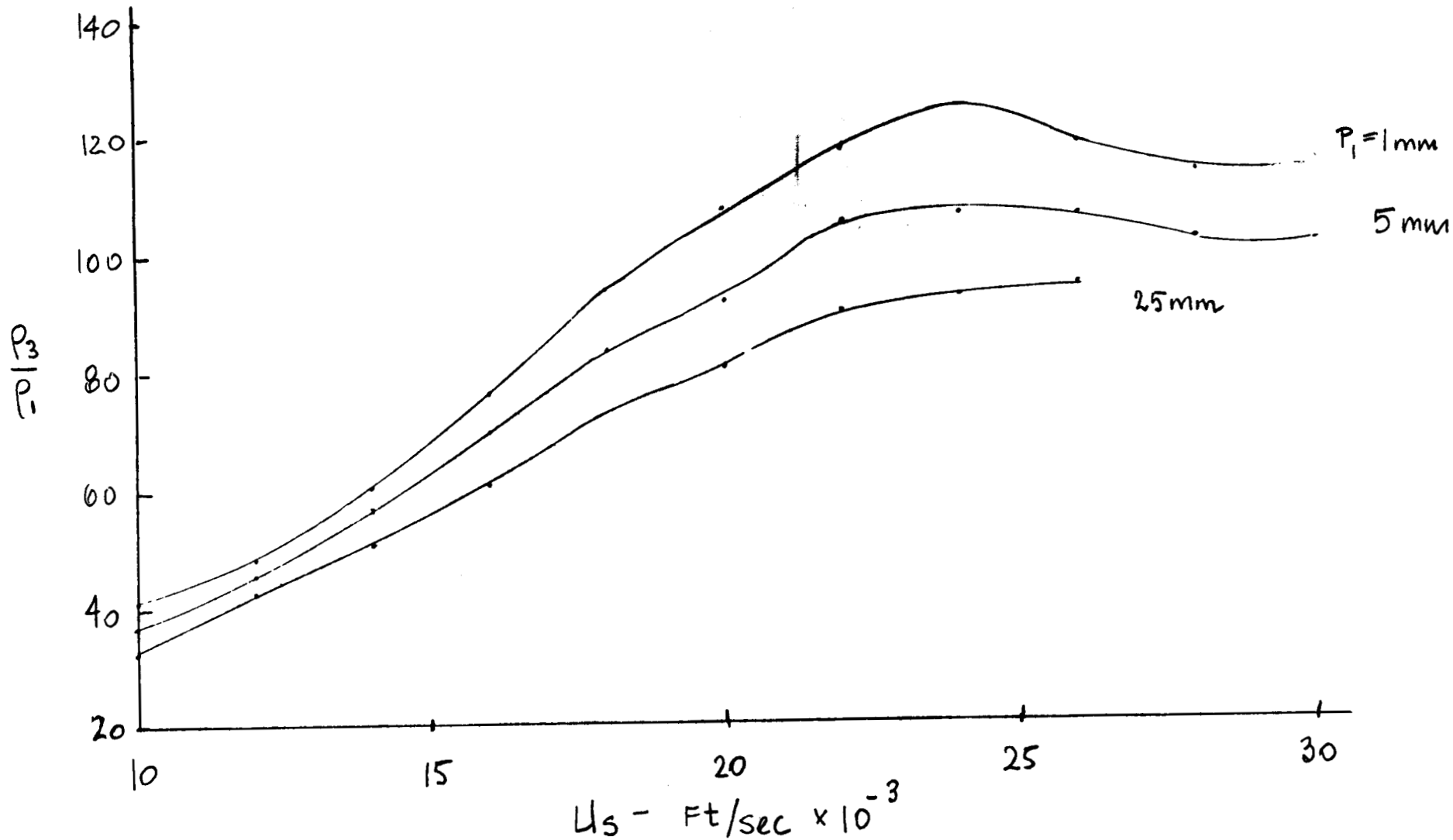

FIG. 3.25

4.0 MISSION INSTRUMENTATION

4.0 SUMMARY & INTRODUCTION

Through the period of this report we have completed the initial phase investigations in all the areas of instrumentation of primary concern. As of this time, no fundamental difficulties are envisioned in measuring temperature, pressure, total density, and carbon dioxide density at altitudes below 80 km in the subsonic regime. The techniques which appear most promising, together with some predictions, instrumentation and possible problem area, are considered in the succeeding sections. In addition, measurement techniques for total molecules in line of sight and total carbon dioxide in line of sight between the probe and the sun are considered, and some predicted parameters are given.

Investigations are now underway to establish the feasibility of measuring oxygen concentration, both in the ambient atmosphere and in terms of molecules in the solar line of sight.

Certain items can be considered in common for most of the instruments under consideration and these include: data rate, data resolution, and environment effects, and these will be discussed briefly in this section. A detailed discussion, applied to each particular instrument, will be presented in the final report.

All parameters being measured (with the exception of the temperature - see below) extend over a range of about 10^4 to 1, taking into account both the change from 80 km to 0 km in altitude and the variation between the three model atmospheres. In general, if we wish to determine the parameter to $\pm$ 20% of it's true value this requires resolving 10^4 into n steps, such that $(1.4)^n = 10^4$, and hence one requires about 28 resolution steps. Alternately, if it were desired to measure the parameters to $\pm$50% of their true value, 14 resolution steps would be required. It should be pointed out that these numbers in no way reflect the inherent accuracy of the measuring device, which should be designed to be at least a factor of two better than the step size. The uncertainty in the measurement refers to each individual data point transmitted, and if data is received without loss for several sequential measurements of

a given parameter over a time period (altitude range) during which it varies by several resolution steps the overall uncertainty is reduced considerably. The step size chosen is - of course - simply a trade off between communication system capacity, sampling rate, and desired resolution. Considering that the parameters change by about a factor of ten for a ten km change in altitude, and that the rate of descent at 80 km is about 0.3 km per second, one finds that it takes about 30 seconds to descent 10 km. To be consistent with a step size of 1.4, seven measurements should be performed during this 30 second period.

Similarly, a step size of two (i.e. $\pm 50\%$) would require a minimum of 3.5 measurements in 30 seconds. A higher measurement rate would statistically decrease the uncertainty in the measurement below that implied by the step size.

Most instruments do not have the desired resolution over a four decade range in the measured parameter, but this problem is generally avoided by using two instruments of similar type but designed for different ranges (i.e. 1-100, and $1\text{-}10^4$). For the instruments discussed later this simply implies a change in "filter" (for the optical and infrared instruments) or a change in counter range (for the total density measurement). Pressure gauges are small enough that two separate units will be provided.

The change in temperatures over the entire subsonic range is only a factor of 8, and hence, to permit useful correlation with theory and prediction this value must be measured far more accurately than $\pm 20\%$. It is planned to measure throughout the entire range to $\pm 35^{\circ}K$, and to measure the region between $150^{\circ}K$ and $350^{\circ}K$ to $\pm 10^{\circ}K$. It is, of course, possible to trade off between the extent and resolution of this narrower measurement range.

It is again emphasized that at present it is planned to perform measurements only in the subsonic regime, after the heat shield has been discarded (see discussion of altimeter, below). This implies that neither the altimeter, nor power supplies would be activated until the desired time, and that some of the instruments will be "caged" during the peak deceleration period

The instruments and their essential components have been examined with respect to the environment (g-loading, ambient temperature) to the degree required to establish that no fundamental problems exist. A more detailed study of the problem, of the type required for the selection of components, particularly insofar as electronic components are concerned, appears beyond the scope of this study. (To give some indication of the effort required, it was estimated that a "limited study" of the possible effects of forces approximating 1000 g's and to define the maximum allowable g level for each of various classes of components, i.e. transistors, microwave oscillators, transformers, would require a 3 man-month effort involving about 12 people with a first cut result in about one month and a final report in two months).

The effect of high g forces in general can be counteracted by the proper design and mounting of the components. The critical components will most probably be among the electronics. Specific consideration has been given to the problem of frequency shift in the microwave oscillators required by the radar altimeter, and the device has been designed incorporating an AFC loop to make operation relatively insensitive to such variations. All the various radiation detectors are solid state devices which minimizes g loading worries, unfortunately, at the expense of increased temperature sensitivity. In those experiments where a cell is used to determine the optical path the cell lengths have been chosen large enough so that the changes due to g forces will be fairly insignificant. Ambient temperature variations are quite critical insofar as the solid state detectors for optical, and infrared radiation are concerned. Devices such as termistors, photodiodes and solid state gamma detectors operate best at temperatures between 0°C and 30°C. It appears that it will be possible to maintain this temperature range down to at least 10 km altitude using an insulated heat sink, possible supplemented by Peltier cooling. In any event, the sensors will be calibrated as a function of temperature between 0° and 30°C, and the temperature of the heat sink will will be monitored periodically. The gamma rays from Fe^{55} are in the 5 kev range and solid state detectors appear impractical. Conversely, if a gamma radiator in the 1 mev range were used, solid state detectors would be applicable, but the absorption

coefficient of nitrogen would drop by a factor of 200, requiring a 20 meter cell to obtain the desired measurement range, and such a cell is obviously impractical. It appears that either a geiger or a "flow" counter will have to be used with the iron gamma radiation and the measures required to construct such devices to survive through the g loading are now under investigation. (A change in sensitivity of less than a factor of ten would not be critical, since the device is self-calibrating). A special type solid state detector for low energy gamma rays is available. It is a surface layer barrier cell, where one simply measures the direct current caused by the incident radiation. Unfortunately, this involves measuring changes in direct current which would tend to give very low accuracy density measurements at the higher altitudes.

The "line of sight" experiments, utilizing the sun as a source for molecular absorption and molecular scattering measurements, pose special problems. They will be mounted on a "sun-seeker", to insure seeing the sun, and this device will be "caged" through the period when the capsule is subjected to high g forces. The sun-seeker, itself, will utilize photodoide sensors, and they - as well as the sensors for the absorption and scattering experiments - will again be mounted on an insulated heat sink, whose temperature is monitored. Since the heat protection system in this case will have to be fairly small and light, it is not expected that these sensors will survive to below 20 km. This does not appear significant, since cloud obscuration problems should occur at about that altitude, or possibly even higher.

No effort has as yet been directed to a design for a "sun-seeker". Such devices have been flown aboard "Viking" and similar type rockets, both by the Naval Research Lab and by the University of Colorado, and similar instrumentation would be applicable to this program.

One major item of investigation has been the radar altimeter, and it is discussed in some detail in a later portion of the instrumentation section. It appears that a satisfactory design has evolved, subject to the g limitations of components discussed previously which will have the same general effect on both the communication system and the altimeter. One item of special

emphasis is the radar antenna, which must face downward in the subsonic regime. Since the antenna must have a "clear aperture" of several square feet, this imposes a severe constraint on the overall capsule design, possibly implying a "flipping" of the capsule after the heat shield has been discarded. It is not required that the antenna be useable in the hypersonic regime, but the radar altimeter is possibly the single most important part of the instrumentation system.

Approximate power requirements for the radar are in the neighborhood of one hundred watts, and it appears that the total power requirement for the entire instrumentation system will be about twice that value. Weight estimates are not yet available since it is not clear how much ruggedization of structures will be required. The aim is to hold the entire instrumentation system, including sun-seeker, radar antenna and power sources to less than fifty pounds.

4.2 TEMPERATURE (150 - 800°K)

The required temperature measurements can be made by means of resistance thermometers located near the surface of the vehicle. The ranges of temperature measurements to be made can be covered by resistance thermometers, with signal outputs sufficiently high to eliminate any need for amplification. Wind tunnel calibrations will be performed on the vehicle shape to determine the local recovery factor and permit velocity corrections. Other than the design of the sensor mounting to withstand the heavy deceleration loading, no particularly difficult problems are anticipated.

Temperature sensors will be provided in fine and coarse ranges. The first type will cover a span of 200 centigrade degrees, from 150°K to 350°K. The error is estimated to be ±10°C (±5%). The second type will cover 700 centigrade degrees, from 100 to 800°K, with an estimated error of ±35°C.

4.3 PRESSURE
(0.1 to 900 psi) (6 x 10^{-3} to 60 atmospheres)

Airborne measurements of pressure are conventionally made using Boudon tube or diaphragm type gages. Gauge of different types are available having high level outputs requiring no external amplification. A check was made on the possible deleterious effects of the extremely high entry decelerations (up to 800 g). Previous experience at MSVD had shown that gages can be designed to operate at 100 g's. A case was found of a Wiancko gage tested and calibrated at 240 g's. Since the present application only requires survival of the high g loading, with measurements made at low g levels subsequent to entry, this data looks very promising.

To check further, the engineering departments of three well-known vendors (Pace Eng., Edcliff Instruments, and Giannini Controls) were contacted and asked to express an opinion on the magnitude of the problem of designing a transducer to withstand 700 to 800 g's and then operate. All three indicated that such a design was feasible within the present state of the art.

The pressure gages will be connected to ports on the outer surface of the vehicle. Wind tunnel testing will be necessary to determine the degree to which the ports are affected by velocity, angle-of-attack, etc. Calculations using the pressures measured on several ports will give an estimate of velocity, to correlate with the radar altimeter and temperature data.

The study during the next period will include a determination of the ranges and quantities of pressure measurements to be made, for each particular gage.

4.4 TOTAL DENSITY
($0^{-3} \times 10^{-2}$ g/cc) or (10^{17}-10^{21} particles/cc)

The feasibility of measuring density by detecting the attenuation of signals from a radio-active source has been investigated. Calculations have been made which show that a measureable change in signal can be obtained using a reasonable path length and source strength. The "best" atmosphere supplied by JPL was used as a basis for initial calculations, with the extreme I and II cases also considered to ensure complete coverage. The analysis shows that the method is promising and can give significant data.

The design of the density instrument is based on the variation of transmission of X-rays with the density of the medium between the source and the detector. As given by Price,*

$$\frac{I}{I_0} = e^{-\mu_m d_m}$$

where $\frac{I}{I_0}$ = fraction of photons remaining in the beam

μ_m = total mass absorption coefficient =

μ = linear absorption coefficient

ρ = mass density of absorber

d_m = mass thickness = d

d = path length

Re-writing

$$\frac{I}{I_0} = e^{-\frac{\mu}{\rho}\rho d}$$

It has been assumed that a source of suitable intensity can be obtained to make the count rate of I_0 sufficiently above the background rate. Mullaney**used about 5 milligrams of

*Price, W.J. "Nuclear Radiation Detection".McGraw-Hill 1958.
**Mullaney, G.J. "Temperature Determination in Flames Using a Radio-active Source of X-Rays" General Electric Report 56-RL-1494 February 1956

Fe^{55} electroplated on a disk of platinum. The resultant counting rate was sufficiently higher than the background count, with a calculated counter error of 0.5%. Based on these results, a source suitable for the density measuring equipment should be obtainable. More detailed calculations of the necessary source strength will be made during the next study period.

In order to predict the response of the density measuring equipment, it was assumed that the path length was 15 cm, the gas was nitrogen with a μ/ρ of 18, and that the density of the atmosphere varied as calculated from the JPL supplied atmosphere. It was further assumed that measurements were to start between 70 and 80 km altitude.

The results, as plotted on curves 4.1 and 4.2, show that the device will be sufficiently sensitive to give good resolution of the density-altitude relationship over the entire range for the "best" predicted case, and will cover over half of the range for the two extreme cases.

In addition to the source strength calculations, the effects of adding carbon dioxide and other possible gases to the nitrogen will be checked. It is not expected that the effect will be serious, since the values of μ/ρ of the diluent gases will not differ materially from that of nitrogen. A further point to be given consideration is the mounting of the equipment on the vehicle, and the method of obtaining a sample of the gas. There are two possible arrangements for the detector to measure the carbon dioxide content. The first would require that a sample of the gas flow through the vehicle. This gas could be caused to flow through a chamber where it's density could be measured using the technique described. Alternatively, the radio-active source could be extended on a boom outside of the vehicle, with the detector at the surface of the vehicle. This method would be more complicated in that an extendable boom 15 cm long would be required, but would have the advantage of making the measurement in the direct atmosphere instead of in a sample bled through the vehicle.

Two additional factors should be noted about the gamma source. Fe^{55} has a half-life of 2.94 years and its strength vs time can be predicted to good accuracy. In addition,

counting rates before entry will give a check on the predicted strength with zero mass between the source and detector.

The calculations given are intended to show feasibility. It is expected that the flight instrument would be calibrated by placing known density gases in the instrument and determining the instrument response.

4.5 CARBON DIOXIDE DENSITY (10^{16}-10^{20} particles/cc)

The study of local carbon dioxide measurement techniques has not progressed to the point of having results available. Infrared absorption, thermal conductivity, and chemical absorption will be studied during the next period.

At the present, the infrared absorption technique looks extremely promising. A low temperature source and a thermistor detector are envisioned, together with a filter in the 790 CM^{-1} region (see Figure 4.4). The gas could be flowed through continuously, same as in the total density measurement, using a cell about 10 cm long.

4.6 MOLECULES IN LINE OF SIGHT-ATMOSPHERE SCATTERING

Computations of the volume scattering coefficient for Rayleigh scattering and the normal optical thickness have been completed for one model of the Venus atmosphere so far. Similar computations for other models are in progress. In first model, a classical and conservative model, was chosen previous to the time the JPL models became available and was used in order to get the computational program checked out. The main parameter in all of these computations is wavelength of the radiation. Values have been determined for sixteen different wavelengths (from 2500Å to 10,000Å at 500Å intervals). The altitudes for which both volume scattering coefficient and normal optical thickness have been computed are surface to 200 km, the interval being 2 km from 0 to 50 km and 5 km above 50 km.

Typical values of the normal optical thickness for this preliminary model are given in Table 1. These may be taken as representative of the order of magnitudes to be expected, although the details will vary with the particular vertical structure assumed. Both normal optical thickness and volume scattering coefficient are relatively insensitive to changes of atmospheric composition.

It is seen that optical thickness is strongly dependent on both altitude and wavelength. This is a fortunate circumstance for the present application, as it provides a relatively sensitive measure of gaseous mass above any altitude and thereby the possibility of a good determination of vertical density structure in the altitude range in which the method is applicable.

Table 1. Typical Values of Normal Optical Thickness at Various Altitudes in the Venus Atmosphere for Selected Wavelengths of Radiation

Altitude-w.length	2500A	4000A	6000A	10,000A
0 km	6.82	0.929	0.176	2.2×10^{-2}
8	4.35	0.593	0.113	1.43×10^{-2}
20	2.00	0.273	5.18×10^{-2}	6.58×10^{-3}
40	0.356	4.84×10^{-2}	9.20×10^{-3}	1.17×10^{-3}
60	2.78×10^{-2}	3.78×10^{-3}	7.19×10^{-4}	9.13×10^{-5}
80	1.94×10^{-3}	2.64×10^{-4}	5.01×10^{-5}	6.36×10^{-6}
100	1.35×10^{-4}	1.84×10^{-5}	3.49×10^{-6}	4.43×10^{-7}
150	1.73×10^{-7}	2.35×10^{-8}	4.47×10^{-9}	5.68×10^{-10}
200	2.22×10^{-10}	3.02×10^{-11}	5.73×10^{-12}	7.29×10^{-13}

Extensive computations* of the radiative distribution are available for the range of optical thickness from 0.02 to 1.0. If one takes this as indicative of the useful range for measurements, the altitudes at which this method is applicable are between 29 km and 62 km for radiation of 2500Å and 0 km to 48 km at 4000Å. Typical normal optical thickness values for the Earth's atmosphere, as computed by Deirmendjian**, are given in Table 2.

Comparison of optical thicknesses of the atmospheres of Venus and the Earth show that for this particular model of Venus atmosphere has an optical thickness nearly an order of magnitude greater at the surface than that of the Earth and that light scattering techniques are applicable at higher altitudes on Venus than on the Earth.

* Coulson, K. L., J. V. Dave, and Z. Sekera - "Tables Related to Radiation Emerging from a Planetary Atmosphere with Rayleigh Scattering" Univ. of California Press, 1960.

** Deirmendjian, D. - "Optical Thickness of the Molecular Atmosphere" Archiv fur Met. Geo. and Bio, B/6, 1955.

Table 2. Normal Optical Thickness at Various Altitudes in the Earth's Atmosphere, as Computed by Diermendjian

Altitude-Wavelength	3750Å	5200Å	8350Å
0 km	0.454	0.118	0.0173
10	0.120	3.11×10^{-2}	4.56×10^{-3}
20	2.55×10^{-2}	6.63×10^{-3}	9.72×10^{-4}
30	5.46×10^{-3}	1.42×10^{-3}	2.09×10^{-4}
50	4.3×10^{-4}	1.1×10^{-4}	1.7×10^{-5}
70	3.7×10^{-5}	9.5×10^{-6}	1.4×10^{-6}
100	2.2×10^{-7}	5.8×10^{-8}	8.5×10^{-9}

4.7 CARBON DIOXIDE IN LINE OF SIGHT-MOLECULAR ABSORPTION

A method to measure the total amount of CO_2 present in the atmosphere of Venus from 80 km altitude on down is being investigated. The method chosen is, in essence, to measure to CO_2 infrared transmission of this atmosphere layer to sunlight. Specific bands of the spectrum are selected by means of narrow band pass filters. The spectrum bands are so chosen that they have various generalized transmission coefficients. Thus the most sensitive band, having the smallest transmission coefficient, will black out first. It will, however, give the most information about the uppermost regions. Another band will give less information about the uppermost regions, but will continue to give information to a greater depth of penetration. Additional pass bands will be used in a similar way. The output of the sensor as a function of altitude may be obtained in the following manner.

The theory of gaseous transmission of a band of infrared radiation is complicated. However, for the purpose of obtaining the amount of CO_2, a generalized transmission coefficient will be used. This supposes that the desired experimental accuracy is not too great and that the radiation band is not located so near a strong absorption that line broadening effects interfere. The line-broadening as assumed to be given by:

$$\alpha = \alpha_o \frac{P}{P_o} \sqrt{\frac{T_o}{T}}$$

where α = half width

P = pressure

T = temperature

the subscripts denote standard conditions

The values of P and T as a function of altitude will be those furnished by JPL.

Tentatively, the region chosen is that between 500 cm^{-1} and 800 cm^{-1}. Typical narrow bandpass filters have a width at half maximum of about 40 cm^{-1} in this region. This method is not expected to be of use below the cloud-top. However, it may indicate when the cloud is being entered.

All measurements will be made below 80 km. The capsule will be descending at the rate of about 0.3 km sec^{-1} so that the data will have good spatial resolution.

Figure 4.2 shows that "best case" of pressure as a function of altitude for Venus. It is assumed that the atmosphere of Venus is of homogeneous composition, and that 10% of it by weight is CO_2. This is a "best case" number. In this case, the pressure of CO_2 would be about 7% of the total pressure. Figure 4.3 shows how the transmissions varies with pressure and path length at 775 cm^{-1} and at T = 300°K. Figure 4.4 shows the transmission* as a function of wave number in the region spanning typical filters for T = 300°K, a total pressure of 1 atm and for a path length of 50 atm cm. Since the curve is so uniform across the region 750 cm^{-1} to 790 cm^{-1}, the filter, having a maximum response of 0.4 at 770 cm^{-1} and dropping linearly with wavenumber to zero at 750 cm^{-1} and 790 cm^{-1}, will have an overall factor of about 0.2

The amount of energy from the sun incident upon a sensor at the location of the Venus orbit is now calculated. Assuming black-body conditions, the spectral emission of the sun's surface is given by Planck's radiation formula. Practically all optical radiation comes from the photosphere. The continuous spectrum of this radiation is a mean of near black-body radiation whose temperature ranges from, say, 4500°K to 7500°K.

* V. R. Stull, P. J. Wyatt, and G. N. Plass, "Theoretical Study of the Infrared Radiative Behavior of Flames - Vol.II, The Infrared Absorption of Carbon Dioxide AFCRL-62-210 (II).

The temperature of a black-body that most nearly matches the continuous spectrum of sunlight integrated over the whole visible disc is about 5750°K. The filter for the first CO_2 absorption sensor has a response centered about 770 cm^{-1}. Using the values of T = 5750°K and $\lambda = 1.29 \times 10^{-3}$ cm, the black-body spectral emission is calculated.

$$W = 5 \times 10^6 \text{ ergs cm}^{-2} \text{ sec}^{-1} \mu^{-1}$$

radiated into 2π steradians.

At a mean SUN-VENUS distance of 10^{13} cm the incident energy is about 2×10^2 ergs cm^{-2} sec^{-1} $micron^{-1}$.

The energy contained in the region from 750 cm^{-1} to 790 cm^{-1} is then the miltiple product of this width in microns, 0.65 μ, the incident energy at the orbit of Venus, 2×10^2 ergs cm^{-2} sec^{-1} μ^{-1}, and the filter factor, 0.2. The result is:

$$E_o = 26 \text{ ergs cm}^{-2} \text{ sec}^{-1}$$

The sensor, a thermistor, is assumed to have an effective sensitive area of 1 cm^2. Therefore, the energy input to the sensor is 26 ergs sec^{-1} or approximately 3 microwatts, outside the atmosphere of Venus, a value more than adequate for a typical thermistor with a noise equivalent power of better than 10^{-8} watts, for a one c.p.s. passband.

4.8 RADAR ALTIMETER

The system as outlined herein is a conventional pulsed radar. It is felt that a simple, reliable, lightweight system is to be preferred if the techniques are feasible. The only complexity introduced so far is the AFC loop which allows narrow-banding of the receiver to reduce the noise power. Further trade-offs will be made on complexity versus noise power reduction.

The following assumptions were made:

10 db scattering loss at surface
vertical incidence only
no plumbing losses yet
no atmospheric attenuation

Included herein are a System Block Diagram, Radar Equation Calculations, Receiver Noise Power Calculations, assumptions, etc. These calculations are performed for various frequencies and antenna sizes with the results shown on a graph of transmitter average power output versus antenna gain for three frequencies of interest.

Additional information to be added at a later date involves signal processing; system power requirements, size and weight, environmental problems etc.

1. Wavelength

$$\lambda = \frac{c}{f}$$

where $c = 3 \times 10^{10}$ cm/sec
f = transmitting frequency (cps)

f	λ	
10 kmc	3 cm	$\approx$ 0.0984 ft.
13.3 kmc	2.25 cm	$\approx$ 0.0740 ft.
35 kmc	0.86 cm	$\approx$ 0.0281 ft.

2. Effective antenna aperture

$A_r = A \times b$ where A = actual antenna area (ft^2)
b = illumination efficiency

	Antenna	10 kmc	13.3 kmc	35 kmc	
	1 ft^2	0.65	0.65	0.6	
A_r	4 ft^2	2.6	2.6	2.4	ft^2
	0.785 ft^2	0.51	0.51	0.47	
	3.14 ft^2	2.04	2.04	1.89	

Assume Antenna = 1 ft sq., 2 ft sq., 1 ft dia., 2 ft dia.

$\therefore$ A = 1 ft^2; 4 ft^2; 0.785 ft^2; 3.14 ft^2

Assume b = 0.65 at 10 kmc & 13.3 kmc
b = 0.6 at 35 kmc

3. Antenna gain

$$G_o = \frac{4\pi A_r}{\lambda^2}$$

$$= \frac{4 \times \pi \times 0.65}{(0.0740)^2}$$

$$G_o = 1490$$

A_r	@ 10 kmc G_o	@ 13.3 kmc G_o	@ 35 kmc G_o
0.6			9540
0.65	844	1490	
2.4			38200
2.6	3380	5970	
2.04	2650	4690	
1.89			30100
0.47			7470
0.51	662	1170	

4. Beamwidth (3db)

$$\theta = \frac{7 \times 10^4}{f \times D}$$

$$= \frac{7 \times 10^4}{10^4 \times 1}$$

$$\theta = 7^o$$

f = mc
D = ft (for square antenna D is for equivalent area)

A	(equiv) D
1 ft^2	1.27 ft
4 ft^2	2.55 ft

f_{kmc}	D_{ft}	θ_o	f_{kmc}	D_{ft}	θ_o
10	1	7°	10	1.27	5.5^o
13.3	1	5.26^o	13.3	1.27	4.15^o
35	1	2°	35	1.27	1.58^o
10	2	3.5^o	10	2.55	2.74^o
13.3	2	2.63^o	13.3	2.55	2.06^o
35	2	1°	35	2.55	0.78^o

5. Doppler Shift (Δf_D)

$$f_D = \frac{2V}{c} \times f_t$$

V = 720 ft/sec @ 250,000 ft. alt.

$$= \frac{2 \times 720 \times 10 \times 10^9}{984 \times 10^6}$$

$c = 984 \times 10^6$ ft/sec

f_D = 14.6 kc

f_t= 10, 13.3, 35 kmc

kmc f_t	kc f_D
10	14.6
13.3	19.5
35	51.2

6. Minimum allowable pluse width based on a pulse limiting condition at 250,000 ft altitude and a 2° beamwidth.

$$* \quad 1 + \frac{C}{2H} = \sec \theta_o \qquad \text{where } \theta_o = \tfrac{1}{2} \text{ beam}$$

$$1 + \frac{984 \times 10^6 \times \tau}{2 \times 250 \times 10^3} = \frac{1}{\cos 1^o} = \frac{1}{0.9998}$$

$$\tau = (\sec \theta_o - 1) \frac{2h}{c}$$

$$= \left(\frac{1}{0.9998} - 1\right) \frac{5 \times 10^5}{984 \times 10^6}$$

$$= (1.002 - 1)\ 5.08 \times 10^{-4}$$

$$\tau = 0.1\ \mu\text{sec}$$

		Altitude			
BW	θ	250 K	500 K	10^6	
2°	1°	0.1	0.2	0.4	Min.Pulse
4°	2°	0.3	0.6	1.2	width in
8°	4°	1.25	2.5	5.0	microseconds

7. Maximum allowable pulse width based on a minimum range requirement of 5000 feet.

$$\tau = R_m + 492 \text{ ft}/\mu\text{sec}$$

$$= \frac{5000}{492}$$

$$\tau = 10\ \mu\text{sec}$$

* Ref. Proceedings IRE 45 (228-238) 1957
Radar Terrain Return at Near-Vertical Incidence
by R. K. Moore & C. S. Williams, Jr.

8. Pulse repetition frequency (PRF)

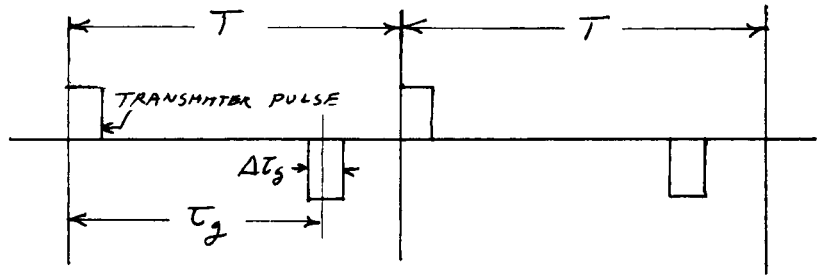

The first range gate appears at time t_g, after the transmitter fires or at 250,000 feet. The transmitter will fire again at T ($t_g + \frac{\Delta\tau_g}{2}$) to prevent leakage of transmitted signal into the receiver. The first altitude ambiquity will, therefore, appear at (T + tg). (Assuming Δt_g small).

For t_g = 250,000 feet

Let T = 300,000 feet

Ambiguous altitude $\therefore$ = T + t_g = 550,000 feet

The time between pulses therefore

$$T = \frac{300{,}000 \text{ ft}}{492 \text{ ft}/\mu\text{sec}}$$

$$T = 610\ \mu\text{sec}$$

$$PRF = 1/T$$

$$= \frac{1}{610 \times 10^{-6}}$$

$$PRF = 1640 \text{ pps}$$

9. Receiver Bandwidth

$$*BW_{IF} = \frac{a}{\tau}$$

where $a = 1.5$

τ = pulse width (sec)

These assumes a $\frac{\sin x}{x}$ distribution for the pulse in the frequency domain and that all the frequencies are passed in the Δf region.

$$BW_{Rec} = BW_{IF} + \Delta f_D$$

$$= \frac{1.5}{10 \times 10^{-6}} + \begin{matrix} (14.6) \text{ @ } 10 \text{ kmc} \\ (19.5) \text{ @ } 13.3 \text{ kmc} \\ (51.2) \text{ @ } 35 \text{ kmc} \end{matrix}$$

BW = 165 kc @ 10 kmc
170 kc @ 13.3 kmc
201 kc @ 35 kmc

10. Equivalent Noise Temperature

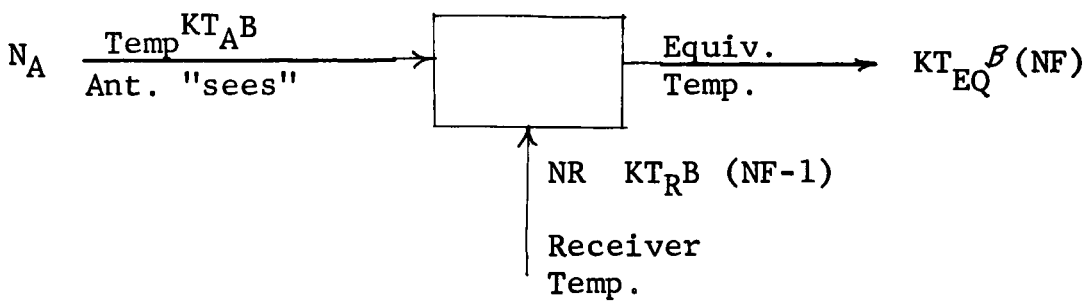

$$T_{EQ} = \frac{(NF-1)\ T_R + T_A}{N_F}$$

$$= \frac{9 \times 291 + .650}{10}$$

$T_R = 291^oK$

$T_A = 650^oK$

$T_{EQ} = 327^oK$ @ 10 kmc NF = 10

$T_{EQ} = 321^oK$ @ 13.3 kmc NF = 12

$T_{EQ} = 315^oK$ @ 35 kmc NF = 15

* Ref. Rad. Lab. Series Vol. III Pg. 367

11. Noise Power in the Receiver

$P_n = K \times T_{EQ} \times BW \times NF$

$K = 1.38 \times 10^{-23}$ Joules/degrees K

$P_n = 7.45 \times 10^{-15}$ watts

$P_n = 9.0 \times 10^{-15}$ watts

$P_n = 1.31 \times 10^{-14}$ watts

	10 kmc	13.3 kmc	35 kmc
BW	165 kc	170 kc	200 kc
T_{EQ}	327° k	321°k	315°k
NF	10	12	15

12. Transmitter Power

$$P_T = \frac{S/N \times 16\pi^2 r^2 P_n}{G_o W \lambda^2 \sigma}$$

Let S/N = 20 db; W = 0.625; $\sigma = 0.1$

r = 250,000 ft.

and

λ(ft.)	P_n(W)	DIA 1 ft. G_{o1}	1 ft.sq. G_{o2}	DIA 2 ft. G_{o3}	2 ft.sq. G_{o4}
.0984	7.45×10^{-15}	622	844	2650	3380
.0740	9.0×10^{-15}	1170	1490	4690	5970
.0281	1.31×10^{-14}	7470	9540	30100	38200

for f = 13.3 kmc; $P_n = 9.0 \times 10^{-15}$; $G_o = 1170$

$$P_p = \frac{100 \times (4)^2 \times \pi 2 \times (2.5)^2 \times 10^{10} \times 9.0 \times 10^{-15}}{1170 \times 0.625 \times (0.0740)^2 \times 0.1}$$

$P_p = 24.7$ watts

13. Average Power

$$P_{avg} = P_p \times \frac{\tau}{T}$$

$$= 24.7 \times \frac{10}{610}$$

$P_{avg} = 0.404$ watts

FIG. 4.1 DENSITY DETECTOR RESPONSE

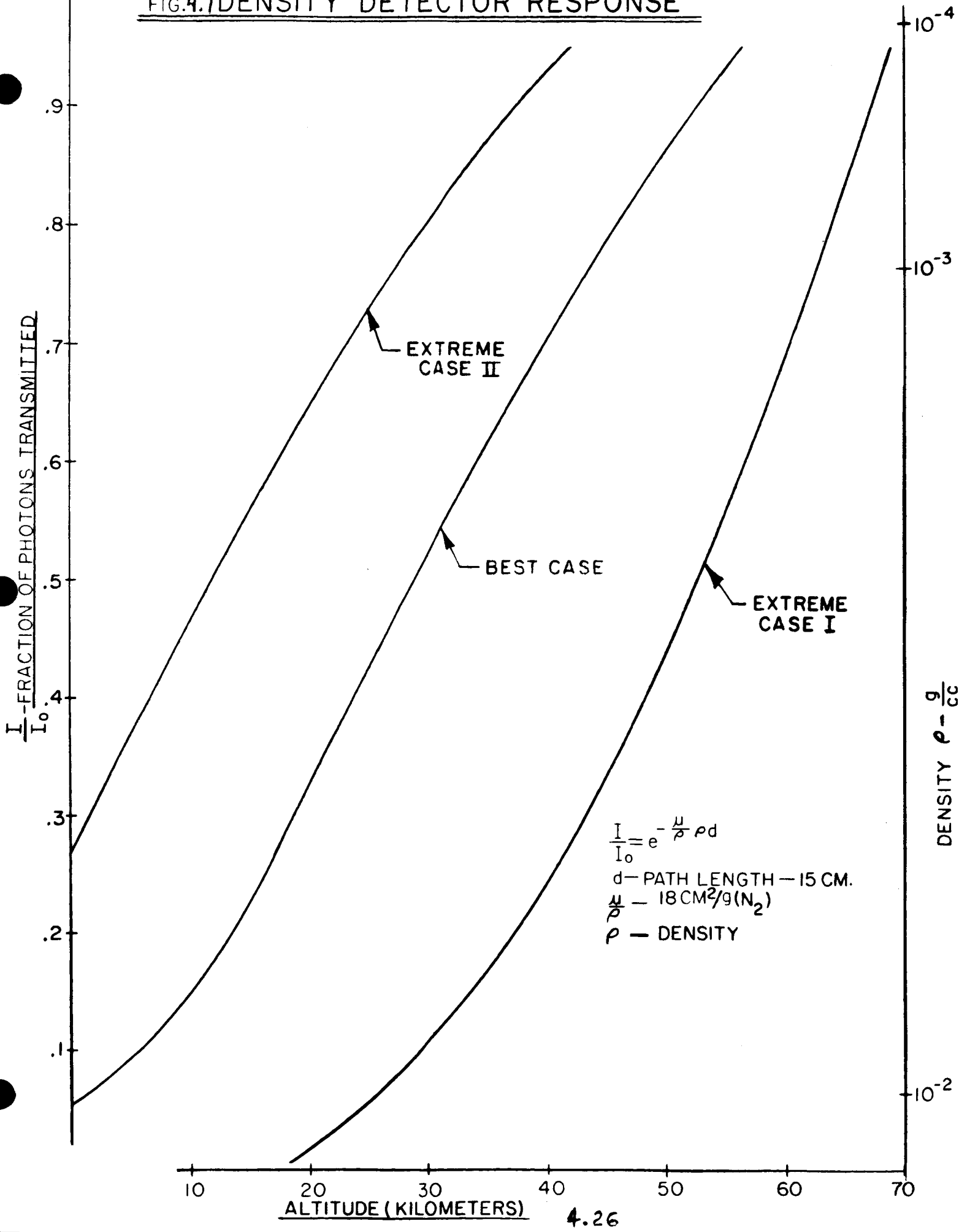

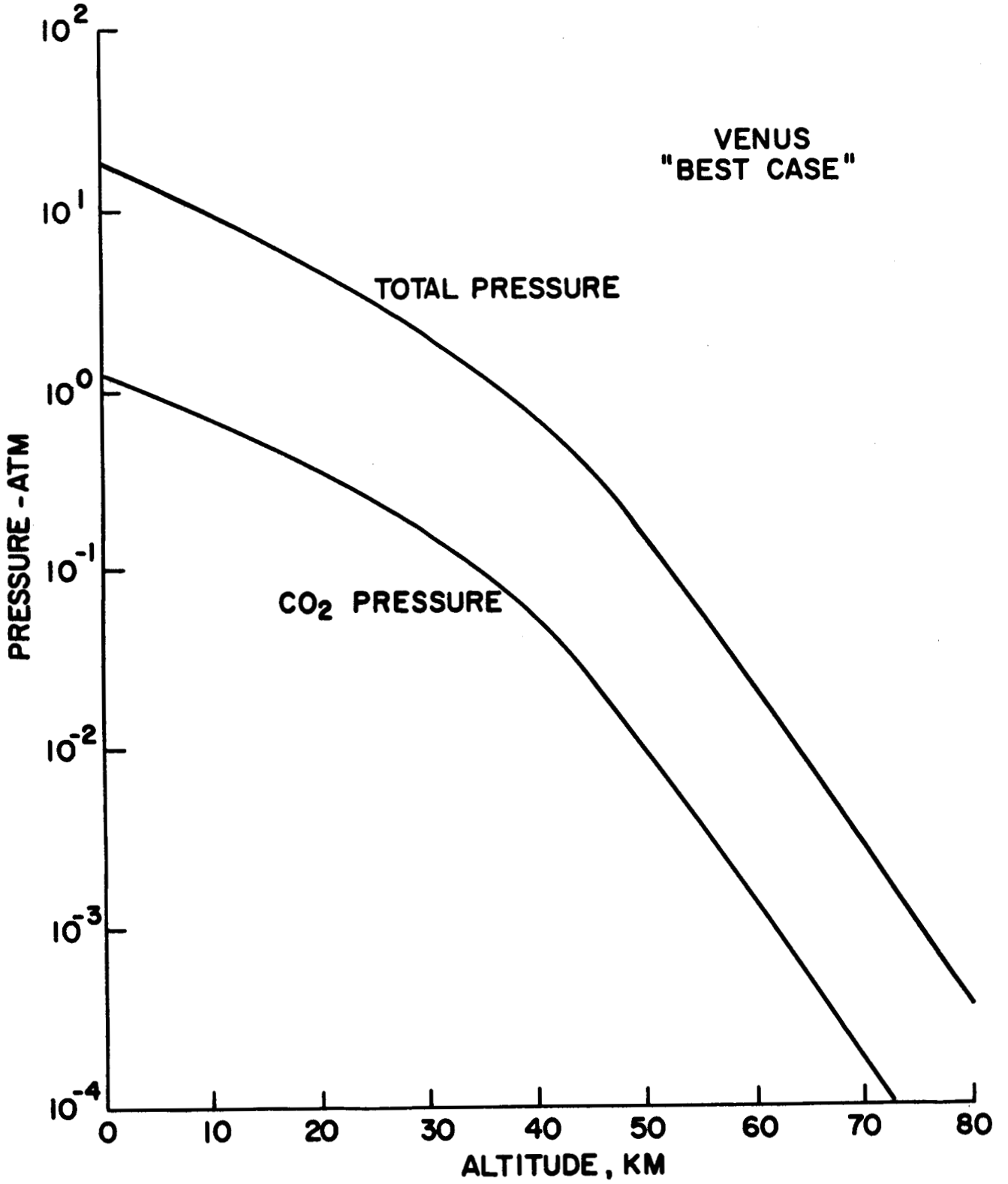
VENUS
"BEST CASE"
TOTAL PRESSURE
CO_2 PRESSURE
PRESSURE - ATM
10^2
10^1
10^0
10^{-1}
10^{-2}
10^{-3}
10^{-4}
0
10
20
30
40
50
60
70
80
ALTITUDE, KM

Figure 4.2

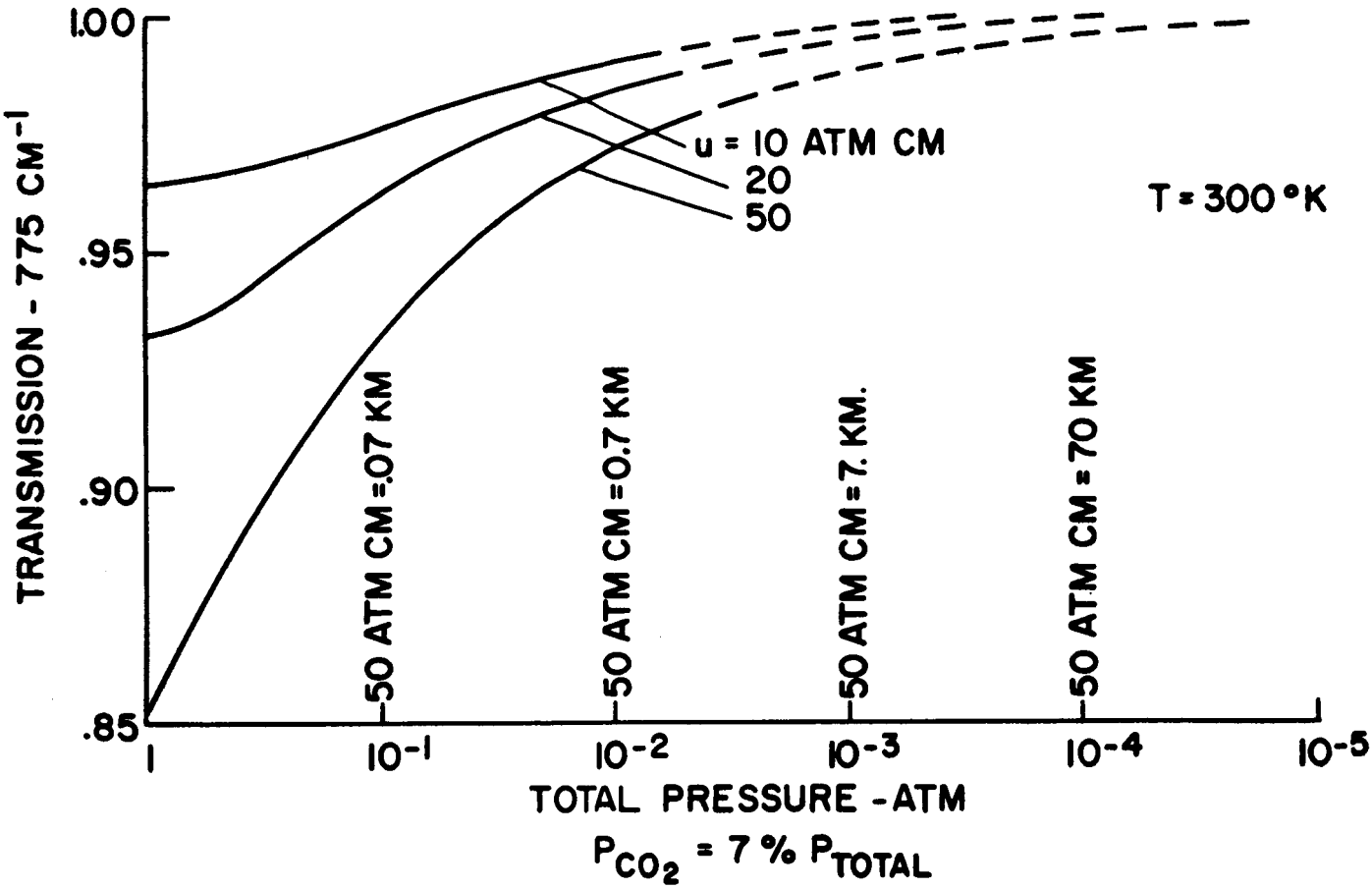
1.00
.95
.90
.85
TRANSMISSION - 775 CM^{-1}
u = 10 ATM CM
20
50
T = 300 °K
50 ATM CM = .07 KM
50 ATM CM = 0.7 KM
50 ATM CM = 7. KM.
50 ATM CM = 70 KM
1
10^{-1}
10^{-2}
10^{-3}
10^{-4}
10^{-5}
TOTAL PRESSURE - ATM
P_{CO_2} = 7 % P_{TOTAL}

Figure 4.3

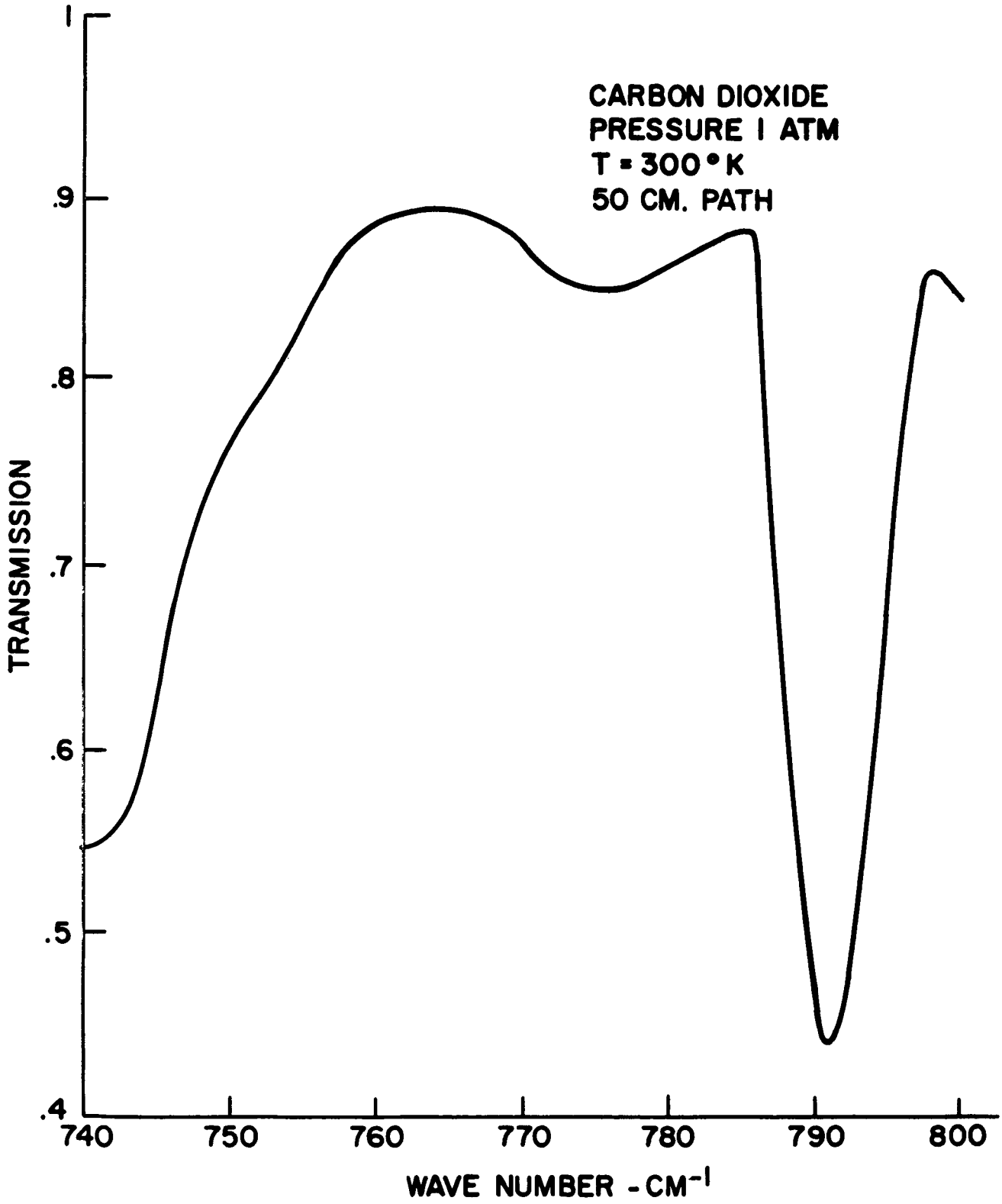
CARBON DIOXIDE
PRESSURE 1 ATM
T = 300 °K
50 CM. PATH
TRANSMISSION
1
.9
.8
.7
.6
.5
.4
740
750
760
770
780
790
800
WAVE NUMBER - CM⁻¹

Figure 4.4

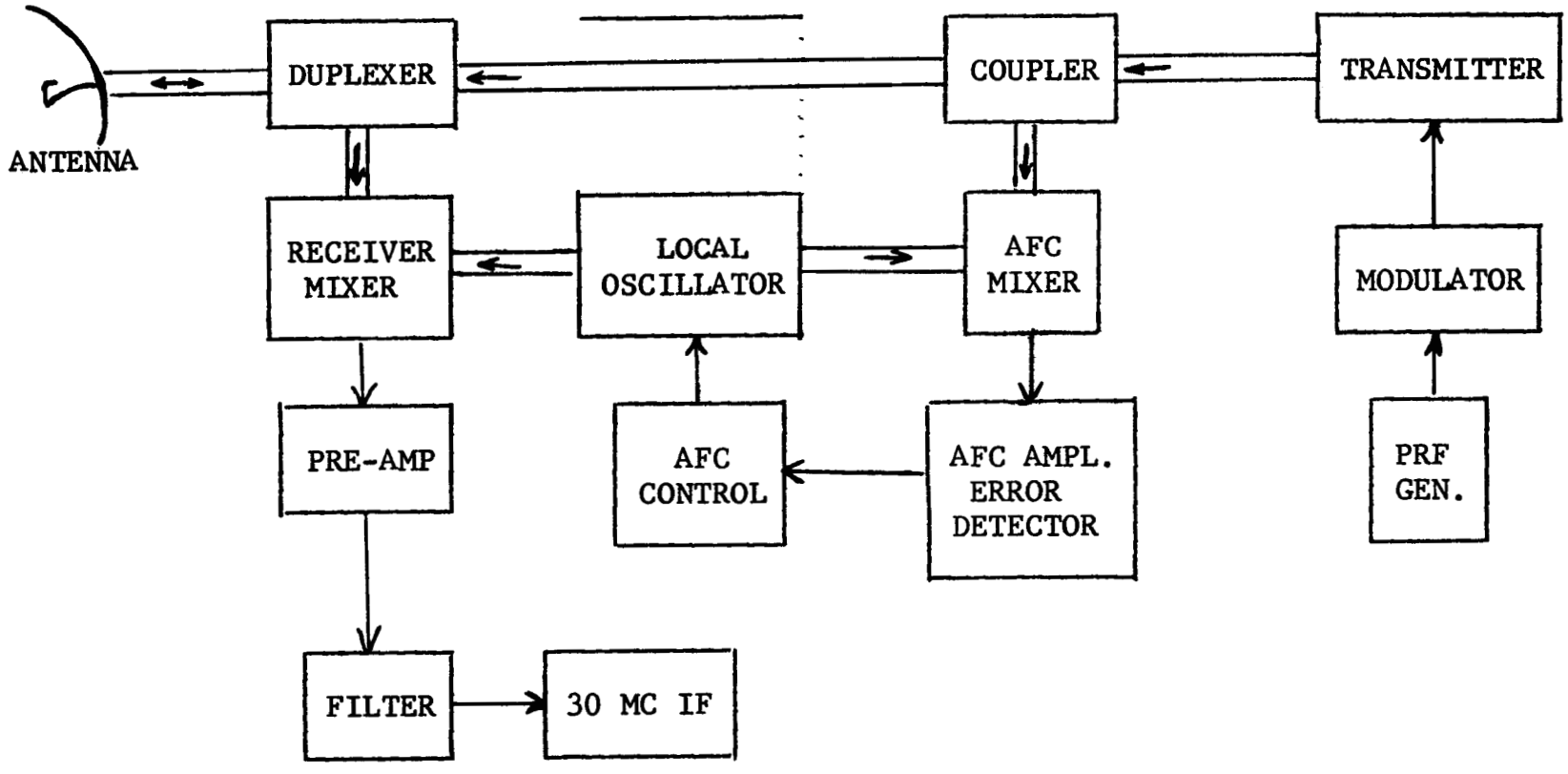

RADAR ALTIMETER

SYSTEM BLOCK DIAGRAM

Figure 4.5

RADAR ALTIMETER AVG. POWER OUTPUT VS REQUIRED ANTENNA GAIN

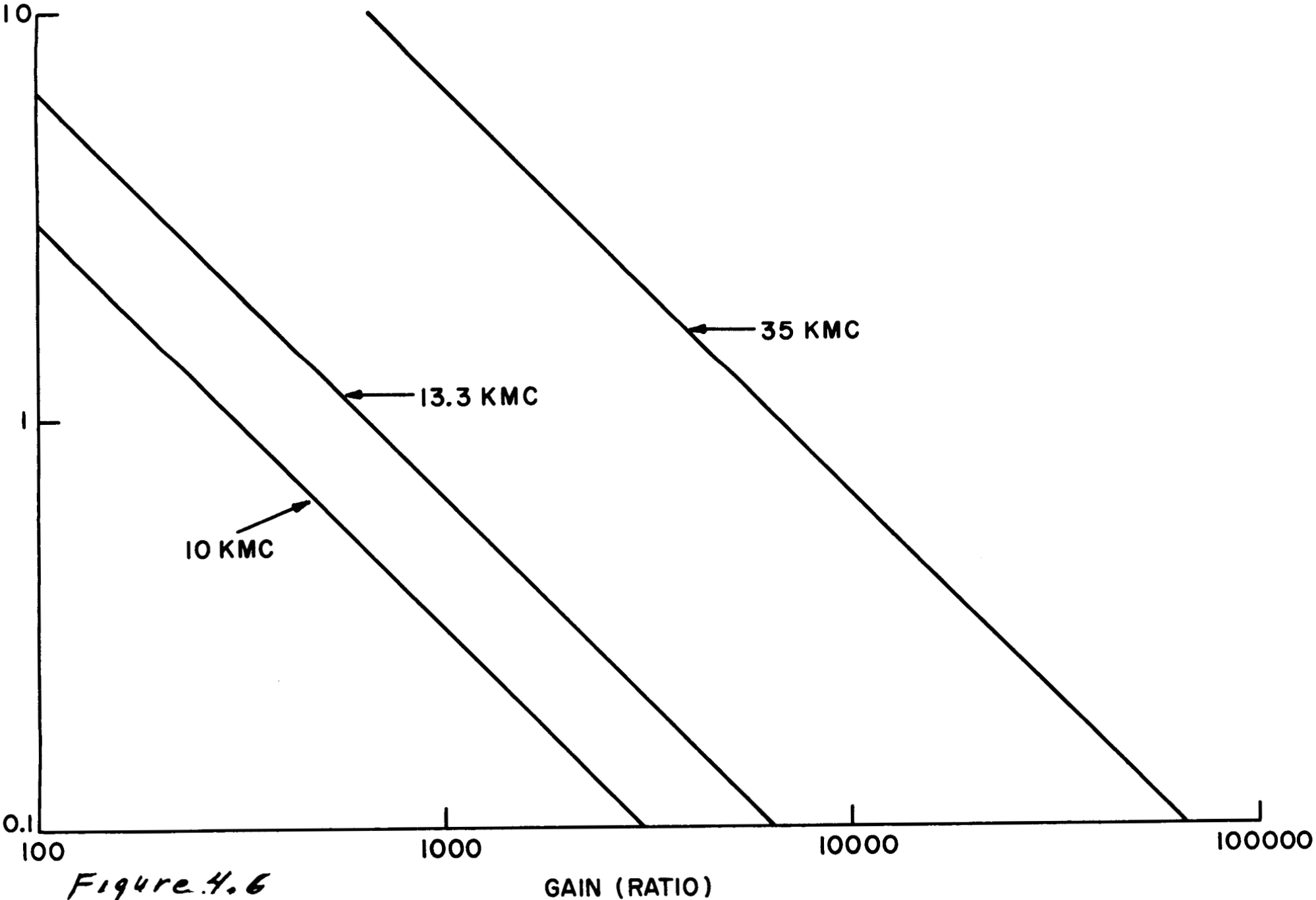

Figure 4.6

5.0 TELEMETRY & POWER SUPPLY

5.1 TECHNICAL STATUS

Work is proceeding generally according to schedule, except for about a three-week slip in the plasma property calculations due to a delay in the trajectory analysis and hence the configuration selection. Work is underway in the following areas:

5.1.1 Relay Link

For post-entry communication over a capsule-to-spacecraft relay link, two general approaches are being considered. The first approach would employ a spacecraft receiver with an IF bandwidth sufficiently wide to include the doppler shift and oscillator instability inherent in the signal. The second approach would employ a phase-lock loop to track the frequency of the received signal.

The major problem in the first approach, of course, is thresholding in the detector. An efficient modulation scheme for use in such a link is PPM-AM, and a preliminary analysis of such a system is included in this report.

The major problem in the second approach is the loop bandwidth required for acquiring and tracking the changing signal frequency. A power calculation for such a link is included in this report. Compatible modulation techniques for this coherent system will be investigated during the second half of the program.

The calculation of the electron densities and collision frequencies for the entry communication problem is just getting underway for a cone-flare configuration entering the Venus atmosphere. Attenuation and reflection calculations for a Discoverer (blunt body) configuration entering the Martian atmosphere have been completed and are included in this report.

5.1.2 Direct Link

A desirable constraint on a direct capsule-to-earth communication link is compatibility with the DSIF ground stations. Therefore, the alternatives available in the design of this link are more limited than in the relay link.

No analysis beyond that done for the proposal has been done on the direct link, although some of the results of the relay link analysis (e.g., tracking bandwidth, oscillator instability, etc.) will be applicable to the direct link. Further investigation of the direct link will be made in the second half of the program.

5.1.3 Error Correction Coding

The study of error correction coding for this application is nearly completed. Single-error correcting, single-error detecting, and double-error correcting codes have been considered, with a view toward determining the saving in transmitter power accruing from this. The size, power, weight, and complexity of the encoding and decoding equipment have also been considered. A report on this effort is included.

5.1.4 Antenna

Antennas are being studied for both a capsule-to-spacecraft relay link (100 to 500 mc) and a direct capsule-to-earth link (2.3 kmc). In the first half of the program, only post-entry communication using a Discoverer configuration has been studied. Entry communication and other configurations will be considered during the second half of the program.

5.1.5 Atmospheric Propagation

Initial investigations of the Venus atmosphere models have shown that the post-entry propagation effects are comparable to those of the Earth.

5.1.6 Power Supply

Work is commencing now in the power supply studies. The initial effort has been directed toward defining the power supply requirements.

5.2 MAJOR ACCOMPLISHMENTS

The following informal reports have been written on communication tasks and are included in this section.

(1) Signal Tracking and Acquisition

(2) Preliminary Report on PPM-AM Telemetry Relay Link

(3) Preliminary Report on Error Correcting Codes

(4) Mars Entry Transmission Study

Brief progress reports have been prepared in the following areas:

(5) Capsule Antenna

(6) Venus Atmospheric Propagation

(7) Power Supply

5.3 SIGNAL TRACKING AND ACQUISITION

5.3.1 Introduction

Due to the characteristics of the Venus capsule mission, frequency uncertainties will exist between the signal observed at the receiver and that generated in the receiver for the capsule-to-spacecraft link. One approach to the problem is to open the bandwidth of the receiver so that it will include the frequency of any predicted incoming signal. This, of course, can lead to excessive noise bandwidths and, therefore, excessive power to overcome thresholding for many types of modulation. A second approach is to track the frequency of the incoming signal so that the receiver bandwidth can be reduced to the minimum desired. This approach will usually result in greater equipment complexity but may be required if other simpler methods prove unsatisfactory. This report, therefore, investigates the capability and requirements of such a system.

5.3.2 Problem Description

Frequency uncertainty in the relay link can result from

1. long-term oscillator drift(transmitter and receiver) during the journey of greater than 100 days.

2. abrupt oscillator frequency change due to high g-loading during capsule entry.

3. oscillator frequency change due to temperature variation if adequate temperature control cannot be maintained during entry and the subsonic descent of the capsule into the relatively hot Venusian atmosphere.

4. doppler shift.

In this report it has been assumed that all but the latter are either negligible or can be made negligible. Long term drift can be eliminated by comparing and correcting the frequency of the transmitter or receiver prior to capsule ejection; further drift should be negligible since the time period between ejection and impact is anticipated to be relatively short. Frequency

variations due to g-loading and temperature change have not yet been evaluated but will probably not be significant if proper precautions are taken in design, especially if the signal frequency to be used is in the lower portion of the band of interest ($\approx$ 100 mc).

The doppler shift has been determined in appendix A under the assumption that the trajectories of the capsule and spacecraft with respect to Venus and each other can be predicted to a relatively high degree. This allows optimization of the system; any uncertainty in parameters such as range, communication time, and spacecraft velocity will result in more stringent requirements on the tracking system.

In order to track the changing frequency of the signal a phase-lock loop will be considered. Several factors must be taken into account in determining the noise bandwidth of the loop and, therefore, the signal power required. These are:

1. thermal noise

2. phase jitter due to oscillator instability

3. sweep rate for signal acquisition

4. doppler rate

Although it is desirable to minimize bandwidth to reduce thermal noise, the latter three items tend to restrict this reduction. It is desirable to follow all variations of the oscillator phase to reduce degradation of the information and to minimize the possibility of loss of phase lock. This is accomplished by widening the loop bandwidth to a value consistent with the stability of a given oscillator or by using an oscillator with adequate stability to operate properly in conjunction with a given bandwidth. For the purposes of this report it will be assumed that the latter is more reasonable; i.e., the bandwidth determined from other considerations will set the stability requirements on the oscillator. These requirements will be determined in a later report after other system parameters are more closely defined.

The dominant factor that limits the minimum loop bandwidth will then be the sweep rate required for signal acquisition. Since only a few minutes of communication will be available, fast acquisition time is mandatory. As noted later the sweep rate required for acquisition should be much greater than the doppler rate and, therefore, the effects of the latter will be negligible. This suggests the possibility of an adaptive system which will switch to a wide loop bandwidth when phase lock is lost and switch back to a narrow bandwidth after the signal has been acquired. This would yield good loop dynamic characteristics during acquisition and reduce phase jitter due to thermal noise during the tracking phase, thereby reducing the probability of loss of lock. Although this procedure is described in the literature, no reference to a working model has been found.

The phase-lock loop considered in this report is a basic Type II loop with the addition of a limiter at the output of the IF section. The limiter provides a gain control function since the gain of the loop depends on the amplitude of the incoming signal. The advantages of limiting were set forth in Reference 3 and the acquisition characteristics of a type II loop with limiting in the presence of noise were recently determined by the Defense Systems Department of General Electric (Reference 1) utilizing a GEESE* model of the system. The results of the latter will be used in the following analysis. Since the Type II loop has been discussed extensively in the literature, the theory of operation will not be re-derived here and only a brief discussion will be given in addition to the results obtained in Reference 1.

In the analysis it will be assumed that a carrier signal is present without regard to how it is derived from the power transmitted from the capsule; i.e., it is of little importance here whether the carrier is transmitted as a carrier (such as in PCM/PS/PM) or is derived from the spectrum containing the information (as in PCM/PS). This will affect the efficiency of

*General Electric Electronic System Evaluator

the communication system but will be tkaen into account when the different modulation schemes are evaluated.

5.3.3 Description of Phase-Lock Loop

The block diagram of the particular phase-lock loop considered in the computer simulation described in Reference 1 is shown in Figure 3-1. The incoming signal is mixed with the local oscillator signal and filtered in the IF amplifier. It is then fed into a band pass limiter. In the locked condition, the IF signal is of exactly the same frequency as the reference oscillator, and only a phase difference exists between them. The phase detector senses any phase error, and its output is a voltage proportional to the sine of the phase difference. This error voltage is filtered and applied to the VCO (Voltage Controlled Oscillator) to control the VCO frequency. The dynamic characteristics of the loop are determined primarily by the characteristics of the control filter, H(s), which is a proportional plus integral filter.

The loop transfer function is (for $\omega_n \gg \omega_1$).

$$\frac{\phi_{VCO}(S)}{\phi_{SIG}(S)} = \frac{K(\omega_2/\omega_1)\ (S + \omega_1)}{S^2 + \left[\omega_2 + K\ (\omega_2/\omega_1)\right] S + \omega_n^2} \tag{3-1}$$

OR

$$\frac{\phi_{VCO}(S)}{\phi_{SIG}} = \frac{K(\omega_2/\omega_1)\ (S + \omega_1)}{S^2 + 2\zeta\omega_n S + \omega_n^2} \tag{3-2}$$

where

ω_2 and ω_1 are the critical frequencies of the loop filter $H(s) = (s + \omega_1) / (s + \omega_2)$

K is the loop velocity constant

ω_n is the loop undamped natural frequency ($\sqrt{K\omega_2}$).

ζ is the loop damping factor ($\approx \frac{1}{2}\sqrt{K\omega_2/\omega_1^2}$)

The phase error response is

$$\frac{\phi_{ERROR}(S)}{\phi_{SIG}\ (S)} = \frac{S\ (S + \omega_2)}{S^2 + 2\zeta\omega_n S + \omega_n^2} \tag{3-3}$$

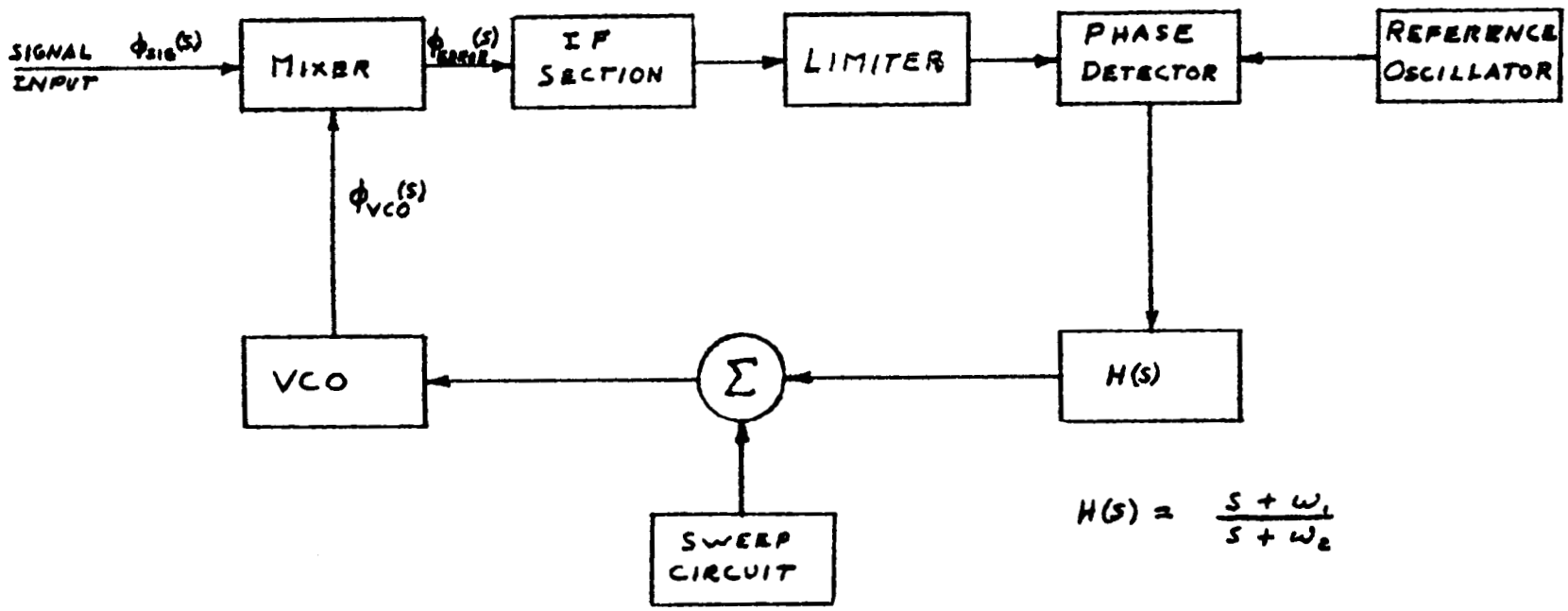

FIGURE 3-1. PHASE-LOCK LOOP BLOCK DIAGRAM

5.3.4 Acquisition Capability of Phase-Lock Loop in the Presence of Noise

In the particular loop tilized in the computer simulation, for a given equivalent noise bandwidth, B_n, the natural frequency, ω_n, is a maximum for a loop damping factor of $\zeta = \frac{1}{2}$. Conversely, for a given natural frequency, the noise bandwidth is minimum when $\zeta = \frac{1}{2}$. The comparative data on systems with damping factors indicate that for $\zeta > \frac{1}{2}$ there is no marked change in acquisition characteristics; but for $\zeta = 1/3$, the acquisition performance is significantly poorer than for $\zeta \geq \frac{1}{2}$. When the IF signal is limited, the loop can be designed so that at some S/N ratio, a high probability of acquisition is obtainable for a given sweep rate. The limiter performs a gain control function which provides good dynamic performance. In addition, when using the limiter and "matching"* the gain at some minimum expected S/N ratio, the loop operates as well at the match point as would a linear loop. (any increase in S/N ratio will improve acquisition performance over that obtainable with a linear loop). The overall system performance is generally better for $\zeta = \frac{1}{2}$, inasmuch as the decrease in probability of acquisition is not as rapid with increasing sweep rate and noise does not degrade the performance as much. The apparent improvement in maximum sweep rate for higher damping factors, and the decrease for lower damping factors, are due to the relative stability of the loops.

From the results an empirical formula was developed in Reference 1 to predict the sweep rate for a 90-percent probability of acquisition. The accuracy of the formula in predicting the 90-percent point is within 10-percent of the measured values, and holds for damping factors equal to, or greater than, 0.5 ($\zeta \geq \frac{1}{2}$).

*"Matching" is the procedure whereby the loop gain is set to give a minimum noise bandwidth $\zeta = \frac{1}{2}$ at one S/N ratio in the IF, $(S/N)_{IF}$. Figure 4-3 shows the factor, α by which the signal voltage out of a limiter varies as a function of S/N ratio into the limiter, (S/N)IF. The point at which $\zeta = \frac{1}{2}$ is set is designated α_o .

$$R_{9,o} \text{ (cps/sec)} = \frac{(\pi/2 - 2.2\,\sigma_o)\ (0.9\,\frac{\alpha}{\alpha_o})\,\omega_{no}^2}{2\,\pi\,(1 + \delta)} \tag{4-1}$$

where

σ_o = calculated rms output phase jitter

δ = overshoot

α = signal suppression factor in limiter

α_o = suppression factor for the $(S/N)_{IF}$ for which loop is "matched".

ω_{no} = natural frequency of loop at matched point.

The calculated rms output phase jitter, σ_o, is given by

$$\sigma_o = \left[\tfrac{1}{2}\left(\frac{N}{S}\right)_{IF}\left(\frac{B_n}{B_{IF}}\right)\right]^{\frac{1}{2}} = \left[\tfrac{1}{2}\left(\frac{N}{S}\right)_{out}\right]^{\frac{1}{2}} \tag{4-2}$$

where,

$(S/N)_{IF}$ is the signal-to-noise ratio in the IF section

B_{IF} is the IF bandwidth

B_n is the loop noise bandwidth

$(S/N)_{out}$ is the signal-to-noise ratio in the loop noise bandwidth.

This equation is plotted in Figure 4-1 along with a curve showing the average experimental values obtained. The calculated value given above is to be used with Equation 4-1; however, the predicted value of phase jitter for a given $(S/N)_{out}$ is to be taken from the experimental curve.

The overshoot, δ, is obtained by considering the phase response of the loop to an input ramp of frequency and is given by

$$= \exp\left[-\frac{\zeta\pi}{1 - \zeta^2}\right] \tag{4-3}$$

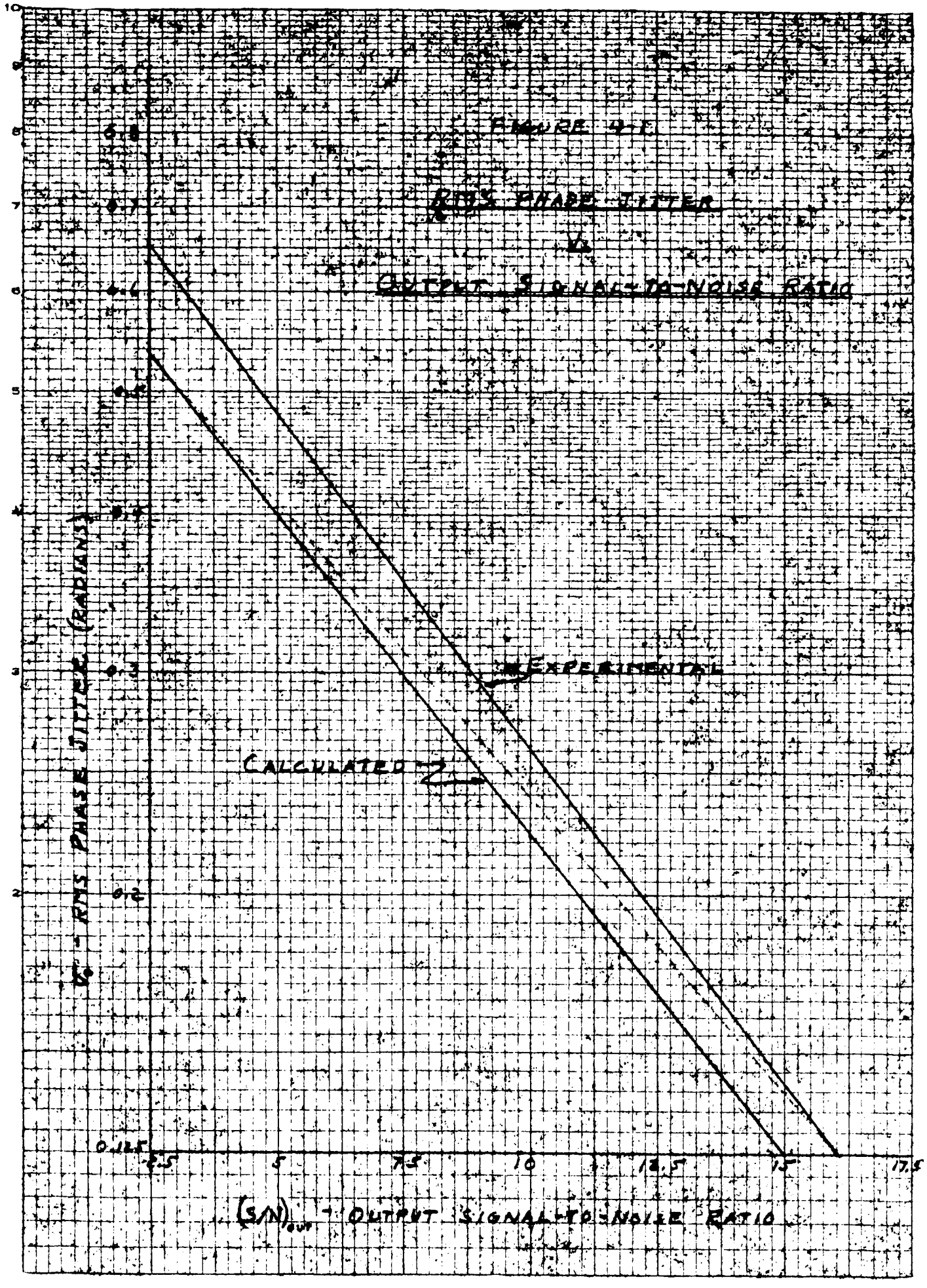
FIGURE 4-1
RMS PHASE JITTER
VS.
OUTPUT SIGNAL-TO-NOISE RATIO
EXPERIMENTAL
CALCULATED
σ_ϕ - RMS PHASE JITTER (RADIANS)
0.8
0.7
0.6
0.5
0.4
0.3
0.2
0.125
2.5
5
7.5
10
12.5
15
17.5
$(S/N)_{out}$ - OUTPUT SIGNAL-TO-NOISE RATIO

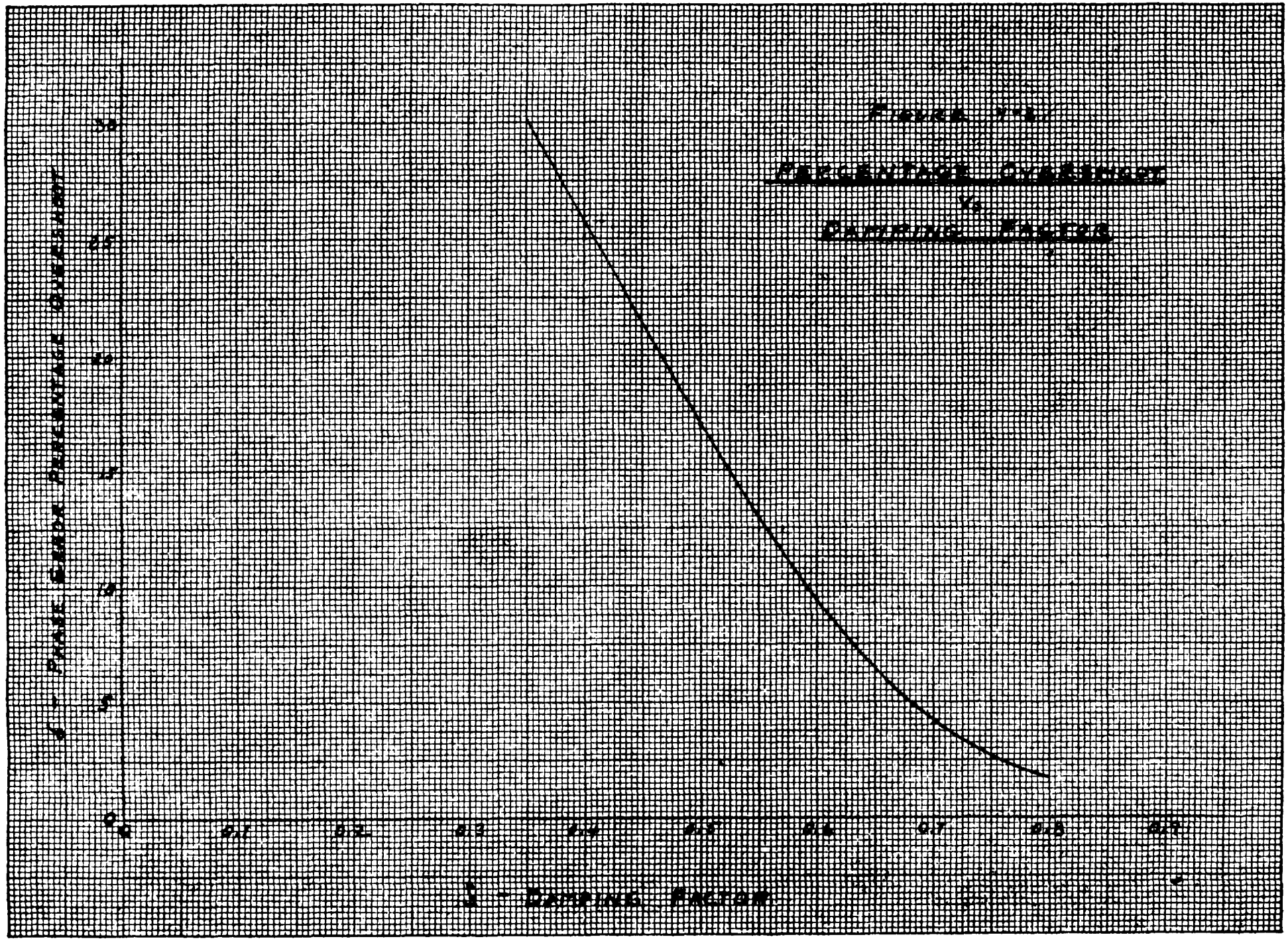
PERCENTAGE OVERSHOOT
VS
DAMPING FACTOR
δ - PHASE ERROR PERCENTAGE OVERSHOOT
0
5
10
15
20
25
30
0
0.1
0.2
0.3
0.4
0.5
0.6
0.7
0.8
0.9
ζ - DAMPING FACTOR

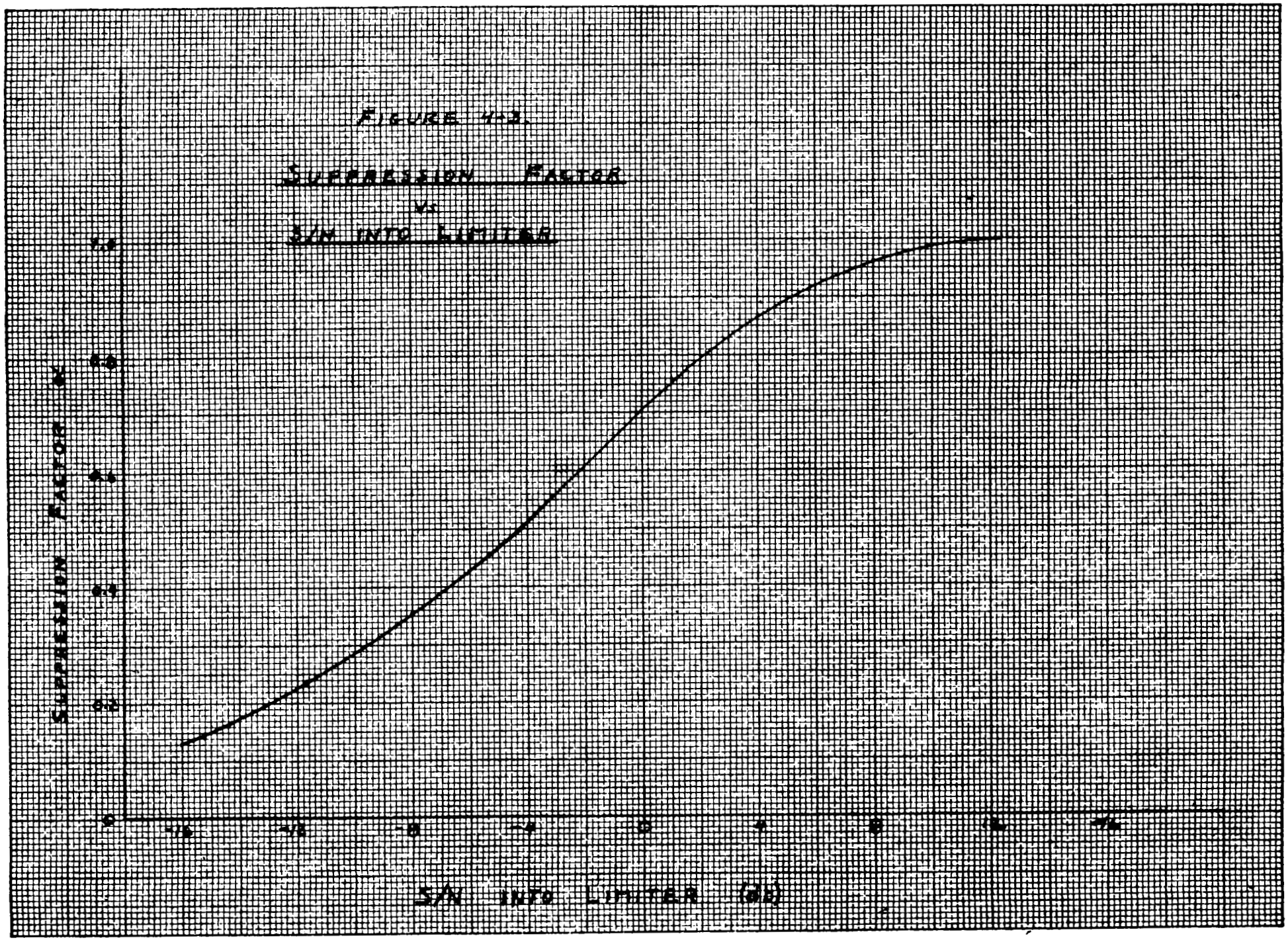
FIGURE 4-2.
SUPPRESSION FACTOR
VS
S/N INTO LIMITER
SUPPRESSION FACTOR
0
0.2
0.4
0.6
0.8
1.0
-16
-12
-8
-4
0
4
8
12
16
S/N INTO LIMITER (dB)

This function is plotted in Figure 4-2.

The signal suppression factor, α, results from the characteristics of an ideal limiter in the presence of noise. The variation of α with S/N at the input to the limiter is shown in Figure 4-3.

The noise bandwidth of the loop, B_n(cps), is related to the natural frequency of the loop, ω_n (rad/sec), by

$$B_n \approx \frac{\omega_n}{4\zeta} (1 + 4\zeta^2) \qquad (4\text{-}4)$$

B_n is minimum when $\zeta = \frac{1}{2}$. Its value at that point is $B_n = \omega_n$.

5.3.5 Analysis

In order to determine the approximate signal tracking and acquisition capability of the capsule-to-spacecraft link and the effects of parameter variations on the link the following reference system will be assumed for a sample bandwidth calculation:

Carrier Power transmitted	:	1 watt
Frequency	:	100 mc
Path Length	:	10,000 km
Capsule Antenna Gain	:	0 db
Spacecraft Antenna Gain	:	0 db
Receiver Noise Figure	:	10 db
Losses	:	3 db
Margin	:	8 db

The sample calculation is shown in Table 5-1. An allowable phase jitter of 20° has been assumed which results in a required S/N ratio of 7.5 db in the loop noise bandwidth, B_n (Appendix B). An average noise figure of 10 db (resulting in an overall system noise temperature of 2900°K) has been assumed for all frequencies to be considered (100 mc to 500 mc). Although this will be pessimistic for the lower frequencies of interest, the decreasing antenna efficiencies at the lower frequencies will tend to nullify

TABLE 5-1 Sample Bandwidth Calculation for Signal Tracking

Carrier Power (1 watt)	0.0 dbw
Transmitter Antenna Gain	0.0 db
Propagation Loss (100 mc; 10,000 km)	-152.5 db
Receiver Antenna Gain	0.0 db
Losses	-3.0 db
Power Available at Receiver	-155.5 dbw
Receiver Noise (1cps; 290°K)	-204.0 dbw
Receiver Noise Figure	10.0 db
S/N Ratio (20° RMS Phase Jitter)	7.5 db
Margin	8.0 db
Power Required at Receiver/cps	-178.5 dbw

Bandwidth available (referred to 1 cps) 20.0 db (B = 200 cps)

the error due to this assumption. Therefore, the capability of the system will be close to that given over the entire range of frequencies.

Utilizing the results of the sample calculation, the allowable loop noise bandwidth is shown in Figures 5-1, 5-2, and 5-3 as a function of transmitted power, signal frequency, and range from capsule to spacecraft.

The results of Appendices A and B can now be used to determine the required loop noise bandwidth. In Appendix A the total doppler shift observed by the receiver was found to be described by (Equation A-8)

$$B_S = \dot{f}_{d\ max}\ T \tag{5-1}$$

where

$\dot{f}_{d\ max}$ is the maximum doppler rate

T is the communication time (time from capsule entry to impact)

Appendix B gives the loop noise bandwidth at the "match" point as a function of sweep time for 90-percent probability of acquisition in a single sweep (Equation B-7).

$$B_{no} = \sqrt{9\ R_{90}} \tag{5-2}$$

Neglecting frequency uncertainties in the capsule-to-spacecraft link other than the doppler shift given by Equation (5-1), the sweep rate can be written as

$$R_{90} = \frac{B_S}{T_L} = \frac{\dot{f}_{d\ max}\ T}{T_L} \tag{5-3}$$

where T_L is the time required for one complete sweep of the defined frequency band, B_S , and is interpreted as the maximum time "lost" in acquiring the signal after loss of phase lock (neglecting the 10-percent probability that more than one sweep is required).

Utilizing Equations 5-2 and 5-3, the required loop noise bandwidth can be expressed as

$$B_{no} = \sqrt{9\dot{f}_{d\ max}\frac{T}{T_L}} \tag{5-4}$$

Defining $\epsilon \equiv \frac{T_L}{T}$, the maximum percentage of communication time or data that is lost during a single acquisition, Equation 5-4 becomes

$$B_{no} = \sqrt{9\ \frac{\dot{f}_{d\ max}}{\epsilon}} \tag{5-5}$$

The required bandwidth is shown in Figures 5-1, 5-2, and 5-3 for different values of ϵ and assuming V_S = 8 km/sec. The intersections of the curves (dashed lines) for available and required bandwidth therefore indicate the minimum signal power required as a function of range, frequency, and percent of lost communication time per acquisition.

It may be noted that the form of the above equation is identical to that commonly used for determining the bandwidth required for loop hold-in in the presence of doppler where $\epsilon \approx 1$. Since, for essentially continuous communication, ϵ must be much less than unity, the requirements for doppler hold-in will be negligible compared to those for acquisition. In fact the doppler rate can be utilized to advantage if the frequency sweeping for acquisition is always in the direction of the doppler change (continuously decreasing frequency). The fact that the function is monotonic also leads to the possibility of continually reducing the highest frequency of the sweep band to the frequency being observed.

The preceding analysis and the above comments apply only if <u>no</u> communication is attempted during capsule entry. In addition to plasma attenuation the variation in doppler frequency during entry is expected to be more severe. It may be described qualitatively as follows: There is negligible doppler prior to entry, and the receiver observes the transmitter frequency, f_o; during the relatively few seconds of entry, the frequency observed will increase to the value corresponding to that for the particular trajectory geometry at that time and for a stationary capsule (Figure A-1, Appendix A). The doppler rate during entry is therefore dependent on the decel-

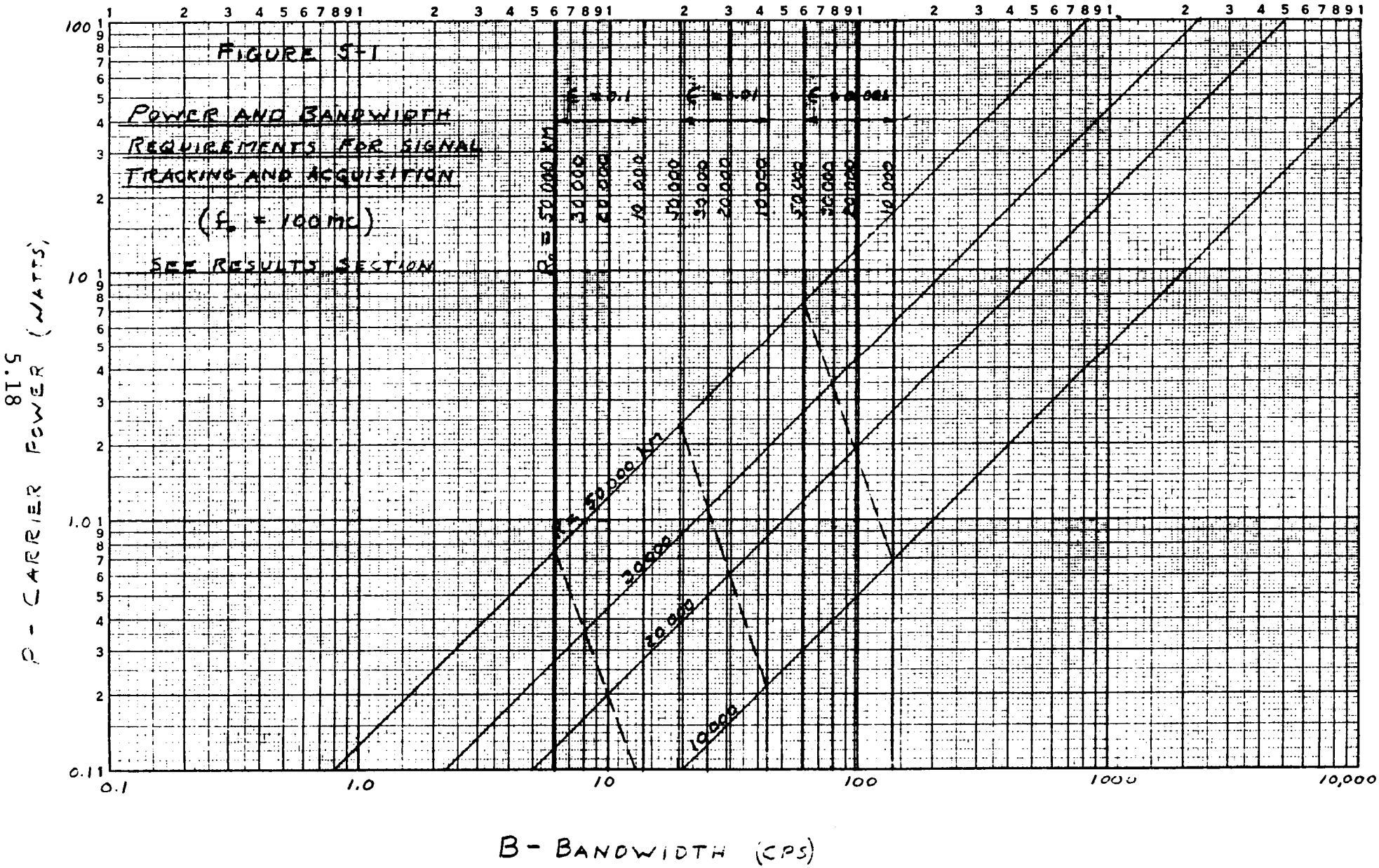
FIGURE 5-1
POWER AND BANDWIDTH REQUIREMENTS FOR SIGNAL TRACKING AND ACQUISITION
(f_0 = 100 mc)
SEE RESULTS SECTION
R_0 = 50,000 KM
30,000
20,000
10,000
50,000 KM
30,000
20,000
10,000
P - CARRIER POWER (WATTS)
B - BANDWIDTH (CPS)
0.1
1.0
10
100
1000
10,000

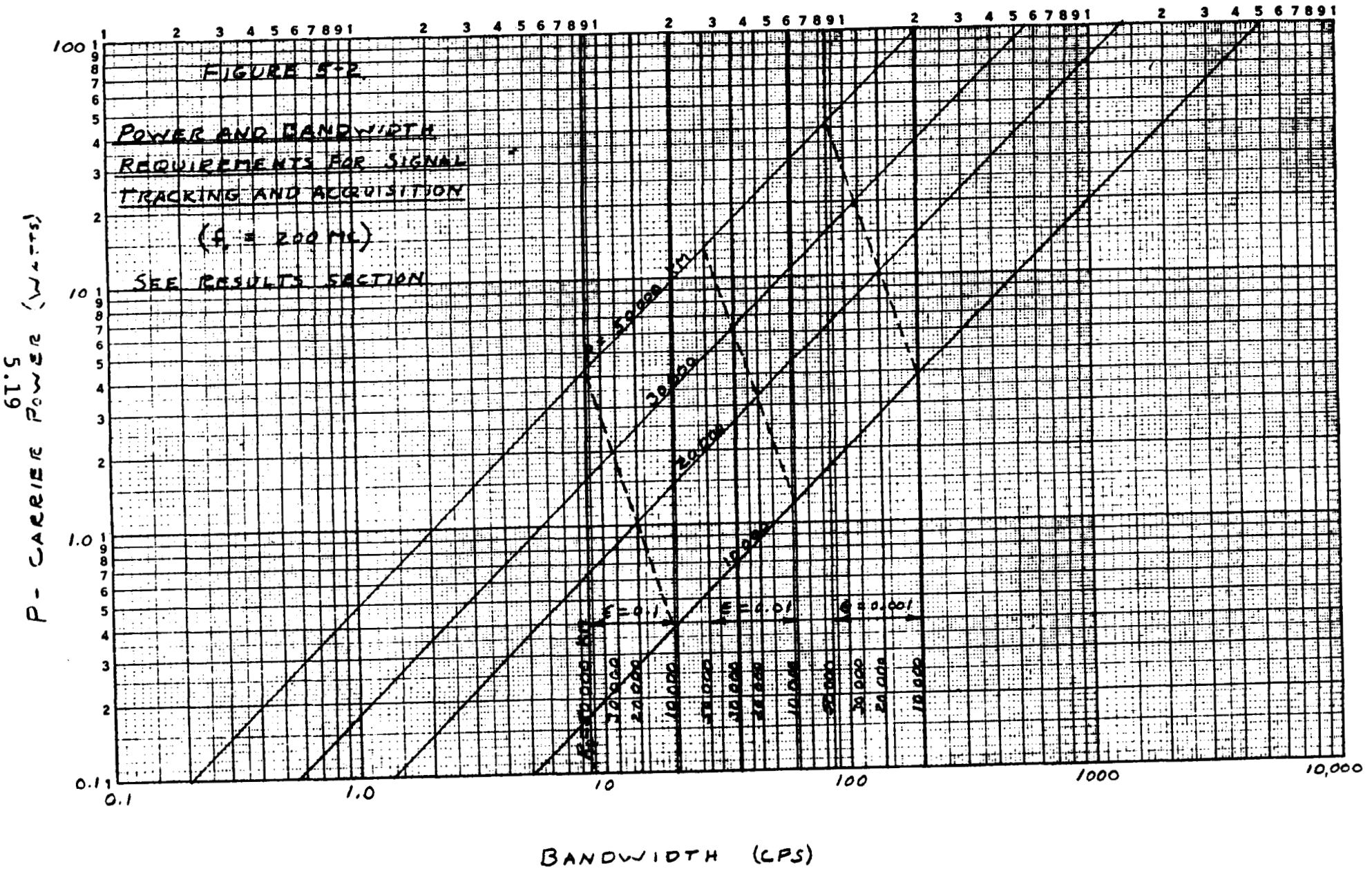
FIGURE 5-2
POWER AND BANDWIDTH REQUIREMENTS FOR SIGNAL TRACKING AND ACQUISITION
(f_c = 200 MC)
SEE RESULTS SECTION
P - CARRIER POWER (WATTS)
BANDWIDTH (CPS)
0.1
1.0
10
100
1000
10,000
50,000 KM
30,000
20,000
10,000
ε = 0.1
ε = 0.01
ε = 0.001

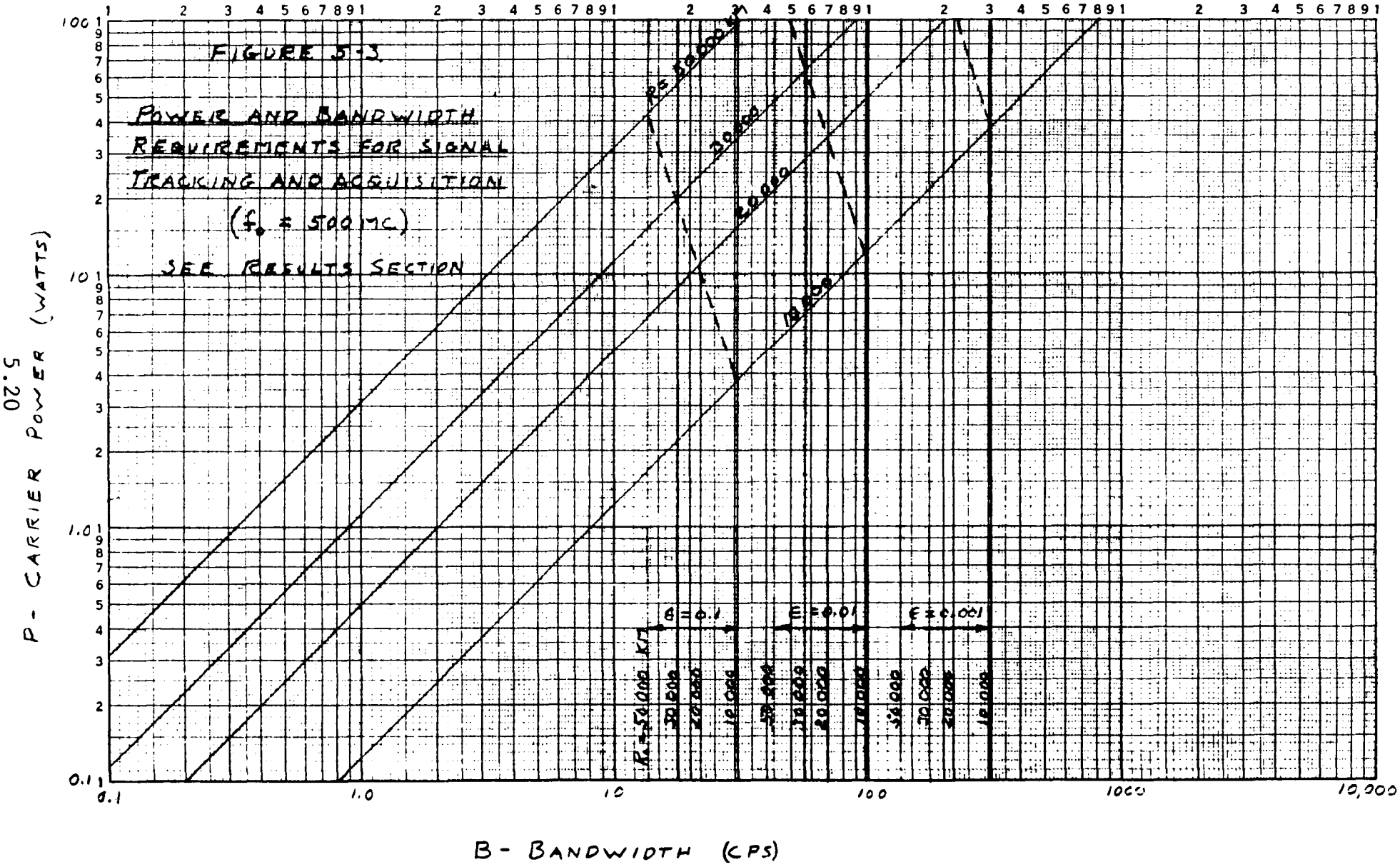
FIGURE 5-3
POWER AND BANDWIDTH REQUIREMENTS FOR SIGNAL TRACKING AND ACQUISITION
(f_0 = 500 MC)
SEE RESULTS SECTION
P - CARRIER POWER (WATTS)
B - BANDWIDTH (CPS)
ε = 0.1
ε = 0.01
ε = 0.001
R = 50,000 KT
30,000
20,000
10,000
0.1
1.0
10
100
1000
10,000

eration of the capsule and the value of θ (Figure A-1) during entry. For $\theta \approx 0$ during entry the doppler rate can be very low; however, significant values of θ are expected.

It should also be noted that in the drawing the dashed lines through the intersections of the curves for available and required bandwidths on the graphs the approximation $R = R_o$ (where R is the communication range used to determine available bandwidth and R_o is the distance from capsule to spacecraft at closest approach used to determine required bandwidth) was made. The effect of this approximation depends on the maximum value of θ during the communication period; for instance, if $\theta_{max} = 30^o$ the actual value of available bandwidth will be three-fourths $\left[(\frac{R_o}{R})^2 = \cos^2\theta \right]$ that shown on the graphs.

5.3.6 Results

The results of the analysis are illustrated in Figures 5-1, 5-2, and 5-3. The curves may be summarized as follows: the solid slanted lines indicate the available bandwidth as a function of carrier power transmitted (P), signal frequency (f_o), and path length (R); the solid vertical lines indicate the bandwidth required as a function of signal frequency, path length at closest approach (R_o), and the maximum percentage of total communication time lost for each acquisition of the signal when phase lock is lost (ϵ); the slanted dashed lines drawn through the intersections of the preceeding curves for $R = R_o$ (the effect of this approximation is discussed in Section 5.3.5) therefore define the minimum carrier power required for particular values of the parameters f_o, R, and ϵ.

These results indicate that a few watts of carrier power will give good tracking and acquisition performance for ranges in the order of 20,000 to 30,000 km if the carrier frequency is in the lower portion ($\approx$ 100 mc) of the frequency band considered. A low frequency is not only desirable because of the lower power required, but also because it will place less stringent requirements on the stability of the oscillators. Although it appears from the analysis that a frequency less than 100 mc might be advantageous, ionospheric reflection and antenna efficiency will probably not allow the use of a lower frequency.

APPENDIX A - DETERMINATION OF DOPPLER VARIATIONS

For the purpose of determining the doppler shift observed at the spacecraft receiver we shall utilize the trajectory geometry indicated in Figure A-1a. A straight-line, constant velocity (V_S) spacecraft trajectory is assumed. The doppler frequency is then given by

$$f_d = \frac{V_r}{c} f_o \tag{A-1}$$

where

V_r is the relative velocity between the spacecraft and capsule (km/sec)

C is the velocity of light (3×10^5 km/sec)

f_o is the transmitter frequency (cps)

the relative velocity may be determined from the geometry and is

$$\begin{aligned} V_r &= \frac{dR}{dt} = \frac{d}{dt}\left[(R_o^2 + X_S^2)^{\frac{1}{2}}\right] \\ &= \frac{d}{dt}\left[R_o^2 + (V_S t)^2\right]^{\frac{1}{2}} \\ &= \frac{V_S{}^2 t}{\left[R_o^2 + (V_S t)^2\right]^{\frac{1}{2}}} \end{aligned} \tag{A-2}$$

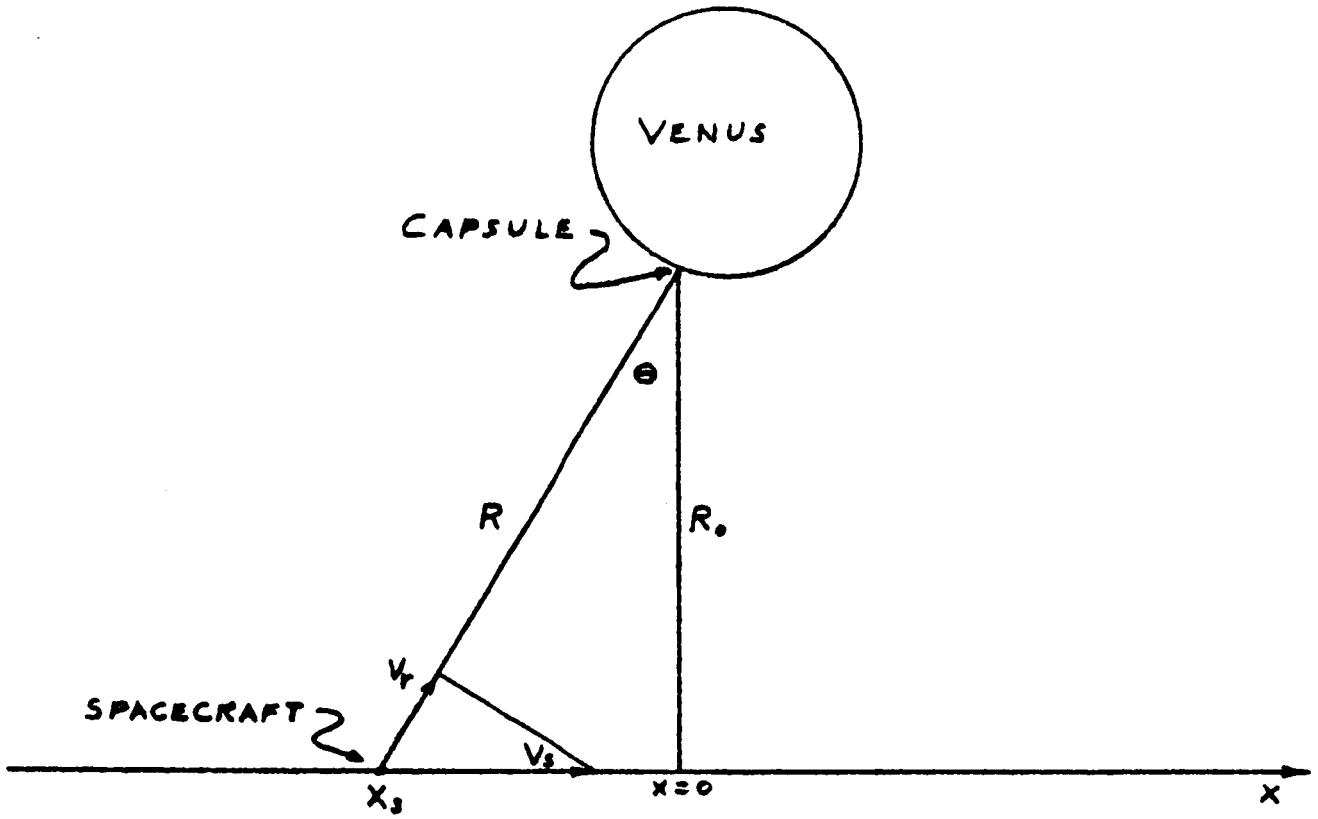

a. TRAJECTORY GEOMETRY FOR DOPPLER CALCULATIONS

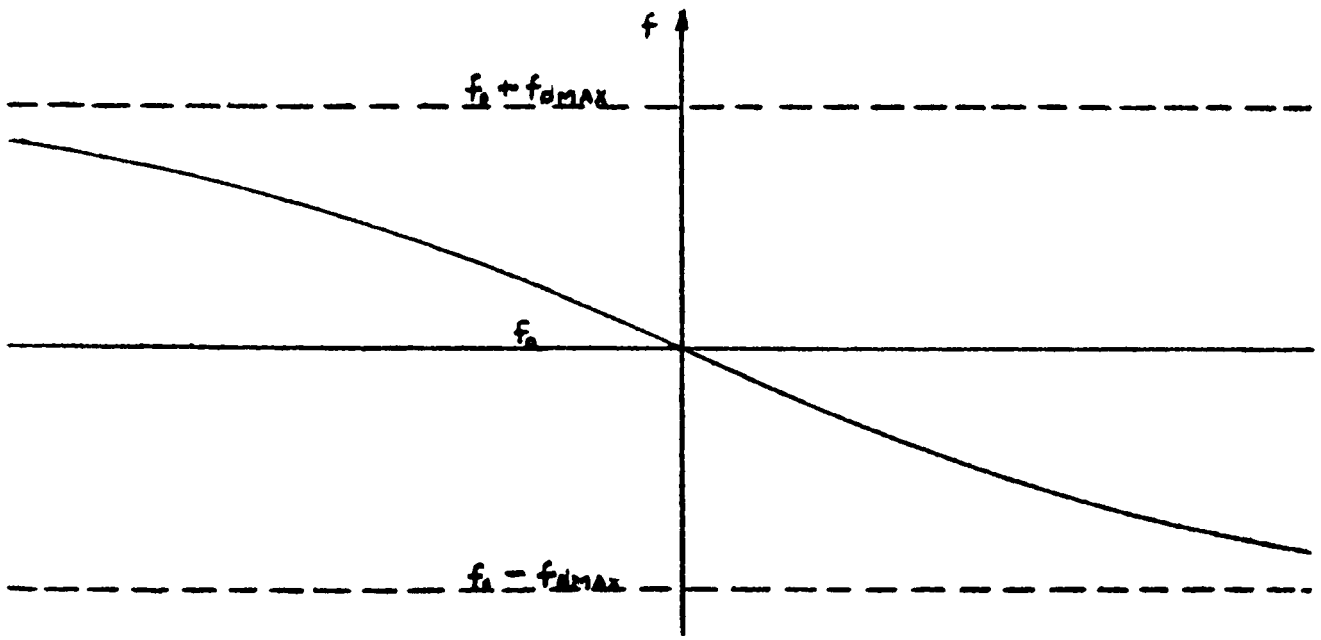

b. CORRESPONDING DOPPLER VARIATION (FOR STATIONARY CAPSULE)

FIGURE A-1. TRAJECTORY GEOMETRY AND RESULTING DOPPLER

where

R	is the range from spacecraft to vehicle (km)
R_o	is the range from closest approach (km)
X_s	is the distance from spacecraft to the point of closest approach (km)
V_s	is the spacecraft velocity with respect to Venus (km/sec)
t	is time (sec)

From (A-1) and (A-2) the doppler frequency is

$$f_d = \frac{V_S f_o}{C} \frac{V_S t}{\left[R_o^2 + (V_S t)^2\right]^{\frac{1}{2}}} = \frac{V_S f_o}{C} \frac{X_S}{\left[R_o^2 + X_S^2\right]^{\frac{1}{2}}} \qquad \text{(A-3)}$$

This function is sketched in Figure (A-1b)

The maximum total doppler shift which can occur is then

$$B_{s\ max} = f_d\ (t = \infty) - f_d(t = -\infty) = 2\frac{V_S f_o}{C} = 2 f_{d\,max} \qquad \text{(A-4)}$$

If, then, transmission is to start when the spacecraft is a large distance from the point of closest approach ($|X_S| \gg R_o$) and end when it is a large distance past the point of closest approach, (A-4) gives the minimum bandwidth which must be swept by the receiver in order to be assured that the received signal is within the sweep band. This case, however, is pessimistic since the receiver will never observe the signal when it is at $f_o \pm f_{d\ max}$. The actual doppler shift is given by

$$B_S = \frac{V_S f_o}{C} \frac{V_S t_2}{\left[R_o^2 + (V_S t_2)^2\right]^{\frac{1}{2}}} - \frac{V_S t_1}{\left[R_o^2 + (V_S t_1)^2\right]^{\frac{1}{2}}} \qquad \text{(A-5)}$$

where

t_1 is the time at which communication begins referred to $t = 0$ at $x = 0$ (assumed here to be immediately after capsule entry)

t_2 is the time at which communication ceases (assumed to be at capsule impact)

In order to simplify further analysis the assumptions will be made that the communication period, T, is centered about $t = 0$; i.e., $t_1 = t_2 = \frac{T}{2}$ and that $R_o > \frac{V_s T}{2}$. The resulting value of B_s will be slightly pessimistic but will be reasonably close to the actual value for the trajectories which are expected (spacecraft is several thousand kilometers from capsule impact area and lags capsule by a few minutes). With this assumption Equation A-5 may be rewritten as

$$B_S = \frac{V_S f_o}{C} \frac{V_S T}{R_o} \tag{A-6}$$

Since the maximum doppler rate, $\dot{f}_{d\ max}$, can be shown to be

$$\dot{f}_{d\ max} = \frac{V_S^2 f_o}{C R_o} \tag{A-7}$$

then equation A-6 may be rewritten as

$$B_S = \dot{f}_{d\ max} T \tag{A-8}$$

The above assumptions have therefore led to the case where the doppler shift is approximated by the product of the maximum doppler rate and communication time.

APPENDIX B - BANDWIDTH REQUIREMENTS FOR ACQUISITION

From Section 5.4 the sweep rate for a 90-percent probability of acquisition is given by

$$R_{90}\ (\text{cps/sec}) = \frac{\left(\frac{\pi}{2} - 2.2\,\sigma_o\right)\left(0.9\,\frac{\alpha}{\alpha_o}\right)\omega_{no}^2}{2\quad(1+\delta)} \tag{B-1}$$

Since a damping factor of ½ was determined to be optimum, this value will be used. Then, from Figure 4-3

$$\delta = 0.17 \tag{B-2}$$

and from Equation 4-4 the noise bandwidth equals the natural angular frequency of the loop

$$B_n = \omega_n \tag{B-3}$$

or, at the "match" point

$$B_{no} = \omega_{no} \tag{B-4}$$

The allowable phase jitter at the match point will be designated to be 20° or 0.35 radians. Figure 4-1 then indicates that a $(S/N)_{out}$ of 7.5 db is required. The calculated phase jitter, σ_o , is found from the same figure to be 0.3 radians.

At the "match" point $\alpha = \alpha_o$; therefore,

$$\frac{\alpha}{\alpha_o} = 1 \tag{B-5}$$

Utilizing the values determined here, Equation B-1 may be reduced to

$$R_{90} = \frac{\left[\frac{\pi}{2} - (2.2)(0.3)\right]\left[0.9\ B_{no}^2\right]}{2\,\pi\,(1 + 0.17)} \tag{B-6}$$

$$= 0.111\ B_{no}^2$$

or

$$B_{no} = \sqrt{9\ R_{90}} \tag{B-7}$$

NOMENCLATURE

$H(S)$	Loop filter transfer function
K	Velocity gain constant
ω_1	Upper critical frequency of loop filter
ω_2	Lower critical frequency of loop filter
ζ	Loop damping factor
ω_n	Loop undamped natural frequency
ω_{no}	Loop undamped natural frequency at "match" point
B_n	Loop noise bandwidth
B_{no}	Loop noise bandwidth at match point
B_{IF}	Bandwidth of intermediate frequency section
B_S	Bandwidth to be swept by frequency sweep circuit
$(S/N)_{IF}$	Signal-to-noise ratio at the output of the IF section
$(S/N)_{out}$	Signal-to-noise ratio in the loop noise bandwidth
R_{90}	Sweep rate for 90-percent probability of acquisition
σ_o	RMS phase jitter in the output signal
α	Signal suppression factor in limiter
α_o	Signal suppression factor for a damping factor of $\frac{1}{2}$
δ	Percent overshoot in phase error for a VCO frequency ramp
f_d	Doppler frequency
$f_{d\ max}$	Maximum doppler frequency
$\dot{f}_{d\ max}$	Maximum doppler rate of change with time
T	Communication period (duration of subsonic capsule)

T_L	Time required for one complete sweep by sweep circuit
ϵ	Ratio of T_L to T
V_r	Relative spacecraft velocity in direction of capsule
V_S	Velocity of spacecraft
f_o	Carrier frequency
C	Speed of Light
R	Range from capsule to spacecraft
R_o	Closest distance of approach of spacecraft to capsule
X_S	Position of spacecraft along trajectory
θ	Angle between the vectors R and R_o

REFERENCES

1. Frazier, J. P. and Page, J.; "Phase-lock Loop Frequency Acquisition Study", General Electric Company, TIS No. R61DSD25, 1 September, 1961.

2. Gruen, W.J.; "Theory of AFC Synchronization", Proceedings of the IRE, August, 1953.

3. Jaffe, R. and Rectin, E.; "Design and Performance of Phase-lock Circuits Capable of Near-Optimum Performance Over a Wide Range of Input Signal and Noise Levels", IRE Transactions on Information Theory, Volume 1T-1, pp 66-76; March, 1955

4. Woods, C.R.; "A Mathematical Model Representing Oscillator Short-Term Stability", General Electric Company TIS No. R61DSD35, 20 September 1961.

5. "Stable Oscillator Investigation", Jet Propulsion Laboratory Research Summary 36-3

6. Eveleigh, V.W.; "Adaptive Phase Locked Loop Study", General Electric Company, TIS No. R62ELS-3, 2 January, 1962.

5.4 PRELIMINARY REPORT ON PPM-AM TELEMETRY RELAY LINK

5.4.1 Introduction

Pulse position modulation - amplitude modulation (PPM-AM) is a particular form of pulse modulation in which the time of occurrence of an RF pulse is varied in proportion to the amplitude of the sampled modulating signal. It can achieve very high output S/N ratios and has the property of being able to work through channels where multipath or common RF channel interference is a problem.

It has been shown* that for a given required output S/N ratio, a PPM-AM telemetry system requires the lowest average power of all the various telemetry systems. This is due largely to the fact that the transmitter duty cycle for PPM-AM is quite low.

One of the main reasons that PPM-AM is not more widely used in terrestrial applications is because it does not trade bandwidth for power so efficiently as the PCM techniques do. However, this is not a constraint on the Venus relay link, since there is no known legislative limit on RF bandwidth occupancy at Venus. Therefore, PPM-AM should be considered a contender for this application.

5.4.2 Calculation of Output S/N Ratio

A convenient (and realizable) type of pulse to use as a basis of this analysis is the "raised cosine" pulse, shown in Figure 1. The mathematical expression for such an envelope is

$$g(t) = \frac{A}{2} (1 + \cos 2\pi f_o t) \tag{1}$$

*See, for example, Nichols and Rauch (Reference 6)

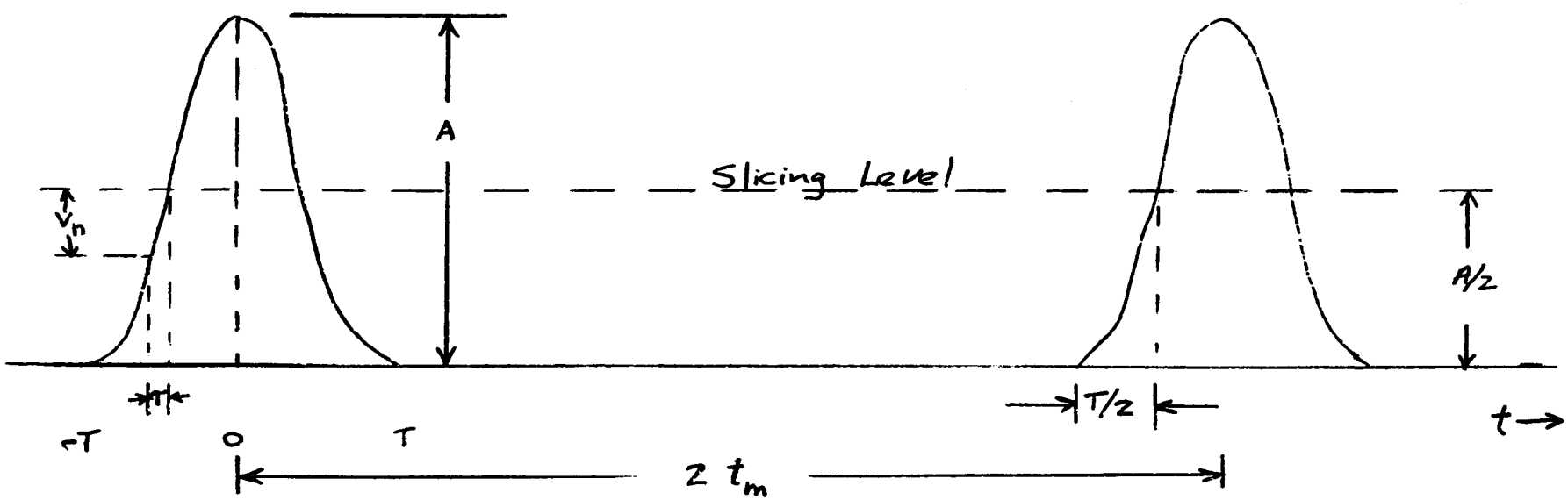

Figure 1 - Raised Cosine Pulse Waveforms

where:

$$f_o = 1/2\,T \tag{2}$$

is the fundamental frequency of the cosine pulse. The corresponding Fourier transform is:

$$G(f) = \int_{-T}^{T} \frac{A}{2}\,(1 + \cos 2\pi f_o t)\,\exp(-j\,2\pi\,ft)\,dt \tag{3}$$

$$= \frac{A \sin(\pi f/f_o)}{2\pi f(1 - f^2/f_o^{\,2})} \tag{4}$$

The power density spectrum for this is shown in Figure 2. It has its first nulls at $\pm f_o$ and is small outside this range. For practical purposes, the bandwidth required for transmission of the pulse may be taken as the range between the first nulls.

Pulses in channels adjacent in time can just touch when full-load signals are impressed on each. The "slicer" operates at half the pulse height, which, for the assumed pulse shape, is also the point of maximum slope. The time available for modulating the pulse position is equal to the channel time minus the pulse duration (2T). The appropriate combination of these factors leads to the PPM "slicer advantage" which, when applied to the RF pulse-to-noise ratio, gives the output S/N ratio in each channel.

As shown in Figure 3, a small noise voltage V_n displaces the time of observation by an increment τ, where

$$\frac{V_n}{\tau} \approx g'(-T/2) = \pi f_o A \tag{5}$$

where $g'(t)$ represents the time derivative of $g(t)$.
The mean-square position error produced by noise may be obtained from equation (5) as:

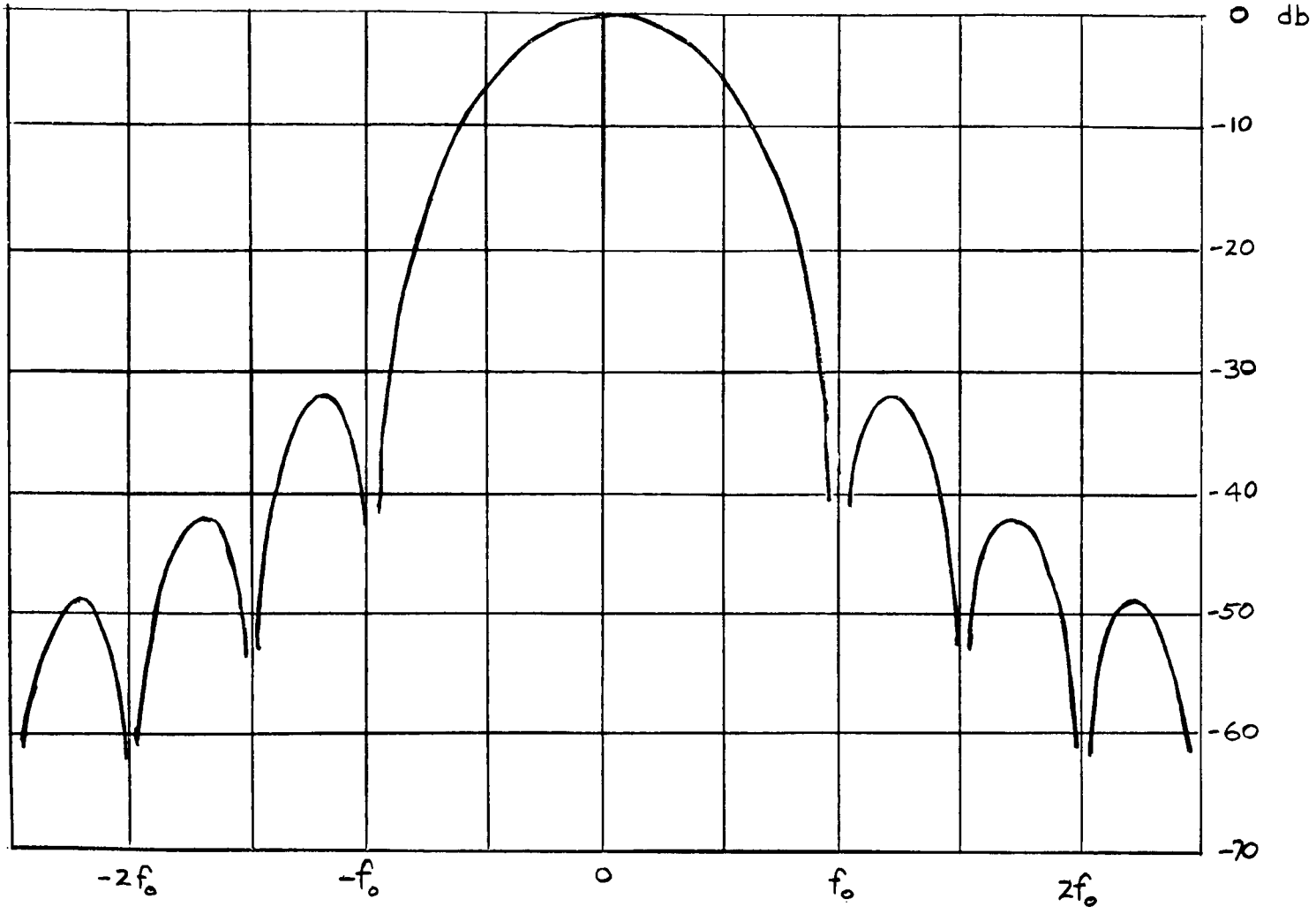

Figure 2 - Power Density Spectrum of Raised Cosine Pulse

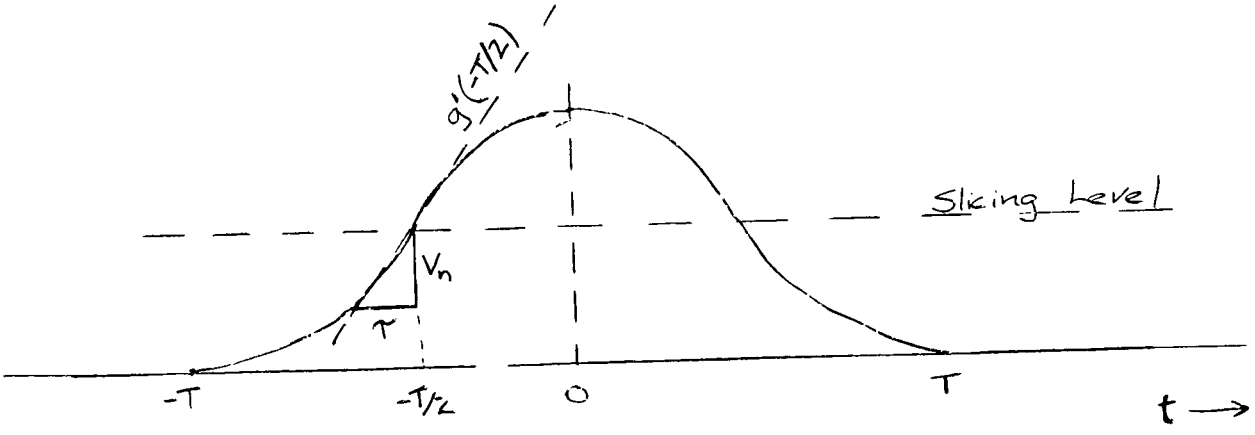

Figure 3 - Effect of Additive Noise

$$\overline{\tau^2} = \frac{\overline{V^2_n}}{(\pi f_o A)^2} \tag{6}$$

Now consider the detection technique illustrated (for a single channel) in Figure 4. Assuming a white noise spectral density N_o, with a pre-detection bandwidth B_{IF}, and a receiver input resistance R, the mean-square noise voltage at the slicer is:

$$\overline{V^2_n} = N_o B_{IF} R \frac{f_o}{B_{IF}} = N_o f_o R \tag{7}$$

Substitution of this into equation (6) yields the mean-square pulse-position error due to this noise:

$$\overline{\tau^2} = \frac{N_o f_o R}{(\pi f_o A)^2} = \frac{N_o R}{\pi^2 f_o A^2} \tag{8}$$

For a modulating signal causing a peak pulse-position displacement of $\pm t_m$, with all signal levels assumed equally likely, the mean-square signal output voltage (power across a unit resistance) is:

$$\overline{s^2} = \frac{1}{2t_m} \int_{-t_m}^{t_m} s^2 \, ds = 1/3 \; t_m^2 \tag{9}$$

The output S/N ratio $(S/N)_o$ may now be calculated from equations (8) and (9):

$$(S/N)_o = \frac{\overline{s^2}}{\overline{\tau^2}} = \frac{t^2_m \pi^2 f_o A^2}{3 N_o R} \tag{10}$$

Since the peak signal envelope power <u>received</u> is A^2/R, and the pre-detection noise power is $N_o B_{IF}$, equation (10) may be written:

$$(S/N)_o = \frac{t^2_m \pi^2 f_o B_{IF} A^2/R}{3 N_o B_{IF}} = (S/N)_i \pi^2 t^2_m f_o B_{IF}/3 \tag{11}$$

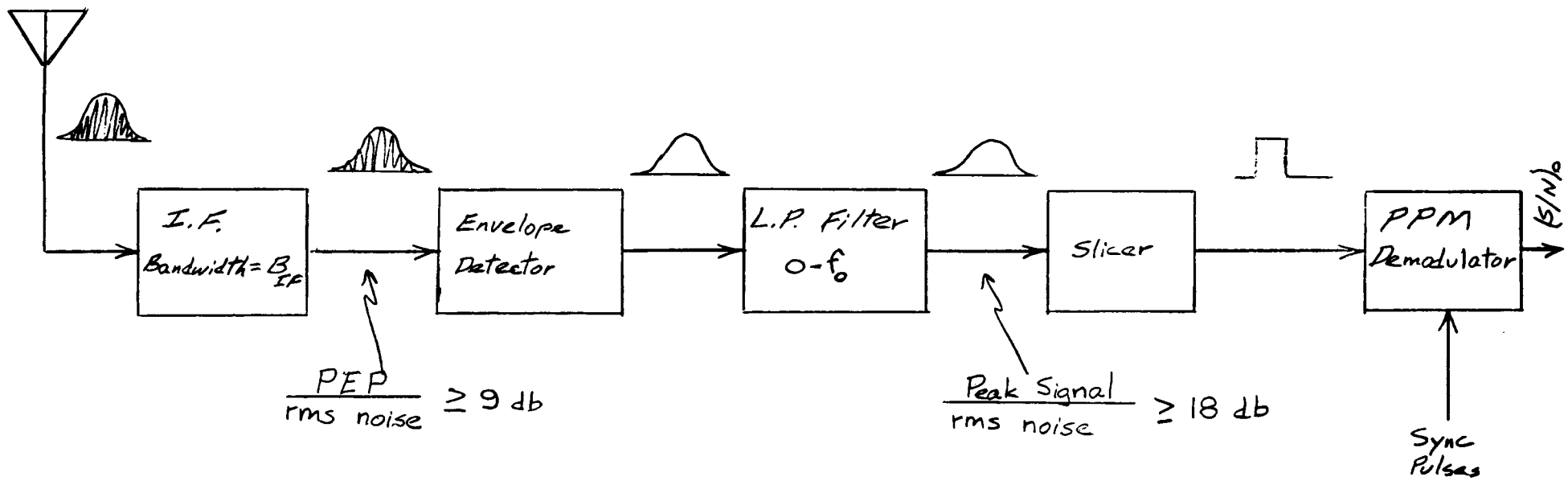

Figure 4 - PPM-AM Detection Technique

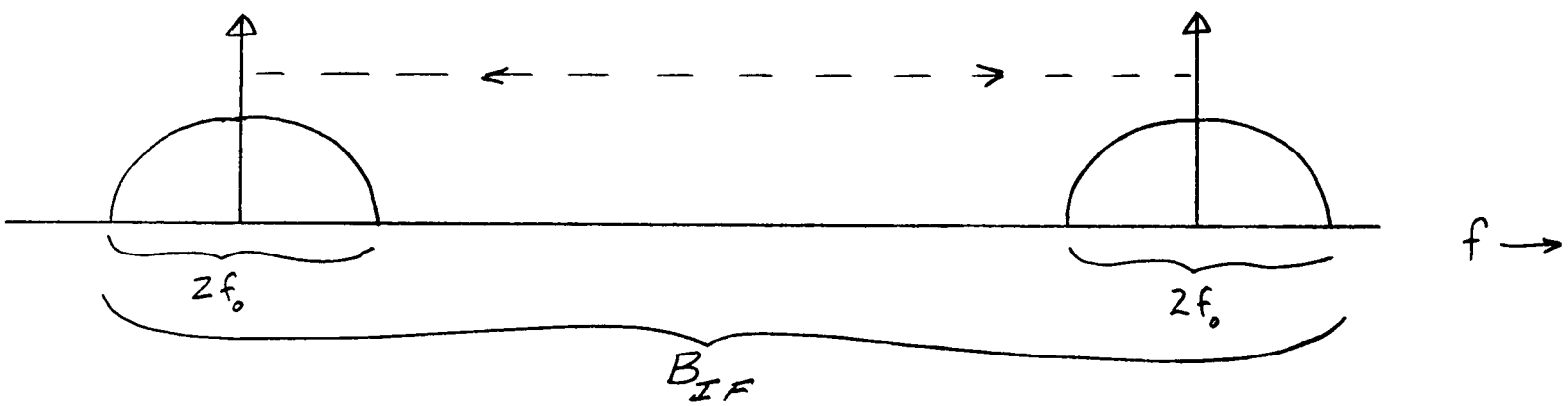

Figure 5 - Spectra of Received Signal

where $(S/N)_i$ is the peak signal to rms noise ratio in the receiver section. This demonstrates the S/N improvement factor of PPM. In decibel form, equation (11) may be written:

$$(S/N)_o = (S/N)_i + 20 \log t_m + 10 \log f_o + 10 \log B_{IF} + 5.1 \text{ (db)} \quad (12)$$

It should be noted here that when operating with large doppler shifts and narrow information bandwidths, the IF bandwidth will be determined by the doppler, rather than by the pulse width. In the absence of doppler, the IF bandwidth could be made approximately $2f_o$.

This analysis, has, of course, assumed a peak pulse to noise ratio sufficiently high so that noise by itself rarely rises to the slicing level; nor is it large enough in the negative direction to suppress a pulse completely. When the pre-detection bandwidth becomes large, a substantial number of false pulses caused by noise begin to occur. This is the threshold point, at which the signal will tend to lose its information bearing properties completely. This important problem is considered in the next section.

5.4.3 Thresholding

As with all systems that exchange bandwidth for noise improvement, PPM experiences a marked improvement threshold. In the PPM-AM detection technique of Figure 4, two thresholds must be considered, viz: the RF threshold of the linear detector and the PPM threshold at the slicer. In conventional PPM-AM systems, the IF bandwidth is $2f_o$, so these two thresholds are related and need not be considered separately. However, when the required IF bandwidth is determined by the doppler shift, then both thresholds must be calculated.

The RF detection threshold is based on the point where the peak noise amplitude equals the peak signal amplitude. A "crest factor" of four is usually assumed for random noise, meaning that the peak-to-rms noise voltage ratio is 4(12 db).

Assuming the random noise has a normal probability distribution, the probability of the noise voltage exceeding a crest factor of 4 is about 6.3×10^{-5}, which is indeed quite small. Since the peak-to-rms voltage ratio of the sinusoidal RF signal is 3 db, and the peak-to-rms voltage ratio of the noise is 12 db, when these peaks are equal the ratio of rms signal voltage to rms noise voltage is 9 db. AM thresholding is a rather gradual process (unlike FM or PM), so just how far above this point one should call "threshold" is somewhat arbitrary, depending upon how much signal degradation can be tolerated. Since the system of Figure 4 includes post-detection filtering, much of the random noise which arrives in the absence of signal will not be passed by the low-pass filter anyway. Because of this and the fact that AM thresholding is so gradual, an RF threshold of 9 db (PEP/rms noise) appears adequate here.

The PPM threshold (at the slicer) is dictated by the general requirement that the noise level alone cannot have a significant probability of rising above the slicing level. Therefore, the PPM threshold will be taken to occur when the peak noise (crest factor of 4) equals half the demodulated pulse amplitude. The probability of noise exceeding this level will then be 3.4×10^{-4} *. As a rough approximation of the error rate in the slicer, we may consider each cps of low-pass filter bandwidth to be represented by two degrees of freedom. That is, there are two samples/sec. of noise per unit bandwidth, or a total of $2f_o$ samples/sec of noise. The rate of occurrence of samples above the slicing level is then $2f_o \times 3.4 \times 10^{-4} = 6.8 \times 10^{-4} f_o$. For f_o on the order of 50 cps, this would yield an error rate of about .034 pps, or about one error every 30 seconds, which appears to be a reasonable thesh-old in this application. Therefore, the PPM threshold will be set at a peak signal/rms noise ratio of 18 db (for peak signal twice the peak noise amplitude).

* Based on a Rayleigh distribution, which is the distribution of the noise envelope.

A comparison of the IF bandwidth (of perhaps 10 kc) with the post-detection bandwidth (of perhaps 50 cps) shows that, unless the IF bandwidth is considerably narrower than this, the RF detection threshold (9 db in the IF bandwidth) will be the limiting factor.

5.4.4 Transmitter Power Calculations

The required S/N ratio at the receiver will be determined by the two threshold requirements determined in the preceding section. The pertinent bandwidths are shown in Figure 5.

Due to doppler effect, the signal spectrum may be received anywhere within the IF bandwidth B_{IF}. For a wide IF bandwidth, the RF threshold will determine the required S/N ratio; while, for a relatively narrow IF bandwidth, the PPM threshold will determine the required S/N ratio. Since there is a 9 db difference between the RF threshold and the PPM threshold, the PPM threshold will become dominant for systems where

(13)

The nominal parameters for the capsule-to-spacecraft communication link which have been assumed for this calculation are as follows:

Transmission frequency	= 100 mc.
Path length	= 10,000 to 50,000 km.
Capsule antenna gain	= 0 db
Spacecraft receiving antenna gain	= 0 db
f_o	= 50 cps
Receiver noise figure	= 10 db
Margin	= 8 db

From these parameters, the following transmitter power requirement can be calculated.

Transmitter peak envelope power (PEP)	10 log P
Capsule antenna gain	0 db
Path attenuation	-152.5 db
Receiving antenna gain	0 db
Misc. RF losses	-3 db
Peak signal power available at receiver:	10 log P-155.5 dbw

Receiver noise density per cps (KTF)	-194 dbw
Bandwidth	10 log B_{IF}
S/N required (in B_{IF})	+9 db
Margin	+8 db
Peak signal power required at receiver:	10 log B_{IF}-177 dbw

Therefore:

$$10 \log P - 155.5 = 10 \log B_{IF} - 177 \quad (14)$$

Which yields:

$$10 \log P = 10 \log B_{IF} - 21.5 \text{ dbw} \quad (15)$$

Equation (15) has been plotted in Figure 6.

5.4.5 Typical System Block Diagram

Figure 7 shows one possible block diagram of a typical n-channel PPM-AM transmitting system*. The frame sampling rate is established by a ring counter chain which is triggered by a master pulse generator. The pulses from the generator cause successive stages to conduct in sequence and to generate pulses distributed uniformly in time. The pulse from one of the counter chain stages is coded and is used as a frame syn-

*Reference 7 - pp.307-308

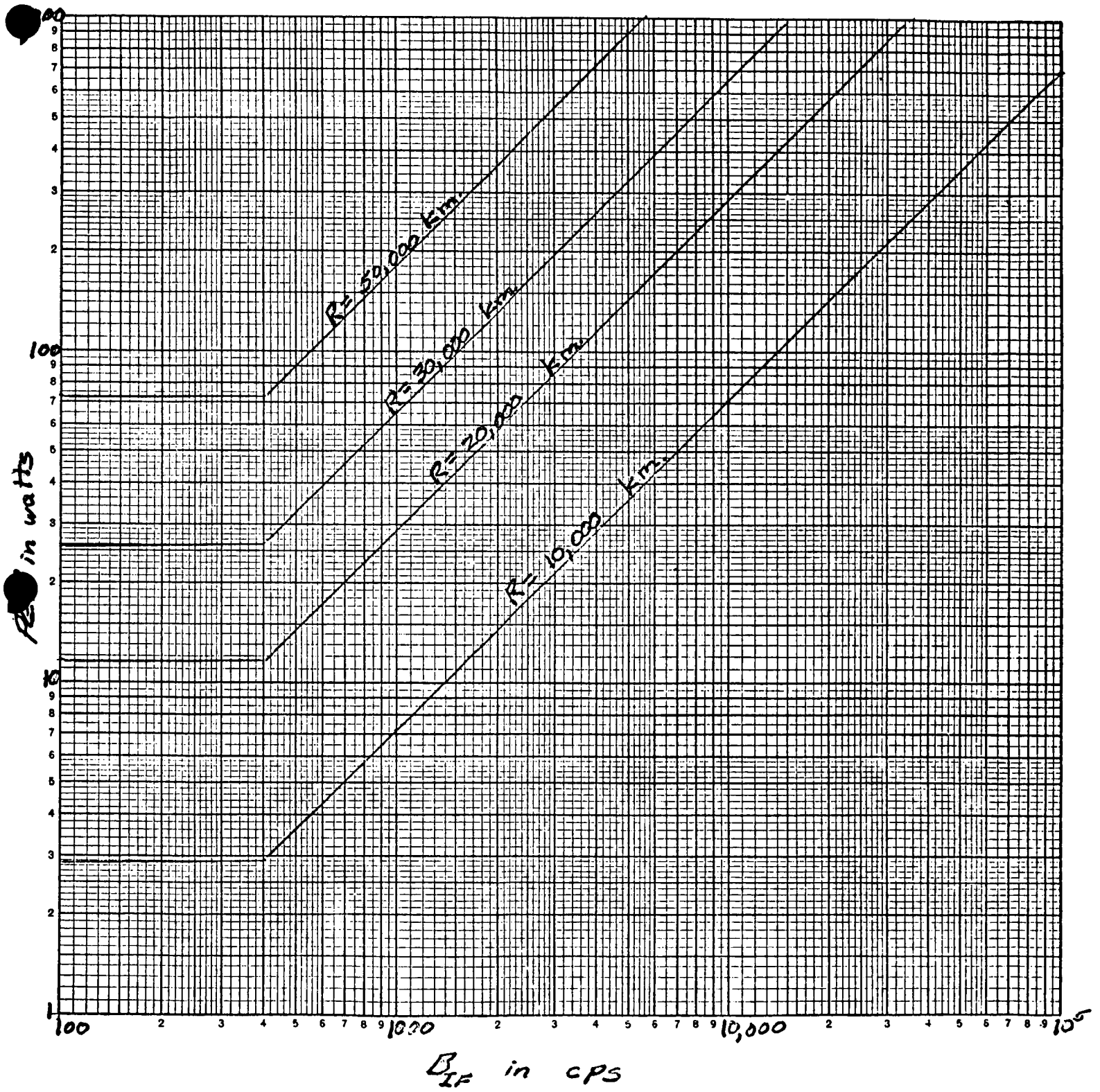

Figure 6

Transmitter PEP Required for Operation above Thresholds

chronizing signal. Each channel pulse produced in the counter chain passes to a corresponding pulse position modulator which generates a pulse delayed with respect to the pulse from the counter chain, the delay being proportional to the modulating signal from the corresponding sensor. The n pulses from the pulse position modulators, together with the coded frame synchronizing signal, pass to a mixer and then to the amplitude modulator of the transmitter, as shown in Figure 7.

Figure 8 shows a block diagram for a typical n-channel PPM-AM receiving system. The multichannel sequence of pulses from the radio receiver passes to a channel synchronizing pulse generator which electronically separates the coded frame synchronizing pulse from the incoming pulse train and develops a sequence of channel synchronizing pulses which mark the reference time for the separate channels. Each of these channel synchronizing pulses triggers a variable pulse width generator in which the pulse width is initiated by the channel synchronizing pulse and terminated by the corresponding channel signal pulse which is also fed into the pulse width generator. Thus, for each channel, a pulse is generated having a width which varies in accordance with the modulation produced by the coresponding instrumentation sensor. These variable-width channel pulses, recurring at the sampling rate generated at the transmitter, pass to suitable metering circuits, where they are then converted to analog signals.

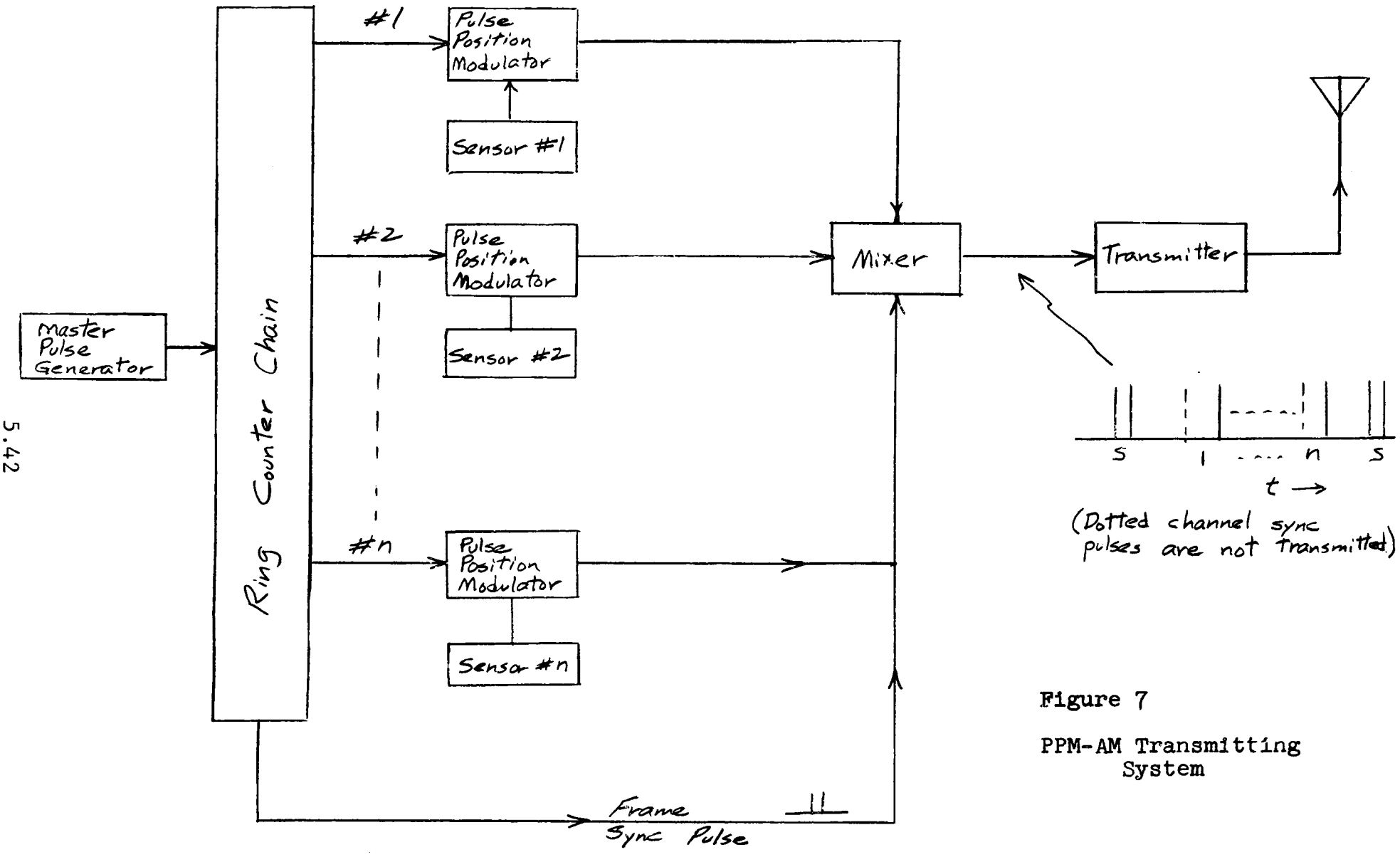

Figure 7

PPM-AM Transmitting System

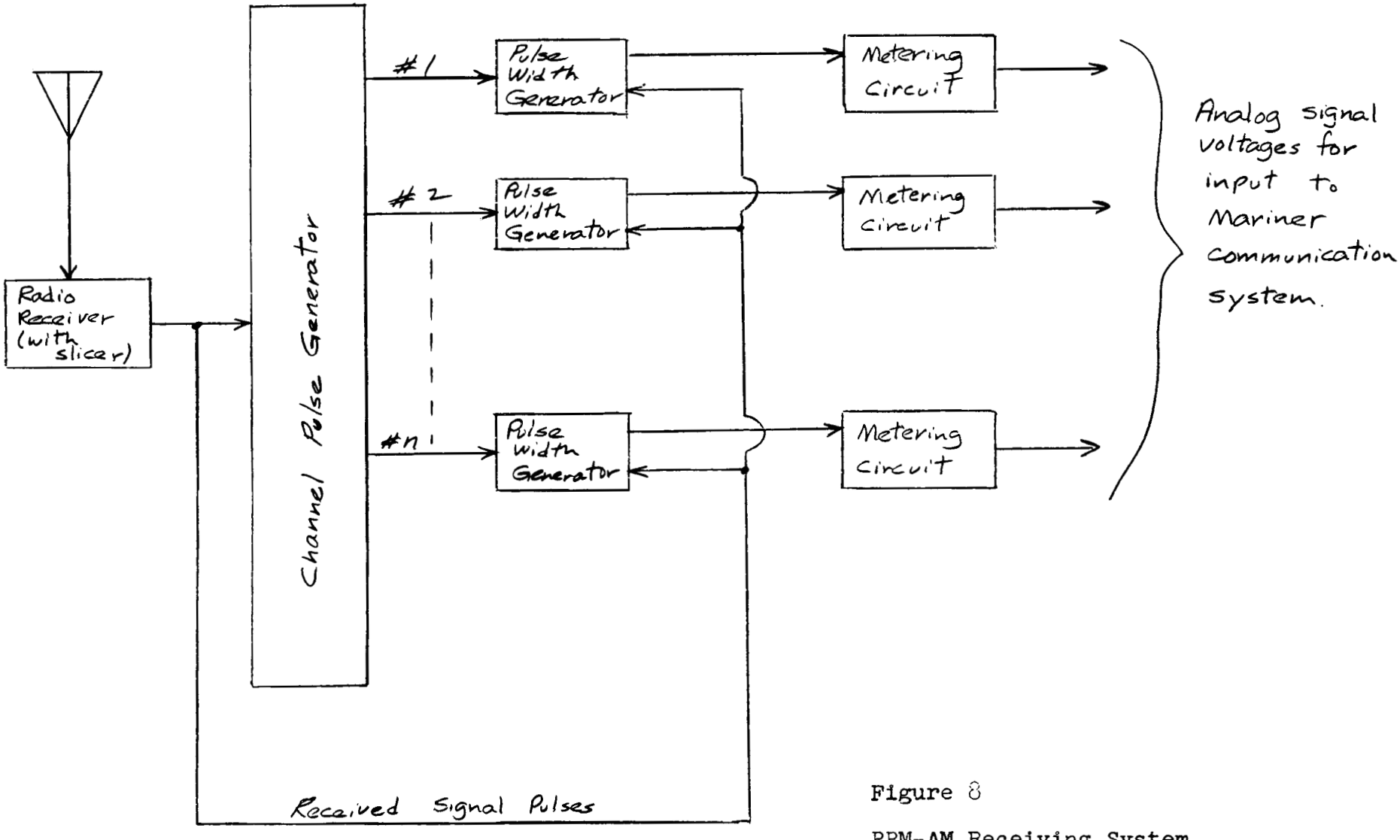

Figure 8

PPM-AM Receiving System

REFERENCES

1) Black, H. S., Modulation Theory, D. VanNostrand Co., Inc. New York, N.Y., 1953.

2) Bennett, W. R., "Effect of Random Noise on Sinusoidal and Pulse Systems", Lecture given at MIT Special Summer Program 6.57s, August, 1960.

3) Golay, M., "Note on the Theoretical Efficiency of Information Reception with PPM," Proc. IRE, September, 1949.

4) Jacobs, I. "Theoretical and Practical Limitations of Weak-Signal Processing Techniques", COSPAR Symposium, April 10, 1961.

5) Kotel'nikov. V.A., The Theory of Optimum Noise Immunity, McGraw-Hill Book Co., New York, N.Y., 1959.

6) Nichols, M. H., and Rauch, L.L., Radio Telemetry, John Wiley and Sons, Inc., New York, N.Y., 1956.

7) Pawley, M.G., and Triest, W.E., "Multichannel Radio Telemetering", Chapter in Advances in Electronics, Vol. IV, Edited by L. Marton, Academic Press, Inc., New York, N.Y., 1952.

8) Putschi, H. N., "Evaluation and Development of a PCM-PS Radio Telemetry System", GE TIS No. R59ELS-34, May 7,1959.

9) Schwartz, M., Information Transmission, Modulation and Noise, McGraw-Hill Book Co., New York, N.Y., 1959

10) Uglow, K. M., "Transmission Systems for Re-entry Telemetry", Report 1201-3, July 30, 1958 (Under a consulting contract with GE)

5.5 PRELIMINARY REPORT ON ERROR CORRECTING CODES

5.5.1 The Problem

In seeking to effect a saving in transmitter power required to transmit transducer outputs from the capsule, a study of various coding techniques was instituted. This is an interim report, and no final conclusions are drawn.

5.5.2 Types of Codes Considered

Examples of single-error correcting, single-error detecting (with probable correction), and double-error correcting codes have been considered.

n = total number of bits in coded word

k = number of message bits in coded word

p = bit error probability for received coded word

p_r = required bit error probability for decoded message

t = number of errors corrected by the code

p_w = word error probability

5.5.3 Procedure

5.5.3.1 In Terms of Bit Error Probability

For a given p_r, the S/N necessary to transmit the uncoded message in the presence of white Gaussian noise is computed. Then, for each coded configuration, the value of p necessary to yield p_r is determined. This p is then expressed in terms of required S/N. The difference between the power required in the uncoded case and that needed in the coded case (both cases yielding the required p_r) represents a saving; however, there is an increase in bandwidth necessary to enable transmission of the longer coded words at the same data rate. The ratio of the increased bandwidth to the original is n/k, and there is a proportional increase in noise power necessitating a compensating increase in signal power to maintain p (and p_r). Subtracting

this increase in signal power from the power saved by coding yields the net power savings resulting from use of the code.

5.5.3.2 In Terms of Word Error Probability

The savings for a given code are computed as a function of the word error probability as well. The required word error probability is translated into p_r, and then into p. The required S/N for p is then determined, and the additional S/N required to compensate for the increased bandwidth is added. To attain the form $\frac{ST}{N/B}$, 3 db is subtracted from the S/N required. Next, $\frac{ST}{N/B}$ for uncoded transmission is determined ($p_r = p$), and the difference in $\frac{ST}{N/B}$ between the uncoded and the Wagner coded cases is the savings from use of the code.

5.5.4 Computation of p

Given a code (n, k, t), and a value of p_r, the decoded word error rate may be given as kp_r*. It is required that the probability of more than t errors in the n bit word be kp_r.

This may be expressed as

$$1-q^n - nq^{n-1}\,p - \cdots - \binom{n}{t} q^{n-t}\,p^t = kp_r \qquad (1)$$

or equivalently

$$1 - \sum_{j=0}^{t} \binom{n}{j} q^{n-j}\,p^j = kp_r \qquad (2)$$

where $q = 1-p$

Ignoring terms of order p^{t+2} and higher, equation (2) reduces to

$$\binom{n}{t+1}\,p^{t+1} = kp_r \qquad (3)$$

*For small P_r (our range of interest) and small n. Where kp_r is a poor approximation, $1 - q_r^k$ is used. Independence of error probability between bits is assumed.

Equation (3) is solved for p.

5.5.5 Computation of Power Saved

A binary symmetric channel perturbed by white Gaussian noise is assumed.

Then,

$$P(1/0) = P(0/1) = \tfrac{1}{2} - \int_0^x f(x)\, dx$$

$$P(0) = P(1) = \tfrac{1}{2}$$

where

P(1/0)	= probability that "1" is received when "0" is transmitted,
P(0/1)	= probability that "0" is received when "1" is transmitted,
P(0)	= probability that "0" is transmitted,
P(1)	= probability that "1" is transmitted,
f(x)	= normal probability density function, and

$$S/N\ (db) = 20 \log_{10} X \tag{4}$$

Now, $p = P(0)\ P(1/0) + P(1)\ P(0/1)$

Therefore,

$$1 - p = \int_{-\infty}^{x} f(x)\, dx \tag{5}$$

Having computed p from equation (3), its value is substituted into equation (5) to find x. Then S/N (db) corresponding to p is found from equation (4).

The increase in power necessary to compensate for the increased bandwidth is computed by transforming the ratio n/k into db.

5.5.6 Results

5.5.6.1 In Terms of Bit Error Probability

Use of a (7, 4, 1) Hamming Code yielded a net power savings of only 0.6 db.

Proceeding to the use of a single parity bit, Tables 1 and 2 indicate a net gain of approximately 2.5 db for $p_r = .001$ and $p_r = .0001$. This code is only error detecting; however, it is the basis for the Wagner Code, which detects and (with high probability) corrects single errors. The detailed analysis of the Wagner Code in relation to our needs is incomplete at this time, and in the tables no account is taken of the (small) probability of not correcting a detected error.

A single example of a Bose-Chaudhuri double-error correcting code (21, 12, 2) has been analyzed, for $p_r = .0001$. A saving of 2.4 db is realizable for this code. Since no significant improvement is expected from the use of a double-error correcting code rather than the Wagner Code, and the encoding equipment required is much greater, no further study of the use of double error correcting codes is planned.

5.5.6.2 In Terms of Word Error Probability

Tables 3, 4 and 5 show the reduction in required $\frac{ST}{N/B}$ from using the Wagner Code rather than uncoded transmission, as a function of p_w, for n = 8, 7, and 6 respectively. Figure 5.5.1 shows the required $\frac{ST}{N/B}$ for the Wagner Code vs. p_w for n = 8, 7, and 6. Figures 5.5.2, 5.5.3, and 5.5.4 compare $\frac{ST}{N/B}$ for the Wagner-coded and the uncoded cases, for n = 8, 7, and 6 respectively.

Table 1. Gain in Required S/N Using Wagner Code, $p_r = .001$ (based on bit error rate)

n	k	p	S/N (db)	S/N Gain due to coding (db)	n/k	S/N Loss due to increased bandwidth (db)	Net Gain in S/N (db)
2	1	.032	5.4	4.4	2.00	3.0	1.4
3	2	.026	5.8	4.0	1.50	1.8	2.2
4	3	.022	6.1	3.7	1.333	1.2	2.5
5	4	.020	6.3	3.5	1.25	1.0	2.5
6	5	.018	6.4	3.4	1.20	.8	2.6
7	6	.017	6.5	3.3	1.667	.7	2.6
8	7	.016	6.6	3.2	1.143	.6	2.6
9	8	.015	6.7	3.1	1.125	.5	2.6
10	9	.014	6.8	3.0	1.111	.5	2.5
11	10	.0135	6.9	2.9	1.10	.4	2.5

Uncoded message S/N = 9.8

Table 2. Gain in Required S/N Using Wagner Code, p_r = .0001 (based on bit error rate)

n	k	p	S/N (db)	S/N Gain Due to Coding (db)	n/k	S/N Loss due to increased bandwidth (db)	Net Gain in S/N (db)
2	1	.01	7.3	4.2	2.00	3.0	1.2
3	2	.0081	7.6	3.9	1.50	1.8	2.1
4	3	.0071	7.8	3.7	1.333	1.2	2.5
5	4	.0063	7.9	3.6	1.25	1.0	2.6
6	5	.0058	8.0	3.5	1.20	.8	2.7
7	6	.0056	8.1	3.4	1.667	.7	2.7
8	7	.0050	8.2	3.3	1.143	.6	2.7
9	8	.0047	8.3	3.2	1.125	.5	2.7
10	9	.0045	8.3	3.2	1.111	.5	2.7
11	10	.0043	8.4	3.1	1.10	.4	2.7

Uncoded message S/N = 11.5 db

Table 3. Gain in Required $\frac{ST}{N/B}$ Using Wagner Code, for n = 8, k = 7 (based on word error rate)

p_w	p	S/N (db)	Additional S/N due to increased bandwidth (db)	$\frac{ST}{N/B}$ required for Wagner Code (db)	$\frac{ST}{N/B}$ required for uncoded transmission (db)	Savings in $\frac{ST}{N/B}$ using Wagner Code (db)
10^{-1}	.0611	3.8	.6	1.4	3.7	2.3
10^{-2}	.0189	6.4	.6	4.0	6.5	2.5
10^{-3}	.0060	8.0	.6	5.6	8.2	2.6
10^{-4}	.0018	9.2	.6	6.8	9.7	2.9
10^{-5}	.0006	10.2	.6	7.8	10.7	2.9
10^{-6}	.0002	11.0	.6	8.6	11.6	3.0

Table 4. Gain in Required $\frac{ST}{N/B}$ Using Wagner Code, for n = 7, k = 6 (based on word error rate)

P_w	p	S/N (db)	Additional S/N due to increased bandwidth (db)	$\frac{ST}{N/B}$ required for Wagner Code (db)	$\frac{ST}{N/B}$ required for uncoded transmission (db)	Savings in $\frac{ST}{N/B}$ using Wagner Code (db)
10^{-1}	.0660	3.6	.7	1.3	3.5	2.2
10^{-2}	.0218	6.1	.7	3.8	6.3	2.5
10^{-3}	.0069	7.8	.7	5.5	8.1	2.6
10^{-4}	.0022	9.1	.7	6.8	9.6	2.8
10^{-5}	.0007	10.1	.7	7.8	10.6	2.8
10^{-6}	.0002	10.9	.7	8.6	11.4	2.8

Table 5. Gain in Required $\frac{ST}{N/B}$ Using Wagner Code, for n = 6, k = 5 (based on word error rate)

P_W	p	S/N (db)	Additional S/N due to increased bandwidth (db)	$\frac{ST}{N/B}$ required for Wagner Code (db)	$\frac{ST}{N/B}$ required for uncoded transmission (db)	Savings in $\frac{ST}{N/B}$ using Wagner Code (db)
10^{-1}	.0722	3.3	.8	1.1	3.2	2.1
10^{-2}	.0258	5.8	.8	3.6	6.2	2.6
10^{-3}	.0082	7.6	.8	5.4	8.0	2.6
10^{-4}	.0026	8.9	.8	6.7	9.5	2.8
10^{-5}	.0008	9.9	.8	7.7	10.6	2.9
10^{-6}	.0003	10.8	.8	8.6	11.4	2.8

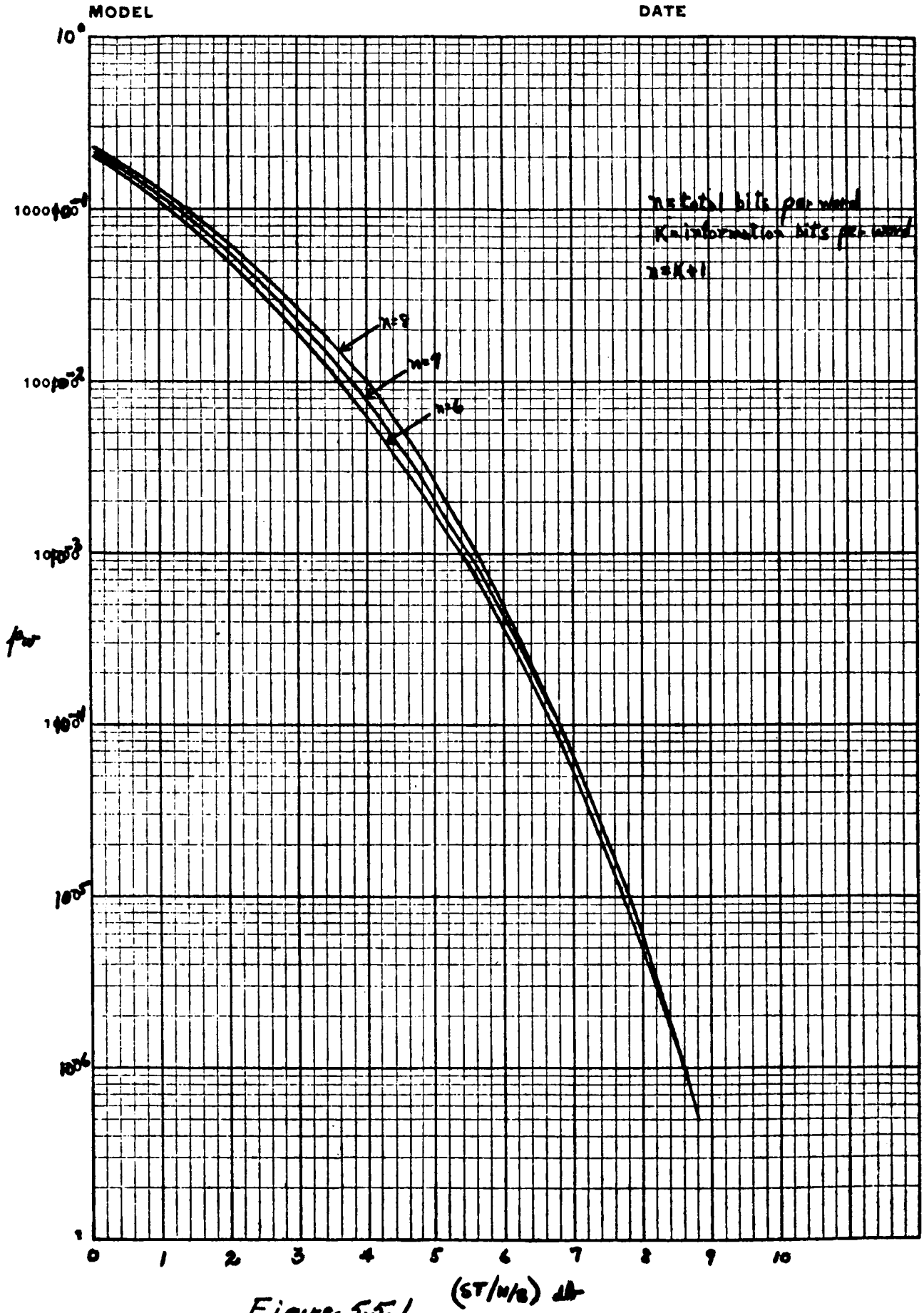

Figure 5.5.1

Word Error Probability – Wagner Codes.

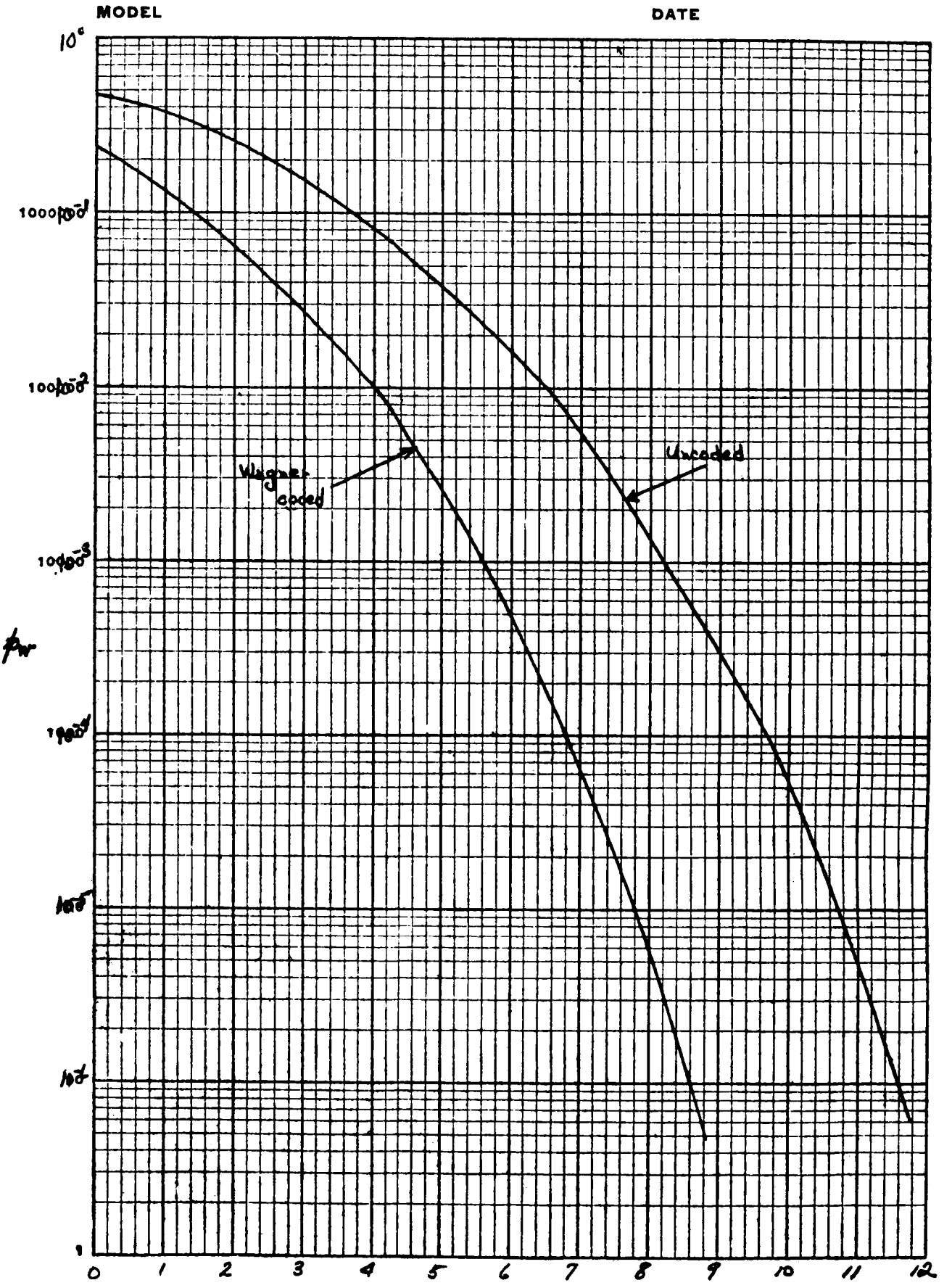

Figure 5.5.2 $(S_T/N/B)$ db

Comparison of Coded and Uncoded Word Error Probabilities.

$n=8$

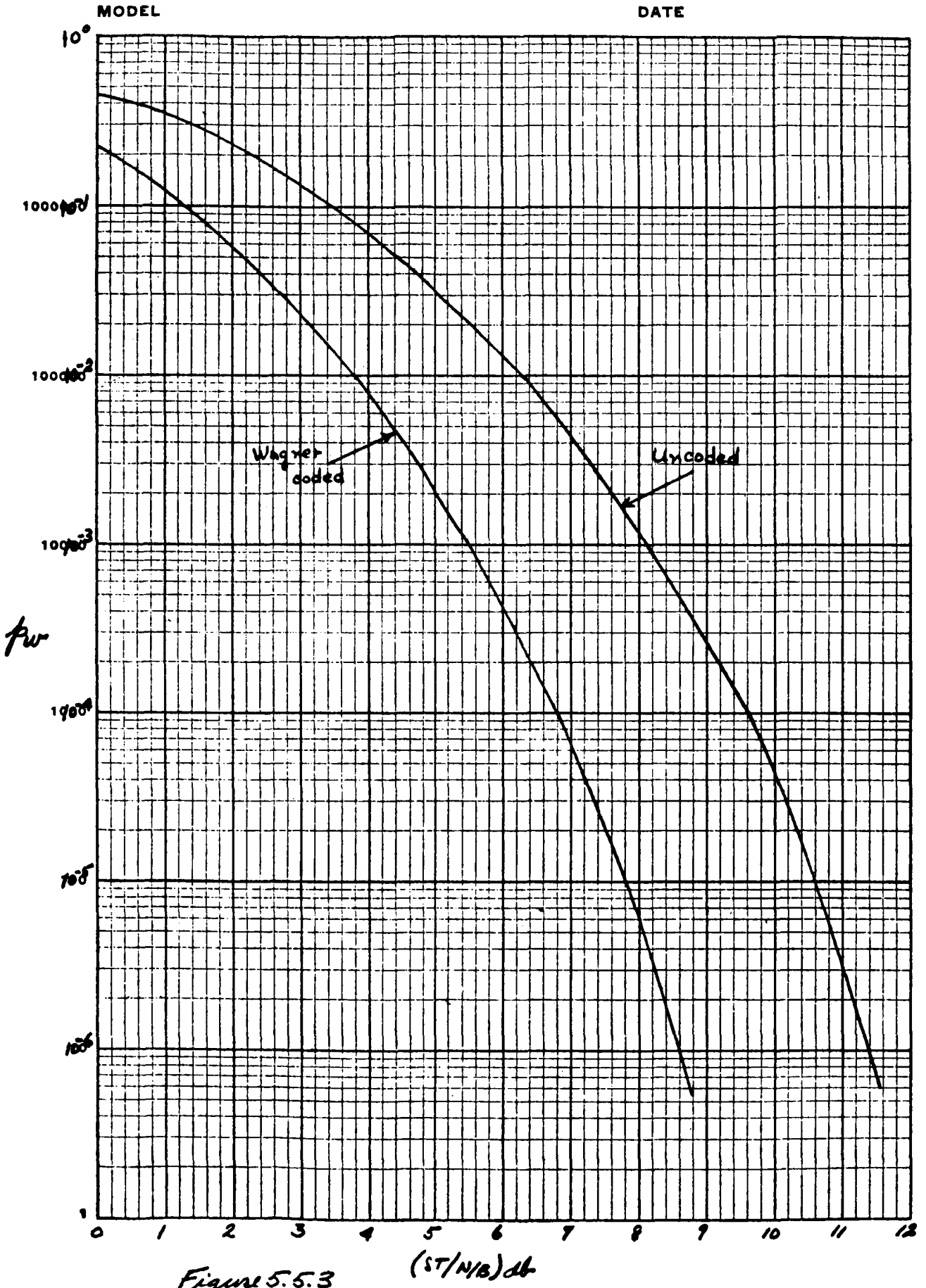

Figure 5.5.3

Comparison of Coded and Uncoded Word Error Probabilities.

$n=7$

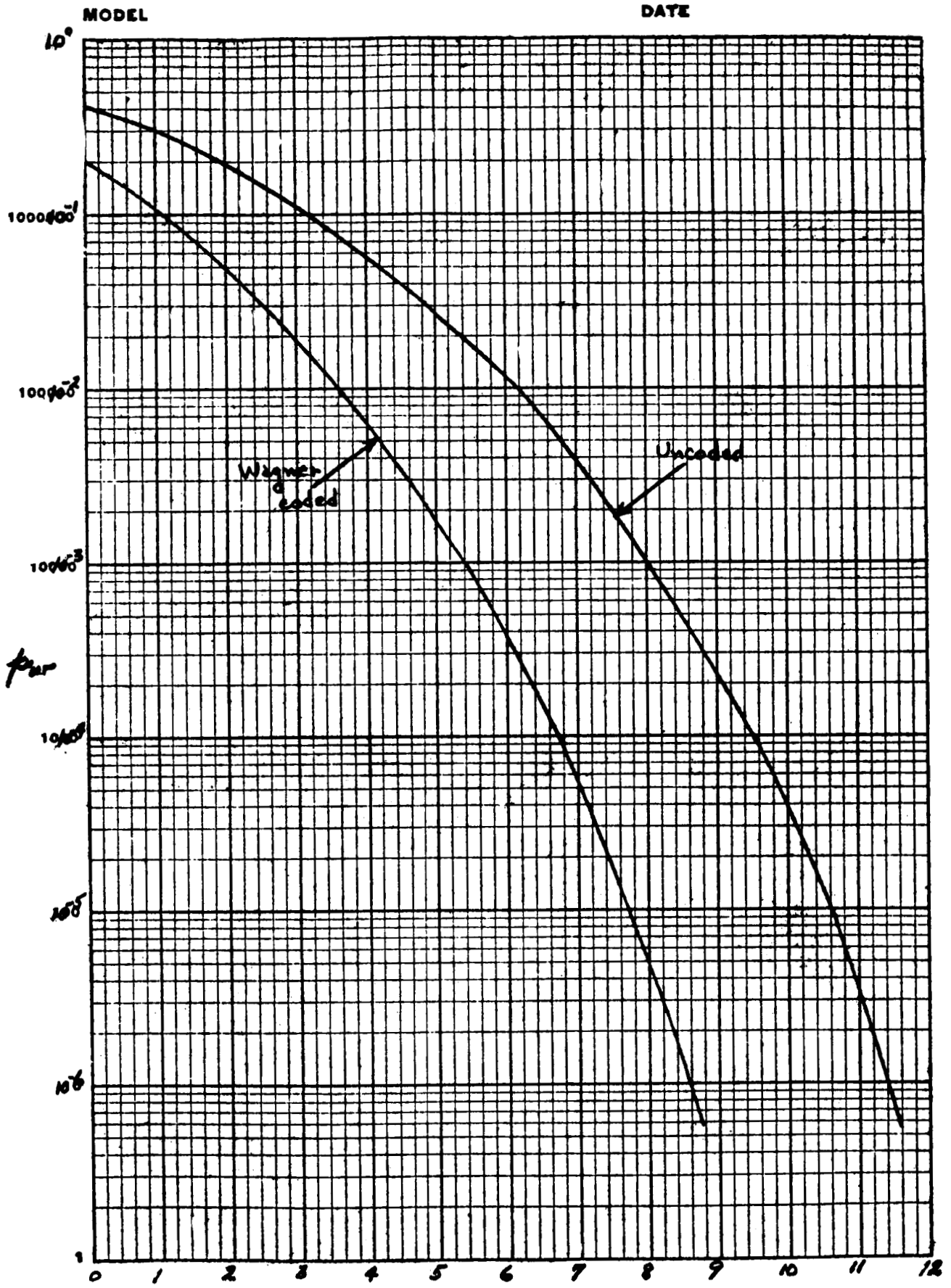

(ST/N_0) db

Figure 5.5.4
Comparison of Coded and Uncoded Error Probabilities.
$n=6$

5.5.6.3 Power and Weight Requirements for Implementation of the Wagner Code

A preliminary study was made to estimate the additional power and weight required to add a single-bit parity check to a seven-bit code. Results are given separately for the primary (capsule) transmitter at which the parity bit is added, and for receiver and recorder (or secondary transmitter) at which the received code must be checked and corrected if required. Results are based on the equivalent number of flip-flops, for convenience. Each flip-flop is rated at 0.1 watts and 0.1 pounds.

Figure 5.5.5 shows the system for adding the parity bit at the primary transmitter. The added power and weight estimates are as follows:

Strobe-Delay	1	
Complementing FF	1	
Reset delay	1.5	
Delay multivibrator	1	
Output gate	0.5	
TOTAL	5.0	= 0.5 watts and 0.5 lbs.

Figure 5.5.6 shows the receiver system for checking and error correction. Synchronization and error decision procedures have not yet been detailed. Added power and weight estimates are as follows:

Parity check	2	
Sync generator	8	
Signal Memory Drive	1	
Error decision	8	
Shift register	12	
Memory register	16	
TOTAL	47	= 4.7 watts and 4.7 lbs.

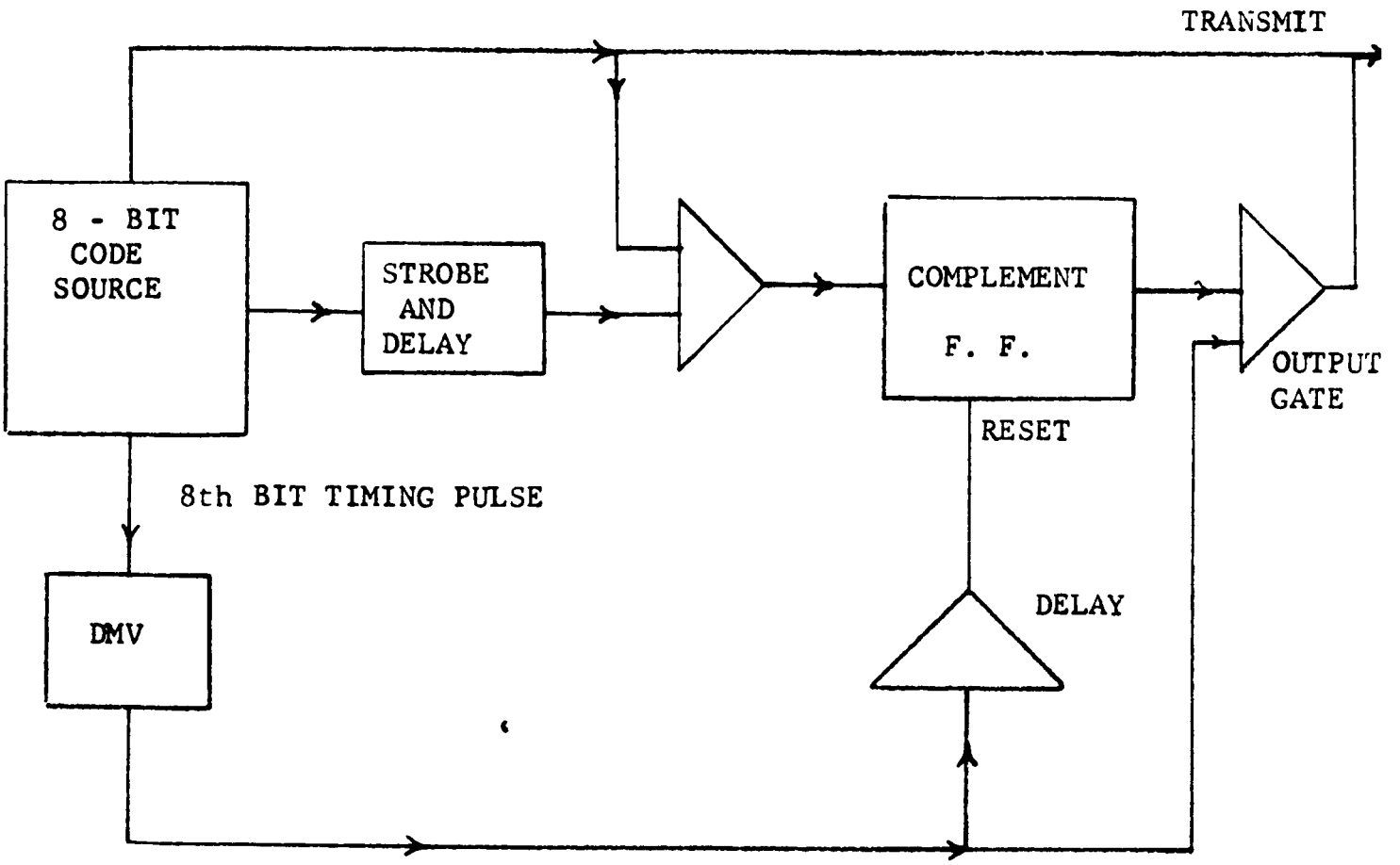

FIGURE 5.5.5

ADDITION OF PARITY BIT

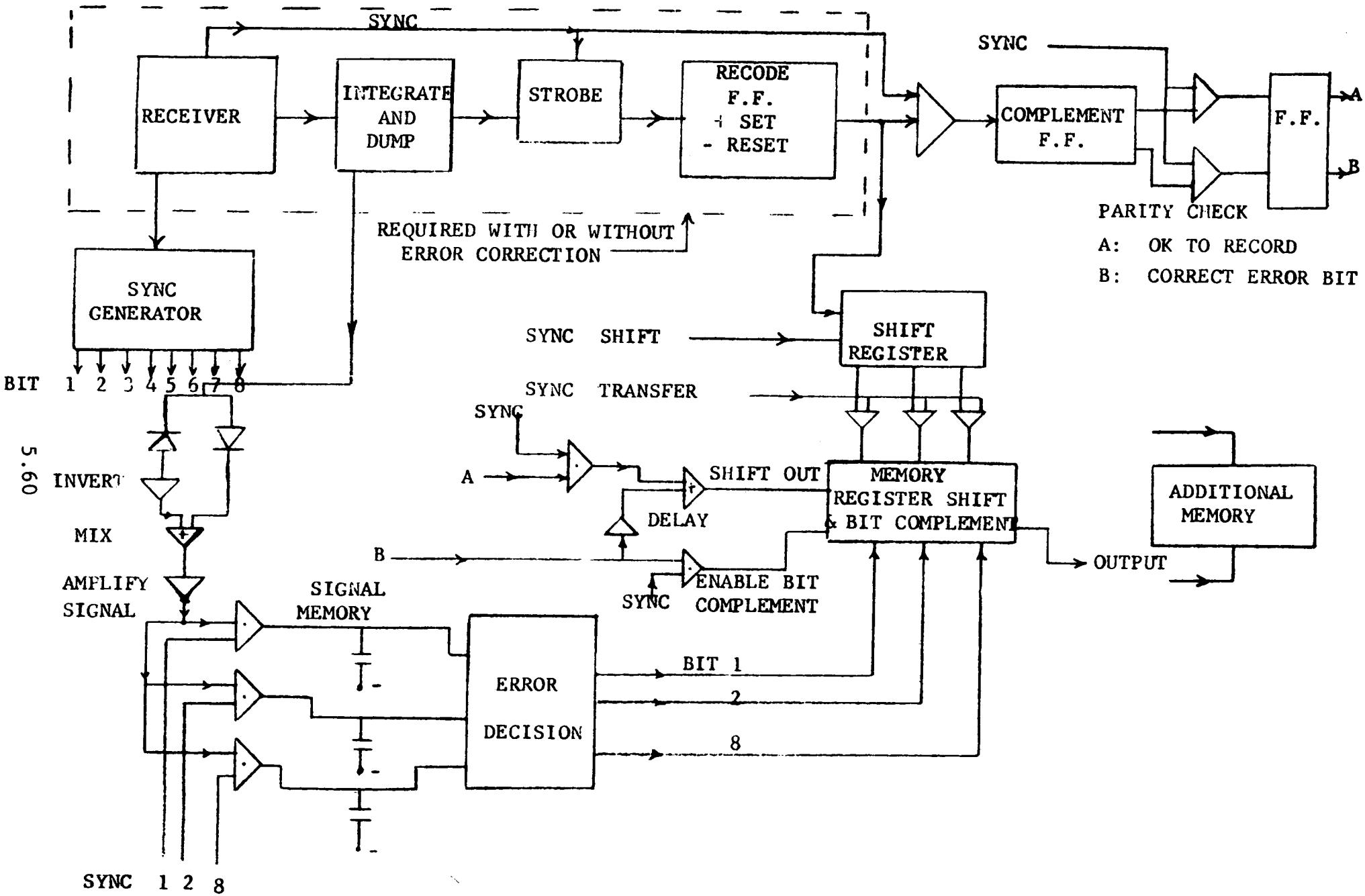

FIGURE 5.5.6

ERROR CORRECTION OF RECEIVED MESSAGE

5.6 MARS ENTRY TRANSMISSION ATTENUATION STUDY

Studies have been made to determine attenuation effects resulting from entry induced plasma for the Mars atmosphere A given in Reference 3. Two physical configurations were used in the analysis; namely, the truncated Discoverer capsule (reference 1) Figure 5.6.1 with a 22° conical section and a "standard" Discoverer capsule with a 10° conical section. The flight trajectory used for both capsules in this study was a vertical entry ($\gamma_e = 90^{\circ}$) from an altitude of 800,000 ft., and initial entry velocity of 25,000 ft/sec., and a ballistic coefficient of 30 lb/ft^2.

Stagnation pressures were computed by application of Earth atmosphere aerodynamic relationships, since the pertinent thermodynamic characteristics of the Mars A atmosphere are quite similar to the Earth's. Static pressures on the conical sections of the capsules were determined by the Prandtl-Meyer expansion techniques, and an isentropic flow expension was assumed aft of the stagnation point. Local thermodynamic properties at the edge of the boundary layer on the conical sections were then evaluated by using the recently calculated thermodynamic properties data for Mars II environment (consistent with Mars A) of Reference 4. The resulting computed values for electron concentration at the conical section are given in Figure 5.6.2.

Using the techniques described in Reference 5, the effects of these electron concentrations on signal attenuation were evaluated by calculating reflection coefficient and attenuation in db/meter, and are shown in Figures 5.6.3 and 5.6.4, respectively. As expected this predicts blackout for frequencies below the plasma frequency, which varies as the square root of the electron concentration. As a result, it becomes apparent that the transmission frequency should be on the order of tens of kmc for communication throughout the entry period. The critical frequency as a function of altitude is presented in Figure 5.6.5.

A more accurate analysis of attenuation which accounts for the sheath thickness and contour might yield more favorable results, if the sheath proved to be effectively thinner than a wavelength. However, since the vehicle is a blunt body, this

is definitely not the case as can be seen from the shock standoff distance shown in Figure 5.6.6. Therefore the frequencies predicted on the simple basis outlined above should give a fairly realistic indication of those required.

The total attentuation at any given frequency and altitude can be determined by multiplying the attentuation in db/meter (Figure 5.6.4) by the shock standoff distance in meters (Figure 5.6.6) and adding that portion due to the reflection coefficient R (Figure 5.6.3) which will be equal to 20 log ($\frac{1}{1-R}$) as indicated in Reference 6.

To facilitate further evaluation and reduction of the given information, calculations have been made for both shock separation distance and boundary layer thickness at the conical section location. Figure 5.6.6 shows this data as a function of altitude. It should be noted that the higher altitude portions of these curves are dashed lines which serves to indicate that the basic continuum relationships used in the computations are not completely valid in the rarefield atmosphere prevalent at these altitudes.

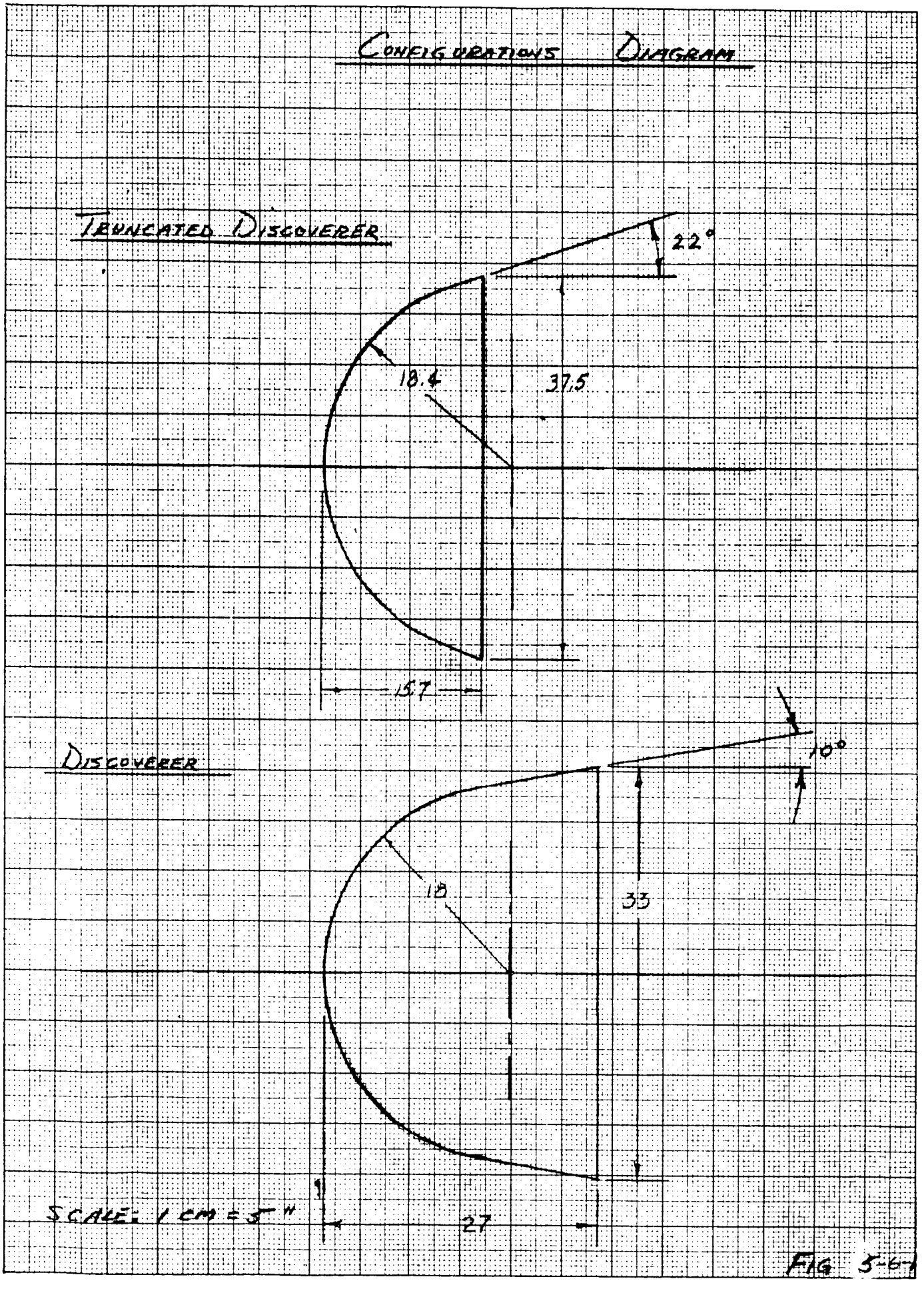
CONFIGURATIONS DIAGRAM
TRUNCATED DISCOVERER
22°
18.4
37.5
15.7
DISCOVERER
10°
18
33
27
SCALE: 1 CM = 5"

FIG 5-6-1

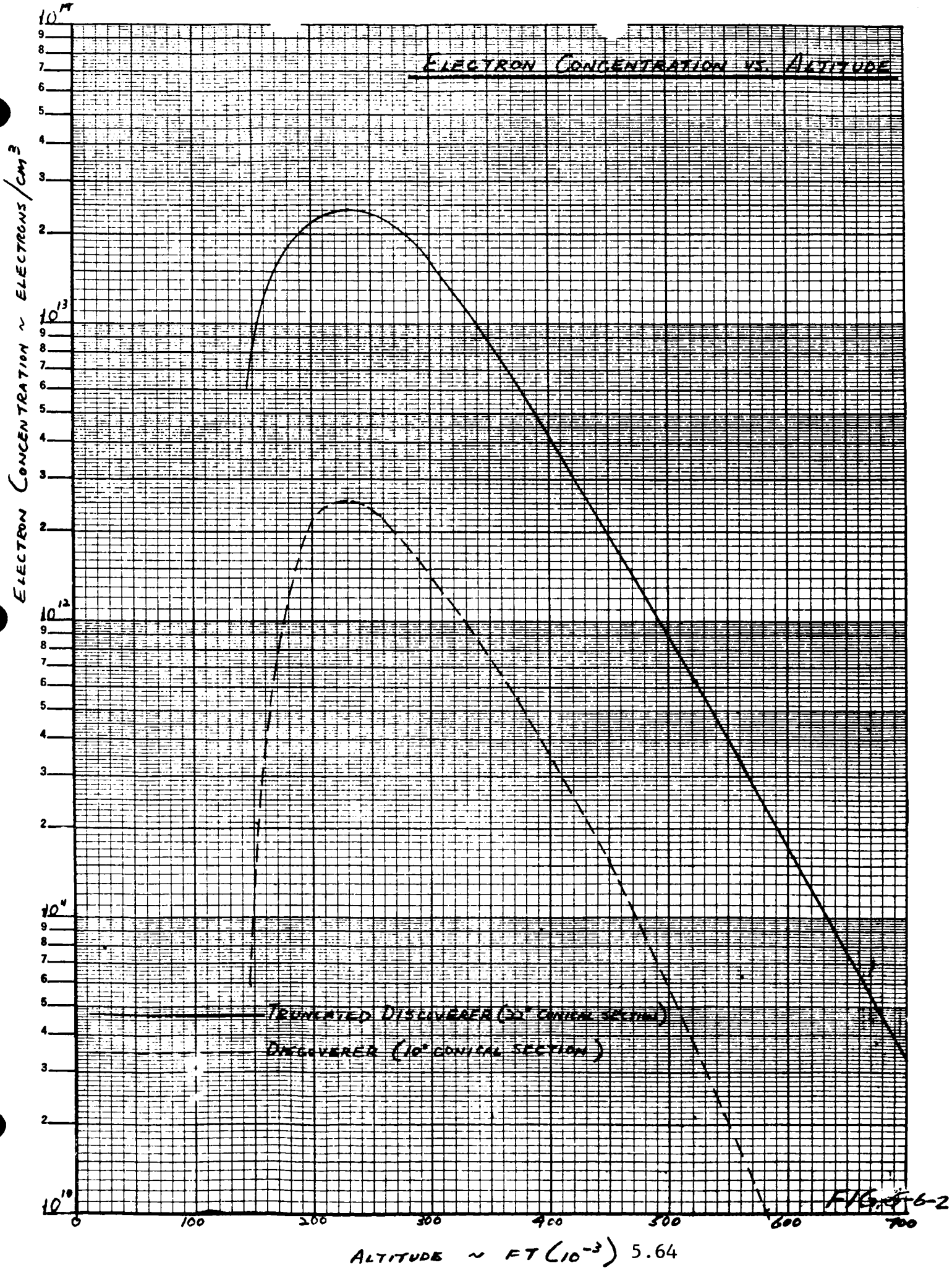
ELECTRON CONCENTRATION VS. ALTITUDE
ELECTRON CONCENTRATION ~ ELECTRONS/CM³
10¹⁴
10¹³
10¹²
10¹¹
10¹⁰
TRUNCATED DISCOVERER (22° CONICAL SECTION)
DISCOVERER (10° CONICAL SECTION)
0
100
200
300
400
500
600
700
ALTITUDE ~ FT (10⁻³)

FIG. 6-2

5.64

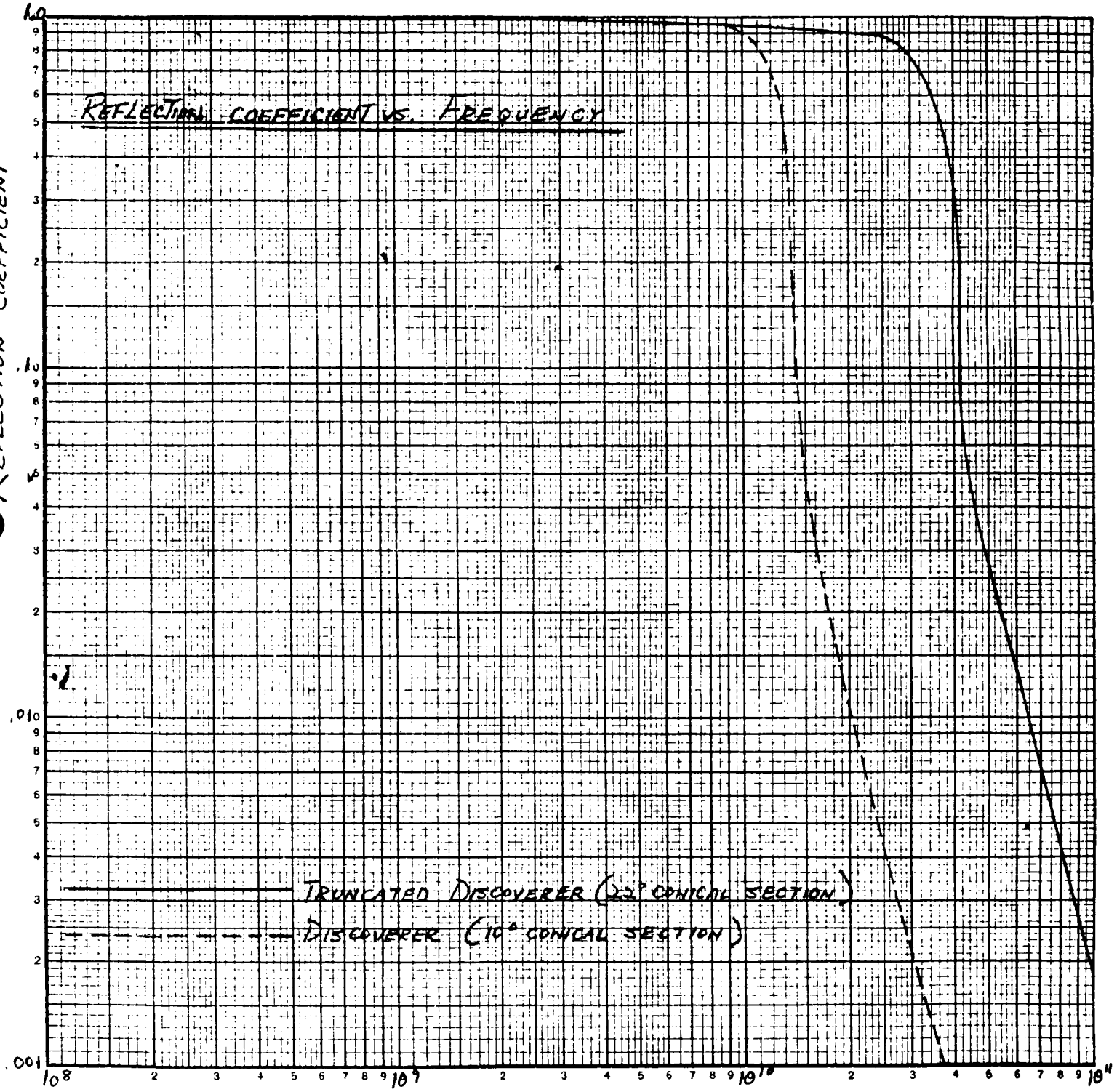
REFLECTION COEFFICIENT VS. FREQUENCY
REFLECTION COEFFICIENT
1.0
.10
.010
.001
10^8
10^9
10^{10}
10^{11}
TRUNCATED DISCOVERER (23° CONICAL SECTION)
DISCOVERER (10° CONICAL SECTION)

f ~ cps

FIG. 5-6-3

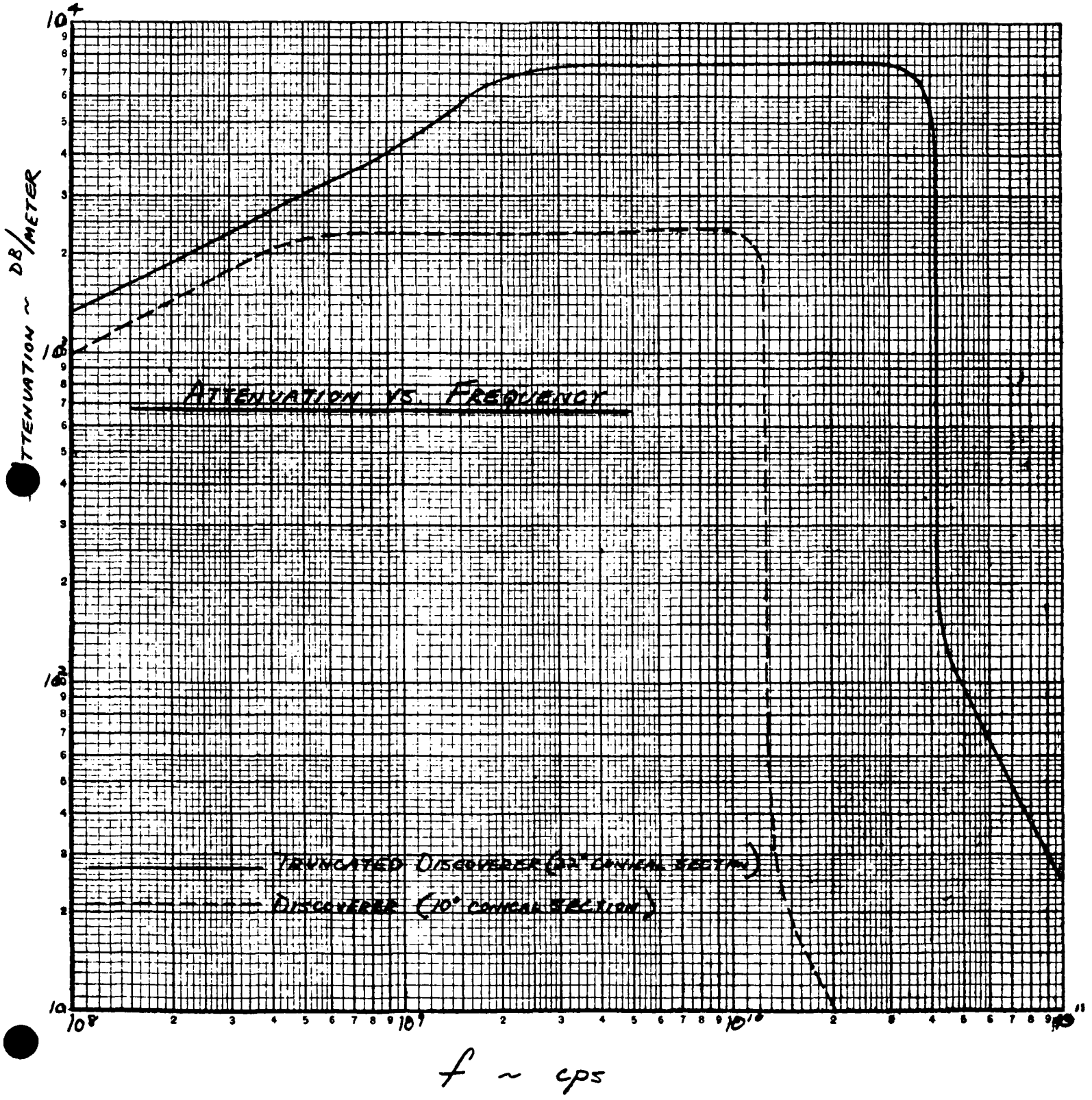
ATTENUATION ~ DB/METER
ATTENUATION VS. FREQUENCY
TRUNCATED DISCOVERER (32° CONICAL SECTION)
DISCOVERER (10° CONICAL SECTION)
f ~ cps

FIG. 5-6-4

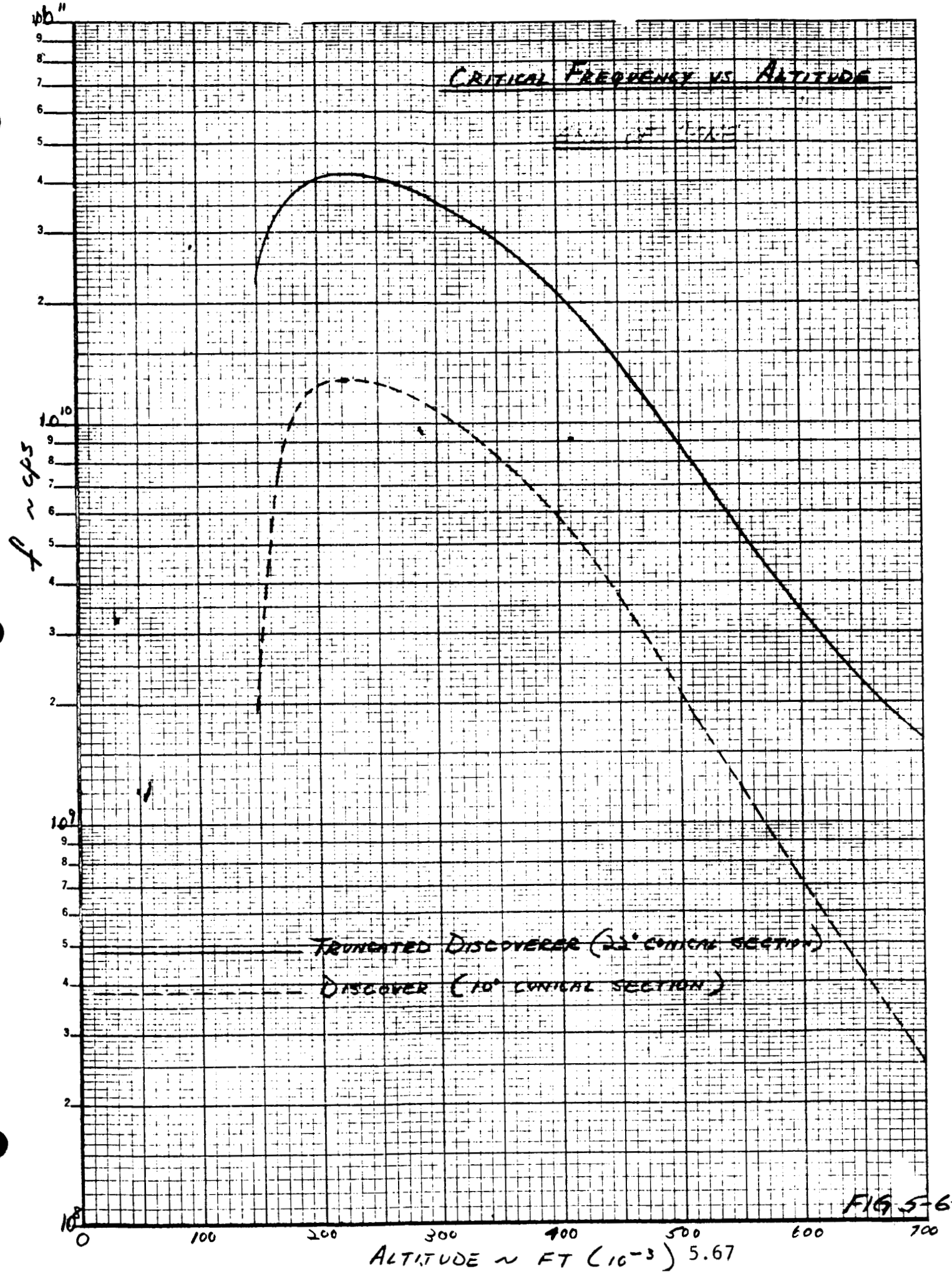
CRITICAL FREQUENCY VS. ALTITUDE
f ~ cps
ALTITUDE ~ FT (10^-3)
TRUNCATED DISCOVERER (22° CONICAL SECTION)
DISCOVER (10° CONICAL SECTION)
0
100
200
300
400
500
600
700
10^8
10^9
10^10

FIG 5-6-5

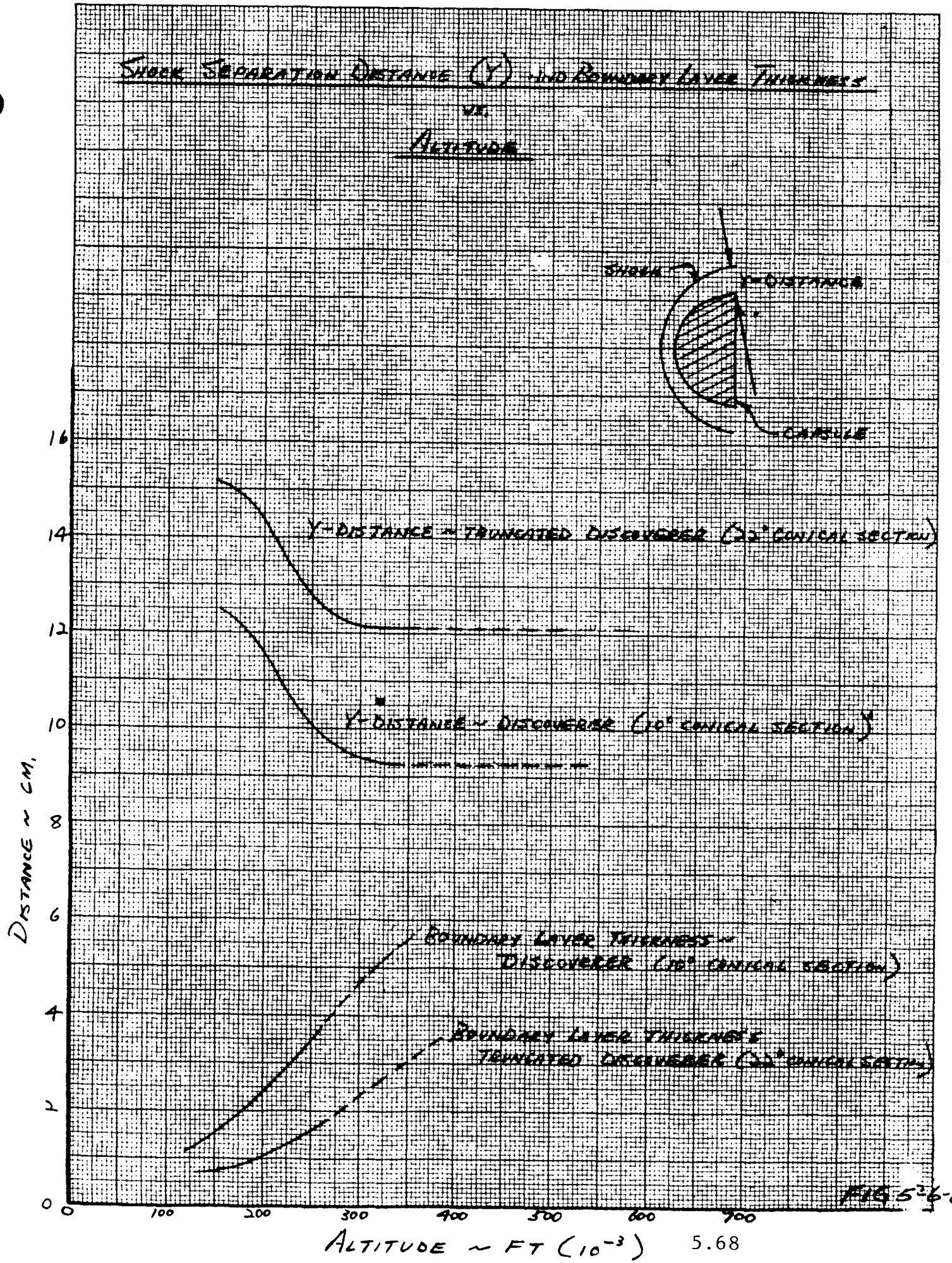
SHOCK SEPARATION DISTANCE (Y) AND BOUNDARY LAYER THICKNESS
VS.
ALTITUDE
SHOCK
Y-DISTANCE
CAPSULE
Y-DISTANCE ~ TRUNCATED DISCOVERER (22° CONICAL SECTION)
Y-DISTANCE ~ DISCOVERER (10° CONICAL SECTION)
BOUNDARY LAYER THICKNESS ~
DISCOVERER (10° CONICAL SECTION)
BOUNDARY LAYER THICKNESS
TRUNCATED DISCOVERER (22° CONICAL SECTION)
DISTANCE ~ CM.
ALTITUDE ~ FT (10^{-3})
0
2
4
6
8
10
12
14
16
100
200
300
400
500
600
700

FIG 5.26-6

REFERENCES

1) DiCristina, V. "Family of Planetary Capsules -- Shape Optimization Study," PIR 7250-25, April 5, 1962.

2) Mundy, A. "Status of Mariner C Trajectories," PIR 8153-106, March 12, 1962.

3) JPL Work Statement SW-2736, December 26, 1961.

4) Browne, W.G., "Equilibrium Thermodynamic Properties of the Environment of Mars" Advanced AeroSpace Physics Technical Memorandum #2. March 26, 1962.

5) Bisbing, P. E. "Asymptotic Forms for the Electrical Properties of Ionized Media", Advanced AeroSpace Physics Technical Memorandum #4, April 17, 1962.

6) Friel, P. J., Rosenbaum, B., "Propagation of Electromagnetic Waves Through Re-entry-Induced Plasmas", American Astronautical Society Preprint 62-18, 8th Annual National Meeting, Washington, D.C. January 1962.

5.7 CAPSULE ANTENNA

5.7.1 Introduction

This progress report is a review of the work done to date on the antenna studies.

In keeping with the capsule and trajectory studies, only the Discoverer configuration has been considered so far. Other configurations will be studied as they come into consideration during the second half of the study program.

Antennas for both a capsule-to-spacecraft relay link (100 to 500mc) and a direct capsule-to-Earth link (2.3 kmc) are being studied.

5.7.2 Design Criteria

For the purpose of the antenna studies, the following design criteria have been assumed:

(a) Radiation Pattern Coverage:

For the direct link, assuming an aerodynamically stabilized entry capsule with the roll axis within approximately 30 degrees from capsule-to-Earth line-of-sight, it appears that a radiation pattern covering the aft hemisphere will suffice. If tumbling is anticipated prior to atmospheric entry, and a communication link is required while tumbling, an additional antenna with a switching arrangement may be necessary.

For the relay link, a pattern covering only slightly more than the aft hemisphere will be required, due to the relative positions of the capsule and spacecraft.

(b) Polarization: The polarization of both the direct-link and relay-link antennas will be right-hand circular.

(c) Power-Handling Requirement:

The antenna must be able to handle RF power of about 25 to 50 watts cw or 100 to 150 watts peak pulse power.

(d) Environment

From the preliminary studies, it can be expected that the environmental conditions will be more severe than encountered in an Earth re-entry vehicle. Rapid deceleration and a long post-entry period will increase thermal problems and shock requirements.

5.7.3 Antenna Configurations

5.7.3.1 Relay Link

To provide the radiation pattern coverage required, it is expected that the antenna will be located somewhere on the aft cover of the capsule. A location of this nature will require inboard antennas, probably an array of cavity-backed slots. The inboard location is necessary due to the aerodynamic and structural entry problems. Using a Discoverer shape, the array will consist of a pair of crossed slots, phase-separated by 90°.

The use of cavity-backed slots necessitates a trade-off in size, weight and antenna efficiency. At 250 mc, a 4-mc bandwidth slotted antenna requires approximately 300 cu. in., and at UHF, approximately 100 cu. in. Losses in both antennas are in the order of 1 to 1.5 db. From the antenna standpoint it is easier to provide an adequate pattern at the lower end of the 100-500 mc range, due to the size of the capsule in wavelengths. However, at 100 mc a large volume is required to provide comparable bandwidth and low loss (1-1.5 db). This trade-off is shown in the following:

Frequency	No. of Slots	Array Weight	Array Volume Cu.In.	Loss
100 mc	2	28 lbs.	1800	4.0 db
200 mc	2	16 lbs.	600	2.0 db
300 mc	2	8 lbs.	400	1.5 db
400 mc	2	6 lbs.	200	1.0 db
500 mc	2	4 lbs.	150	1.0 db

Upon review of this data it would appear that the high frequency end of the range is the most attractive for the antenna function.

Detailed studies of patterns, beamwidths and trade-offs will be completed later in the program.

5.7.3.2 Direct Link

The antenna for a direct communication link should be on the aft cover of the capsule. Due to the environmental conditions, a flush-mounted antenna should be used. To achieve circular polarization there are several possibilities. for example, a helix in a cavity or cavity-backed spiral. A single antenna element would be the simplest arrangement (rather than an array), from a weight, volume, and electrical phasing standpoint. The radiation pattern will cover the aft hemisphere, with circularity of 3 db or better through a 120° cone angle aft. Some work is necessary to determine the power handling capacities of these types of antennas and to trade-off the various parameters. A problem in ablation by-products will also be studied to determine their effect on the aft cover antenna.

5.8 VENUS ATMOSPHERIC PROPAGATION

The object of the atmospheric propagation study was to review the communications aspect of the capsule and to assess any major difficulties encountered in communicating with the fly-by vehicle. The region of concern is the ionosphere of Venus. The attenuation of the signal in the ionosphere depends on the electron concentration, collision frequency, etc., which in turn depend critically on the composition of the Venusian atmosphere. Taking the composition (best model) given by JPL, the collision frequencies were calculated[2], and subsequently the attenuation of the signal was computed.

The results are given below for the following parameters of the ionosphere of Venus.

$N_e = 10^6$/c.c. The critical frequency is 9 mc,

The collision frequencies are:

Altitude in km.	(Collision frequency)
110	6.3×10^6
122	9.8×10^5
133	3.32×10^5
144	1.1×10^5
178	7.1×10^3
235	5.5×10^2
292	10^2

It is to be pointed out that the attenuation depends quite critically on electron concentration and its variation with distance, with a similar situation for the collision frequency. It will be assumed that the ionosphere starts at 122 km, with a constant electron concentration of 10^6/cc all the way up to 292 km. The total attenuation is then 5×10^{-2} over a distance of 270 km at 500 mc. It would, of course, be more at 100 mc.

Clearly, the problem of where the ionosphere begins and the variation of electron concentration with distance, particularly in the region around 100 km where the collision frequency is high, needs to be looked into in more detail.

REFERENCES

1) Brown, J., "Venus Atmosphere Physical Properties," PIR No. 7250-26 A, page "Best Model", April 24, 1962.

2) Drummond, J.E., "Plasma Physics," p. 245, McGraw-Hill Publishers, 1961.

5.9 POWER SUPPLY

Work is just getting started on the power supply studies. The effort to date in the program has been directed toward obtaining a firmer definition of the power supply requirements. It presently appears that batteries will be adequate for this application.

Current estimates of the power supply requirements are as follows:

(a)

Communications	180 watts
Radar Altimeter	100 watts
Instrumentation	60 watts
Total	340 watts

(b) Operating Time - 10 to 50 minutes

(c) Actuation by a "g" - switch upon entry or a timer prior to entry.

(d) Transportation time (non-operating) in Mariner vehicle of 3 to 6 months. Trickle charge is available during this period.

(e) High temperature environment (perhaps 200°C.) may prevail.

(f) Shock at entry may be 400 to 1000 g's

(g) It may be necessary to heat the batteries after separation due to the low ambient temperature.

5.10 PROBLEM AREAS

The current list of problem areas is given below:

5.10.1 Signal Processing

(1) Desirability of Error-Correction Coding
(2) Desirability of Pre-transmission Data Reduction
(3) Storage of Data During Entry
(4) Pre-detection Recording (on the Earth).

5.10.2 Transmission and Reception

(1) Phase-Lock Loop Acquisition and Hold-in Problem
(2) Selection of Optimum Modulation Techniques
(3) Oscillator Instability

5.10.3 Propagation

(1) Calculation of Atmospheric Absorption Characteristics and Critical Frequency
(2) Propagation Through Atmospheric Entry Plasma
(3) Multipath Effect from Surface of Venus
(4) Unknown Characteristics of Venus Atmospheric Noise Environment

5.10.4 Antenna

(1) Possibility of Voltage Breakdown in Venusian Atmosphere
(2) Effect of Ablation By-Products on the Antenna

5.10.5 Internal Capsule Environment

(1) High Temperature
(2) High - "g" Impact Upon Atmospheric Entry

5.10.6 Power Supply

(1) Batteries May Require Heating After Separation

5.11 FUTURE PLANS

Work planned for the second half of the program will be generally as scheduled in the original plan. In particular, the following tasks will be pursued:

5.11.1 Modulation

Several modulation techniques will be investigated, viz,: PCM/PS, FM, FM/FM, FM/PM, and FSK. The investigation will cover both theoretical and practical considerations, including the acquisition requirement of each technique.

5.11.2 Entry-Communication

The feasibility of communication during atmospheric entry will be analyzed (based on the model atmospheres), following the choice of trajectory and vehicle configuration.

5.11.3 Antenna

Antenna design trade-offs will be investigated further, including antennas for communication during entry. Detailed estimates of radiation patterns and antenna design will be prepared.

5.11.4 Power Supply

With the preliminary power supply requirements as now estimated, trade-off studies are commencing on the power supply. These studies will involve mainly an investigation of when and how one might best activate the batteries, realizing that they will start out in the extreme cold of outer space (after separation) and will then enter the very hot entry environment. Methods of activation include "g" - switches and timers.

5.11.5 Signal Processing

Following the establishment of the instrumentation data rates, pre-transmission data reduction and storage of a limited amount of data during entry will be considered. Pre-detection recording of the RF signal received on the Earth (over a direct link) will also be investigated.

5.11.6 Propagation

The Venus atmospheric absorption characteristics will be refined. The feasibility of propagation through the entry plasma will be determined. An approximate calculation of possible multipath interference for the relay link will be made and reviewed with JPL to determine if further study in this area is necessary.

5.11.7 Component Investigation

A limited investigation of electronic components available or presently under development to meet the requirements determined by these analyses will be made during the second half of this program. Specific recommendations regarding further studies in this area and development of any long lead-time items will be made if they appear advisable.

6.0 CAPSULE PARAMETRIC ANALYSIS

6.1 AERODYNAMIC DESIGN

6.1.1 Introduction

Feasibility of capsule entry into the Venusian atmosphere to define atmospheric properties and their variation with altitude is the subject of the current study. The capsule is to be ejected from a fly-by space bus and may not jeopardize the basic mission of the bus. Controlling parameters and problem areas in accomplishing such a mission are to be defined.

Falling within the regime of aerodynamic design is an investigation of basic parameters influencing capsule configuration and associated trade-offs to allow successful completion of the mission. From a gross viewpoint, several preliminary considerations can be listed.

1. Maximize payload weight
2. Minimize thermal protection requirements
3. Reduce axial loading to acceptable levels
4. Minimize plasma sheath
5. Maximize subsonic altitude
6. Provide stable platform for measurements

Within the framework of overall system constraints on the configuration, a parametric analysis has evolved.

To examine in more detail specific problems arising in capsule design for a Venusian entry, several general types of configurations have been selected. Aerodynamic characteristics have been generated for the selected configurations.

At this mid-point in the four month study, tasks are in various stages of completion in accordance with the program plan. This report indicates progress to date and outlines future efforts.

6.1.2 Parametric Configuration Analysis

Basic parameters and their effect on entry design have been analyzed, including trade-offs between parameters where possible.

Rather than to define one optimal configuration, the approach has been "to investigate and establish controlling parameters as they effect the performance and capability of a capsule design". (1)

6.1.2.1 Venus Point Mass Trajectories

Utilizing the results of a large number of point mass trajectories (2), the effect of atmospheric model, initial velocity, entry angle and ballistic coefficient on entry design have been considered.

6.1.2.1.1 Atmospheric Models

Three atmospheric models (Best, Extreme I and II - (3) have been examined. Holding initial entry velocity, altitude and ballistic coefficient constant at nominal values (12 KPS, 350 K and 60.8 respectively) the effect of atmospheric model was isolated. Figure 6.1.1 shows the variation of maximum axial loads, and altitude at which they occur, with atmospheric model. Extreme I gives the largest axial loads and therefore becomes the design limit from the viewpoint of maximum loads. It is interesting to note that while the axial loads are higher for Extreme II than Best, the maximum occurs at a lower altitude. This results from the variation in density gradient with altitude for the two atmospheres. Differences in maximum g_x's among the models are approximately 25% of the largest values, independent of entry angle. Variation in altitude at which $(g_x)_{max}$ occurs is approximately 33%, again roughly independent of entry angle.

6.1.2.1.2 Entry Velocity

Variations in maximum axial loads with initial velocity is shown in Figure 6.1.2. Ballistic coefficient was held constant and only the "worst" atmosphere, Extreme I, was considered. Differences between $(g_x)_{max}$ values at 14 and 11 KPS are approximately 37% of the larger values, independent of entry angle (except near capture where the values converge). One additional kilometer/sec. of initial velocity, in the range from

11 to 14, is equivalent to approximately 110 additional g's at maximum loading for a straight in ($\gamma_i = 90^o$) entry.

6.1.2.1.3 Entry Angle

Figures 6.1.1 and 6.1.2 show entry angle to be an extremely strong parameter on axial loads. Maximum axial loads, for extreme entry conditions (V_i = 14 KPS, Extreme I atmosphere), are 910 g's for a 90° entry, but only 70-80 g's near capture entry angles (γ_i 15°). While planning an entry for minimum capture is unrealistic, a nominal entry angle of 30° into Extreme I atmosphere would give maximum axial loads of 260 to 405 g's for corresponding entry velocities of 11 to 14 KPS. Although the variation of $(g_x)_{max}$ with entry angle is non-linear, $\frac{\partial (g_x)_{max}}{\partial \gamma_i} \approx 11$ g/DEGREE, $(20^\circ < \gamma_i < 40^\circ)$, and for V_i = 12 KPS entry into Extreme I atmosphere.

6.1.2.1.4 Ballistic Coefficient

Figure 6.1.3 shows the variation in altitude with ballistic coefficient at which $(g_x)_{max}$ and M = 1 occur. Variations for ballistic coefficients from 20 to 100 are not large, less than 10% of the maximum value. For 30° entry into Extreme I atmosphere at V_i = 12 KPS, maximum axial load occurs at 250,000 ft. and M = 1 at 225,000 ft. with $\pm$ 5% variations with W/C_DA changes between 20 and 100.

Time from M = 1 to impact for various ballistic coefficients is shown in Figure 6.1.4. Subsonic time, for a 30° entry, decreases significantly from 46 to 22 min. with increasing W/C_DA from 20 to 100. These values for the most dense atmosphere, Extreme I, would be lower for the "less severe" atmospheric models.

6.1.2.2 Configuration Selection Program

An existing program to optimize configuration selection (4) has been utilized to establish trends with variation of capsule geometry. While the program is basically formulated for use in conjunction with weapon system preliminary design,

it has been modified to permit its use for the planetary capsule study. One major difficulty arises in calculation of ablation weights and thicknesses. For Venusian entry, the higher entry velocities and atmospheric properties result in extremely high heat transfer rates. A large portion of the total heating may come from gas cap radiation as opposed to convective heating. Crude estimates of hot gas radiative heating as a factor of convective heating have been utilized in the computer studies. Methods to adequately preduct thermodynamic requirements for Venusian entry conditions are currently under development. Until these results are available, interpretation of configuration selection program studies must be considered preliminary.

From the volume envelope available for the capsule (1) basic geometric limits on vehicle length and diameter have been established. A nominal entry velocity of 40,000 fps has been used for entry angles of 15 to 90 degrees. While one of the final variables of the study will be payload weight, nominal weight of 78 lbs. (based on communication and instrumentation estimates) has been chosen for comparison with total weights of surveyed configurations.

6.1.2.2.1 Blunt Sphere Cones

Blunt sphere cones have been surveyed over a range of bluntness ratios and cone angles. Preliminary results (figures 6.1.5-6.1.16) have been compared on the basis of payload weight to total weight, heat shield weight to total weight and ballistic coefficient. Consideration has been given static margin and volume characteristics. Figures for near capture entry angles are presented for various base diameters from 20 to 50 inches. A similar set of results for straight-in entry are currently being analyzed.

a. Ratio of Payload Weight to Total Weight

The basic trend appears to be an increase in the ratio of payload weight to total weight with increasing cone angle and bluntness ratio. The increase with bluntness ratio is more significant at lower cone angles.

b. Ratio of Heat Shield Weight to Total Weight

Heat shield weight as a percentage of total weight decreases with increasing cone angle. At lower cone angles, there is also a decrease with increasing bluntness ratios. The preliminary nature of these results, awaiting more precise heating analyses, is again emphasized.

c. Ballistic Coefficient

A decrease in W/C_DA is noted with increase in cone angle. For lower cone angles, a large decrease also occurs with increasing bluntness ratio.

These preliminary results show a trend toward large bluntness ratio, high cone angle configurations. These types of configurations will require significant afterbodies to provide adequate volume and satisfactory stability characteristics throughout the angle of attack range.

6.1.3 Selected Configuration Types and Their Aerodynamic Characteristics

Three general types of configurations have been selected for more detailed analyses. While nominal weights and base diameters (200 lbs and 33 inches respectively) have been chosen, these parameters can be scaled up or down within the study limits.

6.1.3.1 Discoverer Type

Figure 6.1.17 shows the basic type of configuration. This capsule represents a successful Earth re-entry vehicle and shows adaptability to Martian entry (5). Its selection, early in the program, has been made to permit an analysis of the entry guidance requirements. Complete aerodynamic charactertics are present in reference 6.

6.1.3.2 Apollo Type

Preliminary study results show the desirability of a more blunt, lower W/C_DA configuration. Figure 6.1.18 shows an Apollo type configuration. Aerodynamic characteristics for nominal angles of attack are presently available and they are currently being extended throughout the angle of attack range up to 180°.

6.1.3.3 Cone-Flare Type

This type of configuration, Figure 6.1.19, is primarily being investigated as an aid to hypersonic communications. Aerodynamic characteristics are presently being generated.

6.1.4 Problem Areas

a. Accurate definition of thermal requirements to allow more precise parametric configuration analysis.

b. Dynamic stability characteristics of blunt configurations including the effect of various afterbodies.

6.1.5 Future Work

a. Continued parametric analysis of configuration variables integrating the results of 3° of freedom trajectories and more accurate heating estimates.

b. Generation of complete aerodynamic characteristics for the selected configuration types.

c. Trade-off considerations among basic parameters to indicate advantages or disadvantages of realistic combinations of controlling parameters.

d. Consider Venusian results in view of Martian mission.

REFERENCES

1. "Venus-Mars Capsule Study", JPL EPD-33.

2. McDevitt, M.; "Flight Mechanics Progress Report" GE MSVD (to be published).

3. Brown, J.; "Venus Atmosphere Physical Properties", GE MSVD PIR 7520-26A, 24 April 62.

4. Lipson, S.; "Modified Configuration selection Program for Ball. R/V", GE MSVD R61SD302, January 1961.

5. "Suitability of the Discoverer and NERV entry Vehicle for Mars Atmospheric Entry", GE MSVD 30 April 62.

6. Katz, G. D.; "Mars Entry Vehicle-Aerodynamic Design Summary" GE MSVD ADM 4:65, 4 April 1962.

6.2 POINT MASS ENTRIES

Entry trajectories have been computed on an IBM 7090 computer, using a 3 degree-of-freedom, in translation, point mass program. The three Venus atmospheric models which were considered were furnished by JPL (1). Drag coefficient values were obtained as functions of both Mach Number and altitude as shown in Figures 3-1.6 and 3-1.7 of Reference 2.

Entry altitude for all trajectories was 350 km. Variables which were considered, included entry angle (0 to 90° down from horz.), entry velocity (11 to 14 km/sec.) and W/C_DA (20 to 300 earth lb/ft^2). A trajectory run log is presented in Table 6.2.1 and shows that most trajectories utilized Extreme I atmosphere since it produced the highest axial loads. This is demonstrated in Figure 6.2.1 which shows maximum deceleration and altitude at maximum deceleration, as functions of entry angle for the three model atmospheres.

Peak deceleration versus entry angle is presented in Figures 6.2.2 and 6.2.3 for the Extreme I and "Best" atmospheres respectively for entry velocities of 11, 12, 13 and 14 km/sec. This information is cross-plotted in Figure 6.2.4 and 6.2.5 to obtain the angular entry corridor between the peak deceleration limits of 100, 200, 300 and 400 earth g's and a skip limit which is defined as the minimum entry angle for capture during the initial entry.

Figure 6.2.6 presents range and time from entry to impact versus entry angle. The influence of W/C_DA on time to impact and altitude for peak deceleration and Mach 1 is in Figure 6.2.7. Entry time histories showing altitude, dynamic pressure, velocity, and axial g's have been selected for representative trajectories (corresponding to log numbers 6, 7, 10, 11, 12, 13, 17, 19 and 21) and are presented in Figures 6.2.8 to 6.2.25 respectively.

6.2.1 General Data

The relationship between hyperbolic excess velocity (V_{∞}) and local velocity is presented in Figure 6.2.26 and should prove helpful in using the results in the following sections. Figure 6.2.27 presents entry path angle (DFH) as a function of vacuum perifocus for an entry altitude of 350 km. and hyperbolic excess velocities between 0 and 10 km/sec.

TABLE 6.2.1

Trajectory	Atmosphere*	Entry Velocity V_E (Kilometers/Sec)	W/C_DA (PSF)	Entry Angle (Degrees Down from Local Horizontal) γ_E
1	II	12	60.8	90
2	II	12	60.8	30
3	II	12	60.8	15
4	II	12	60.8	12
5	I	12	60.8	12
6	B	12	60.8	90
7	B	12	60.8	30
8	B	12	60.8	15
9	B	12	60.8	12
10	I	12	60.8	90
11	I	12	60.8	30
12	I	12	60.8	15
13	I	12	20	30
14	I	12	40	30
15	I	12	100	30
16	I	12	200	30
17	I	12	300	30
18	I	11	60.8	30
19	I	13	60.8	30
20	I	12	60.8	14.5
21	I	12	60.8	13.25
22	I	11	60.8	90
23	I	13	60.8	90
24	B	11	60.8	90
25	B	14	60.8	90
26	B	13	60.8	90
27	I	12	100	15
28	I	12	100	90
29	I	12	20	15
30	I	12	20	90

* I = Extreme Model I
II = Extreme Model II
B = Best Model

6.2.2 Retrorocket Requirements

Figures 6.2.28, 6.2.29 and 6.2.30 show retrorocket velocity increments required to obtain a capsule virtual perifocus (r_p) equal to one Venus radius for various bus perifoci, as a function of steering distance from Venus (r) and hyperbolic excess velocity (V_∞). The retrorocket was assumed to fire impulsively and perpendicular to the resultant probe velocity to obtain maximum turn angle.

6.2.3 Approach Geometry Data

It is the purpose of this section of the study to determine if the maximum probe to bus communication time after probe entry is sufficient to permit the bus to be used as an information relay link.

The bus is assumed to approach the surface of Venus as close as two Venus radii. If terminal guidance is required, then, at some yet to be determined time before bus perifocus, a retrorocket will be fired causing the velocity vector of the probe to be rotated such that planetary entry will occur, while the bus continues on its original trajectory. Since the probe has a smaller virtual perifocus than the bus, its average velocity will be greater and result in the probe arriving at Venus first. This concept is demonstrated in sketch 1 which shows relative arrival geometry and defines some terms used in this report.

Communication time was assumed to start when the probe was 1 radius from the center of Venus and to end when "line of sight" limits from the surface of Venus were reached. In a discussion with Dr. W. C. King and R. Pahmeier, it was determined that ionosphere reflection will not limit communication for probable transmission frequencies. In the calculations, two items were considered compensatory and were neglected. They were 1) atmospheric refraction, and 2) atmospheric effect on entry range. It was also assumed that the limiting true anomaly for the bus during time of entry is 90° (i.e., straight line path). This last assumption will produce slightly optimistic values of communication time for the lower hyperbolic excess velocities.

Data is presented showing the maximum probe to bus communication time during entry as a function of bus perifocus ratio $(r_p/r_o)_B$ probe perifocus ratio $(r_p/r_o)p$, hyperbolic excess velocity

(V_∞), and distance from Venus at capsule ejection (r_s/r_o). Partial results of this study are presented in Figure 6.2.31, which shows communication time versus hyperbolic excess velocity for a bus perifocus ratio of 2.0 radii and for steering ratios and probe perifocus ratios between 10-100 Venus radii and 0.1-0.8 Venus radii respectively. Figure 6.2.32 shows similar data for a bus perifocus ratio of 3.0 radii. Figure 6.2.33 shows time before perifocus versus distance from Venus and can be used to find the distance from Venus when the final approach guidance maneuver is performed.

For each set of bus and probe conditions where only r_s/r_o is varied, there is a minimum communication time which corresponds to increasing r_s/r_o values for increasing bus perifocus ratios $(r_s/r_o)B$. This can be explained best by examining the effect of r_s/r_o on the beginning and end limits of communication time. As r_s/r_o is decreased, the probe will lead the bus less at the start of communications. But also as r_s/r_o is decreased, the impact point moves such that the terminal line of sight limit increases communication time until infinite communication time is achieved. These opposing trends combine to produce a minimum value. Time permitting, an attempt will be made to define the minimum communication conditions analytically.

It can be seen from Figures 6.2.31 and 6.2.32 that very little communication time is gained by increasing the steering ratio beyond 50 radii. But, communication time is extended considerably by increasing the probe perifocus ratio (i.e. entry angle becomes less steep). It is therefore evident that communication time is limited by the steep entry trajectory even though actually entry time is greater for the shallow entry. Preliminary entry trajectories have indicated that probe perifocus ratio must be greater than .8 for the peak deceleration to be less than 400 g's. Figure 6.2.7 shows that entry time for a 30° entry path angle attains a limit of approximately 30 min. for very low W/C_DA. It is, therefore, obvious that adequate communication time is available for bus perifocus ratios equal to or greater than 3.0 Venus ratii, For smaller bus perifocus ratio or smaller probe perifocus ratio, communication time is obtained by cross-plotting the data of Figures 6.2.26 and 6.2.27.

6.2.4 Future Plans

Three-degrees of freedom (in-plane translation and pitch rotation) are presently being computed with appropriate parametric variations. This will establish the effects of entry angle of attack, pitch rate, and c.g. off-set on angle of attack envelope and normal accelerations. Selected six-degree of freedom trajectories will be made to check the three-degree of freedom results and to determine the effect of high spin rates.

Guidance requirements are to be determined as functions of distance from Venus, V_∞, and entry corridor.

Calculations will be made to show the payload trade-off as a function of entry conditions. These calculations will consider the effects of both heat shield weight and instrumentation weight.

REFERENCES

1. JPL Document EPD33, Revised March 29, 1962.

2. "Suitability of the Discoverer and Nerv Entry Vehicle for Mars Atmospheric Entry", Vol. I, GE MSVD, April 30, 1962.

6.3 ENTRY TRAJECTORY MODULATION

6.3.1 Discussion

Several methods of entry trajectory modulation through the use of a variable vehicle drag are described herein. The purpose of this drag modulation will be to reduce the peak vehicle deceleration during atmospheric entry.

An examination of the point-mass trajectories (Figure 6.2.1 to 6.2.25) results in these conclusions:

a. Because of the high atmospheric density, relative to Earth and Mars, vehicles in the range of W/C_DA's being considered go subsonic at altitudes on the order of 150,000 to 200,000 ft. The vehicle descent time for these altitudes is of the order of 20 to 30 minutes with no auxiliary drag devices. Thus, it may be tentatively concluded that no need for terminal braking exists based on descent time requirements.

b. The entry trajectories mentioned above show the existence of a serious situation during the early phase of entry; namely, the presence of axial accelerations on the order of 500-600 g's. Accelerations of this order clearly point to the need for trade-offs in the areas of the necessary vehicle structure, controlled entry corridor and modulation of the entry trajectory through variable vehicle drag or retro-rocket use.

As shown in Figure 6.3.1 drag modulation reduces the peak deceleration by spreading the integrated deceleration over a greater altitude band. This spreading is accomplished by increasing the vehicle W/C_DA (or decreasing the drag) with increasing dynamic pressure according to the following relation which is obtained by equating the vehicle drag force and inertia force.

$$a = \frac{q}{W/C_DA}$$

where a - deceleration in g's

q - dynamic pressure

6.3.2 Types of Drag Modulation

Two types of drag modulation can be used to obtain peak load reduction. They are:

a. a continuously variable drag

b. a step-wise drag change

6.3.2.1 Continuously Variable Drag

Vehicles with controlled drag surfaces satisfy the variable drag requirement. The Avco Drag Brake (1) or vehicles with controlled flaps, etc. fall into this category. Studies involving the drag brake, which is similar in operation to an up-side-down umbrella, have indicated large reductions in peak re-entry loads, depending of course on the specific vehicle design and entry trajectory. These reductions are possible because of the wide range of drag area that is designed into the vehicle. The corresponding reduction for a vehicle with flaps would tend to be smaller since the variable drag range would be less. Figures 6.3.1 and 6.3.2 illustrate the effect on the entry altitude deceleration profile for a drag brake vehicle and a vehicle with flaps respectively. It should be noted that these figures represent relative trends between the two types of variable drag vehicles.

The variable nature of the above drag devices requires rather complex sensing and actuating systems. These systems, in combination with the attendent structure of these devices, consume a considerable portion of the total vehicle weight.

In addition to weight required, a second complication arises in considering the use of variable drag devices for the Venus entry. For entry flight path angles (γ_e) approaching $\gamma_e = 90^o$, the deceleration pulse is quite short, on the order of a few seconds. The duration of this pulse would be enlarged by the use of variable drag; however, it is suspected that problems would arise with respect to the reaction time of the variable device.

6.3.2.2 Step - Wise Drag Modulation

A second method of trajectory modulation through drag variation exists which does not require the complex sensing and actuating system mentioned in the previous section. This method is step-wise drag modulation in which the vehicle drag is varied as a step function. The fact that the drag variation is in the direction of decreasing drag suggests that a high initial vehicle drag could be obtained through the use of an auxiliary drag device which would be jettisoned to provide the step change in drag. A few concepts of auxiliary drag devices, for the configurations described in reference 2 are shown in Figure 6.3.3. These concepts represent one-step drag variation. Figure 6.3.4 presents the results of using a variation in drag for a typical Martian entry trajectory. As can be seen from Figure 6.3.4 a reduction in peak g's of approximately 30% is realized through the use of one-step drag modulation.

In terms of the Venus trajectories, it is difficult to predict the reduction in peak g's that can be gained from one-step modulation. The latest Venus trajectories do show, however, a very sharp deceleration pulse for the lower W/C_DA's. This sharp pulse would tend to decrease the effectiveness of drag modulation. Modulation of the higher W/C_DA trajectories would no doubt be more beneficial.

Several conclusions can be drawn thus far concerning the use of drag modulations for the Venus entry capsule.

a. Variable drag devices offer very good peak load reduction characteristics; however, these devices are rather heavy and complex. In addition the Venus entry trajectories show very sharp G loading risers which would probably present strong reaction time problems to the variable device.

b. Step-wise drag modulation offers an alternate method of reducing peak load but here again the sharp rise of the load curve would probably limit the modulation to one-step. One-step modulation could be obtained with jettisonable, body-fixed or towed devices as pictured in Figure 6.3.3.

c. In order to determine the extent of peak load reduction, several point-mass trajectories are planned. This reduction when viewed in terms of system requirements will indicate the feasibility of further pursuit of peak load reduction through drag modulation.

FIGURE 6.3.1

REDUCTION IN PEAK DECELERATION THROUGH DRAG MODULATION

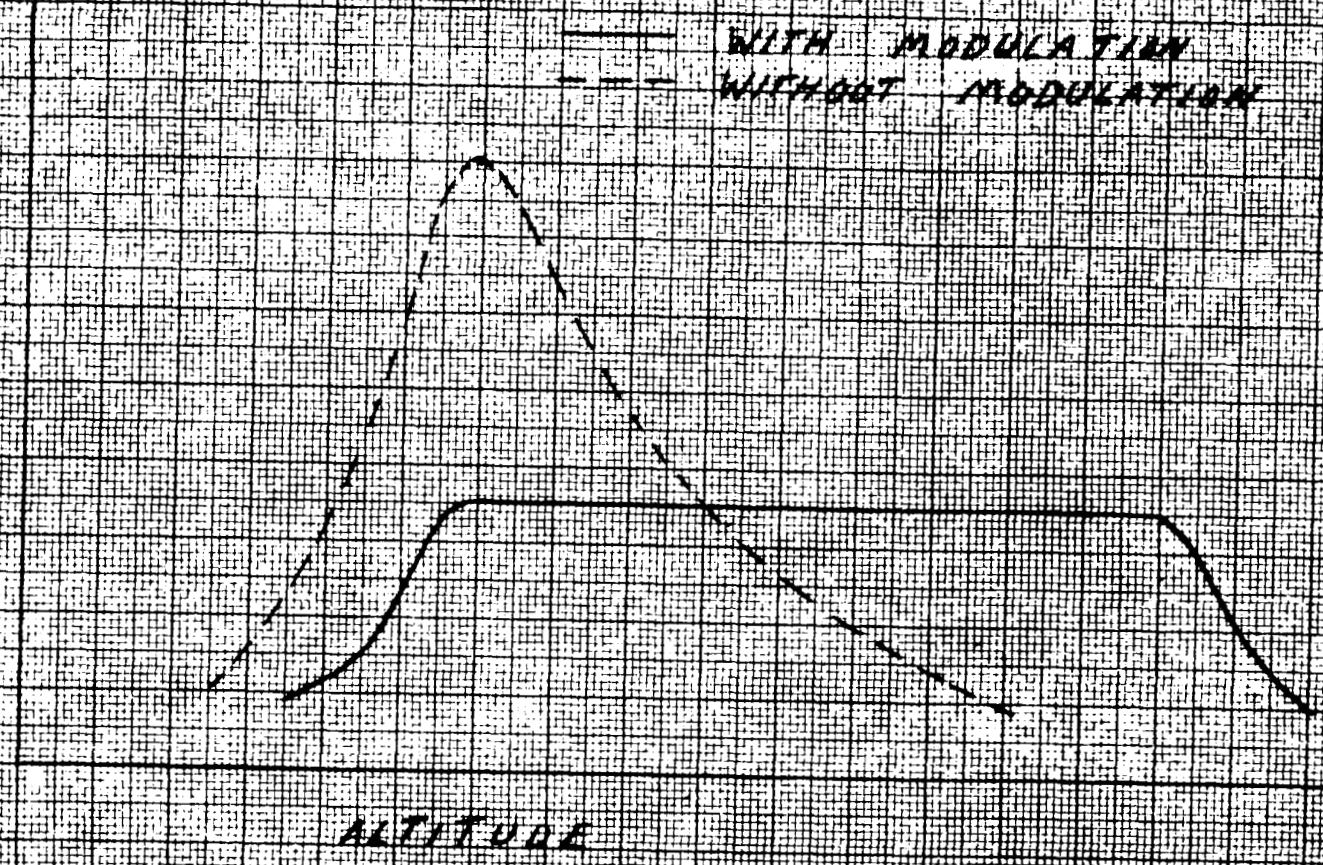

FIGURE 6.3.2

REDUCTION IN PEAK DECELERATION THROUGH DRAG MODULATION WITH LIMITED VARIABLE DRAG (FLAPS)

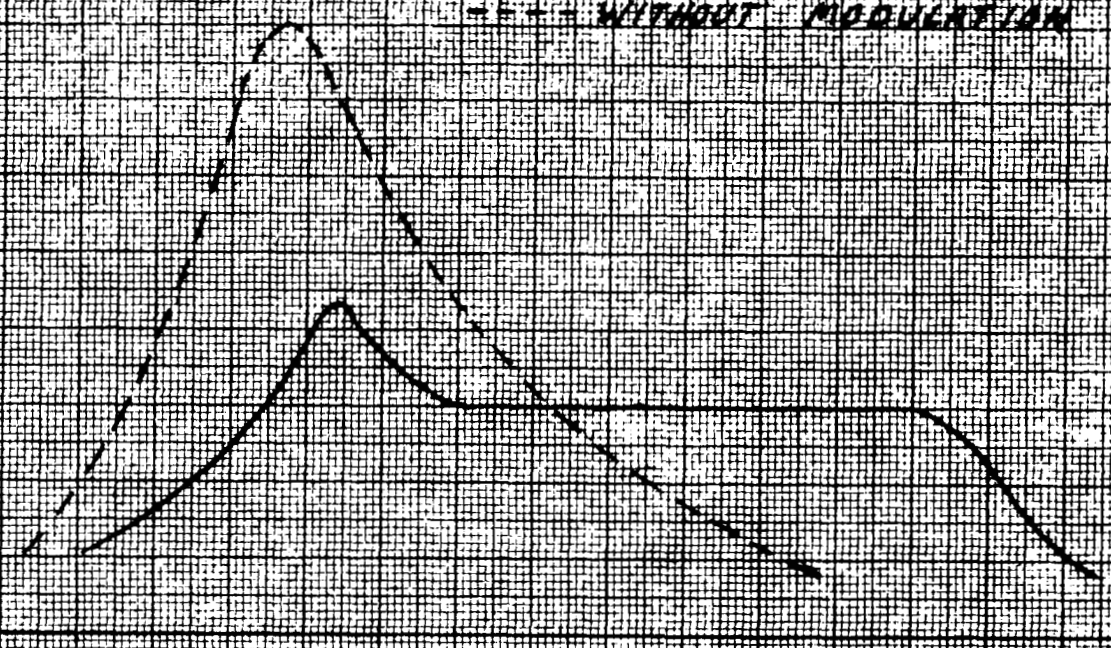

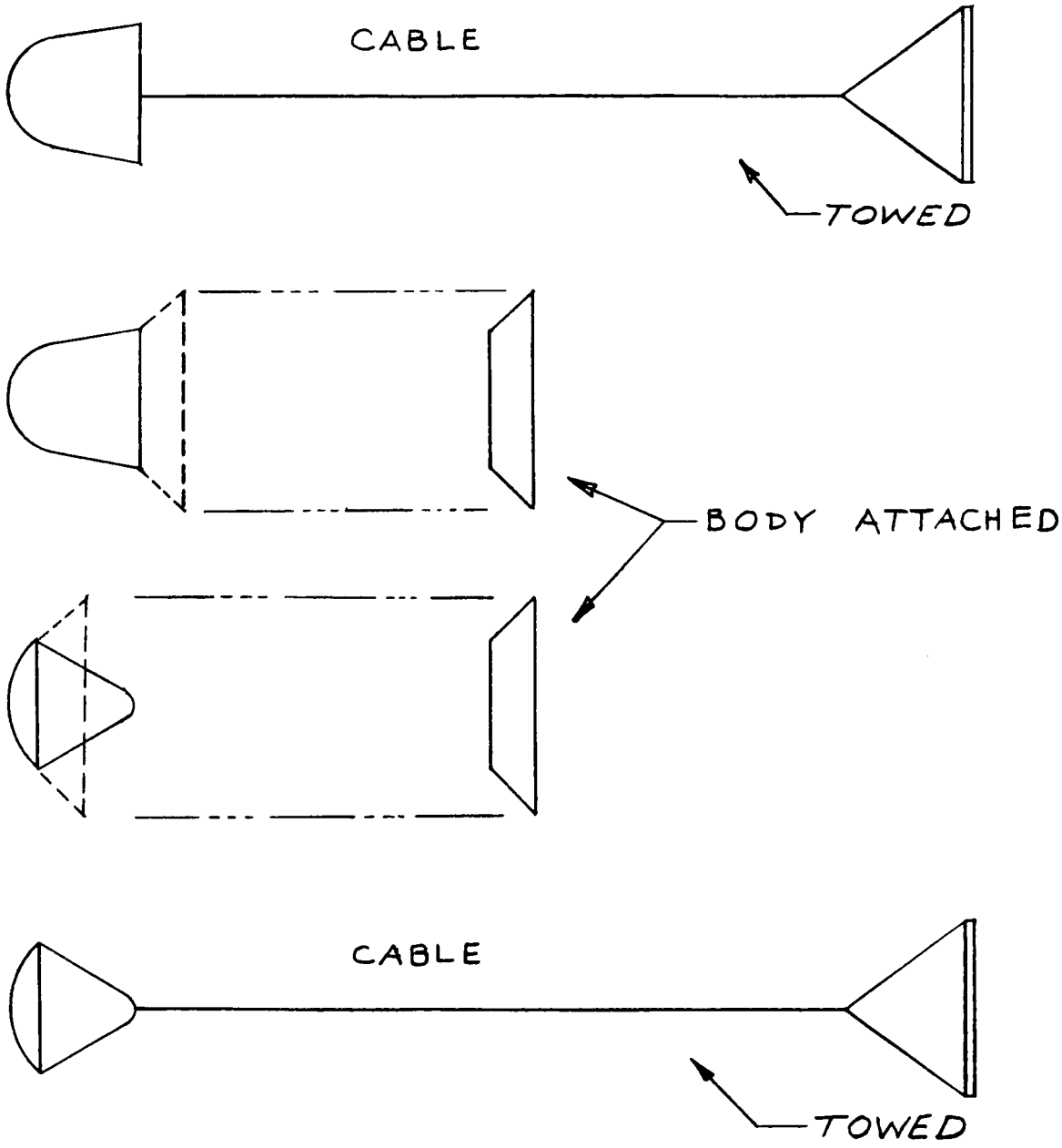

AUXILIARY DRAG DEVICES

FIG. 6.3.3.

FIGURE 6.3.4

EFFECT OF ONE-STEP DRAG MODULATION ON ENTRY DECELERATION

TYPICAL MARS ATMOSPHERE

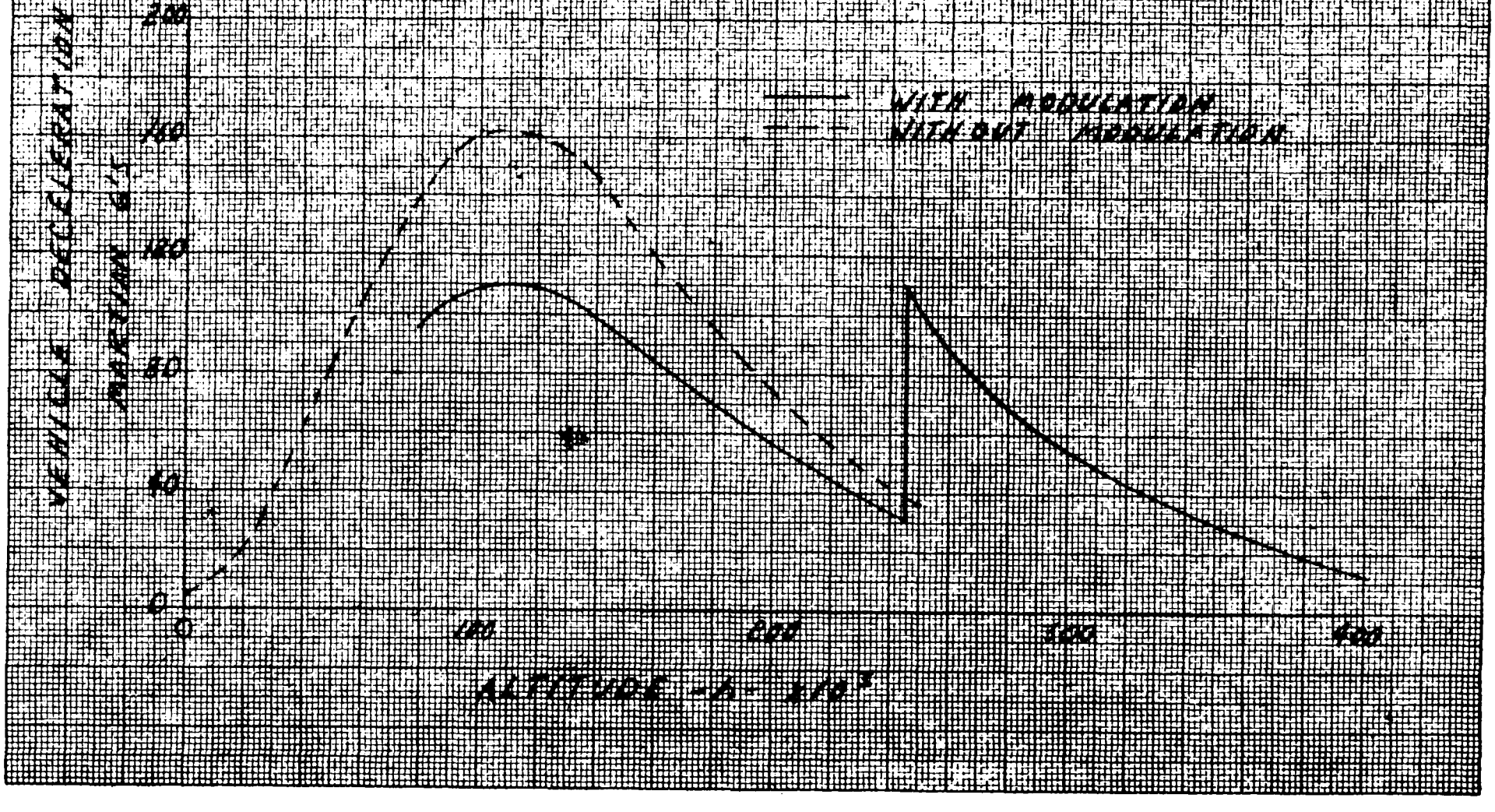

REFERENCES

1. Detra, R. W., et al; "The Drag Brake Manned Satellite System", Avco-Everett Research Lab., Research Report #64 August 1959.

2. Katz, G. D.; "Preliminary Configuration Selection" GE MSVD PIR 8152-149, March 1962.

3. Katz, G. D., McMullen, J. C.; "Modification of the Mars Entry Capsule to obatin Increased Parachute Descent Time" GE MSVD PIR 8152-180, April 1962.

4. McMullen, J. C., Smith, A. M.; "A Study of the Parachute Deceleration of a Discoverer of Nerv Type Capsule Entering the Martian Atmosphere" GE TIS 62SD142.

5. Wiant, H. W., Fredette, R. O.; "A Study of High Drag Configurations as First Stage Decelerators" WACD TN 56-320, July 1956.

6. Wackelin, H. G., Fredette, R. O.; "Dynamics of Separating Bodies, Volume II" AFOSR - 106, Holloman Air Force Base, March 1961.

6.4 EXTERNAL THERMODYNAMICS

6.4.1 Parametric Study

The object of this study will be to determine the variation of heat shield requirements with W/C_DA and entry angle for each of the vehicles considered in each of the model atmospheres. The evaluation of convective and radiative heating will be based on the best approximations available at the time the analyses are performed. The range of parameters over which the relationships will be studied are:

Ballistic coefficient	W/C_DA	20-200 (PSF)
Entry angle (down from local horizontal)	γ_E	$\sim 15^o$-90°

Atmospheres: Extreme I - Best - Extreme II

Configurations: Discoverer Appolo-Type, Slender Cone - Flare

Materials: Phenolic Nylon Only

If each of the four variables is considered for three values, then the number of cases becomes 81, which is clearly too many for the time period available. In order to develop trends (which hopefully will be reliable) early in the study, it is planned that the Discoverer configuration will be evaluated over the range of the other variables. A matrix of test conditions is shown for these cases. The relationships which may be derived from the evaluation of these cases are:

a. heating vs W/C_DA $\qquad \gamma = 30^o$

b. heating vs γ_E $\qquad W/C_DA = 60$

c. Comparison between Extreme Model I atmospheres and Best atmospheres.

$W/C_DA = 60, \qquad \gamma_E = 30, \qquad \gamma_E = 90$

An improved heating law should be available by the time that the evaluation of the cases in the first matrix has been completed. This second law would then be used to verify or modify the trends observed with the first law, perhaps to the extent of considering all the cases in the matrix. At this point, it should be possible to formulate a second matrix in which two configurations are considered; the Discoverer (shape B)and the Apollo-type (shape A). For purposes of comparing two different configurations, a more sensibly parameter would be W/A, rather than W/C_DA since the hypersonic drag coefficients vary so widely for the two shapes. The use of W/A as a similarity parameter bases the equivalence of two vehicles on the total weight and on the base diameter which would make similar vehicles conform to approximately the same mission requirements (e.g. payload weight, size). As an example, comparison will be made between a Discoverer vehicle with W/C_DA approximately 60 and an Apollo-type with W/C_DA approximately 30. An estimate of the second matrix based on the improved heating laws is shown as Stage II. Relationships which should be forthcoming are:

a. Comparison between shape A and B for approximately W/A for low path angle and W/C_DA between 20 and 60.

b. Comparison between vehicles on vertical entry $\gamma_E = 90$

c. Comparison for $\gamma_E = 30^\circ$, $W/C_DA = 20$ to 200

d. Relationship between heating encountered in Extreme Model I and Best atmospheres for Discoverer shape with W/C_DA approximately 60 at path angles between 15° and 90°.

Definition of further cases to be analyzed will be based on the results of the first two phases.

6.4.2 Methods

6.4.2.1 Heating Laws

During the period in which the basic thermodynamic relationships for the Venus atmosphere are being developed, a first approximation to the heating equations will be employed. The equations will be those which obtain for the Earth's atmosphere with amplification factors to account

for effects of ionization on the convective heat transfer and for the effect of CO_2 on hot gas radiation. As improved estimates of the heating equations become available, they will be employed in the analyses.

6.4.2.2 Variation with Body Position

Since the derived heating equations are expected to obtain for the stagnation point only, the variation of heat flux with body position will be taken to be the same as the variation in integrated flux in the Earth's atmosphere.

The relationships may be stated with the following notation:

c = convective

r = radiative

v = in Venus atmosphere

E = in Earth atmosphere

(x) = at location X

o = stagnation point

q = instantaneous flux

Q = integrated flux

$$\frac{q_v(x)_c}{q_v(o)_c} = \frac{Q_E(x)_c}{Q_E(o)_c}$$

$$\frac{q_v(x)_r}{q_v(o)_r} = \frac{Q_E(x)_r}{Q_E(o)_r}$$

6.4.2.3 REKAP

An attempt will be made to rescale the REKAP program to study the response of thick layers of ablation materials to extremely high fluxes. The response will be analyzed for triangular pulses with reduced blocking action to

account for the relatively high radiative input. In addition, surface temperatures are expected to reach the sublimation temperature of the char material. Revision of the REKAP program to include the effects of char sublimation on the energy balance at the shield surface will be investigated.

6.4.3 Progress and Plans

6.4.3.1 Progress

a. An approximate stagnation point convective heating law has been derived which includes an estimate of the ionization effects, this being calculated for the cases shown in Program Matrix I, Table 6.4.1.

b. Revision of the REKAP program has begun.

c. An approximate equation for hot gas radiation is being derived and awaits required data on emissivity as a function of temperature and density.

6.4.3.2 Plans

The second version of the heating laws will be available shortly and it will be evaluated for some of the trajectory cases in Matrix I. Heat pulses derived by this method will be simulated on the revised REKAP program and the shield degradation will be determined for the cases in Matrix I and II.

TABLE 6.4.1

PROGRAM MATRIX - STAGE I - SEVEN CASES

CONFIGURATION: DISCOVERER

HEATING LAWS: First Approximation

ATMOSPHERES: Extreme Model I, Extreme Model II, and "Best" Model Atmospheres

γ_E ↓ \ W/C_DA →	20	60	100	200	300
15		XI			
30		XB			
	XI	XB			XI
45					
60					
90		XB			
		XI			

XI = Extreme Model I Atmosphere
XB = Best Model Atmosphere

TABLE 6.4.2

PROGRAM MATRIX - STAGE II - SEVENTEEN CASES

Heating Laws - Improved Over First Approximation

γ_E ↓ \ W/C_DA →	20	30	40	60	100	200
15	A XB	A XB	B XB	B XB		
30	A XB	A XB	B XB	B XIXB	B XB	B XB
45						
60						
90	A XB	A XB	B XB	B XBXI		

XI = Extreme Model I Atmosphere
XB = Best Model Atmosphere
A = Apollo Shape ($W/C_DA \approx 30$)
B = Discoverer Shape ($W/C_DA \approx 60$)

6.5 INTERNAL THERMODYNAMICS

6.5.1 Present Status and Major Accomplishments

Shield temperatures for the Venus vehicle have been calculated. Figures 6.5.1 and 6.5.2 are plots of maximum and minimum shield temperatures (T_{sMAX} and $T_{s\ MIN}$) versus kt/E for several values of α / E. One plot was made for S = 846 BTU/hr-ft^2 (at Venus), and another was made for S = 445 BTU/hr-ft^2 (at Earth). These plots were made assuming a vehicle of cylindrical shape with no internal heat generation and solar incidence perpendicular to the longitudinal axis. Figure 6.5.1 (S = 846 BTU/hr-ft^2) is the case which produces the greatest thermal gradients in the shield. A first cut at α/E values for the vehicle coating indicates that an overall value of $\alpha_o/\epsilon_o \approx 1 \pm .16$ is necessary for maintaining capsule temperature in the range 14°F is 160°F. Since the maximum allowable thermal to gradient in the shield (i.e., $T_{sMAX} - T_{s\ MIN}$) is limited to 300°F, this would mean that for $\frac{\alpha}{\epsilon} \approx 1.16$ a value of kt/E $\approx$ 1 would be necessary. This could be achieved by using a .02 inch thick pure magnesium shield liner (k $\approx$ 90 BTU/hr-ft^{2}F). For this condition (kt/E = 1), the extremes of T_s are:

$$T_{sMAX} = 790^oR = 330^oF \text{ at } S = 846 \text{ BTU/hr-ft}^2$$

$$T_{sMIN} = 490^oR = 30^oF \text{ at } S = 445 \text{ BTU/hr-ft}^2$$

However, this value of T_{sMIN} is not the worst case. The worst case may be evidenced when the solar flux is incident on the dome only (view angle = 0°).

Due to contact resistance between the dome and shield liners, essentially no heat is conducted from the dome to shield. Figure 6.5.3 shows the minimum shield temperature for this condition. It may be seen that in order to maintain the minimum shield temperature above -150°F (310°R), several possible combinations of ϵ_c, ϵ_{si} and ϵ_{so} exist. Since ϵ_c will probably be around .04 (due to entry requirements at Venus) and ϵ_{so} may become as large as .1, ϵ_{si} = .1 will be required.

6.5.2 Future Plans

Future plans will include examination of the three types of

temperature control systems which were proposed for the Mars vehicle. These are: 1) α/ε coating system, 2) α/ε control (clam-shell) system, and 3) superinsulation system. It appears that these same types of systems will be feasible for the Venus vehicle (Reference - Vol. I of report on work performed under JPL Contract #950226, "Suitability of the Discoverer and Nerv Entry Vehicle for Mars Atmospheric Entry").

Parametric curves of maximum and minimum capsule temperature ($T_{s\ max}$ and $T_{s\ min}$) versus $\varepsilon_e A T/\omega C_p$ for several values of (A_p/A_T) (α/ε) will be made. These will determine the allowable combinations of ε_e and α/ε which will maintain capsule temperature within the range 14°F to 160°F.

Capsule temperature during entry will be calculated and necessary thermal control methods will be determined.

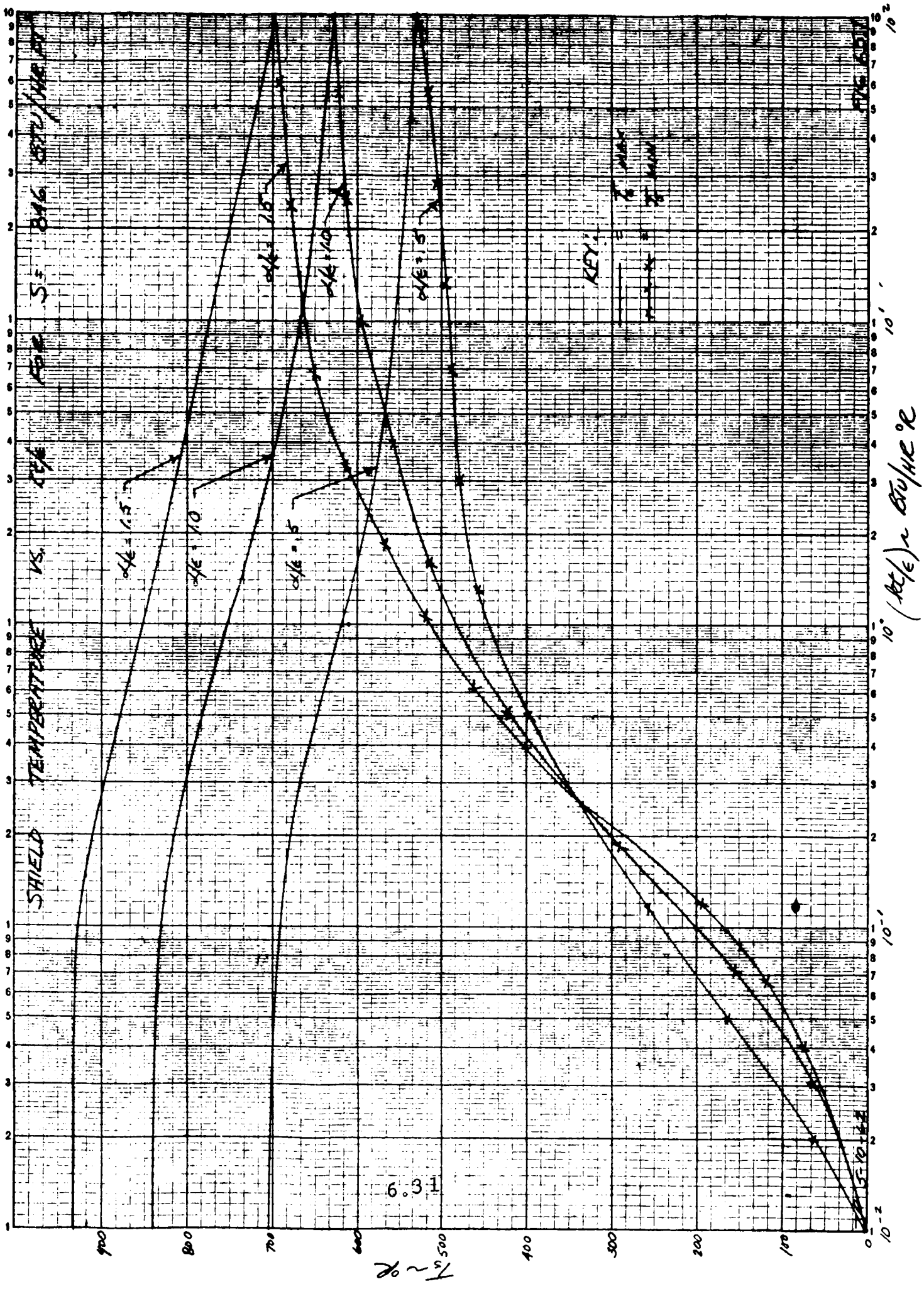
SHIELD TEMPERATURE VS. Kt/ε FOR S = 846 BTU/HR FT
α/ε = 1.5
α/ε = 1.0
α/ε = .5
KEY:
T_s ~ °R
(kt/ϵ) ~ BTU/HR °R
FIG 6.31

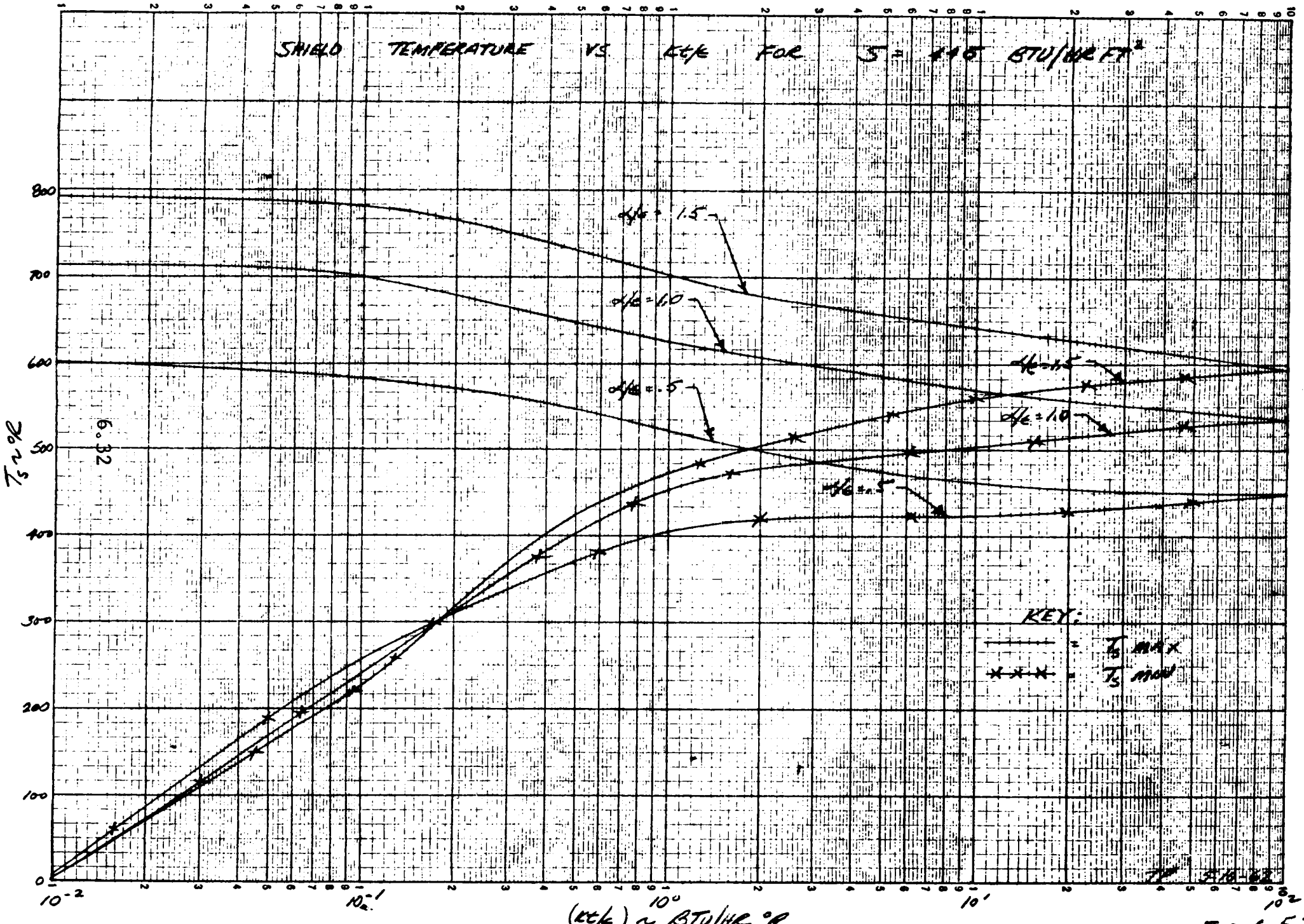
SHIELD TEMPERATURE VS. Kt/ε FOR S = 440 BTU/HR FT²
α/ε = 1.5
α/ε = 1.0
α/ε = .5
α/ε = 1.5
α/ε = 1.0
α/ε = .5
KEY:
= Ts MAX
= Ts MIN
Ts ~ °R
(Kt/ε) ~ BTU/HR °R
6.32

FIG 6.5.2

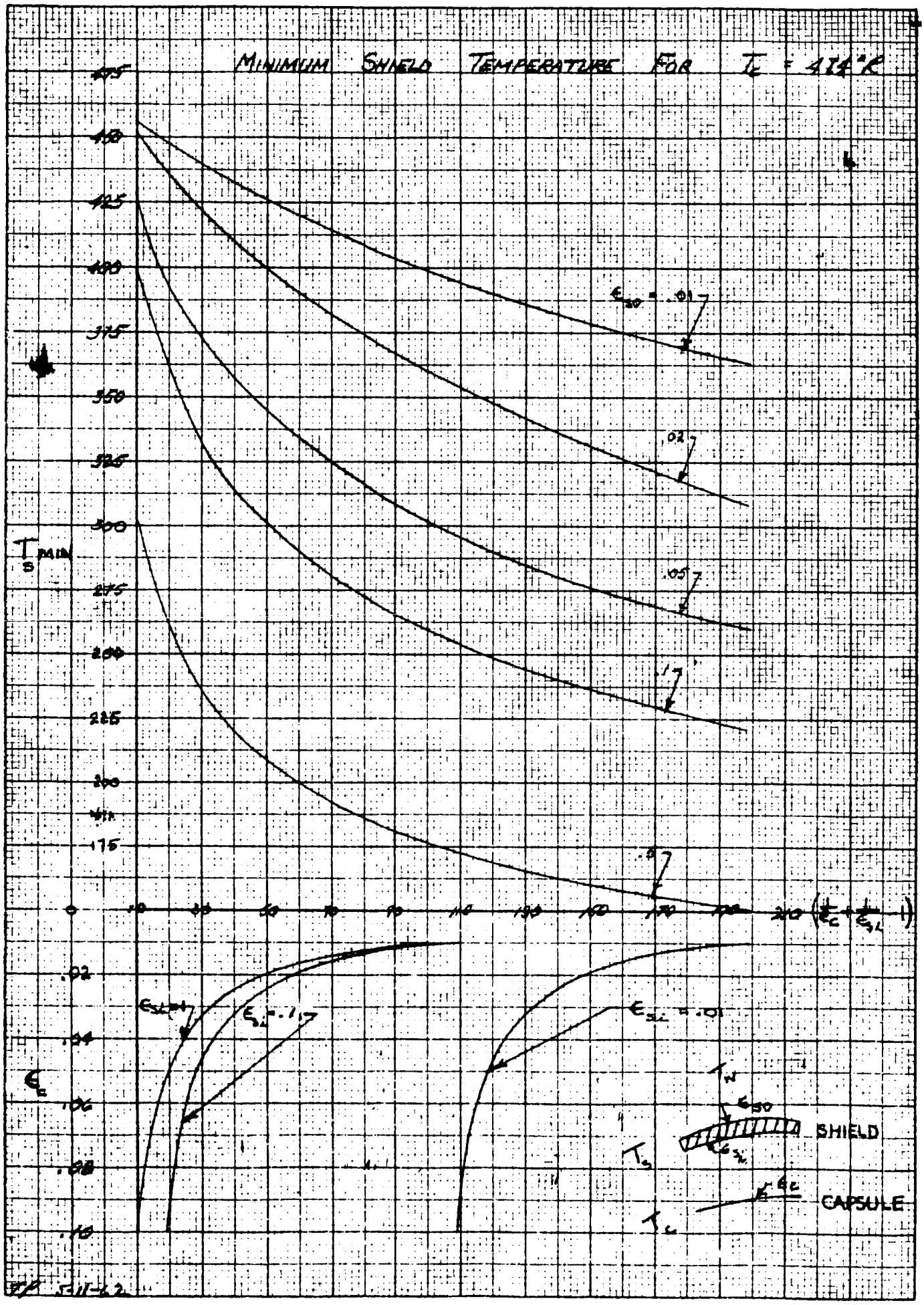
MINIMUM SHIELD TEMPERATURE FOR T_c = 414°K
$T_{s\,MIN}$
ϵ_{s0} = .01
.02
.05
.1
.5
ϵ_c
ϵ_{sL} = .1
ϵ_{sL} = .01
T_N
ϵ_{s0}
SHIELD
T_s
ϵ_{sL}
ϵ_c
CAPSULE
T_c

FIG. 6.5.3

NOMENCLATURE

k - thermal conductivity - BTU/hr-ft-^{o}F

t - shield thickness - ft.

E - emissivity - dimensionless

α - solar absorptivity - dimensionless

$\frac{\alpha}{E}$ - ratio of solar absorptivity to emissivity - dimensionless

S - solar heat flux per unit area - BTU/hr-ft^2

A - area - ft^2

E_e - effective emissivity (emissivity based on capsule and sink temperatures) - dimensionless

w - weight - lbm.

C_p - specific heat - BTU/lbm. ^{o}F

Subscripts

o - overall or outer

s - shield

i - initial or inner

p - projected

T - total

6.6 VEHICLE DESIGN

6.6.1 General

The vehicle design effort has been limited to a general survey of bonding materials and techniques, and a preliminary investigation of a suitable adapter section to support the capsule.

6.6.1.1 Bond Materials

Bonding materials which have been qualified for use on MSVD produced contractual products are listed in Table 6.6.1. These materials will be evaluated for environmental compatibility and use on a typical Venus capsule. In addition to these bonding materials, GE is presently developing and evaluating a unique bonding system which greatly exceeds the high and low temperature capabilities of existing bonding materials and promises to solve the bond problem caused by the differences in the thermal expansion, between most ablation materials and their supporting substructure when subjected to large temperature fluctuations. Details of this system are presently classified as "company confidential" but may be released by the end of this program.

6.6.1.2 Adapter Section

The adapter section investigation has been conducted to check physical compatibility with the field joint and available payload envelop, and to obtain a feel for adapter section weight which falls between 12 and 20 lbs. for vehicles weighing from 200 to 430 lbs. This figure will be refined during the second half of the study.

6.6.2 Future Plans

Future plans include a general design investigation of suitable structures for the three study configurations, including parametric presentations of vehicle structural weight vs. vehicle total weights, payload volume vs. total vehicle weight, structural and thermal protection and control component weight vs. entry angle and heat shield design.

TABLE 6.6.1

Item	Bond Designation	Bond Type	Use Classification*	Successful Applications	Environmental** Temp. for which qualified	Operating Temp. data	Remarks
1.	GE-M&P #50	Hard	Secondary Bond	Phenolic Nylon to Aluminum Substructure Phenolic Refrasil to Aluminum Substructure	0 F to +150 F	Classified	
2.	GE-M&P #1045	Hard	Secondary Bond	GE Century Series Ablators to Aluminum Substructure	+20 F to +140 F	Classified	Phenolic Type Resin
3.	Adlock	Hard	Primary Bond	Phenolic Nylon to Phenolic Glass In-Process bonding of other phenolic resin filled substructure to phenolic resin filled ablators	-100 F to 280 F	Classified	
4.	RTV 60	Soft	Secondary Bond	Phenolic Nylon Ablators to Magnesium and Aluminum Substructures	-35 F to +160 F	Classified	Requires adhesive primer which effects application to various materials
5.	R411 N Neoprene	Soft	Secondary Bond	GE 124A & Phenolic Nylon to Aluminum Substructures	-80 F to +160 F	Classified	Same as Item 4
6.	Polyurethane	Soft	Secondary Bond	GE 124A & Aluminum Sub structures	-100 F to +200 F	Classified	Same as Item 4

* Primary bond designates material used in-process fabrication of basic components. Secondary bond designates material used to join components after component fabrication.

** Environmental temperatures for which bonds are qualified are generally for storage and/or handling conditions and are not necessarily indicative of their capability during operation, but rather are specific contractual requirements.

6.7. STERILIZATION

6.7.1 Discussion

The ambitious United States program to explore the surface of the planets of our solar system has been made greatly complicated by the requirement to prevent contamination by terrestrial microorganisms. Associated with these requirements imposed by academicians wishing to explore more fuller understanding of the nature and origins of life as we know it, are the needs to insure high reliability of performance. These points have predicated the development of a vehicular design that can be sanitized and made sterile by proven techniques.

Basic sterilization criteria described by J.P.L. follow. These criteria are expected to remain in effect at least until sufficient data have been obtained and shown to offer feasible alternate solutions. Additional information concerning the biology and chemistry of the respective planets would have important implications.

6.7.1.2 Fly-by

"For fly-by missions in which the spacecraft or bus trajectory will be biased in order to avoid sterilization, the probability of impact can be no greater than 10^{-4} for Mars or 10^{-3} for Venus. The more stringent value for Mars reflects the belief that the Martian environment would be more hospitable to terrestrial organisms."

6.7.1.3 Landing or Atmospheric Contact

"Any spacecraft, capsule, or fragment thereof having a probability greater than 10^{-4} of contacting the planet Mars or its atmosphere must be rendered sterile prior to launch such that the over-all probability of a single organism arriving at Mars is no greater than 10^{-4} for an individual mission. The corresponding value for a Venus mission is 10^{-3}."

6.7.1.4 Booster Vehicle Disposition

"The probability of the boost vehicle's final stage impacting Mars or Venus must not exceed the values 10^{-4} or 10^{-3}, respectively (unless the final stage is to be sterilized).

In determining the probability of impact of the spacecraft or booster vehicle, all factors must be considered, including the reliability of any maneuver which could significantly affect the chances of impact."

6.7.1.2.1 Basic Approach to Sterilization of Mariner System

"For those missions requiring sterilization, the sterilization criteria demand the use of only the most effective and proven procedures applied with rigid controls. Based on this philosophy, the following essential steps for sterilization of Mariner have been established:

6.7.1.2.1.1 Assemble into final configuration the complete system required to be sterilized due to significant probability of contact with a planetary target.

6.7.1.2.1.2 Heat sterilize the complete system in its final configuration.

6.7.1.2.1.3 Conduct subsequent tests and calibrations by means of external contact only. Minimize surface contamination. Fill system fluids which could not be heated through bacteriological filters which have been sterilized as an integral part of the system. Filters subsequently removed.

6.7.1.2.1.4 Enclose sterile system within a bacteriologically sealed shroud envelope.

6.7.1.2.1.5 Surface sterilize shroud cavity with ethylene oxide gas mixture.

6.7.1.2.1.6 Introduce shroud purging and air conditioning gases through integrally sterilized bacteriological filter. Maintain positive pressure within the shroud during as much of the time as possible.

6.7.1.2.1.7 Maintain shroud seal until system is boosted safely above contamination which may exist in the Earth's atmosphere.

Should failure occur after heat sterilization, (1) the complete system would be replaced with a heat sterilized spare system, or (2) repairs would be made to individual components and the system again heat sterilized as a complete assembly."

6.7.1.2.2 Sterile Assembly

In order to accomplish the production of vehicles with long term reliability, the exploration of clean room procedures has been accelerated. By means of controlled environment areas with restricted access, contamination by particulate matter, fungi, molds and higher forms has been greatly reduced. The sterile assembly of space vehicles in such clean room facilities has yet to be accomplished. The prevailing philosophy at the J.P.L. is to avoid sterile assembly as a means for accomplishing a reentry vehicle compatable with the above requirements. These possibilities should, however, not be overlooked for certain components and subsystem assemblies.

6.7.1.2.3 Sterilization by Thermal Means

An extensive bibliography can be relied upon to substantiate the suitability of thermal measures to kill microorganisms. Heat soaking is by far the most feasible method compatable with known construction and assembly operations. A primary objective of the study has been to identify components which are incompatable with the effective periods of dry heat soaking. Studies performed with the microorganisms found in soil samples, vermiculite and sand (highest thermal resistance) indicated that temperatures of 125° C for 26 hours are necessary to insure a complete kill of microorganisms. The list of incompatable items has fortunately been rather short. Continued study will insure an accurate identification of troublesome components.

6.7.1.2.4 Gaseous Sterilization

The widespread application of ethylene oxide to sterilize fabrics, foodstuffs, cosmetics and delicate dressings has suggested the usefulness of this substance for the sterilization of space vehicles. Terminal applications of this material to the surface

of completed structures has been successful. Chemical reactions with spacecraft materials, motors and instruments has not been disclosed for long term applications.

A major stumbling block to a more extensive utilization of the gaseous sterilants has also been from the inability of this substance to permeate and thus sterilize the surfaces between joined sections. An effort is currently being applied to resolve these problems.

6.7.2 Problem Areas

The present list of subsystems on a Venus reentry capsule incapable of being sterilized by thermal means, reflect the findings already reported for the Mars capsule. At the time of this report, the design specifications of the Venus capsule have not been adequately described to identify specialized problems. At this time, the means to sterilize biologically oriented experiments seem particularly difficult. When the complete nature of these experiments are made available to this group, studies shall be commenced to obtain a workable solution.

6.7.2.1 Pyrotechnics

Literature study has disclosed that groups of charges are available with auto-ignition points below the temperatures needed for sterilization. It appears that thermal sterilization of selected pyrotechnics with provisions for pressure depreciation shall result in the production of explosive bolts, motors and attachments that can tolerate terminal thermal soaking.

6.7.2.2 Batteries

Power sources for the Venus capsule have not been revealed to this office. With the selection and grading of the the thermodynamic elements, compatability to heat sterilization methods shall be established. The General Electric Company has personnel available who have been active in this area on the Ranger Program. Discussion with George Hobby have suggested that separate sterilization of electrolytes, plates and containers prior to activation, is a feasible method.

6.7.2.3 Joined Surfaces

The undesirable characteristics of liquid sterilants employed to treat joints and mated surfaces has spurred increased effort to identify alternate solutions. Zone heating, sterile assembly and gaseous sterilants offer promising compromises to thermal methods when they are contra-indicated. Plans are being formulated to study the feasibility of gaskets which would permit sterilization with one of the gaseous mixtures of ethylene oxide. Ethylene oxide and freon 12 have been selected as the most desirable sterilizing mixture. This formulation must be specially prepared.

6.7.3 Future Plans

6.7.3.1 Meetings are scheduled with each of the subsystem study groups. Sterilization requirements shall be integrated with the particular problem areas.

6.7.3.2 Increased effort shall be applied to the identification of decelerating devices that will tolerate thermal sterilization methods.

6.7.3.3 Development of program to obtain additional information on long term effects of gaseous sterilants on materials peculiar to space vehicles, i.e., use of ETO on large volumes of solid fuels.

6.7.3.4 Formulas for dose calculations for dry heat sterilization by Wilmot Castle Co. shall be applied to design selection criteria.

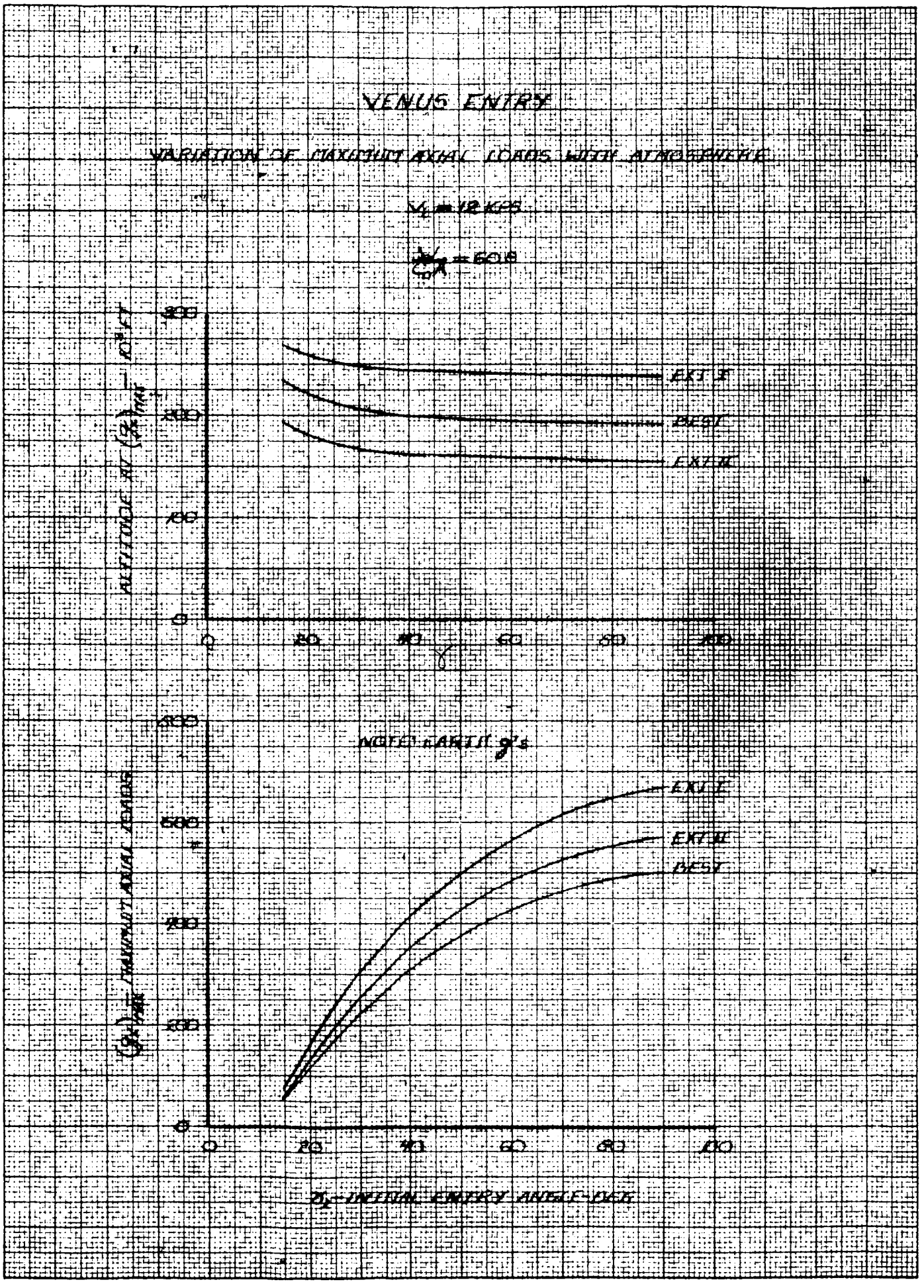
VENUS ENTRY
VARIATION OF MAXIMUM AXIAL LOADS WITH ATMOSPHERE
V_i = 12 KPS
$\frac{W}{C_D A}$ = 60.8
ALTITUDE AT $(g_x)_{MAX}$ — 10^3 FT
300
200
100
0
EXT I
BEST
EXT II
0
20
40
60
80
100
γ
NOTE: ARTH g's
$(g_x)_{MAX}$ — MAXIMUM AXIAL LOADS
800
600
400
200
0
EXT I
EXT II
BEST
0
20
40
60
80
100
γ_i — INITIAL ENTRY ANGLE-DEG

FIG. 6.1.1

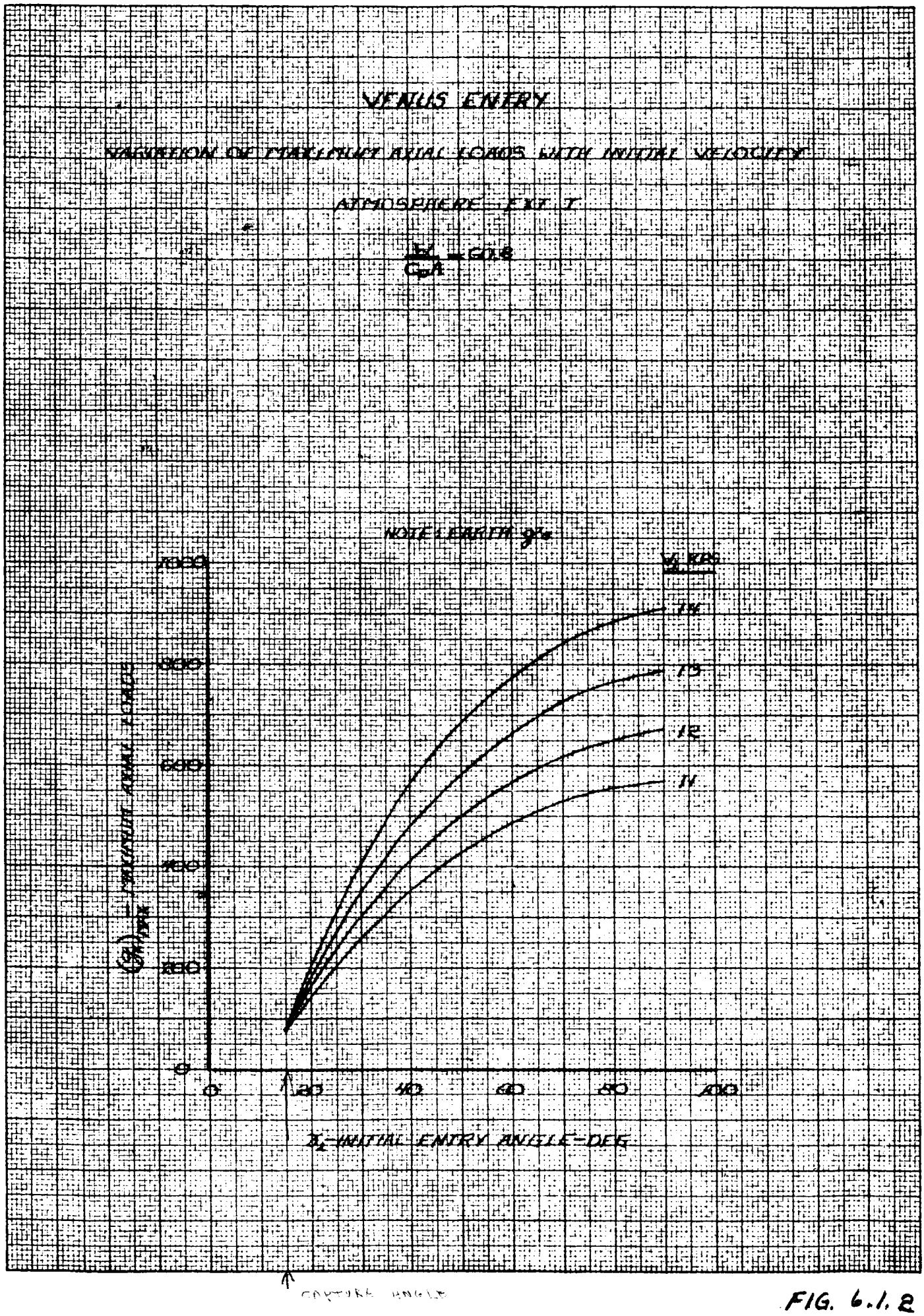
VENUS ENTRY
VARIATION OF MAXIMUM AXIAL LOADS WITH INITIAL VELOCITY
ATMOSPHERE - EXT. T
NOTE: EARTH g's
1000
800
600
400
200
0
0
20
40
60
80
100
14
13
12
11
INITIAL ENTRY ANGLE-DEG
CAPTURE ANGLE

FIG. 6.1.2

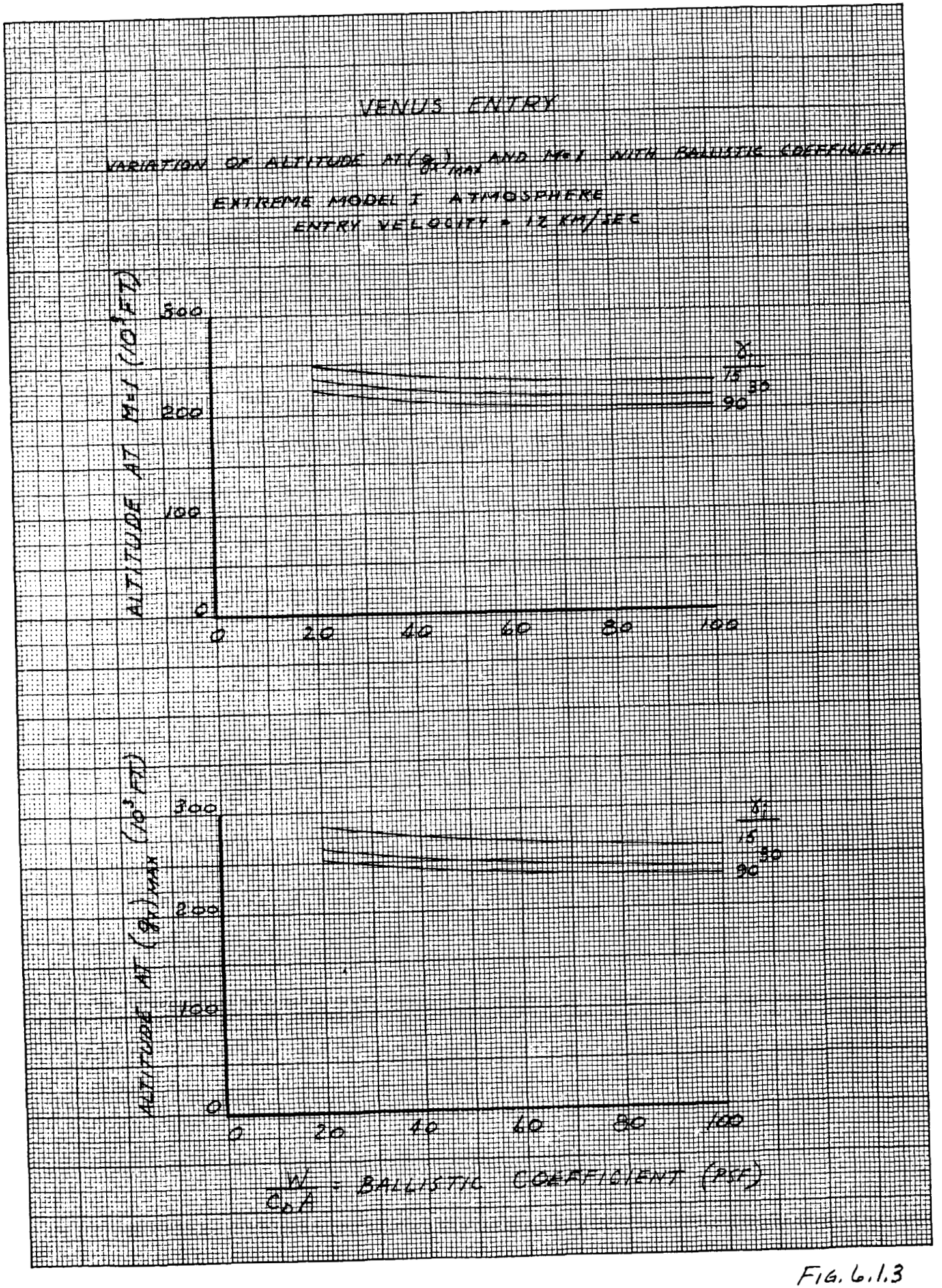
VENUS ENTRY
VARIATION OF ALTITUDE AT $(q_R)_{MAX}$ AND M=1 WITH BALLISTIC COEFFICIENT
EXTREME MODEL I ATMOSPHERE
ENTRY VELOCITY = 12 KM/SEC
ALTITUDE AT M=1 (10^3 FT)
500
200
100
0
0
20
40
60
80
100
γ_i
15
30
90
ALTITUDE AT $(q_R)_{MAX}$ (10^3 FT)
300
200
100
0
0
20
40
60
80
100
γ_i
15
30
90
$\frac{W}{C_D A}$ = BALLISTIC COEFFICIENT (PSF)

FIG. 6.1.3

VENUS ENTRY

VARIATION OF SUBSONIC TIME WITH BALLISTIC COEFFICIENT

EXTREME MODEL 1 ATMOSPHERE

V_i = 12 KILOMETERS/SECOND

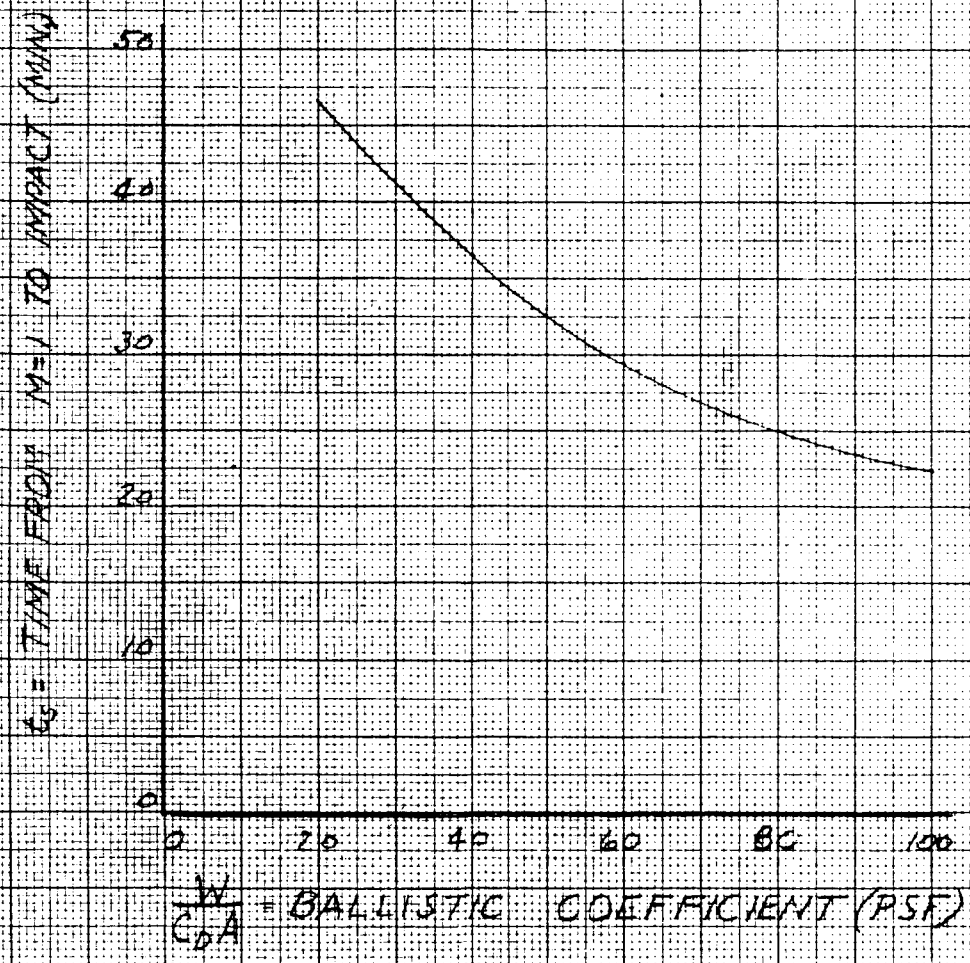

FIG. 6.1.4

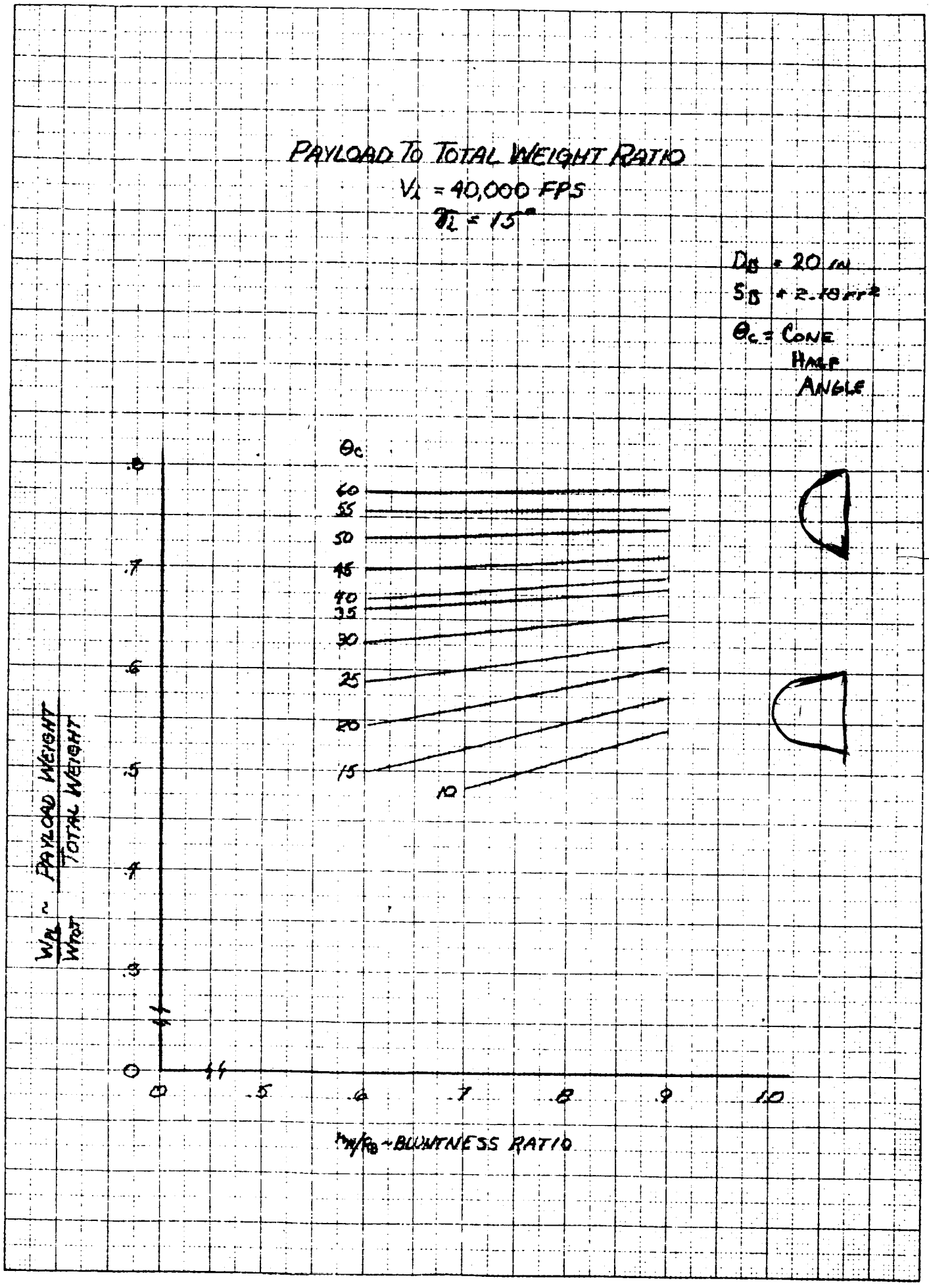
PAYLOAD TO TOTAL WEIGHT RATIO
V_L = 40,000 FPS
γ_L = 15°
D_B = 20 in
S_B = 2.18 ft²
θ_c = CONE HALF ANGLE
θ_c
60
55
50
45
40
35
30
25
20
15
10
20"
W_{PL}/W_{TOT} ~ PAYLOAD WEIGHT / TOTAL WEIGHT
0
.3
.4
.5
.6
.7
.8
0
.5
.6
.7
.8
.9
1.0
r_N/r_B ~ BLUNTNESS RATIO

FIG. 6.1.5

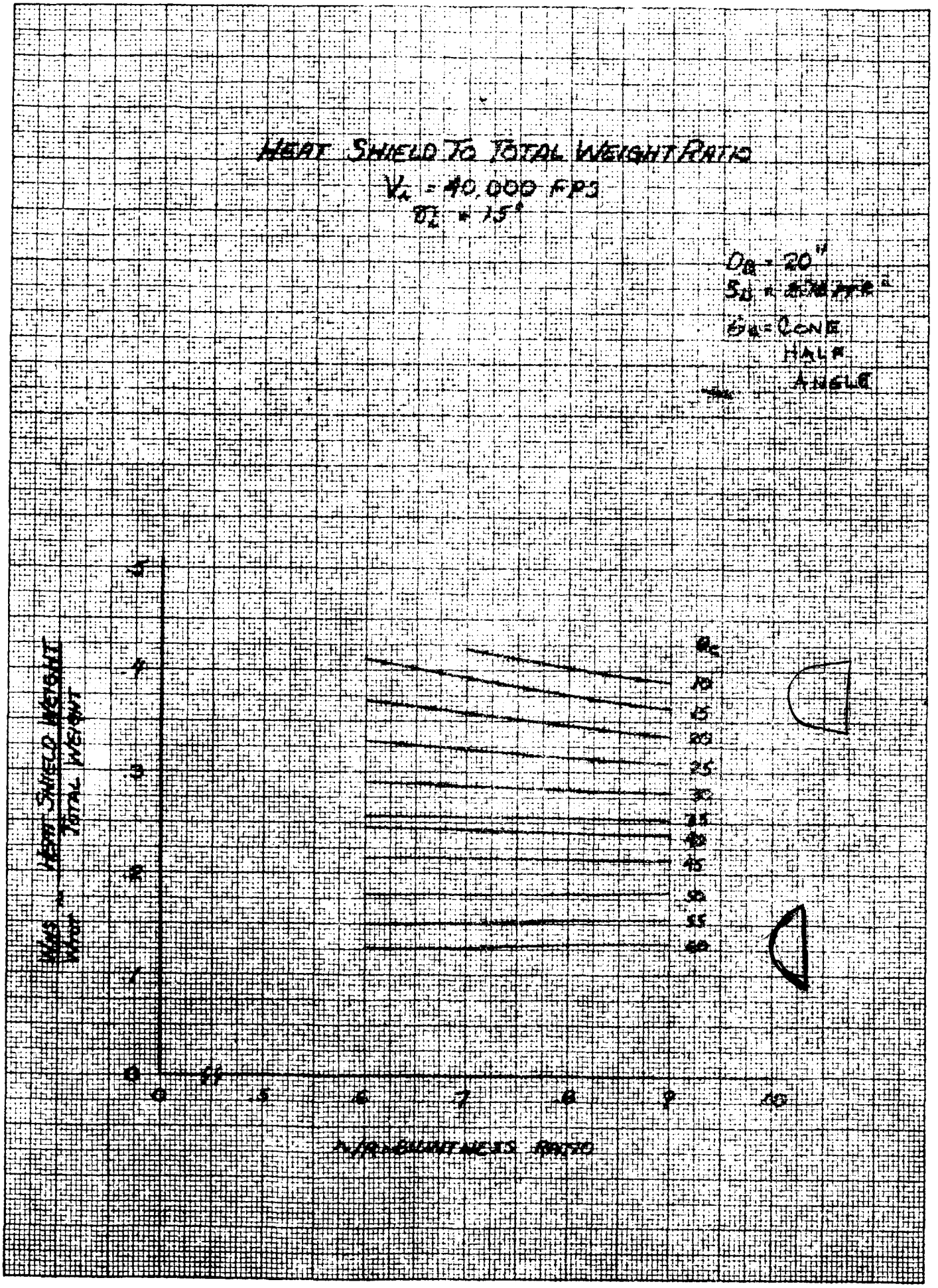
HEAT SHIELD TO TOTAL WEIGHT RATIO
V_i = 40,000 FPS
θ_i = 15°
D_B = 20"
S_B = [illegible]
θ_B = CONE HALF ANGLE
θ_c
10
15
20
25
30
35
40
45
50
55
60
W_{HS}/W_{TOT} = HEAT SHIELD WEIGHT / TOTAL WEIGHT
.4
.3
.2
.1
0
.4
.5
.6
.7
.8
.9
1.0
NOSEBLUNTNESS RATIO

FIG. 6.1.6

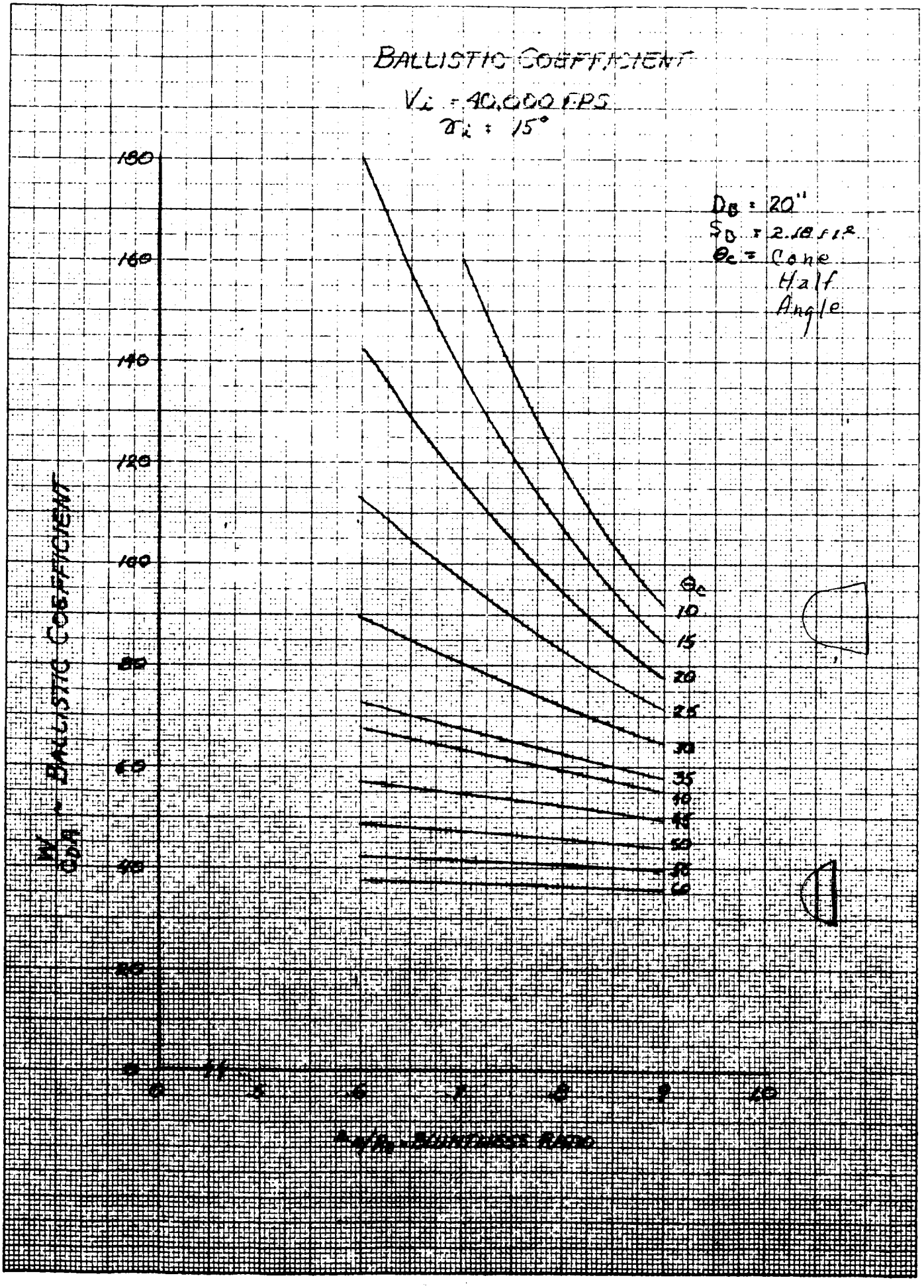
BALLISTIC COEFFICIENT
V_i = 40,000 FPS
γ_i = 15°
D_B = 20"
S_B = 2.18 ft²
θ_c = Cone Half Angle
θ_c
10
15
20
25
30
35
40
45
50
55
60
180
160
140
120
100
80
60
40
20
0
.5
.6
.7
.8
.9
1.0
$\frac{W}{C_D A}$ - BALLISTIC COEFFICIENT
Δ_a/R_a - BLUNTNESS RATIO

FIG. 6.1.7

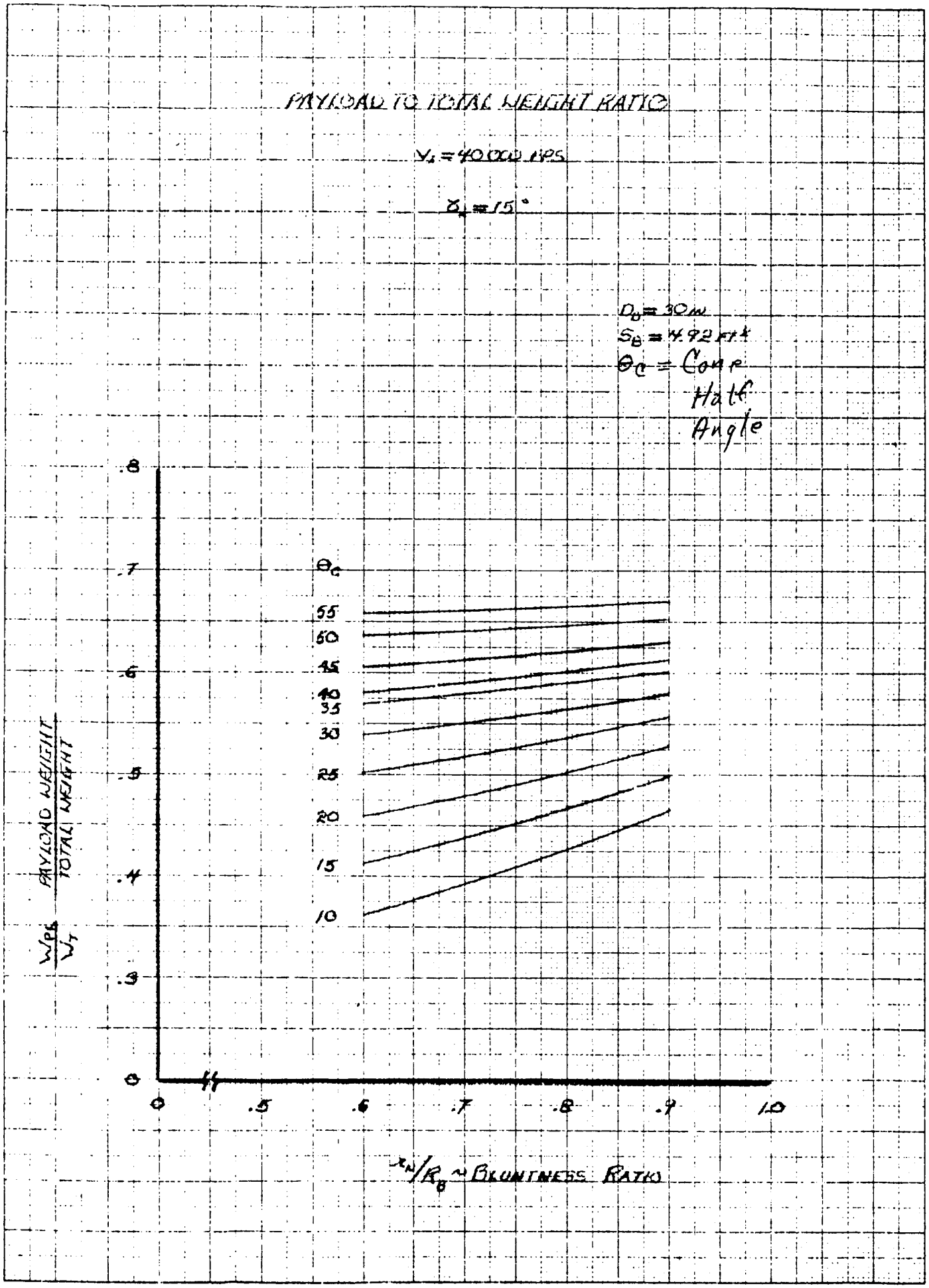
PAYLOAD TO TOTAL WEIGHT RATIO
$V_i = 40000$ FPS
$\gamma_i = 15°$
$D_B = 30$ IN
$S_B = 4.92$ FT²
θ_C = Cone Half Angle
θ_C
55
50
45
40
35
30
25
20
15
10
.8
.7
.6
.5
.4
.3
0
W_{PL}/W_T PAYLOAD WEIGHT / TOTAL WEIGHT
0
.5
.6
.7
.8
.9
1.0
r_N/R_B ~ BLUNTNESS RATIO

FIG. 6.1.8

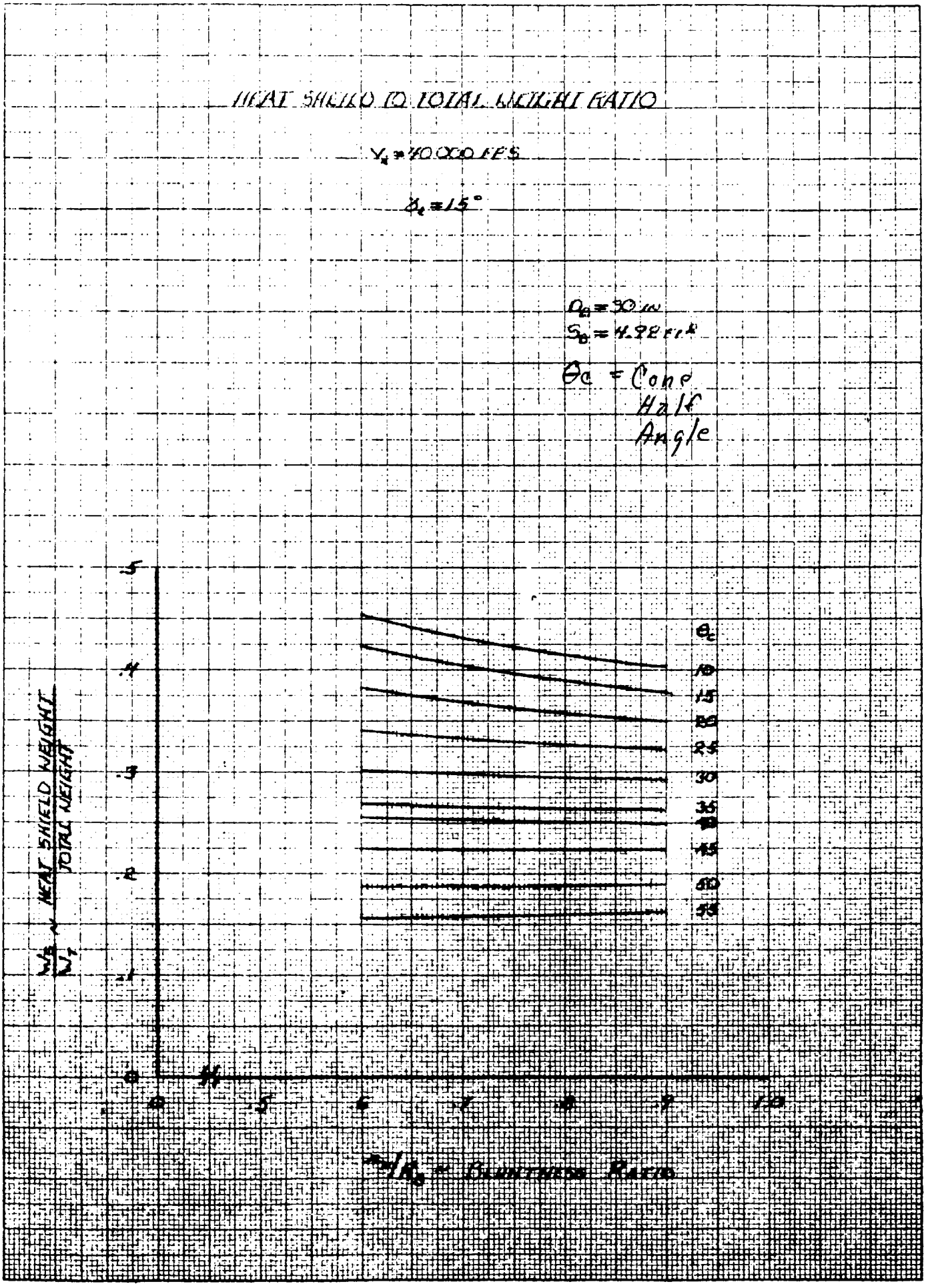
HEAT SHIELD TO TOTAL WEIGHT RATIO
V_E = 40 000 FPS
γ_E = 15°
D_B = 30 in
S_B = 4.98 ft²
θ_c = Cone Half Angle
W_S ~ HEAT SHIELD WEIGHT
W_T TOTAL WEIGHT
.5
.4
.3
.2
.1
0
.4
.5
.6
.7
.8
.9
1.0
θ_c
10
15
20
25
30
35
40
45
50
55
m/K_D ~ BLUNTNESS RATIO

FIG. 6.1.9

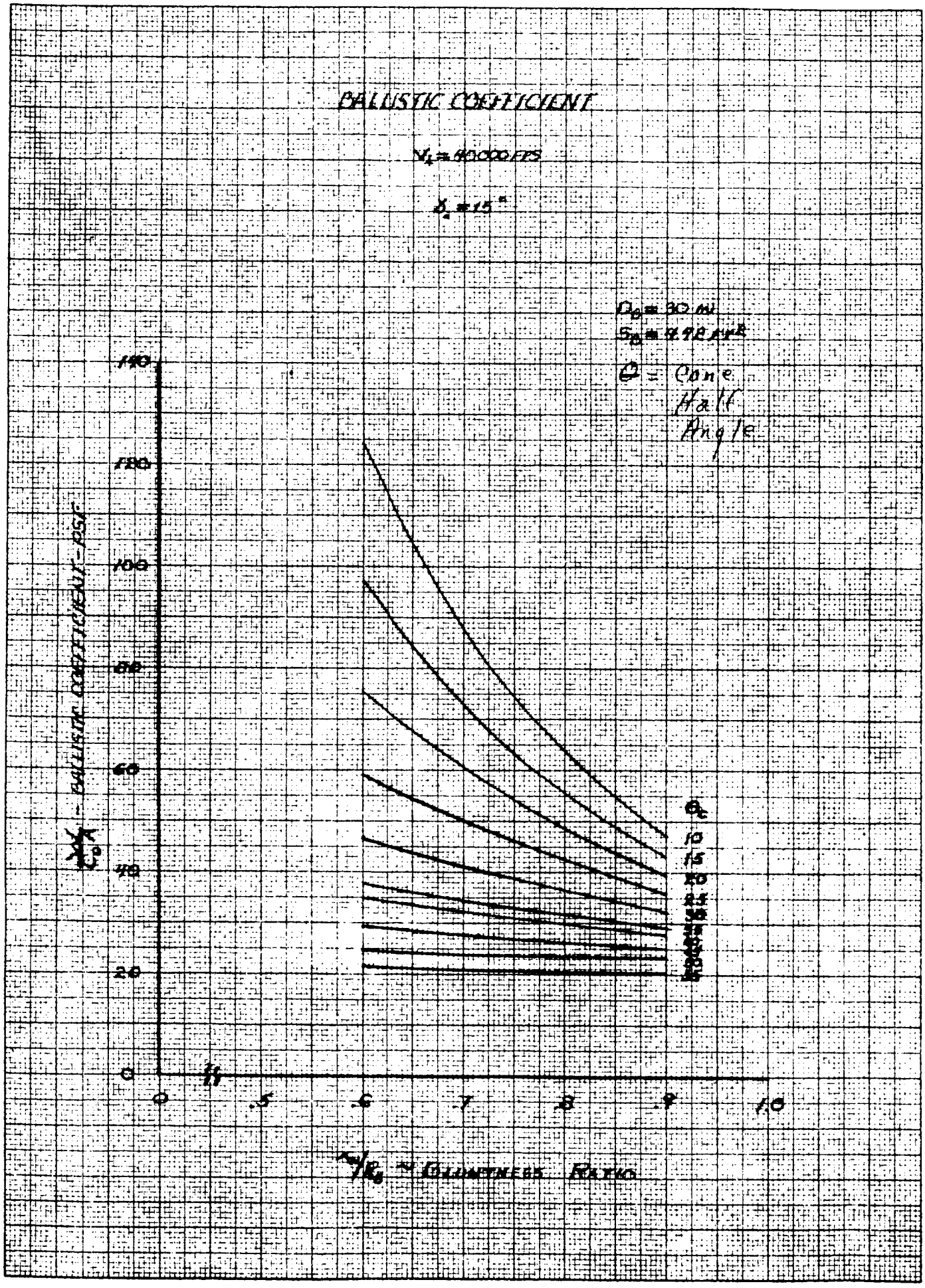
BALLISTIC COEFFICIENT
V_1 = 40000 FPS
γ_c = 15°
D_0 = 30 in
S_0 = 4.92 ft²
θ = Cone Half Angle
θ_c
10
15
20
25
30
140
120
100
80
60
40
20
0
0
.5
.6
.7
.8
.9
1.0
BALLISTIC COEFFICIENT - PSF
BLUNTNESS RATIO

FIG. 6.1.10

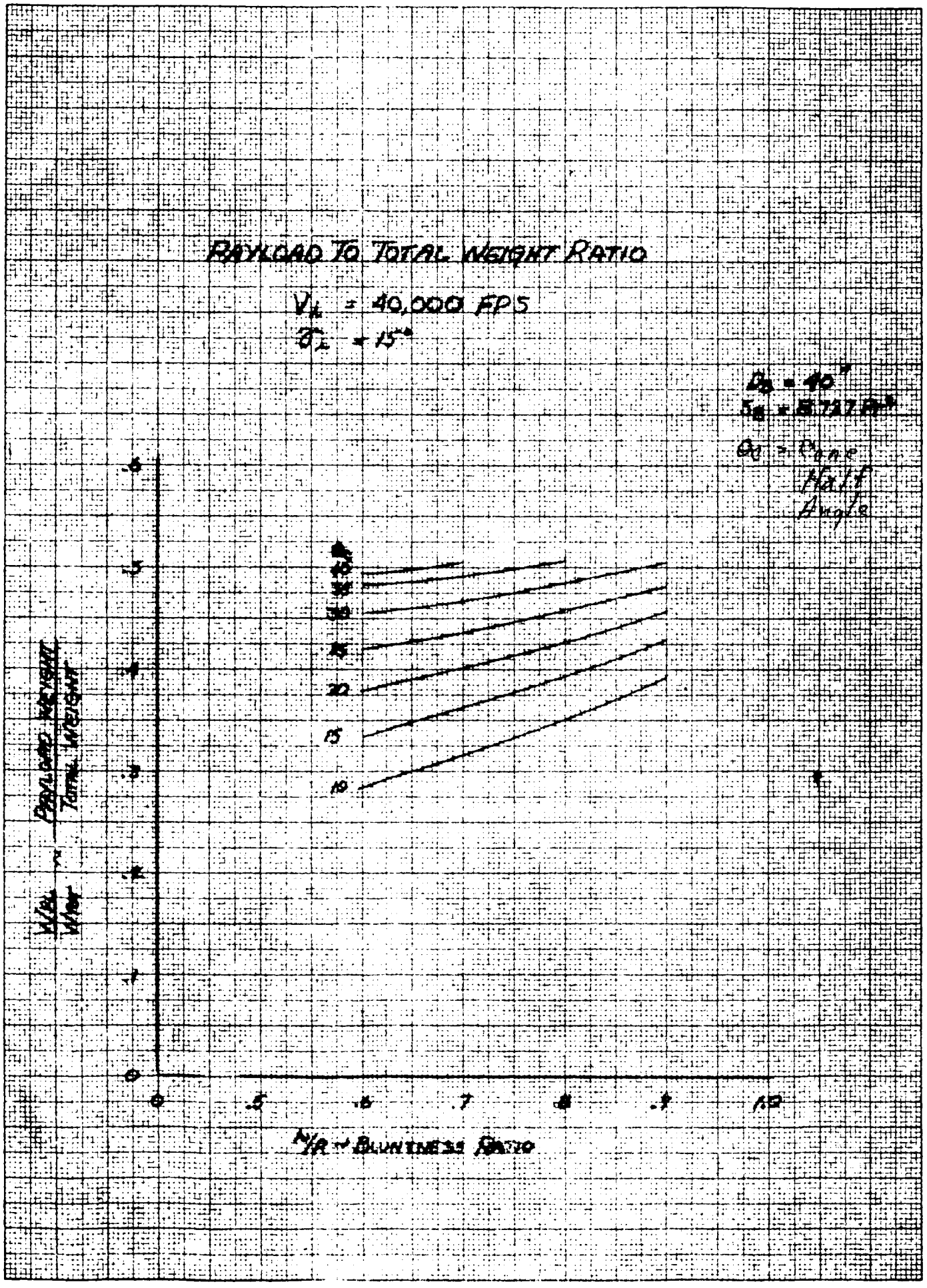
PAYLOAD TO TOTAL WEIGHT RATIO
V_L = 40,000 FPS
σ_L = 15°
D_B = 40"
S_B = 8.727 Ft²
θ_c = Cone Half Angle
40
35
30
25
20
15
10
.6
.5
.4
.3
.2
.1
0
$\frac{W_{BL}}{W_{TOT}}$ ~ $\frac{\text{PAYLOAD WEIGHT}}{\text{TOTAL WEIGHT}}$
0
.5
.6
.7
.8
.9
1.0
N/R ~ BLUNTNESS RATIO

FIG. 6.1.11

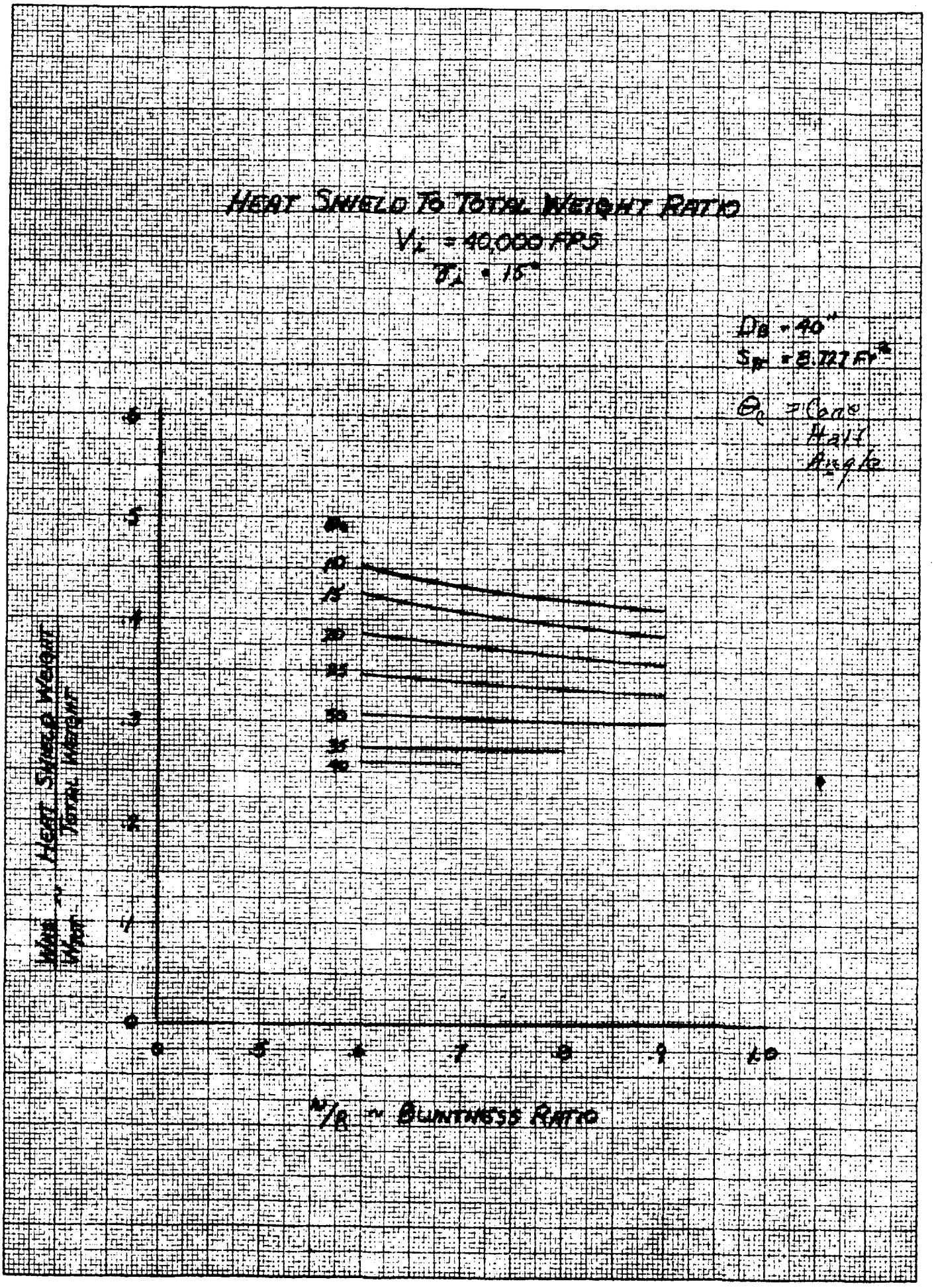
HEAT SHIELD TO TOTAL WEIGHT RATIO
V_i = 40,000 FPS
γ_i = 15°
D_B = 40"
S_p = 8.727 FT²
θ_c = Cone Half Angle
θ_c
10
15
20
25
30
35
40
.6
.5
.4
.3
.2
.1
0
0
.5
.6
.7
.8
.9
1.0
W_{HS}/W_{TOT} ~ HEAT SHIELD WEIGHT / TOTAL WEIGHT
N/R ~ BLUNTNESS RATIO

FIG. 6.1.12

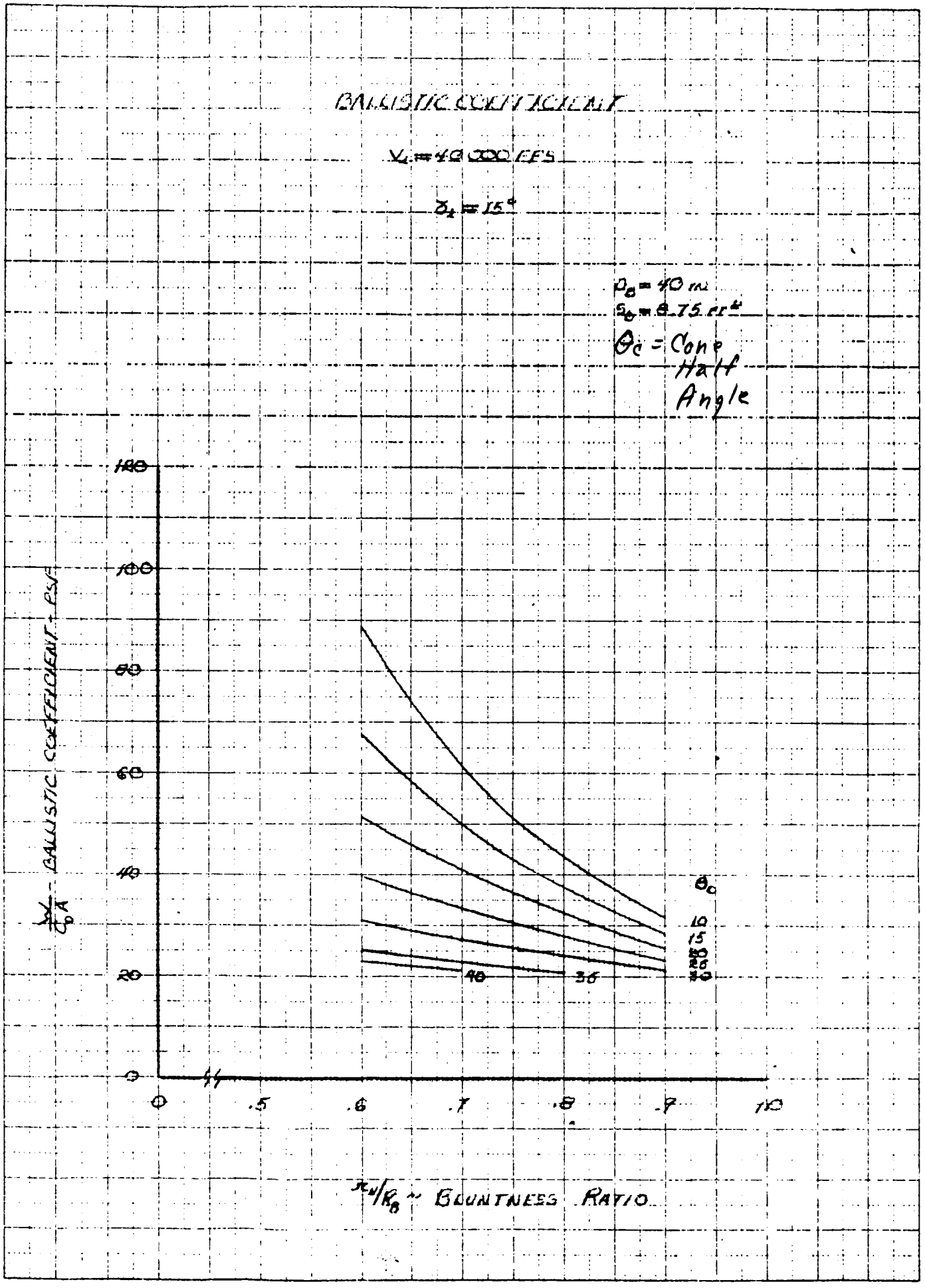
BALLISTIC COEFFICIENT
$V_1 = 40\,000$ FPS
$\gamma_1 = 15°$
$D_B = 40$ in
$S_B = 8.75$ ft²
θ_c = Cone Half Angle
$\frac{W}{C_D A}$ - BALLISTIC COEFFICIENT - PSF
120
100
80
60
40
20
0
0
.5
.6
.7
.8
.9
1.0
θ_c
10
15
20
30
40
36
r_N/R_B ~ BLUNTNESS RATIO

FIG. 6.1.13

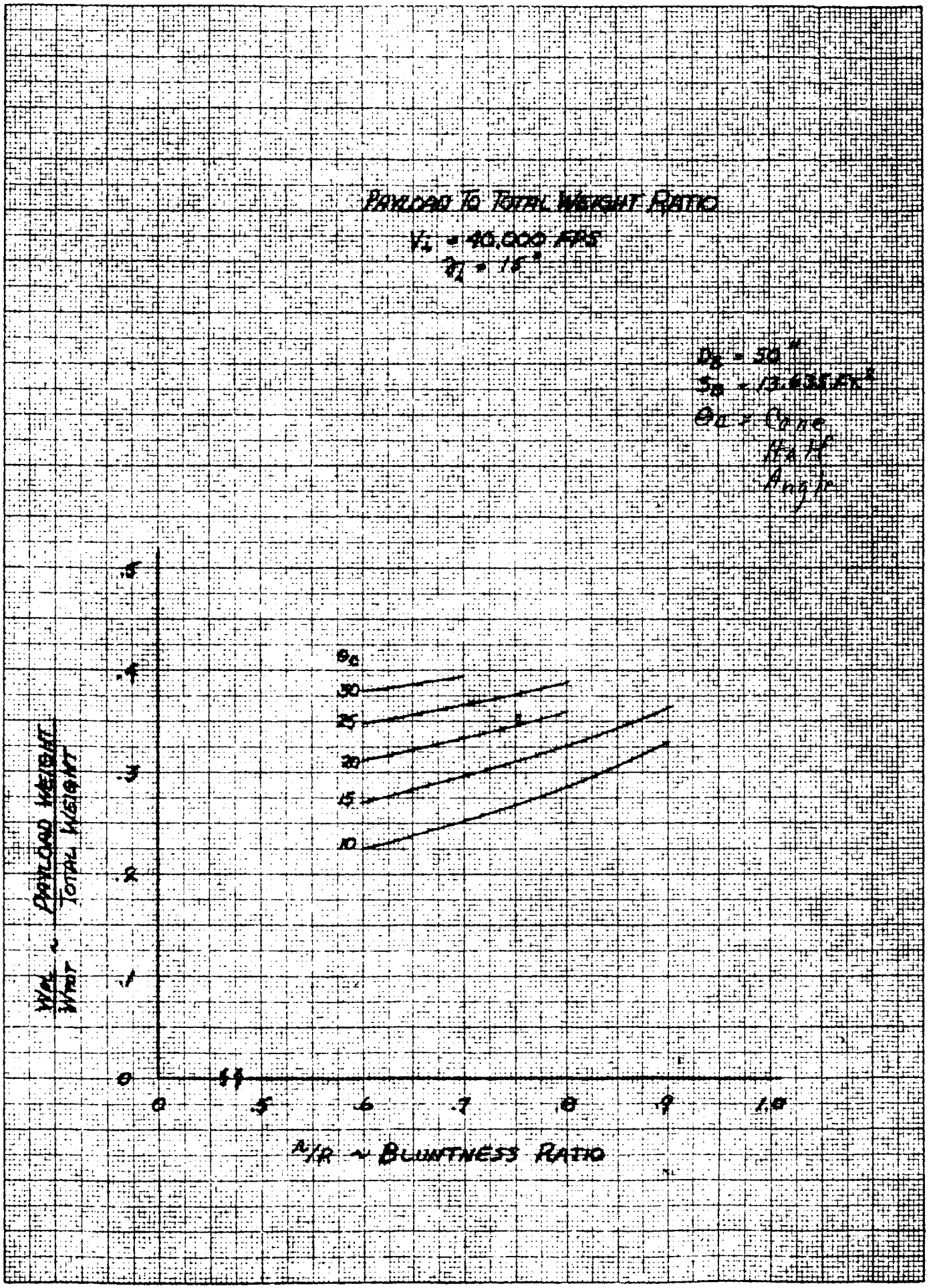
PAYLOAD TO TOTAL WEIGHT RATIO
V_i = 40,000 FPS
γ_i = 15°
D_B = 50"
S_B = 13.635 FT²
θ_c = Cone Half Angle
θ_c
30
25
20
15
10
.5
.4
.3
.2
.1
0
0
.5
.6
.7
.8
.9
1.0
W_{PL}/W_{TOT} ~ PAYLOAD WEIGHT / TOTAL WEIGHT
r/R ~ BLUNTNESS RATIO

FIG. 6.1.14

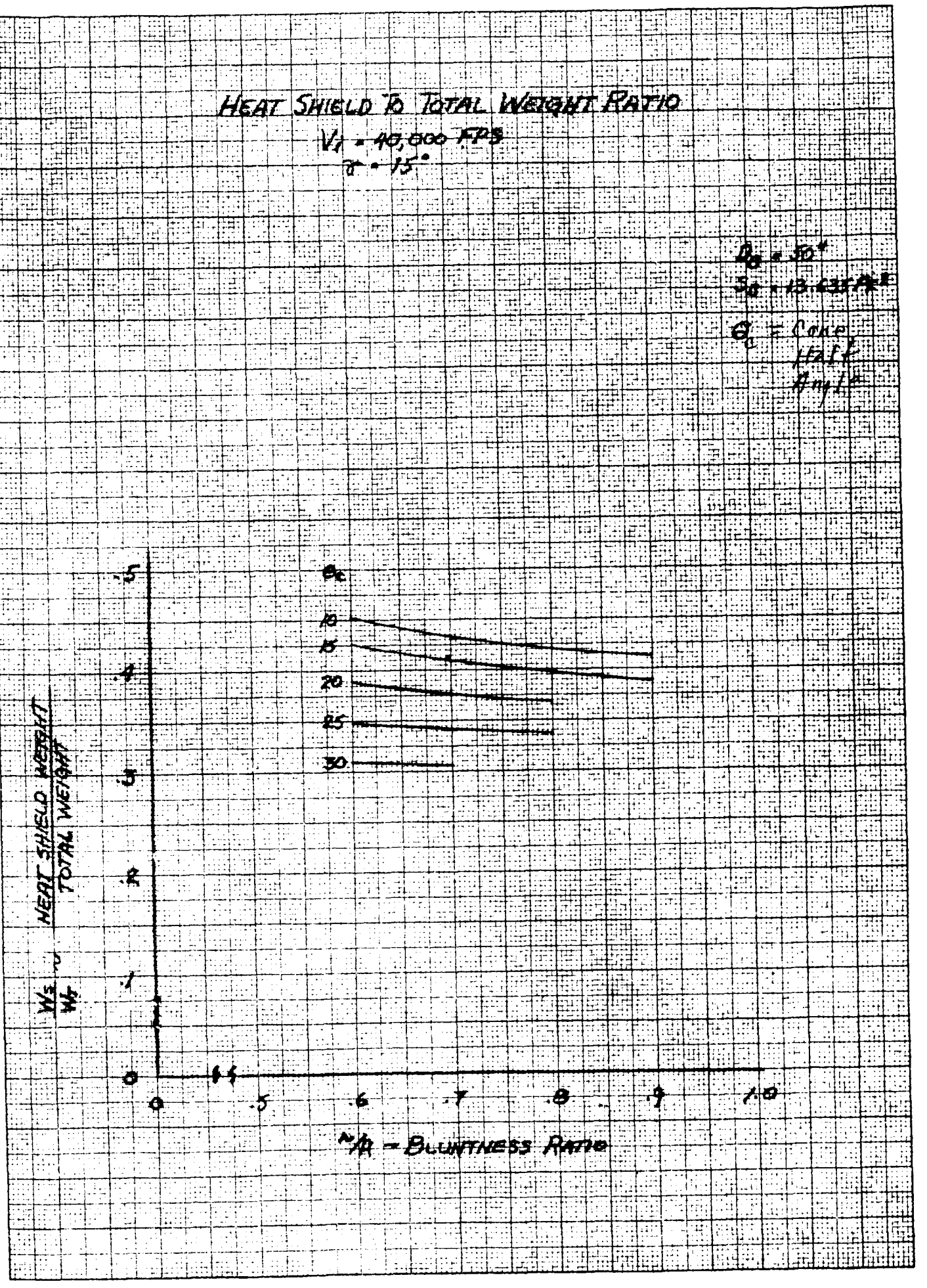
HEAT SHIELD TO TOTAL WEIGHT RATIO
V_1 = 40,000 FPS
γ = 15°
θ_c = 50°
S_0 = 13.635 ft²
θ_c = Cone Half Angle
θ_c
10
15
20
25
30
W_s/W_t ~ HEAT SHIELD WEIGHT / TOTAL WEIGHT
.5
.4
.3
.2
.1
0
0
.5
.6
.7
.8
.9
1.0
r/R - BLUNTNESS RATIO

FIG. 6.1.15

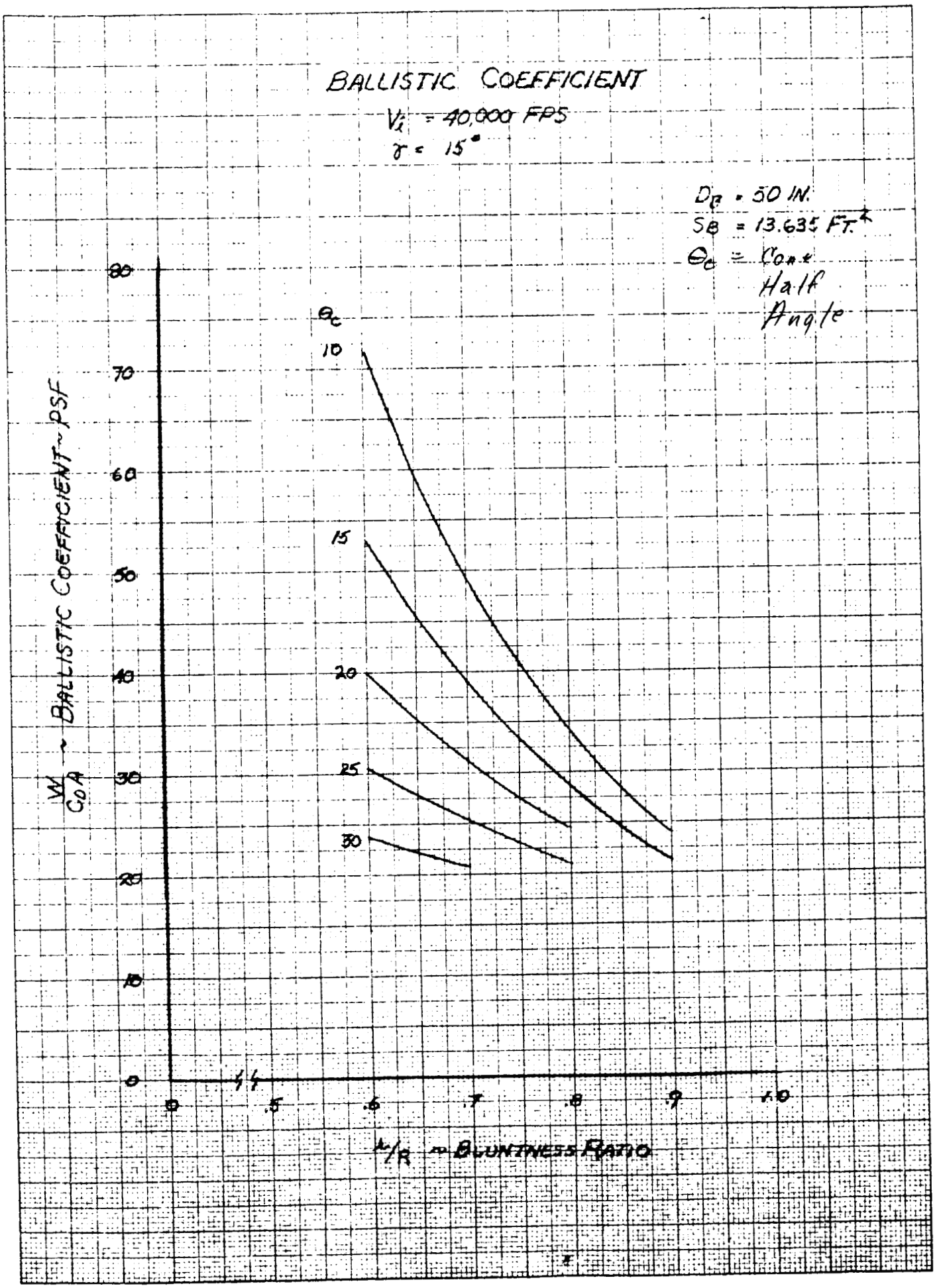
BALLISTIC COEFFICIENT
V_i = 40,000 FPS
γ = 15°
D_B = 50 IN.
S_B = 13.635 FT.²
θ_c = Cone Half Angle
θ_c
10
15
20
25
30
$\frac{W}{C_D A}$ ~ BALLISTIC COEFFICIENT ~ PSF
0
10
20
30
40
50
60
70
80
0
.5
.6
.7
.8
.9
1.0
h/R ~ BLUNTNESS RATIO

FIG. 6.1.16

VENUS -MARS ENTRY CAPSULE

DISCOVERER TYPE

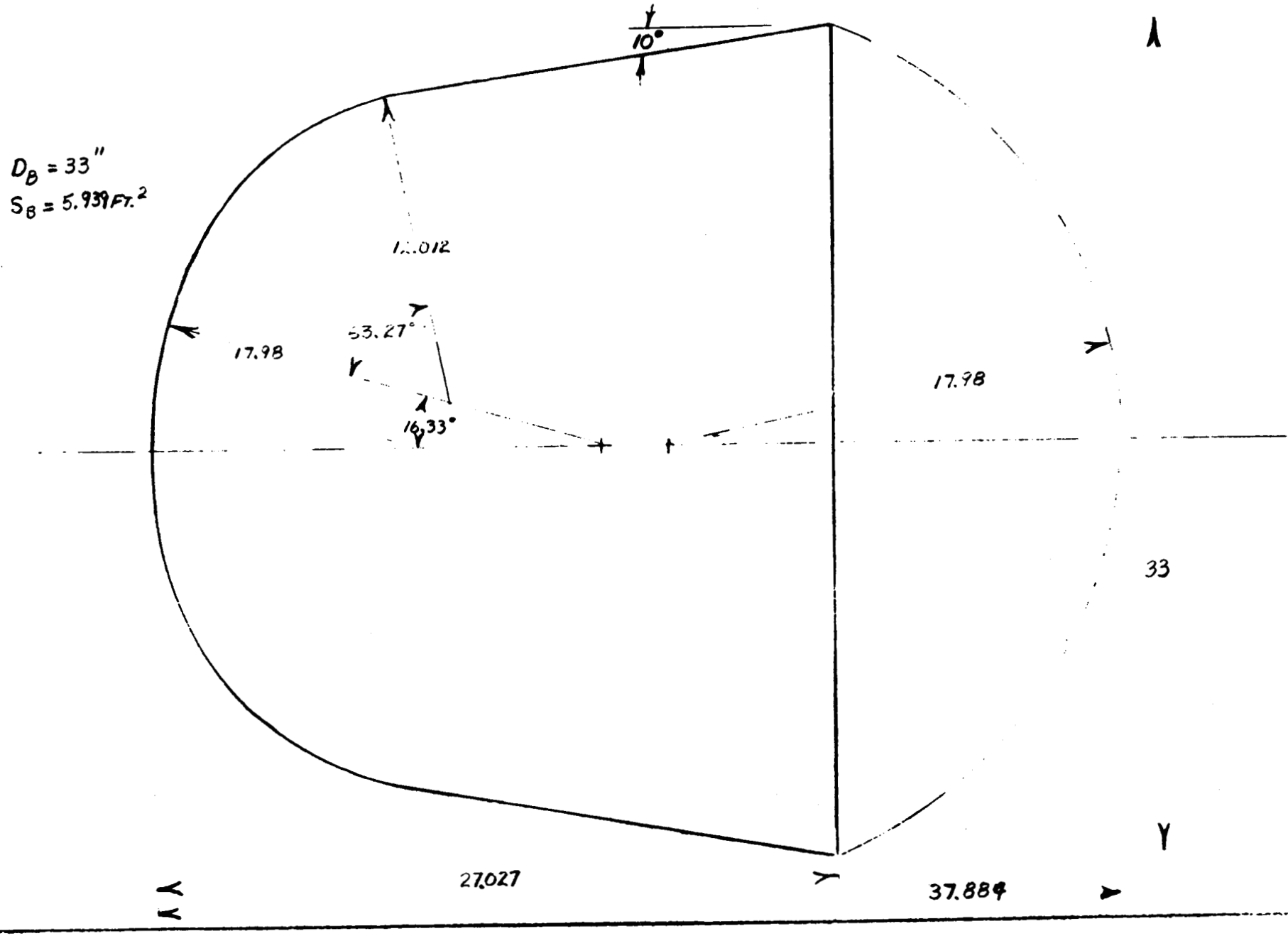

FIG. 6.1.17

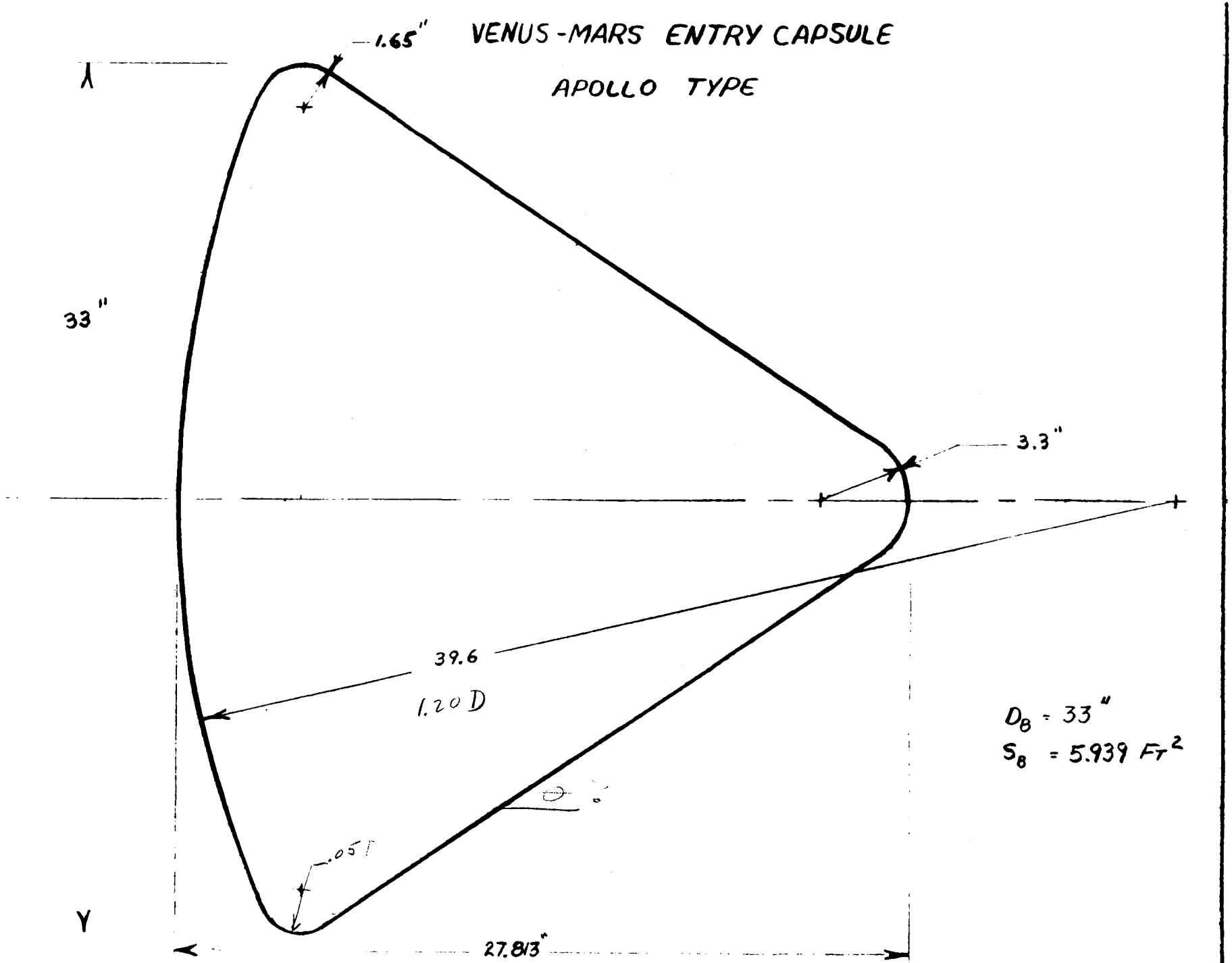
VENUS-MARS ENTRY CAPSULE
APOLLO TYPE
1.65"
X
33"
3.3"
39.6
1.20 D
.05 D
Y
27.813"
D_B = 33"
S_B = 5.939 FT^2

FIG. 6.1.18

VENUS-MARS ENTRY CAPSULE

CONE-FLARE TYPE

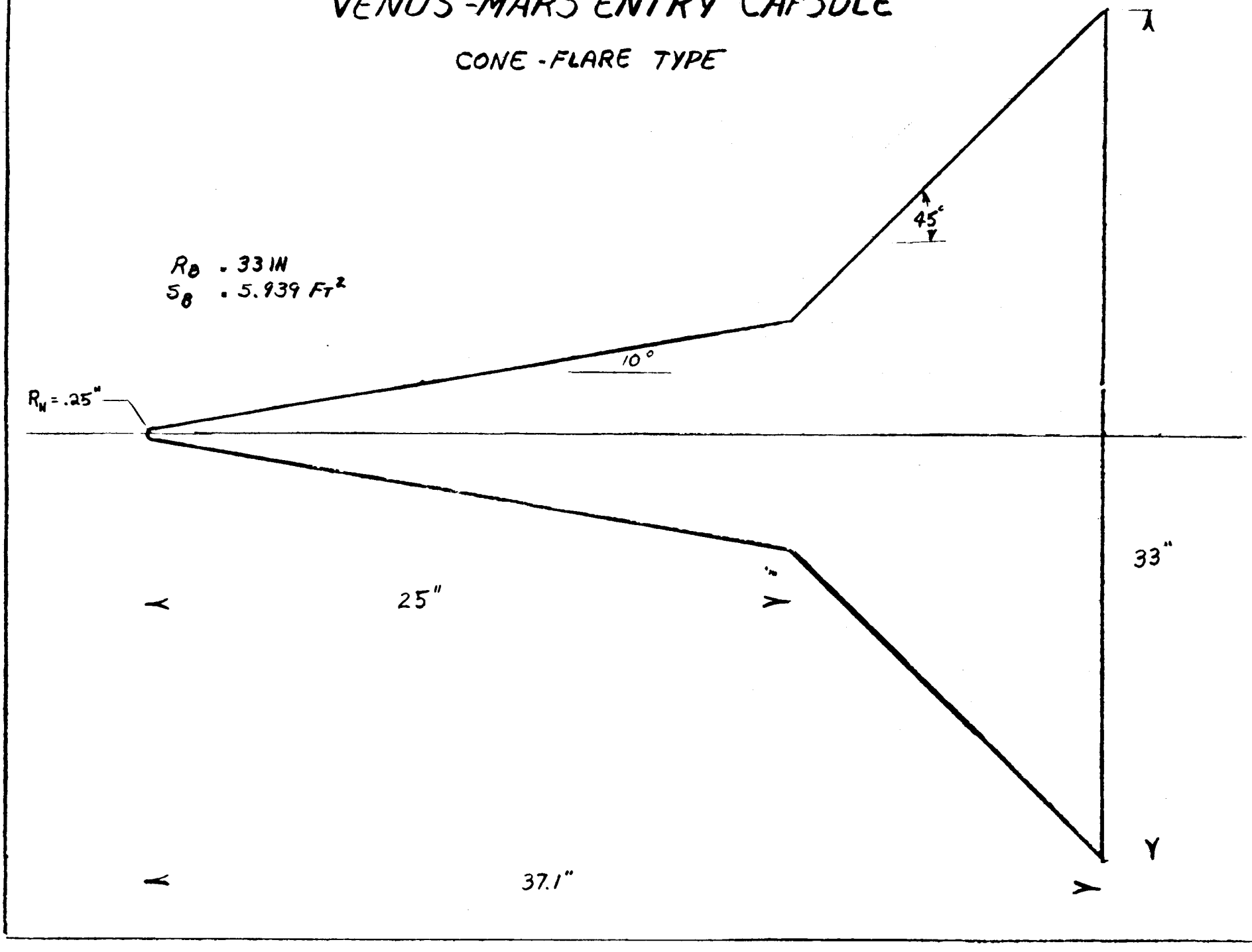

FIG. 6.1.19

FIG. 6.2.1

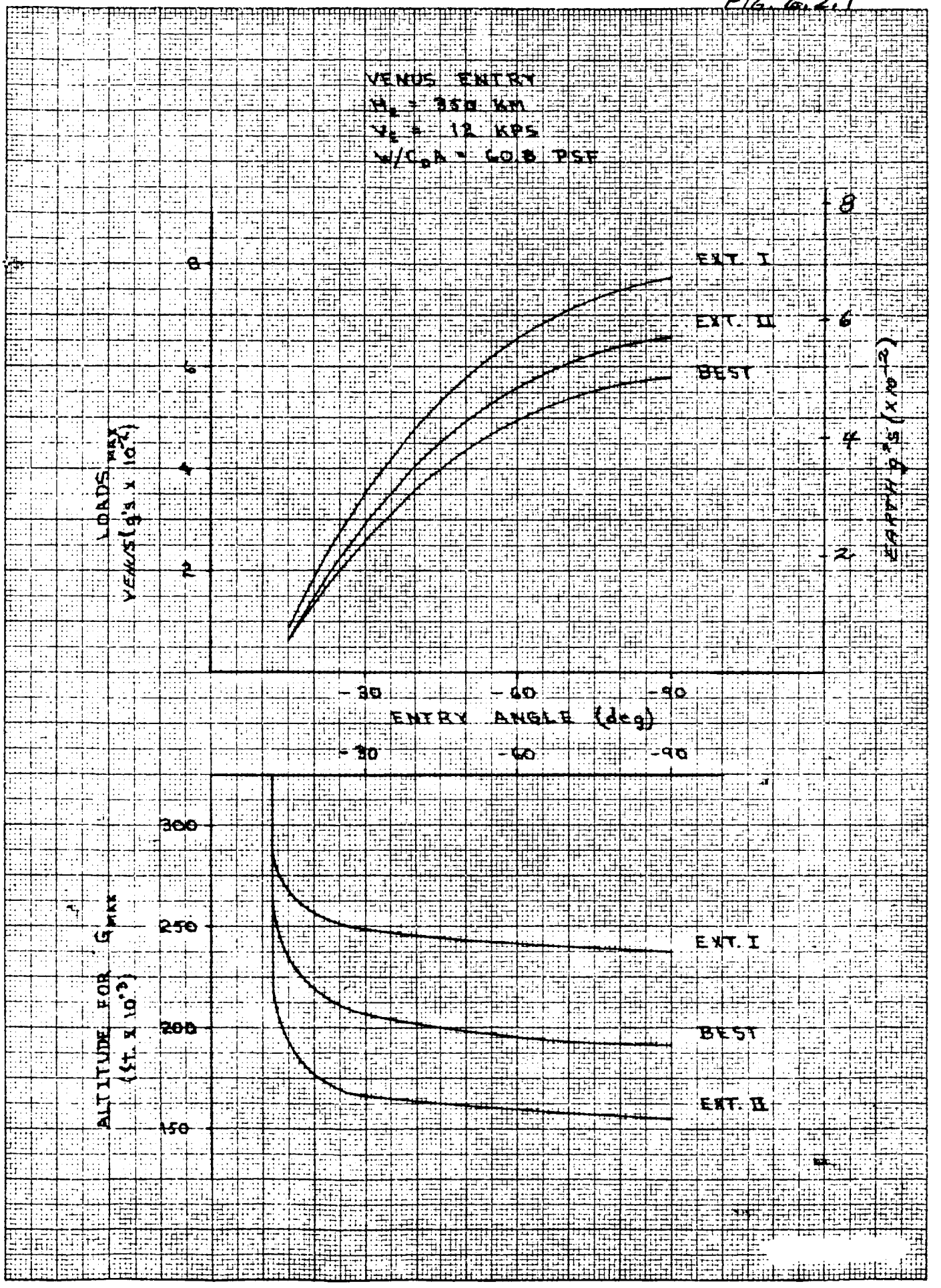

VENUS ENTRY
H_E = 350 KM
V_E = 12 KPS
W/C_DA = 60.8 PSF
EXT. I
EXT. II
BEST
LOADS MAX
VENUS (g's x 10^{-2})
EARTH g's (x 10^{-2})
8
6
4
2
-30
-60
-90
ENTRY ANGLE (deg)
ALTITUDE FOR G_{MAX}
(ft. x 10^{-3})
300
250
200
150

SKETCH 6.2.1

APPROACH GEOMETRY

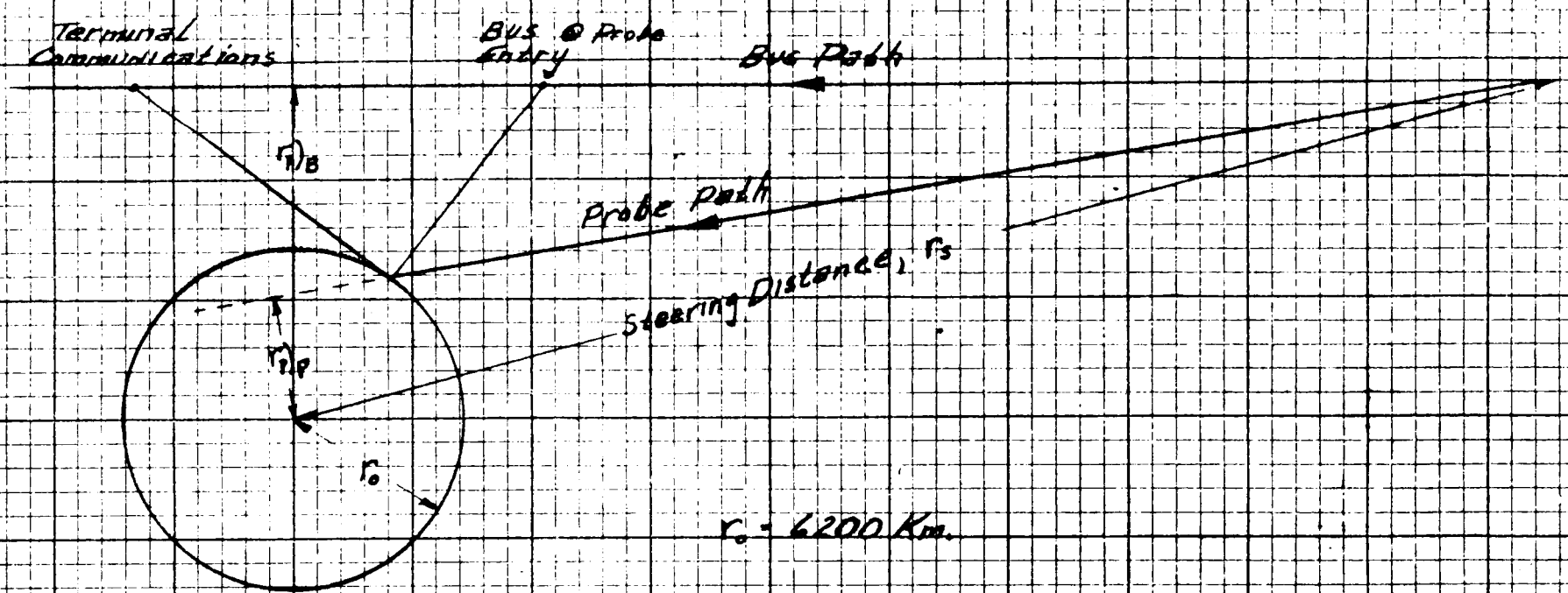

Fig. 6.2.2

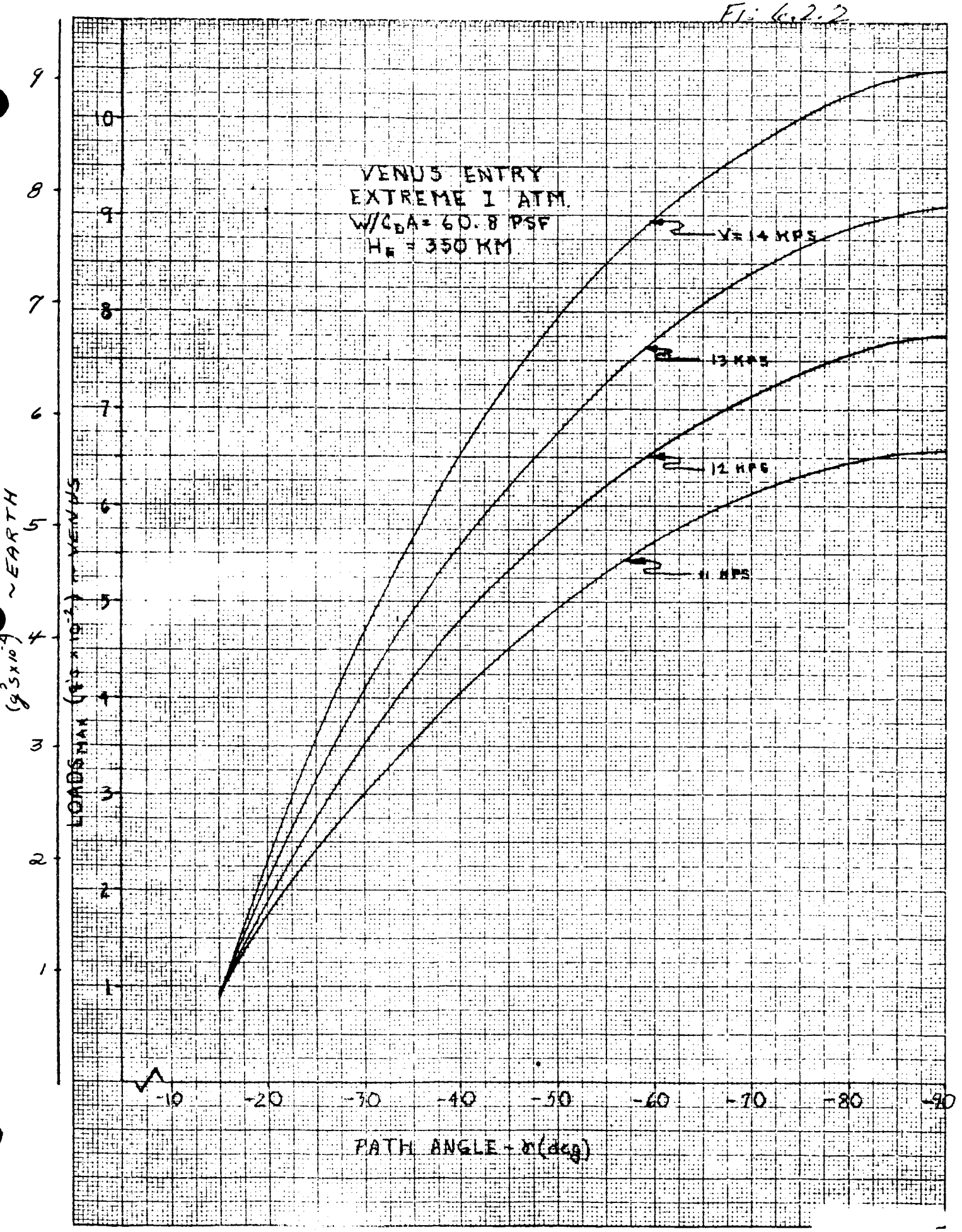
VENUS ENTRY
EXTREME I ATM.
W/C_DA = 60.8 PSF
H_E = 350 KM
V = 14 KPS
13 KPS
12 KPS
11 KPS
LOADS MAX (g's x 10^-2) ~ VENUS
(g's x 10^-2) ~ EARTH
PATH ANGLE - γ (deg)
-10
-20
-30
-40
-50
-60
-70
-80
-90

FIG 6.2.3

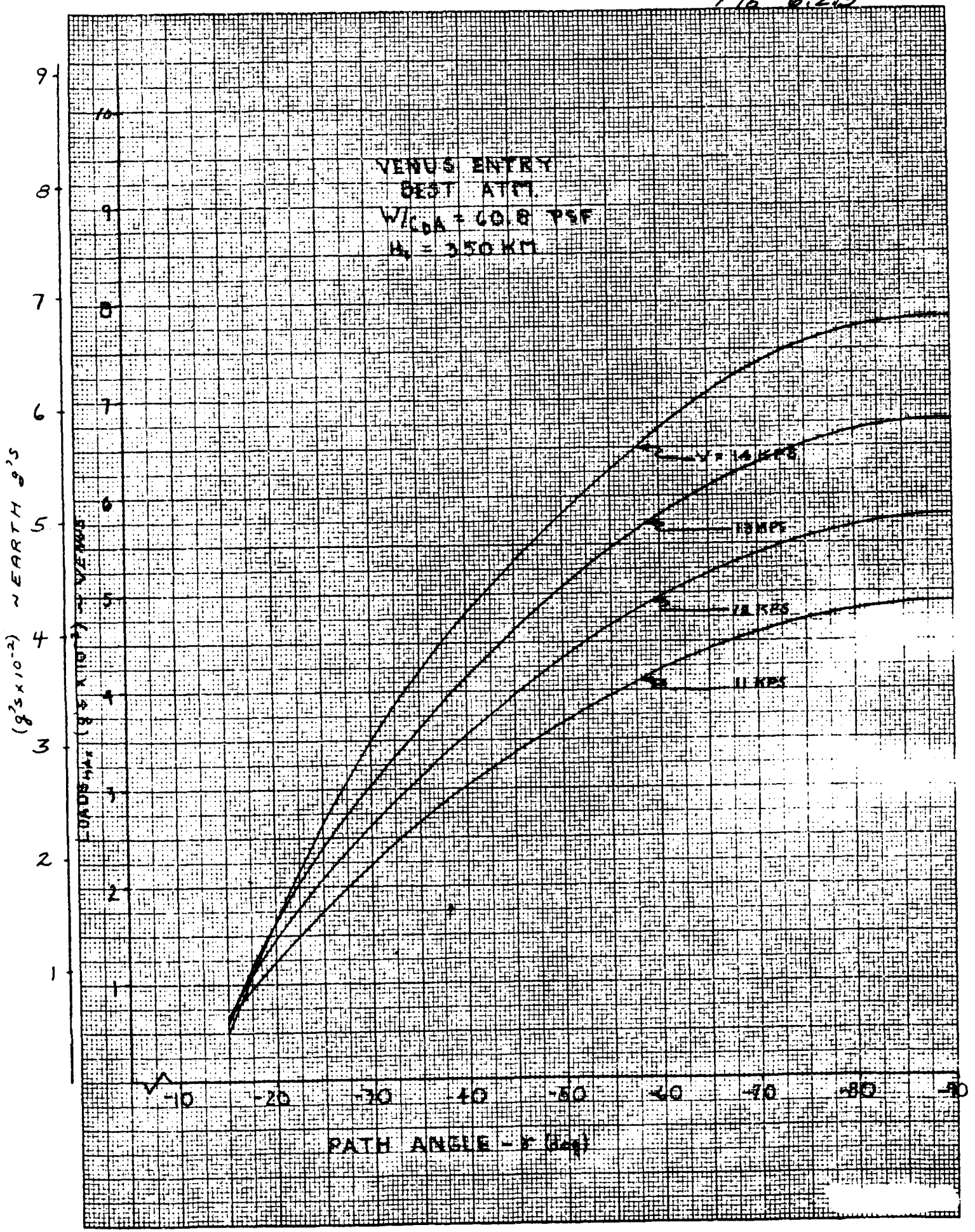
VENUS ENTRY
BEST ATM.
W/C_DA = 60.8 PSF
H_0 = 350 KM
V = 14 KPS
13 KPS
12 KPS
11 KPS
LOADS MAX (g's x 10^-1) ~ VENUS
(g's x 10^-2) ~ EARTH g's
PATH ANGLE - γ (deg)
-10
-20
-30
-40
-50
-60
-70
-80
-90

FIG 6.2.4

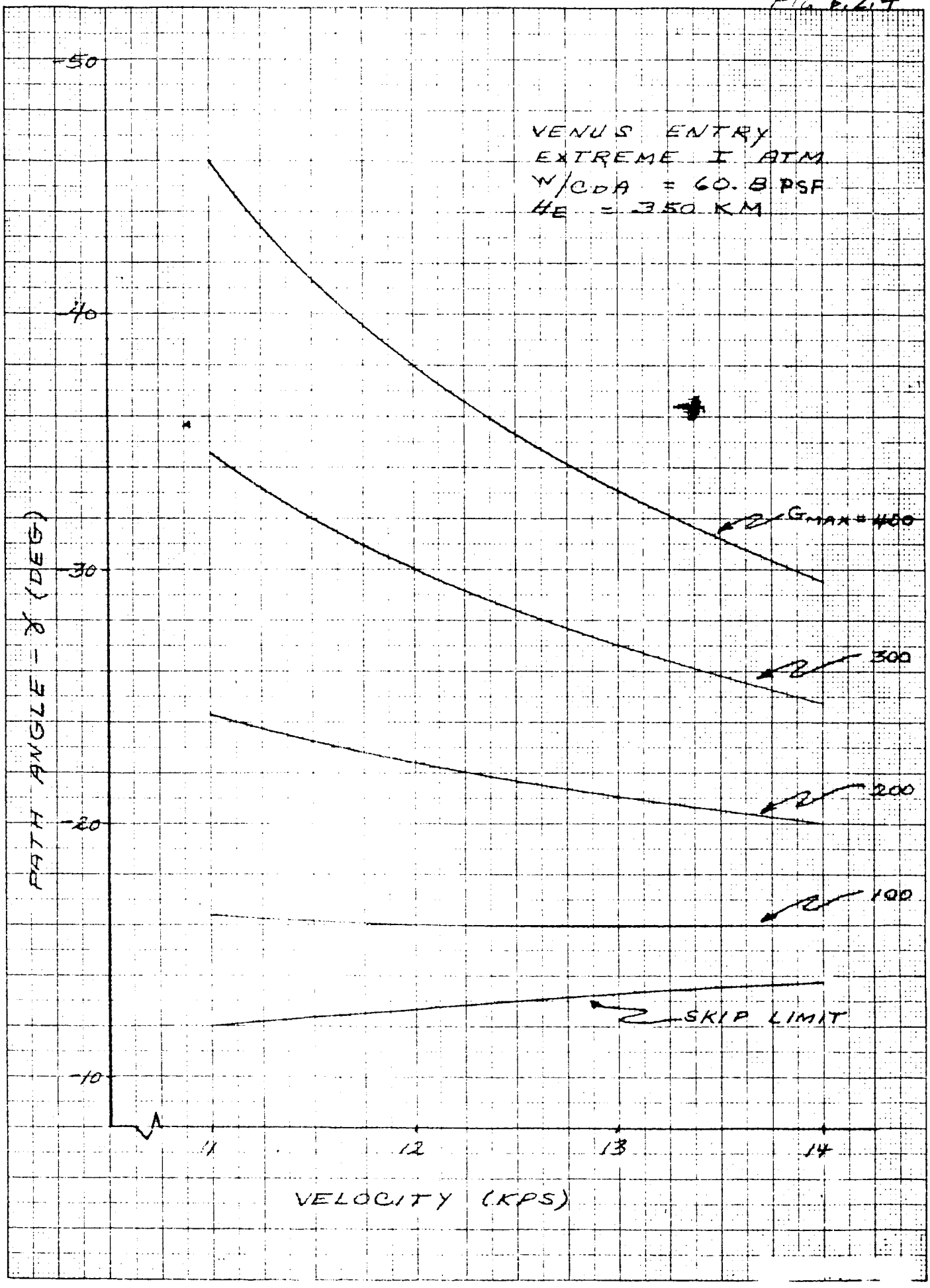
VENUS ENTRY
EXTREME I ATM
W/CDA = 60.8 PSF
H_E = 350 KM
G_{MAX} = 400
300
200
100
SKIP LIMIT
-50
-40
-30
-20
-10
PATH ANGLE - γ (DEG)
11
12
13
14
VELOCITY (KPS)

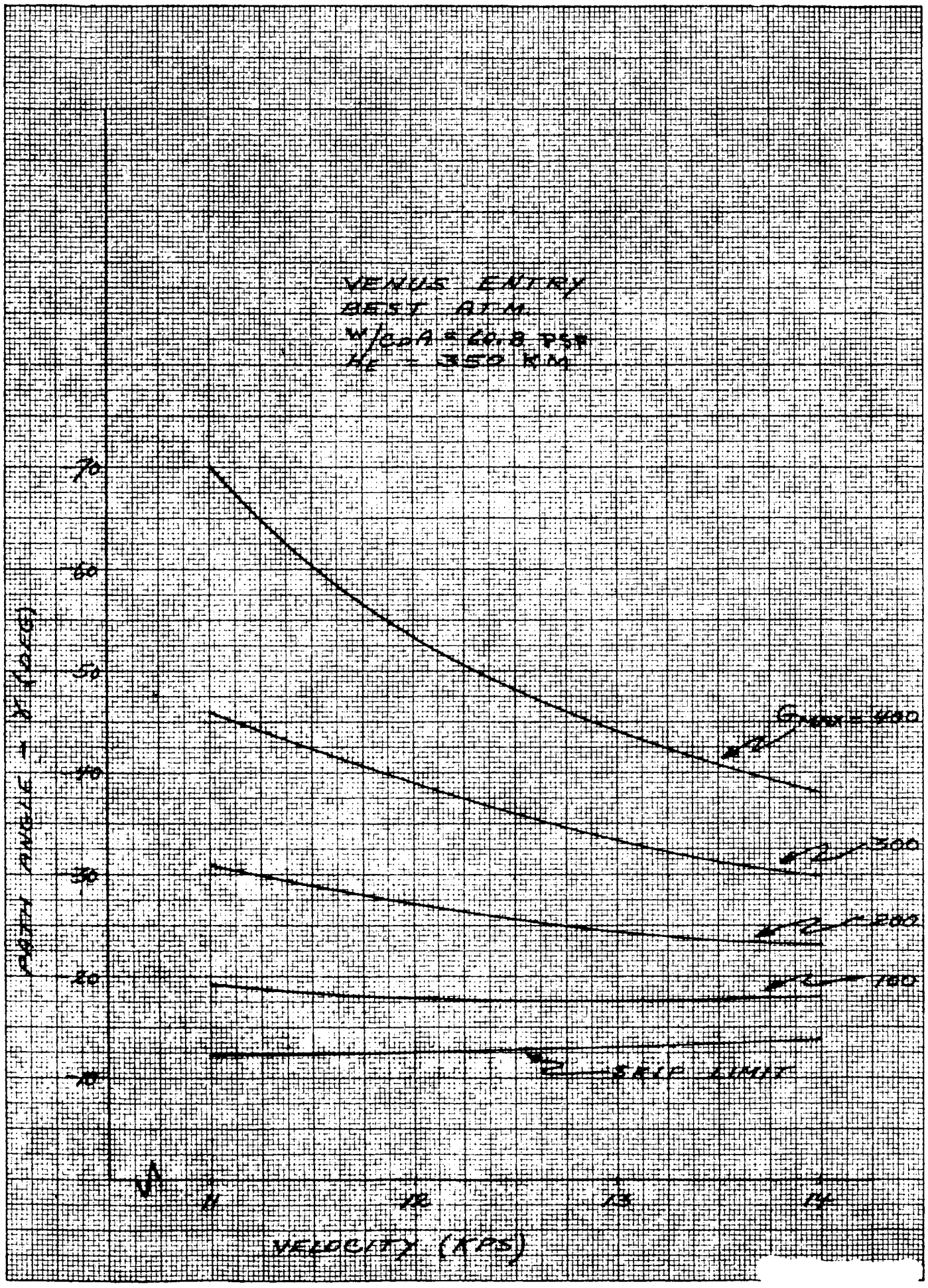
VENUS ENTRY
BEST ATM.
W/C_DA = 20.8 PSF
H_E = 350 KM
70
60
50
40
30
20
10
ENTRY ANGLE γ (DEG)
G_MAX = 400
300
200
100
SKIP LIMIT
11
12
13
14
VELOCITY (KPS)

FIG 6.2.6

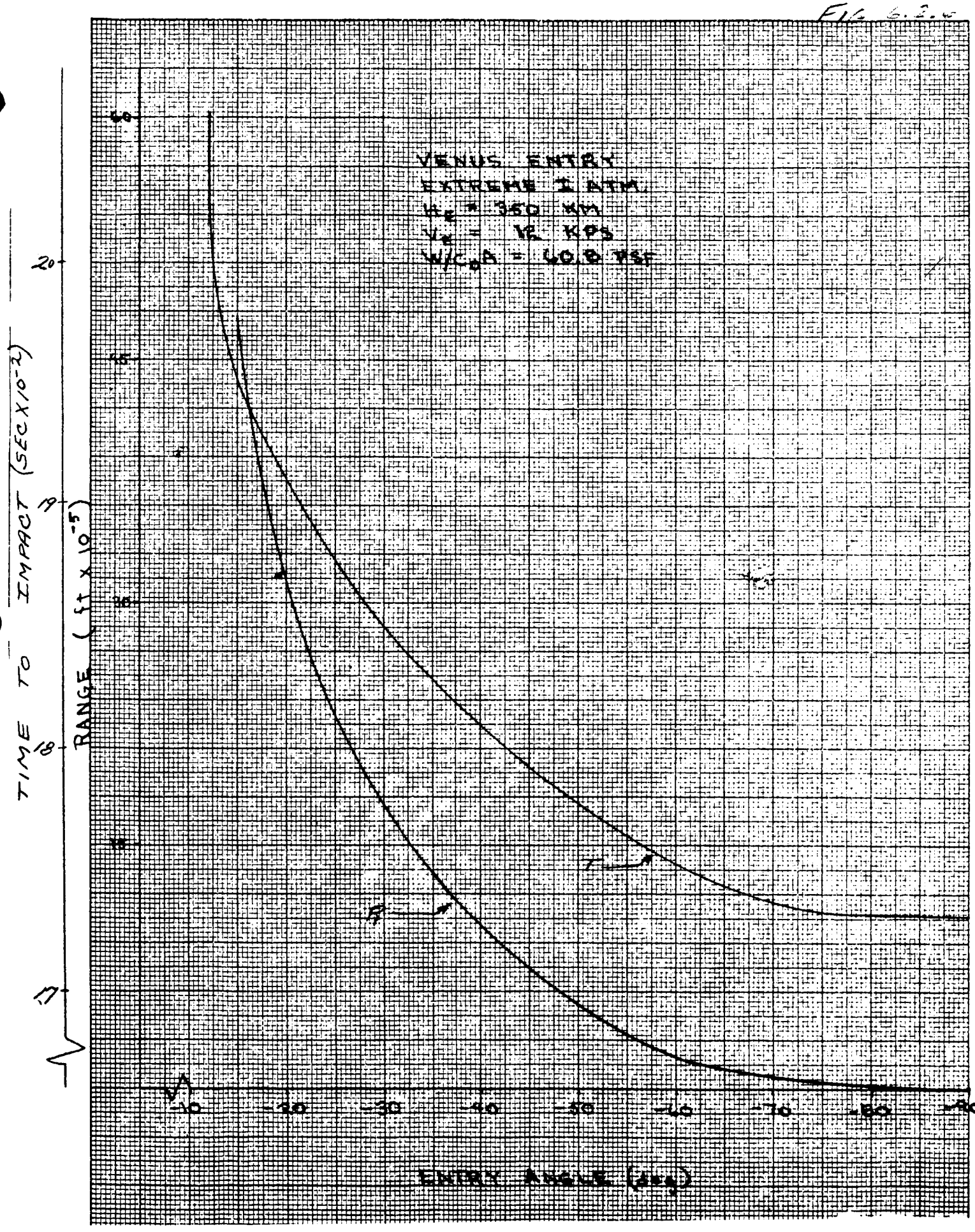

VENUS ENTRY
EXTREME I ATM.
H_E = 350 KM
V_E = 12 KPS
W/C_DA = 60.8 PSF
TIME TO IMPACT (SEC X 10^{-2})
RANGE (ft X 10^{-5})
20
19
18
17
60
45
30
15
-10
-20
-30
-40
-50
-60
-70
-80
-90
ENTRY ANGLE (deg)

FIG 6.2.7

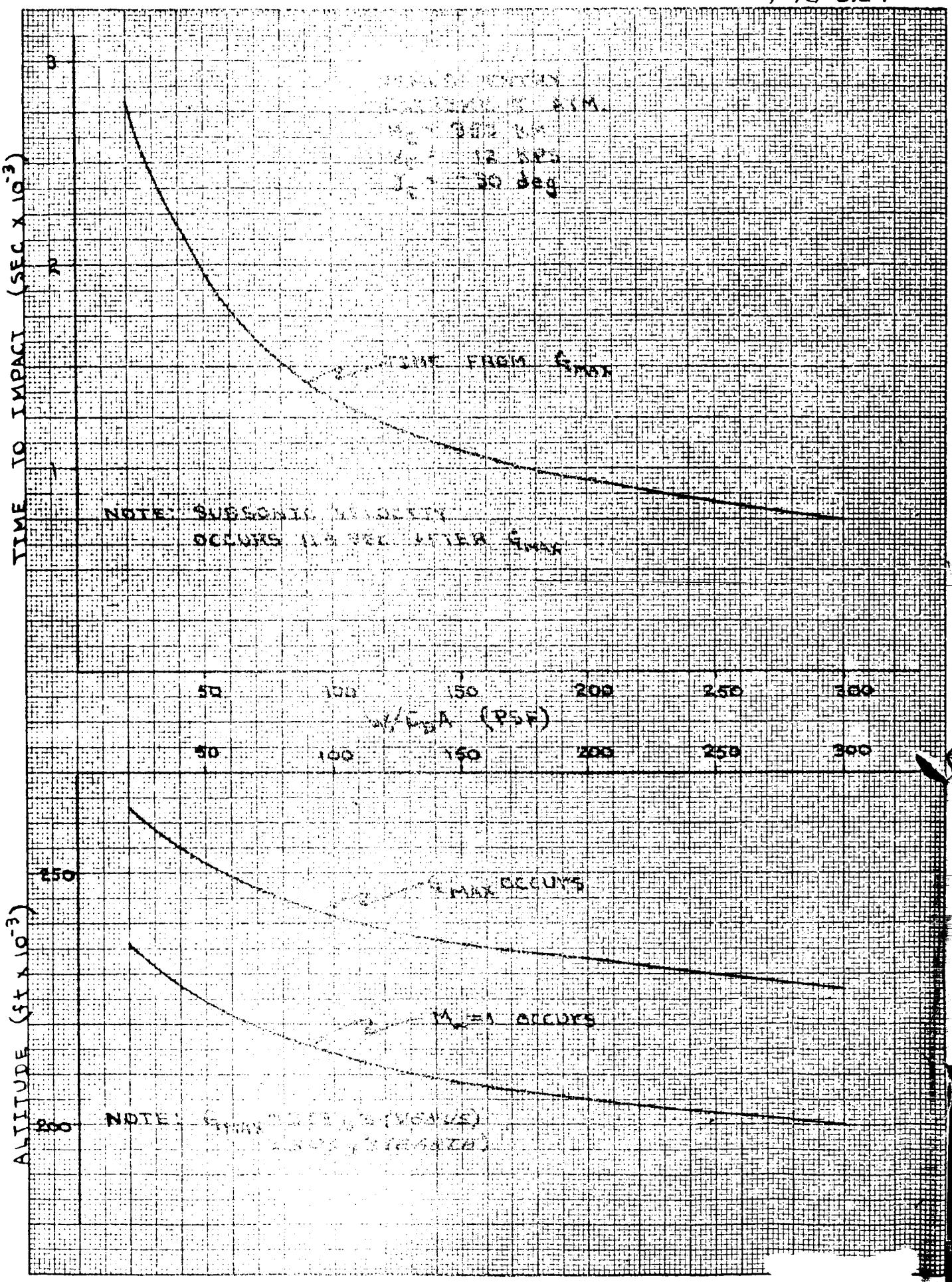
TIME TO IMPACT (SEC X 10^-3)
TIME FROM q_MAX
NOTE: SUBSONIC
OCCURS
AFTER q_MAX
50
100
150
200
250
300
W/C_DA (PSF)
ALTITUDE (ft X 10^-3)
250
200
q_MAX OCCURS
M_∞=1 OCCURS
NOTE:

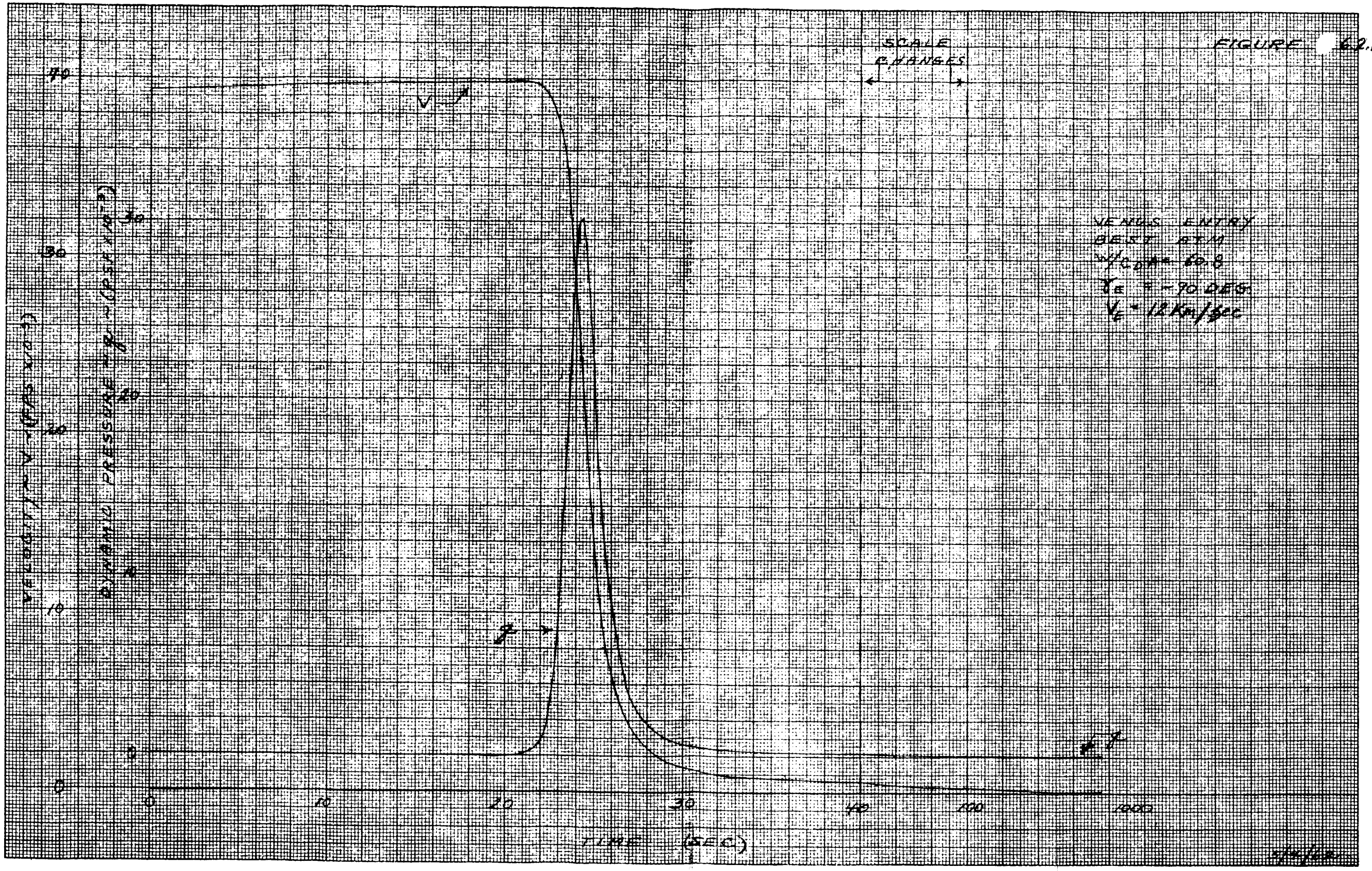

SCALE CHANGES
V
q
VENUS ENTRY
BEST ATM
W/C_D A = 60.8
γ_E = -90 DEG
V_E = 12 Km/sec
VELOCITY ~ V ~ (FPS x 10^-3)
DYNAMIC PRESSURE ~ q ~ (PSF x 10^-3)
TIME (SEC)
0
10
20
30
40
100
1000

FIGURE 6.2.8

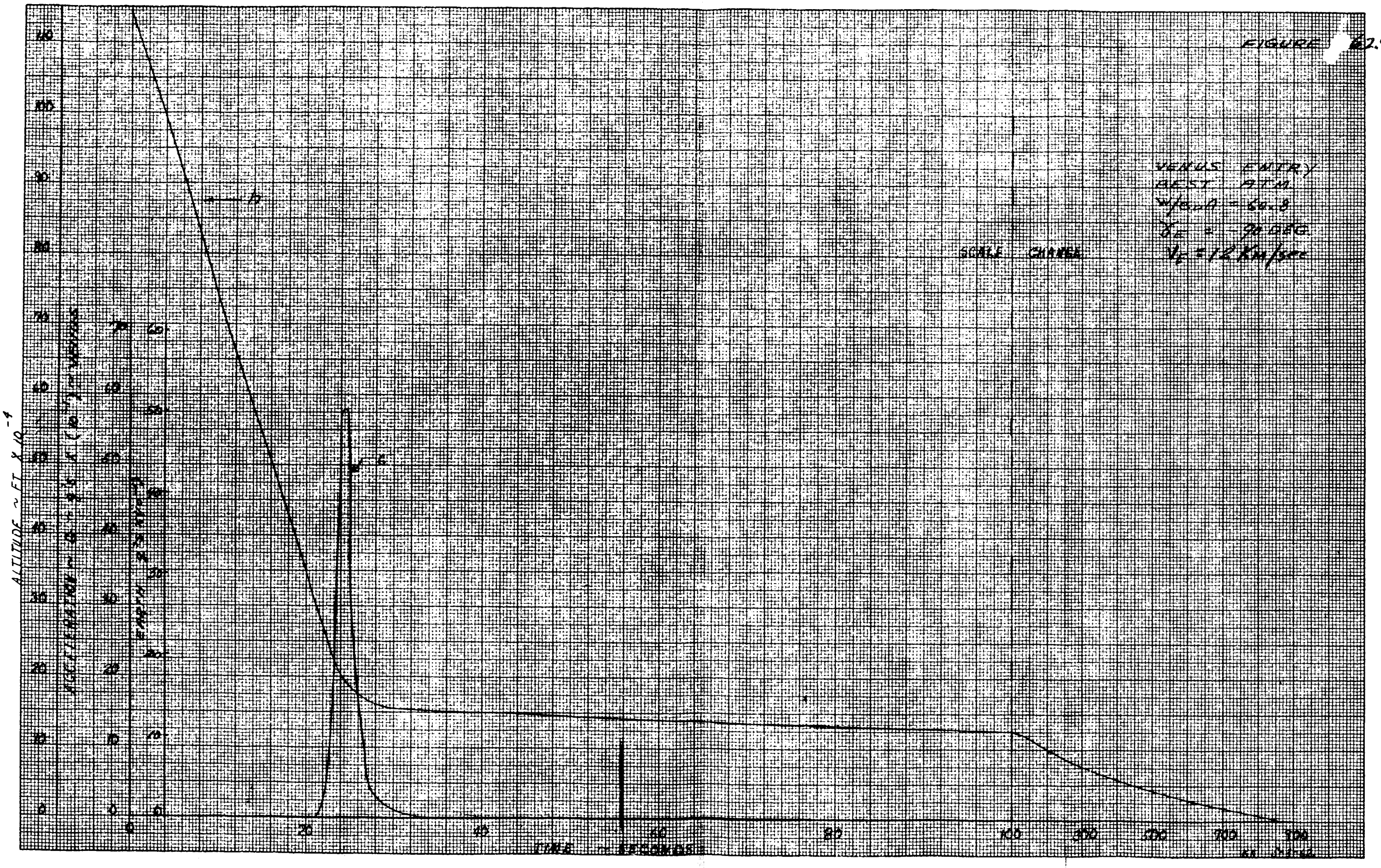

FIGURE 62.9
VENUS ENTRY
BEST ATM
W/C_DA = 60.8
γ_E = -90 DEG
V_E = 12 Km/sec
SCALE CHANGE
ALTITUDE ~ FT X 10^-4
ACCELERATION ~ G ~ g's X (10^-1)
EARTH g's X (10^-1)
TIME ~ SECONDS
b
c
0
20
40
60
80
100
300
500
700
900

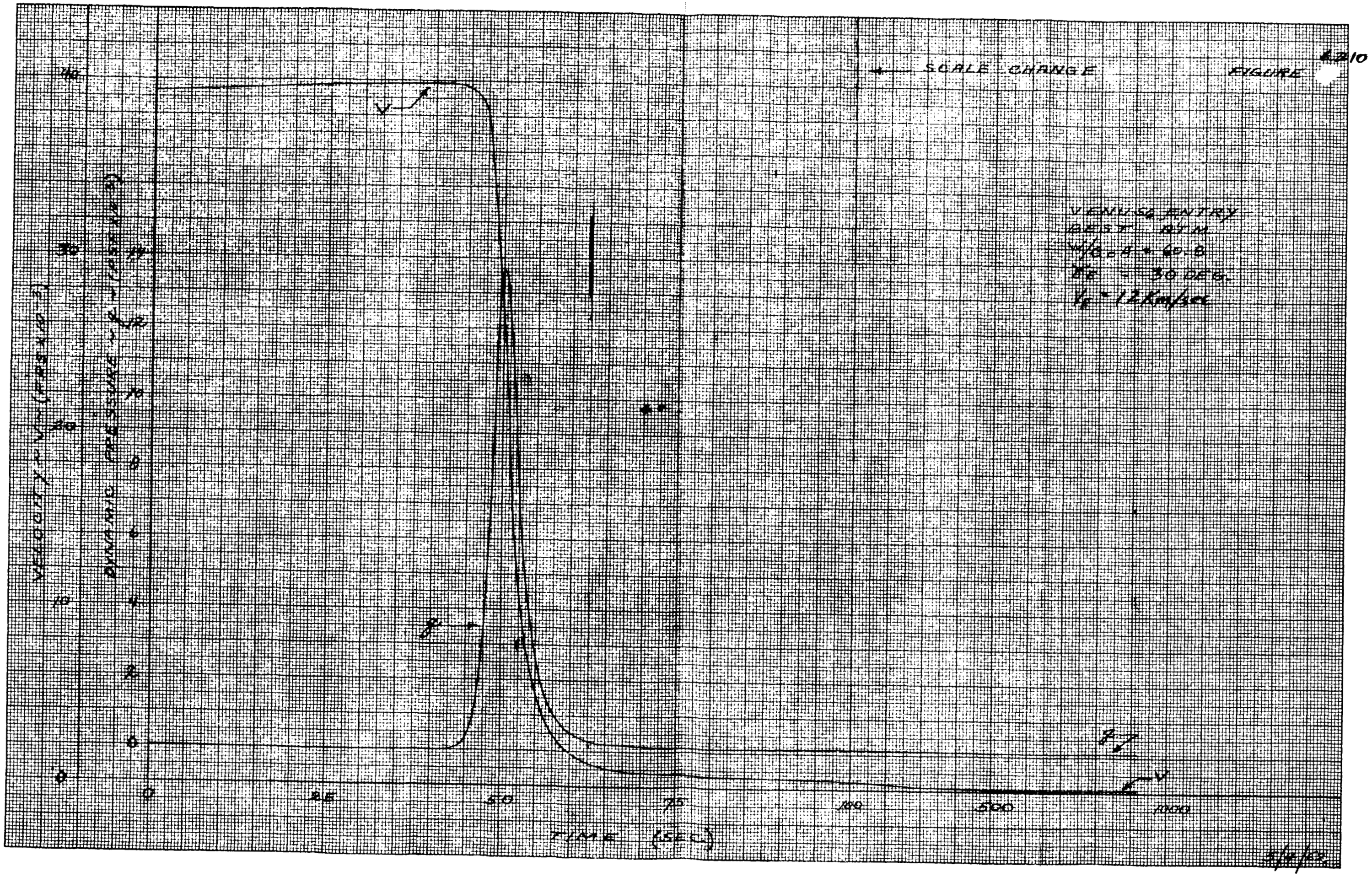

SCALE CHANGE
FIGURE 6.2.10
VENUS ENTRY
BEST ATM
W/C = 60.8
γ_E = -30 DEG.
V_E = 12 Km/sec
VELOCITY ~ V ~ (FPS x 10^-3)
DYNAMIC PRESSURE ~ q ~ (PSF x 10^-3)
TIME (SEC)
0
25
50
75
100
500
1000
10
20
30
40
2
4
6
8
10
12
14
V
q

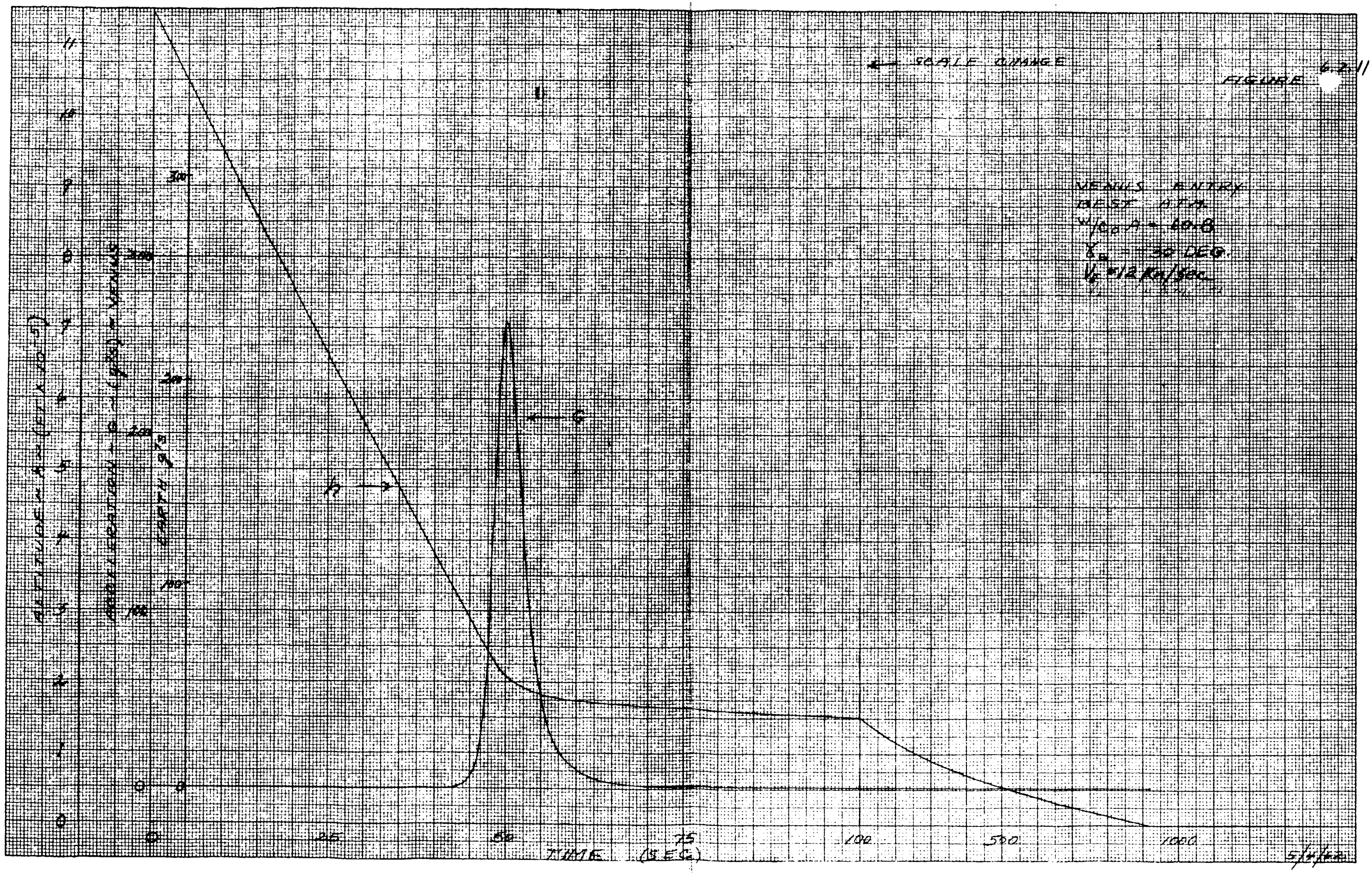

FIGURE 6.2.11
← SCALE CHANGE
VENUS ENTRY
BEST ATM.
W/C_D A = 40.8
γ_E = -30 DEG.
V_E = 12 Km/Sec.
ALTITUDE ~ h ~ (FT X 10^-5)
ACCELERATION ~ G ~ (g's) ~ VENUS
EARTH g's
h →
← G
TIME (SEC)
0
25
50
75
100
500
1000
5/4/62

FIGURE 6.2.12

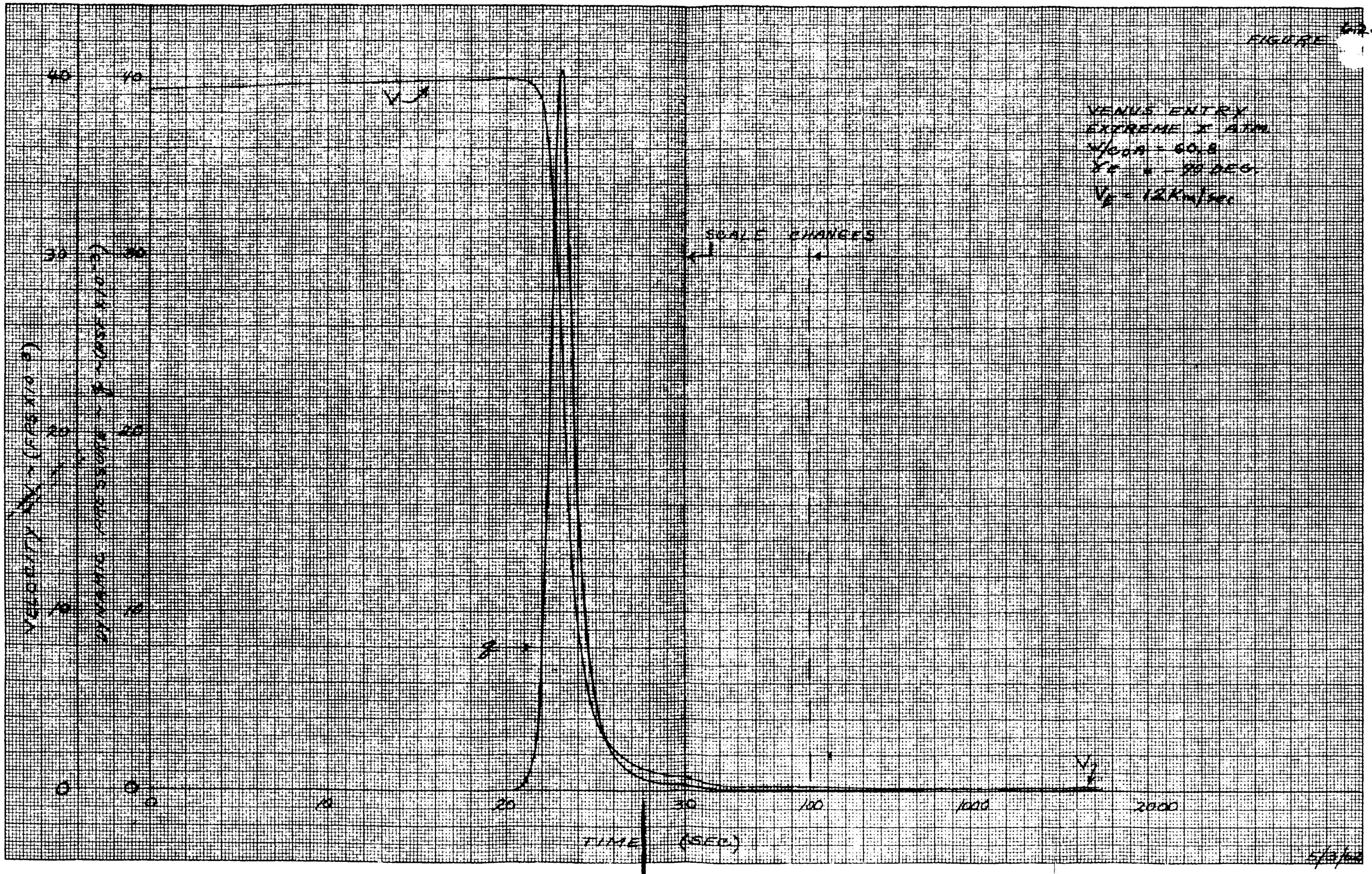
VENUS ENTRY
EXTREME I ATM.
W/CoA = 60.8
γE = -90 DEG.
VE = 12 Km/sec
SCALE CHANGES
VELOCITY ~ (FPS X 10^-3)
DYNAMIC PRESSURE ~ q ~ (PSF X 10^-3)
TIME (SEC)
0
10
20
30
40
100
1000
2000
V
q

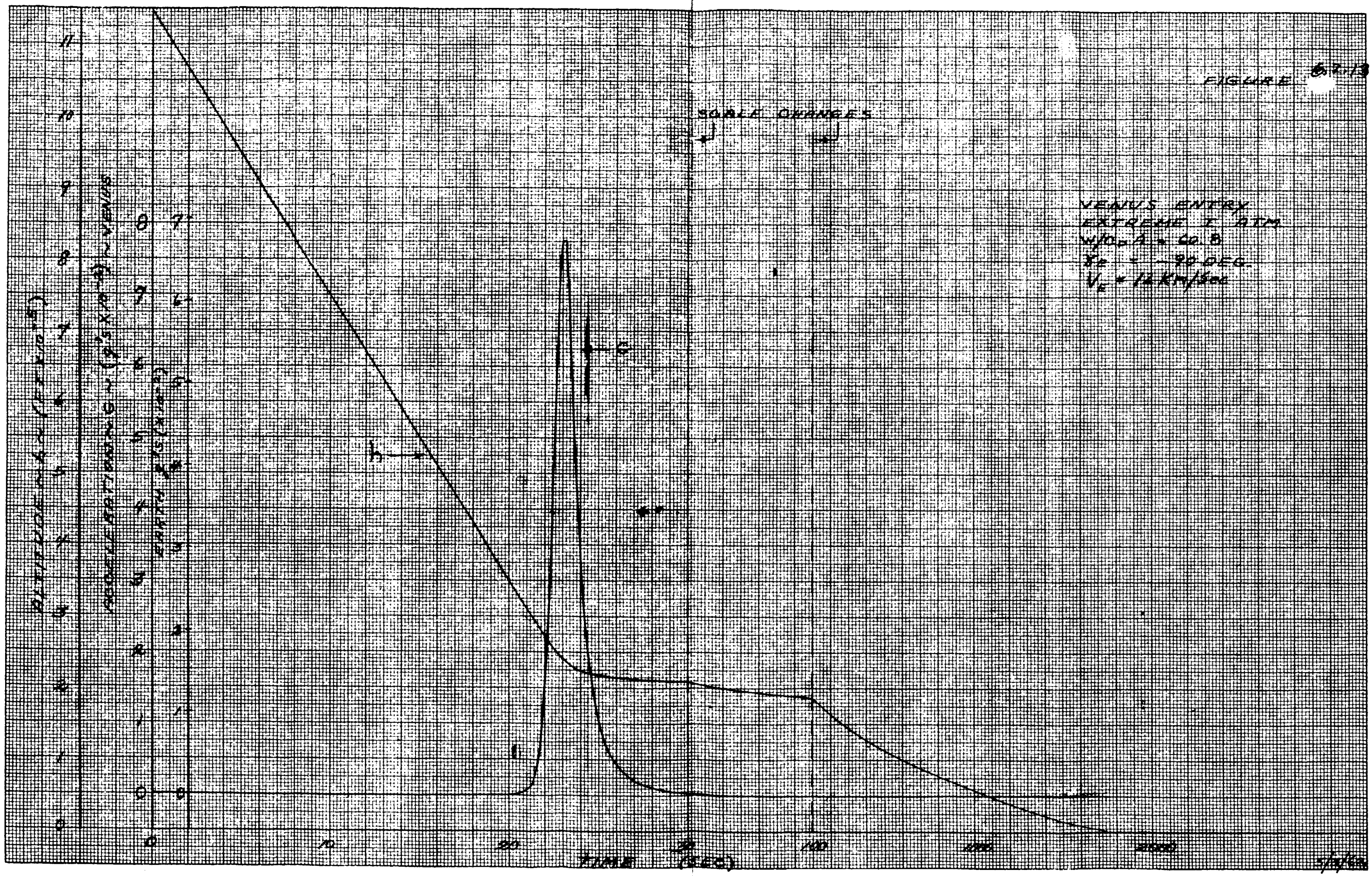

FIGURE 6.2.13
SCALE CHANGES
VENUS ENTRY
EXTREME I ATM
W/C_D A = 60.8
γ_E = -90 DEG.
V_E = 12 KM/SEC
ALTITUDE ~ h ~ (FT x 10^-5)
ACCELERATION ~ G ~ (g's x 10^-2) ~ VENUS
EARTH g's (x 10^-2)
TIME (SEC)
h
G

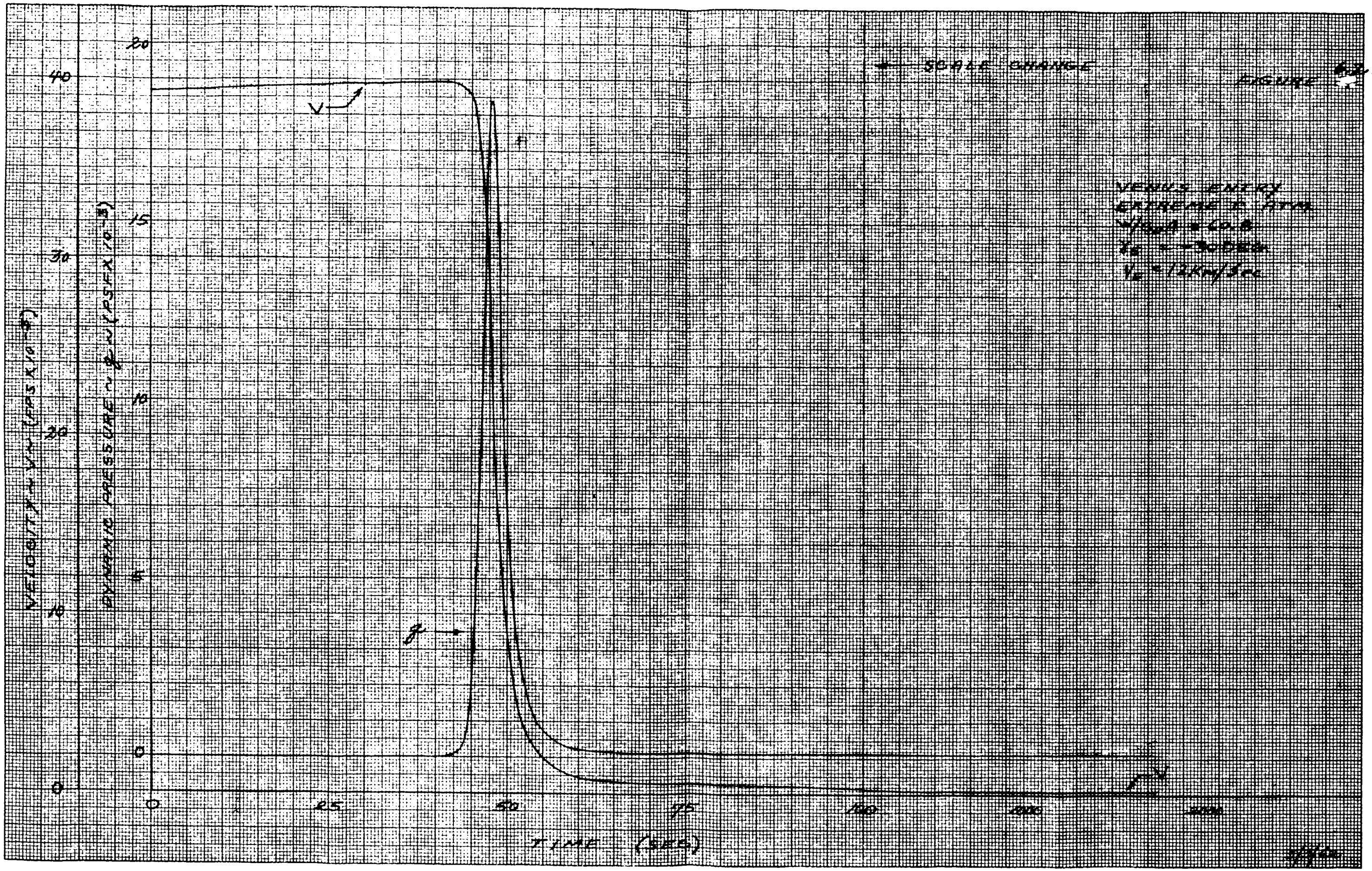

FIGURE 6.2-14
SCALE CHANGE
VENUS ENTRY
EXTREME I ATM
γ_E = -30 DEG
V_E = 12 Km/Sec
VELOCITY ~ V ~ (FPS X 10^-3)
DYNAMIC PRESSURE ~ q ~ (PSF X 10^-3)
TIME (SEC)
V
q
0
10
20
30
40
5
15
25
50
75
100
1000
2000

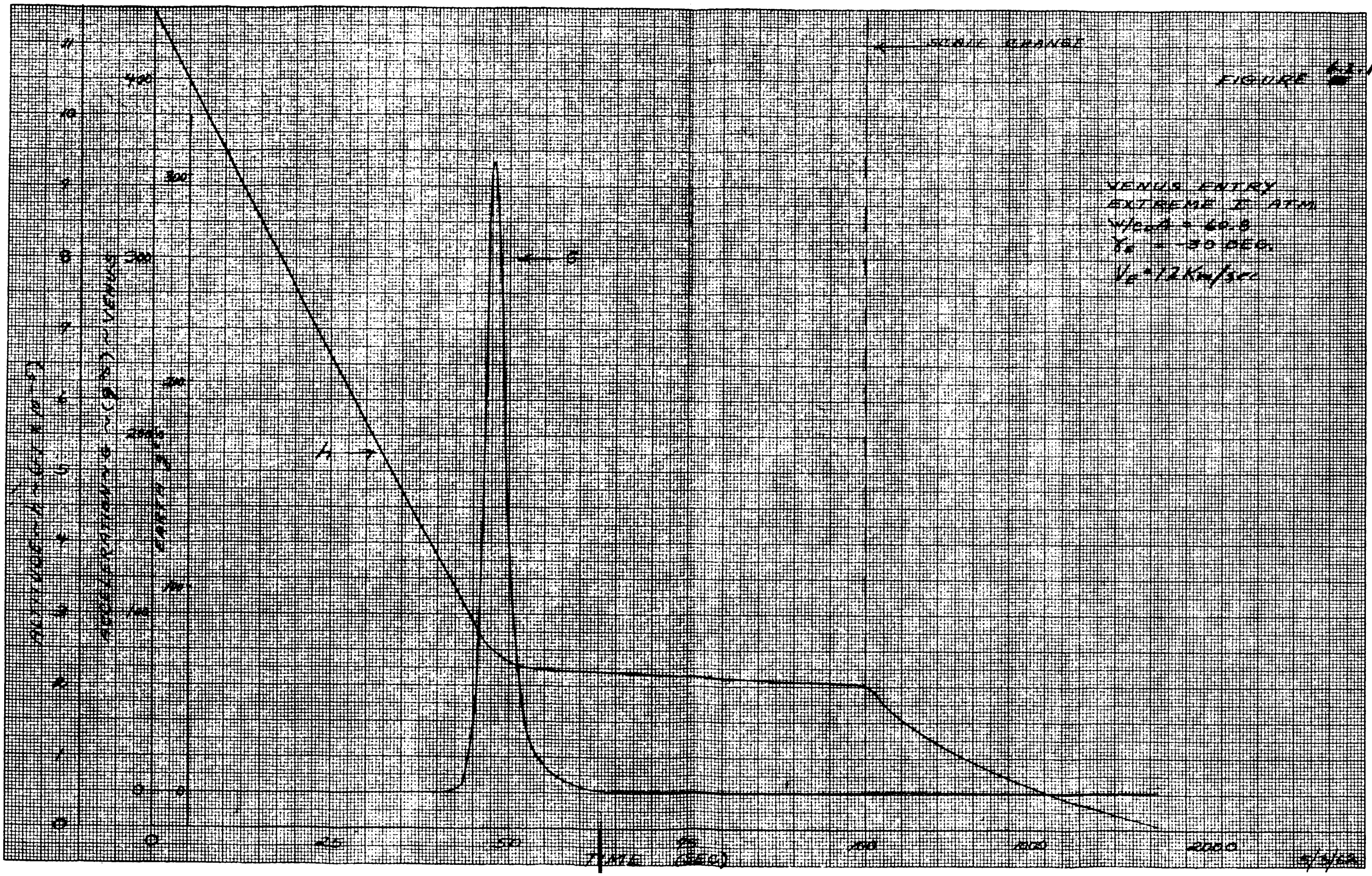

FIGURE 6.2.15
VENUS ENTRY
EXTREME I ATM
W/C_DA = 60.8
γ_E = -30 DEG.
V_E = 12 Km/sec
SCALE CHANGE
ALTITUDE ~ h ~ (FT × 10^-5)
ACCELERATION ~ G ~ (g's) ~ VENUS
EARTH g's
TIME (SEC)
0
25
50
75
100
1000
2000

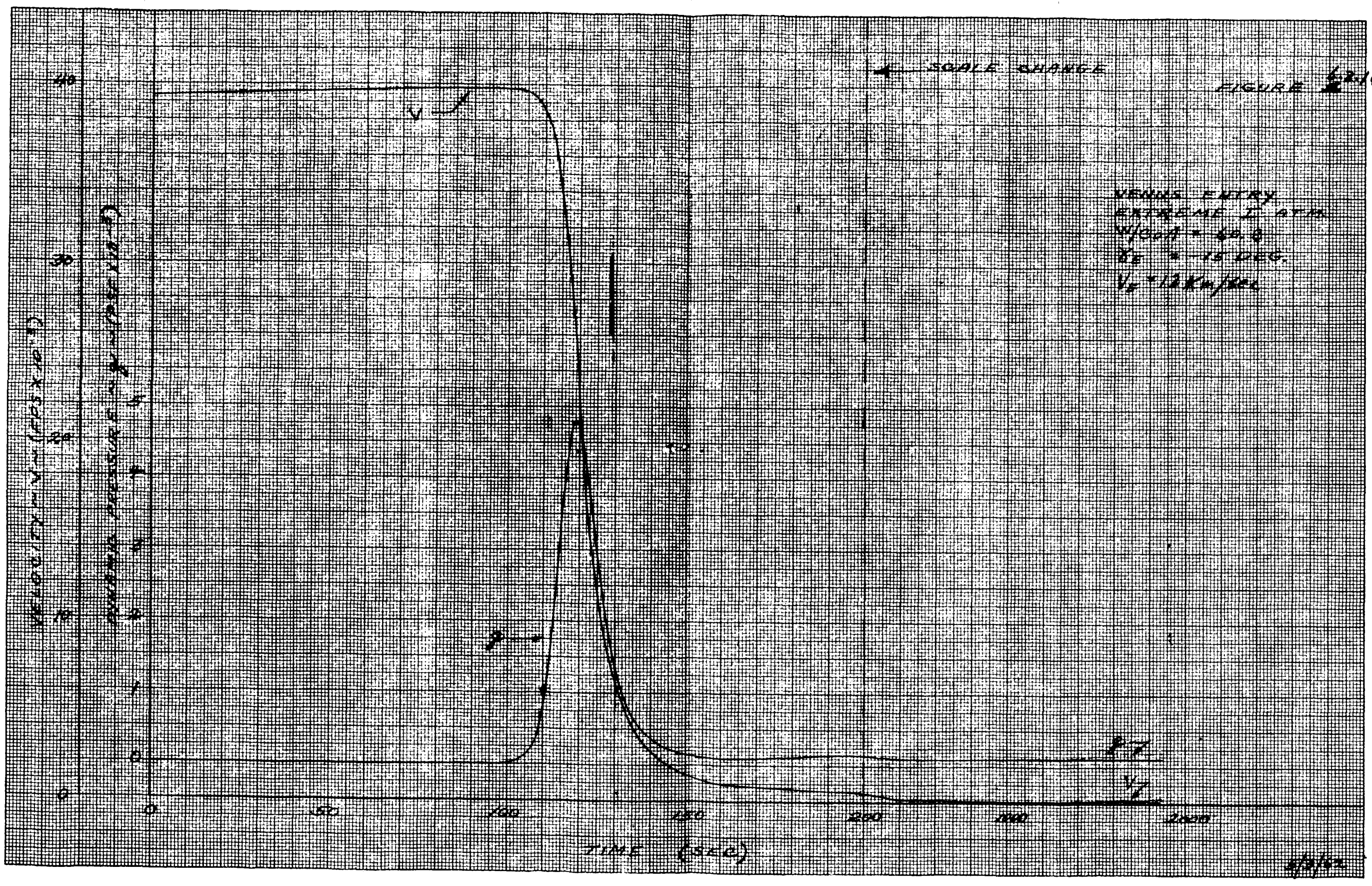

SCALE CHANGE
FIGURE 6.2.16
VENUS ENTRY
EXTREME I ATM
W/CoA = 60.0
γ_E = -15 DEG.
V_E = 12 Km/sec
VELOCITY ~ V ~ (FPS X 10^-3)
DYNAMIC PRESSURE ~ q ~ (PSF X 10^-3)
TIME (SEC)
V
q
0
50
100
150
200
1000
2000
10
20
30
40
1
2
3
4
5

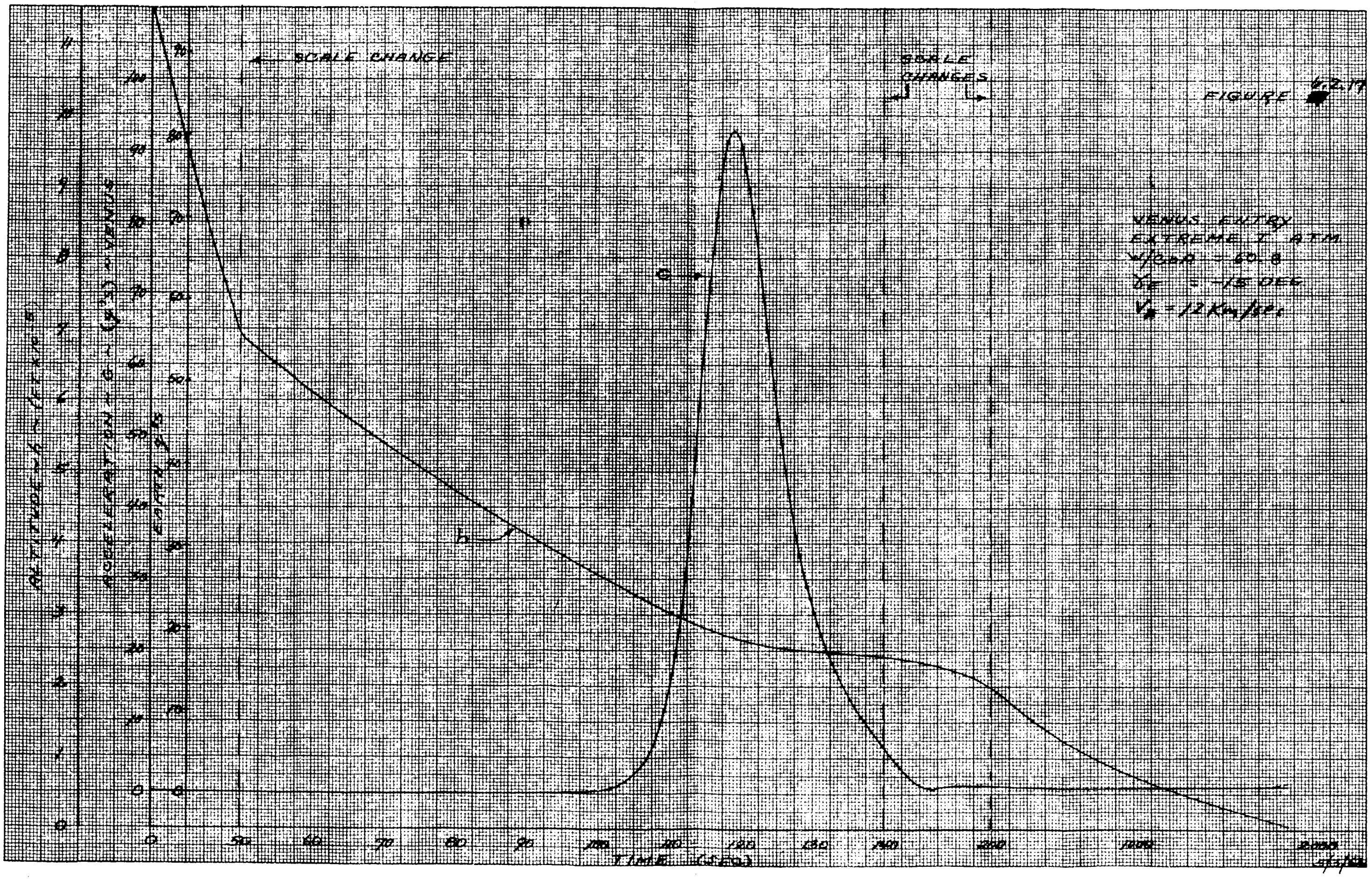

SCALE CHANGE
SCALE CHANGES
FIGURE 6.2.17
VENUS ENTRY
EXTREME I ATM
W/CDA = 60.8
γ_E = -15 DEG
V_A = 12 Km/sec
ALTITUDE ~ h ~ (FT x 10^-5)
ACCELERATION ~ G ~ (g's) ~ VENUS
EARTH g's
TIME (SEC)

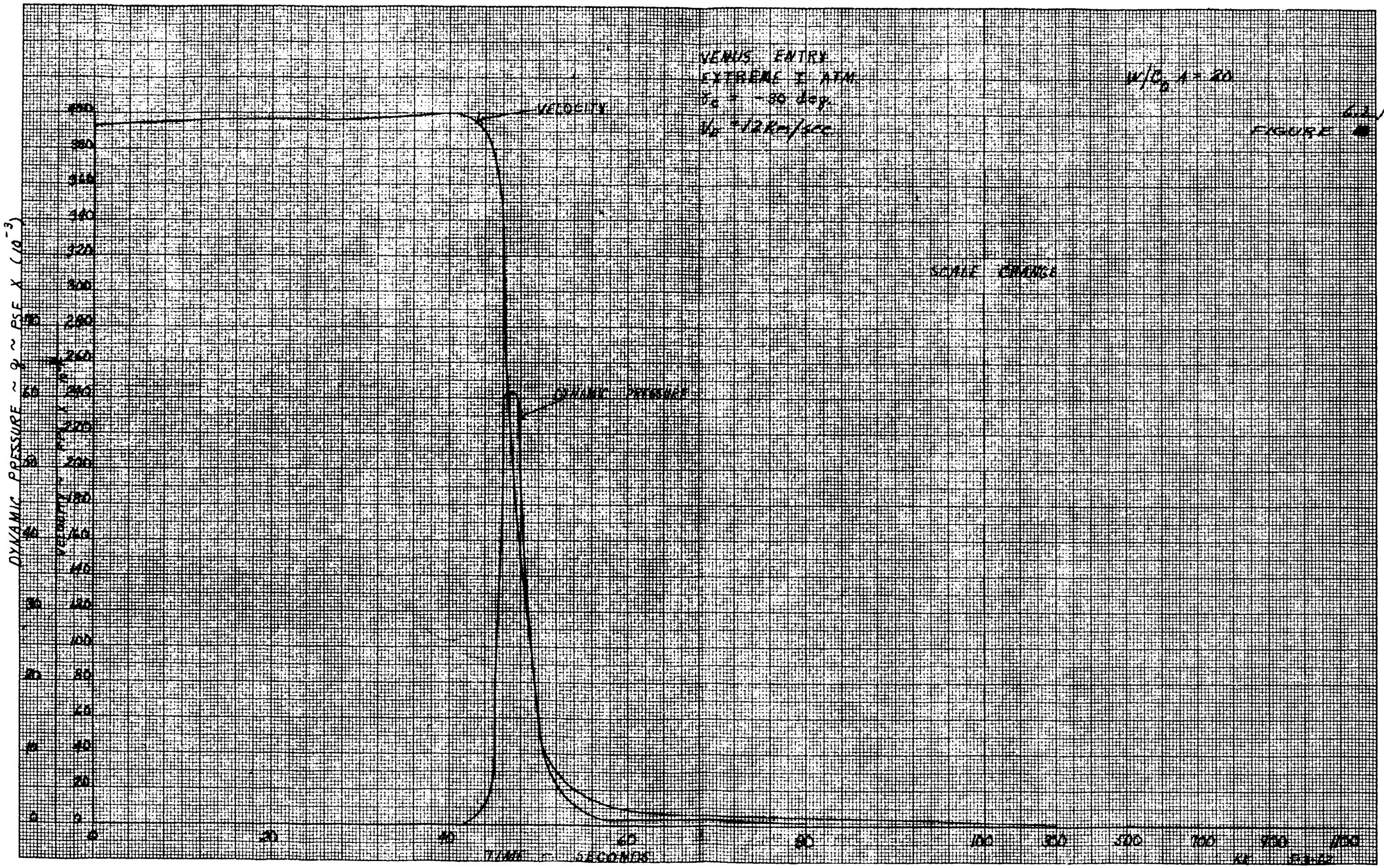
VENUS ENTRY
EXTREME I ATM.
γ_e = -30 deg.
V_E = 12 Km/sec
$W/C_D A$ = 20
VELOCITY
DYNAMIC PRESSURE
SCALE CHANGE
DYNAMIC PRESSURE ~ q ~ PSF X (10^{-3})
VELOCITY ~ FPS X
TIME ~ SECONDS
0
20
40
60
80
100
300
500
700
900
1100

FIGURE 6.2.18

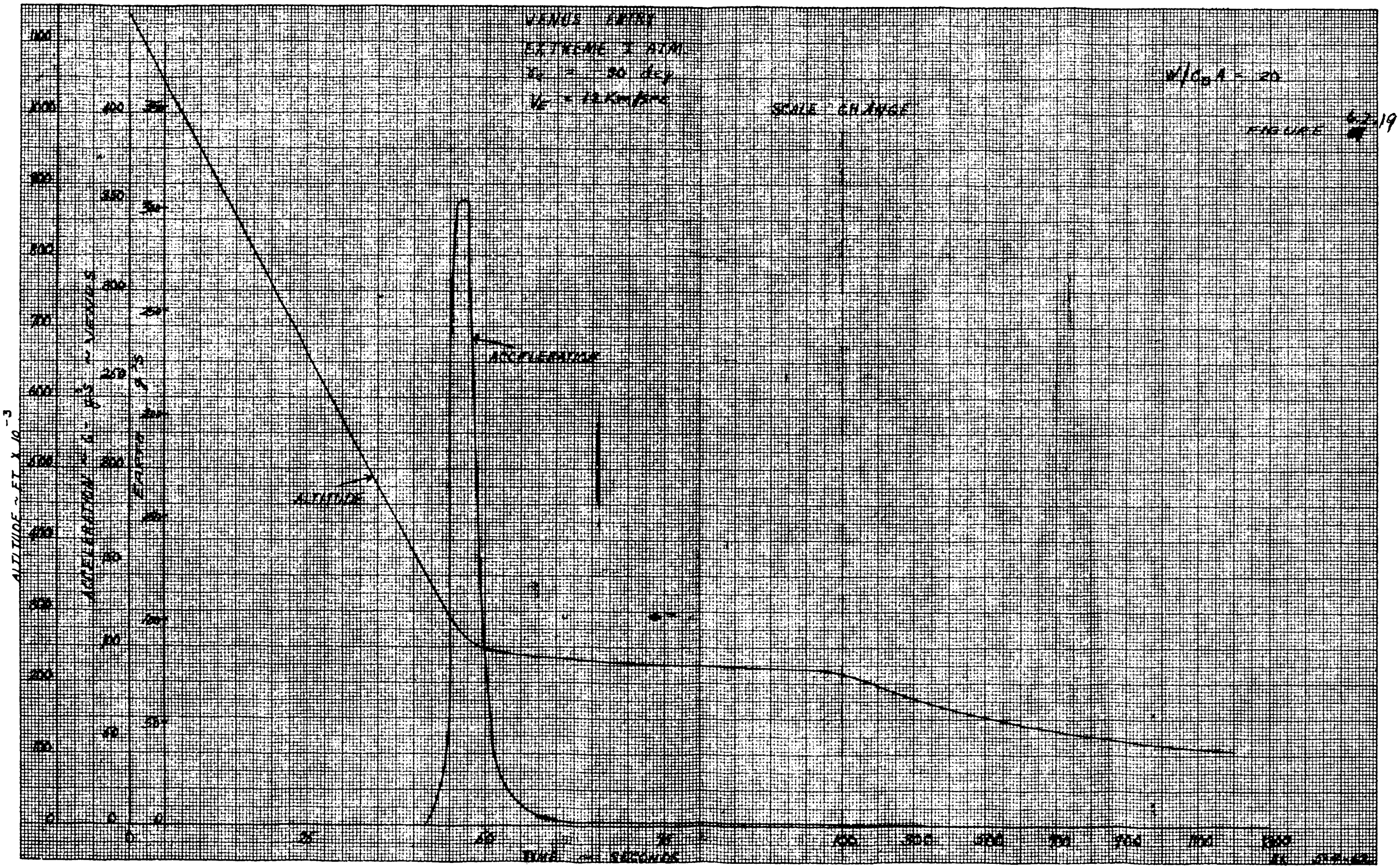
VENUS ENTRY
EXTREME I ATM
γ_e = 30 deg
V_E = 12 Km/sec
SCALE CHANGE
$W/C_D A$ = 20
ACCELERATION
ALTITUDE
ALTITUDE ~ FT X 10^-3
ACCELERATION ~ G - FS ~ VENUS
EARTH
TIME ~ SECONDS
0
25
50
75
100
300
500
700
900
1100
1300

FIGURE 6.2.19

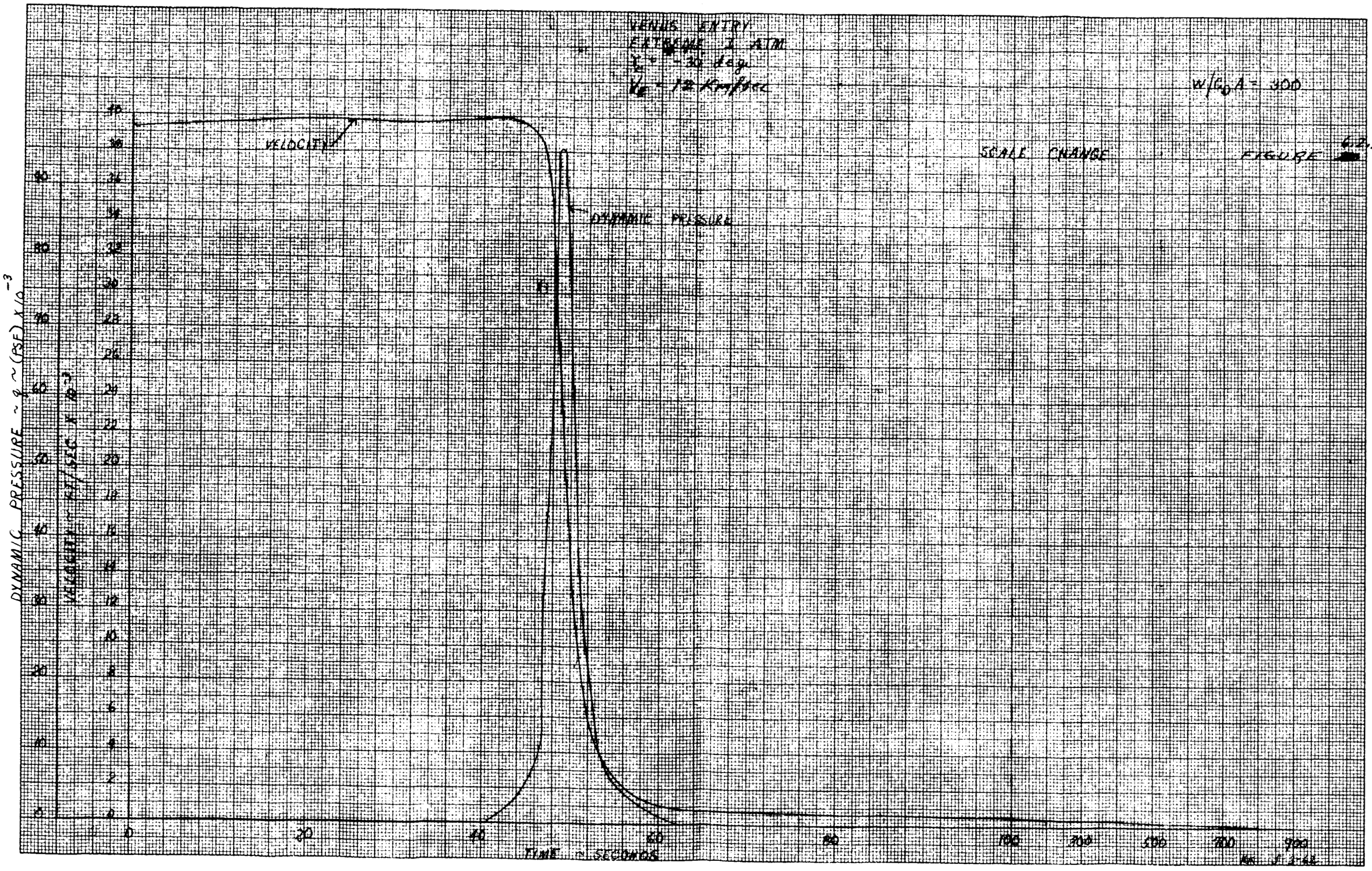
VENUS ENTRY
EXTREME I ATM
γ_E = -30 deg
V_E = 12 Km/sec
$W/C_D A$ = 300
VELOCITY
DYNAMIC PRESSURE
SCALE CHANGE
FIGURE 6.2.20
DYNAMIC PRESSURE ~ q ~ (PSF) X 10^-3
VELOCITY ~ FT/SEC X 10^-3
TIME ~ SECONDS
0
20
40
60
80
100
200
300
400
500

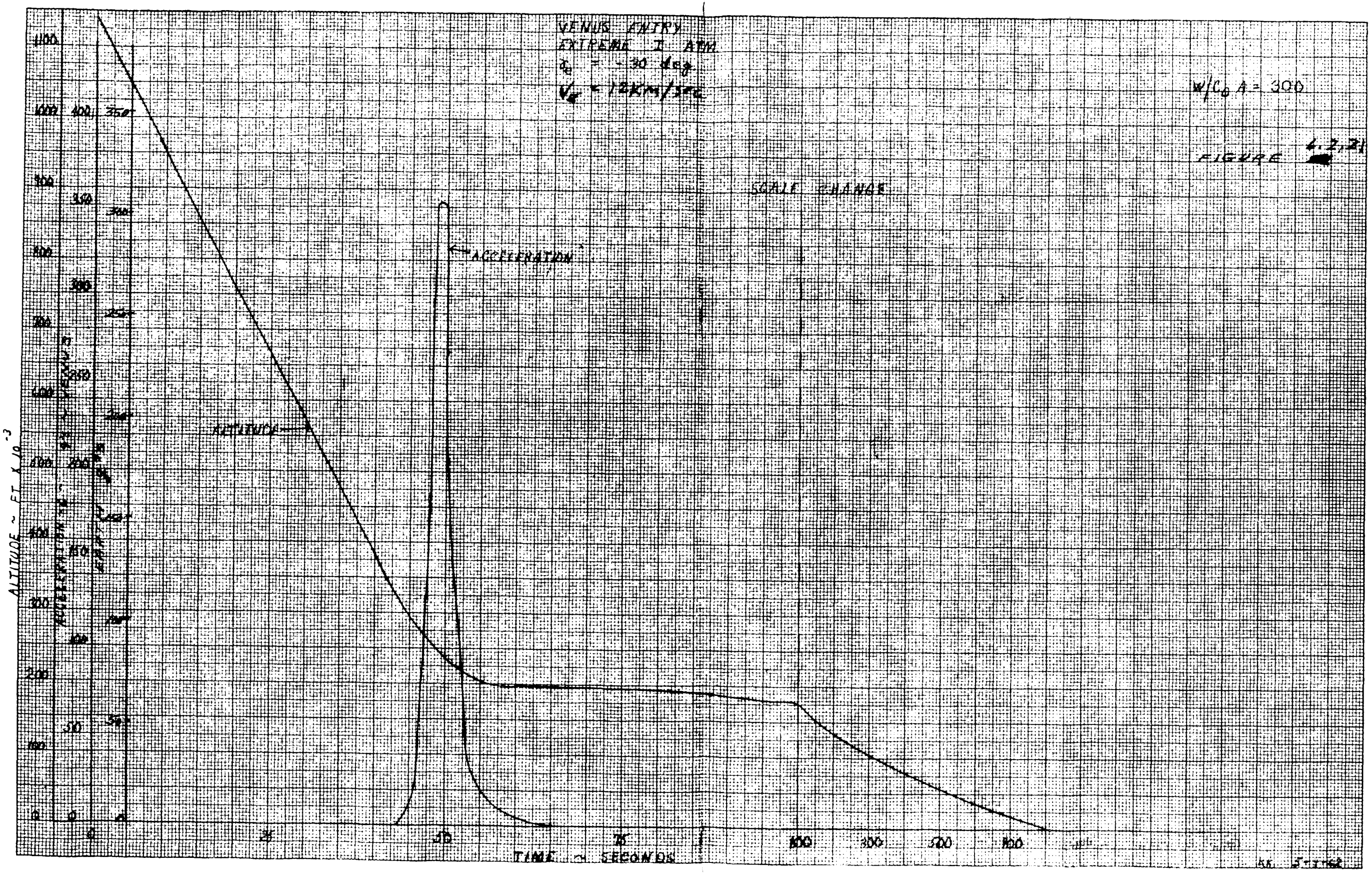
VENUS ENTRY
EXTREME I ATM
γ_e = -30 deg
V_e = 12 Km/sec
W/C_D A = 300
SCALE CHANGE
ACCELERATION
ALTITUDE
ALTITUDE ~ FT X 10^{-3}
TIME ~ SECONDS
0
25
50
75
100
300
500
800

FIGURE 4.2.21

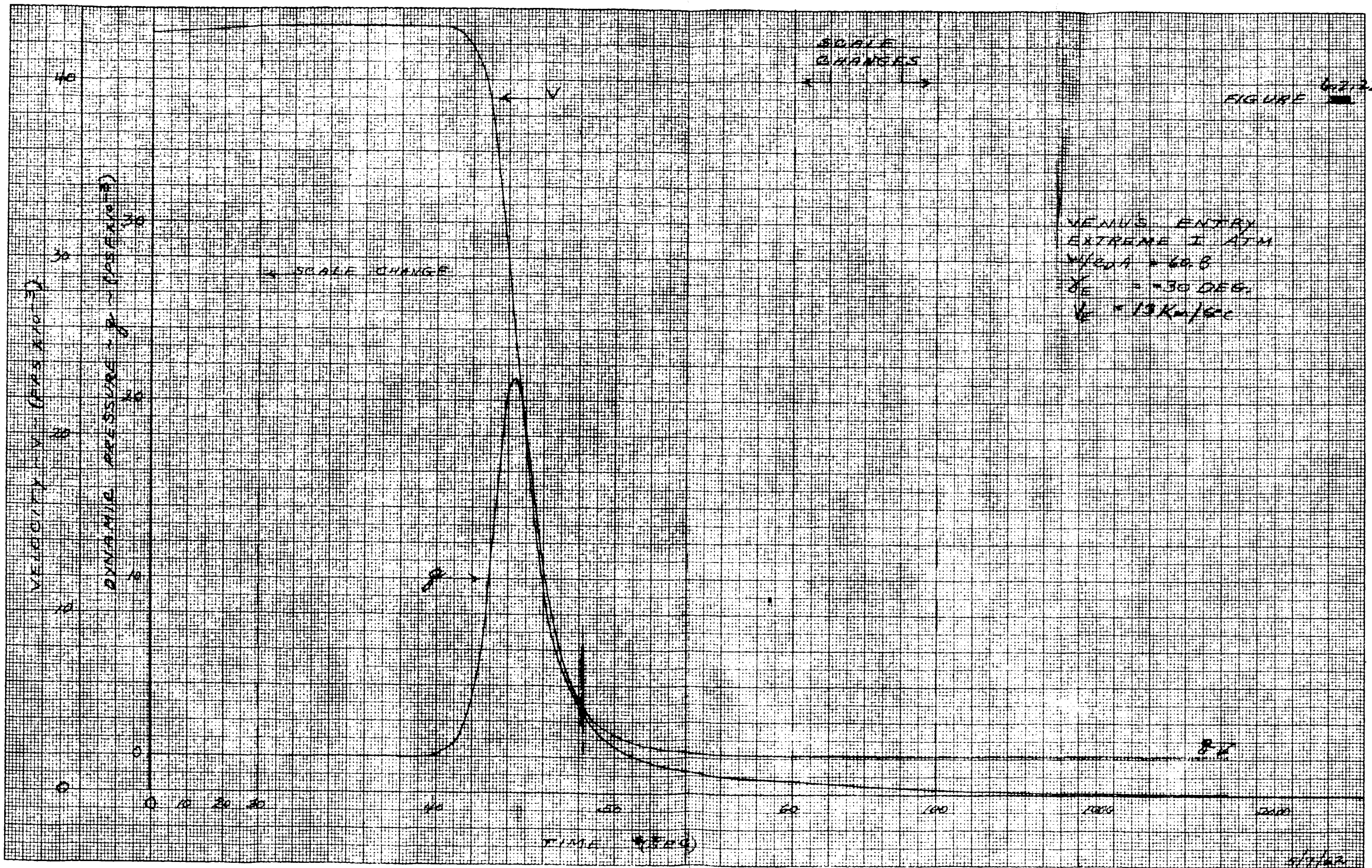

FIGURE 6.2.22
SCALE CHANGES
V
SCALE CHANGE
VENUS ENTRY
EXTREME I ATM
W/C_DA = 60.8
γ_E = -30 DEG.
V_E = 13 Km/sec
VELOCITY ~ V ~ (FPS x 10^-3)
DYNAMIC PRESSURE ~ q ~ (PSF x 10^-3)
TIME ~ (SEC)
0
10
20
30
40
50
60
100
1000
2000

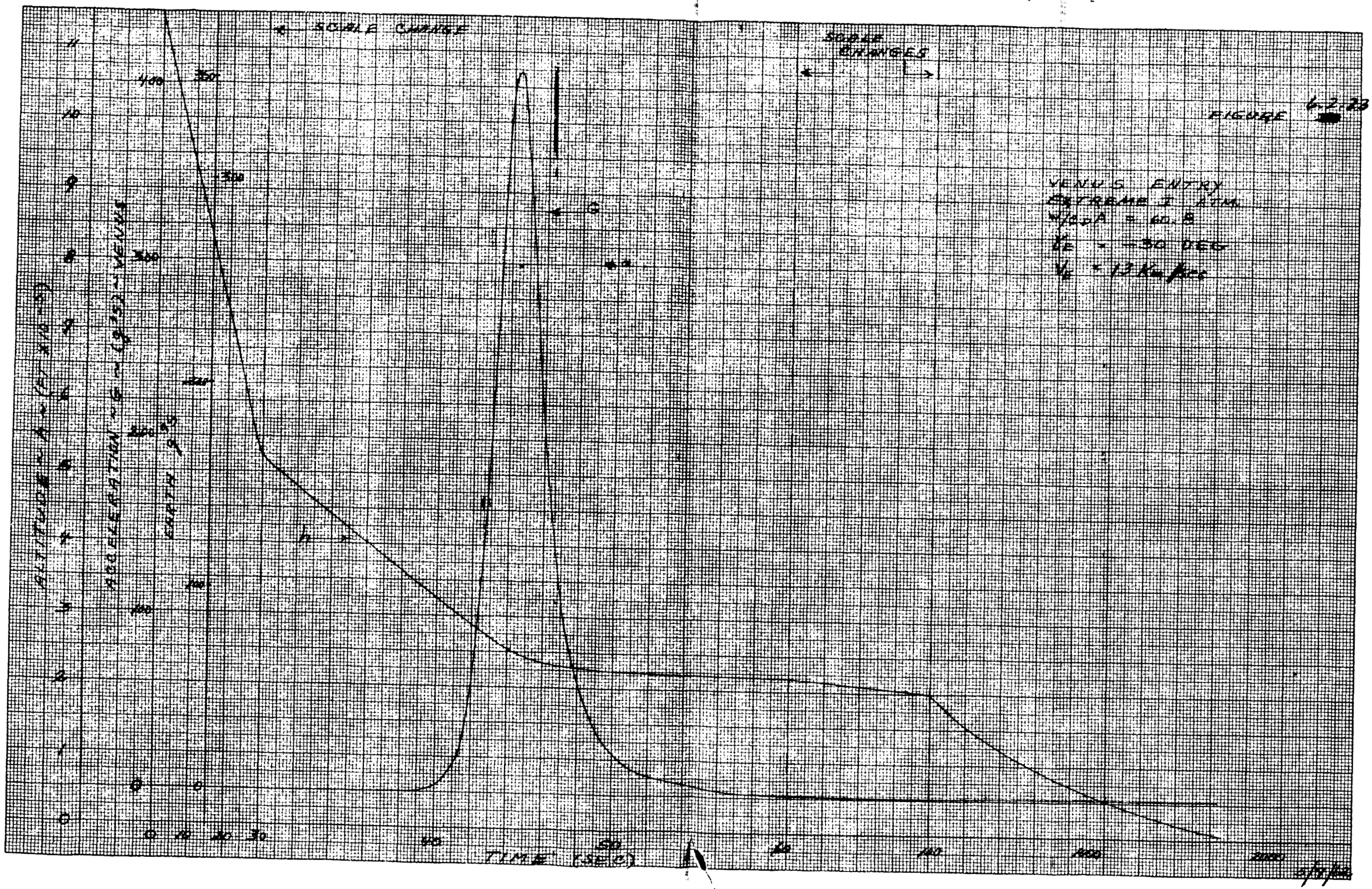

SCALE CHANGE
SCALE CHANGES
FIGURE 6.2.23
VENUS ENTRY
EXTREME I ATM.
W/CDA = 60.8
γE = -30 DEG
VE = 13 Km/sec
ALTITUDE ~ h ~ (FT x 10^-5)
ACCELERATION ~ G ~ (g's) ~ VENUS
EARTH g's
TIME (SEC)
h
G

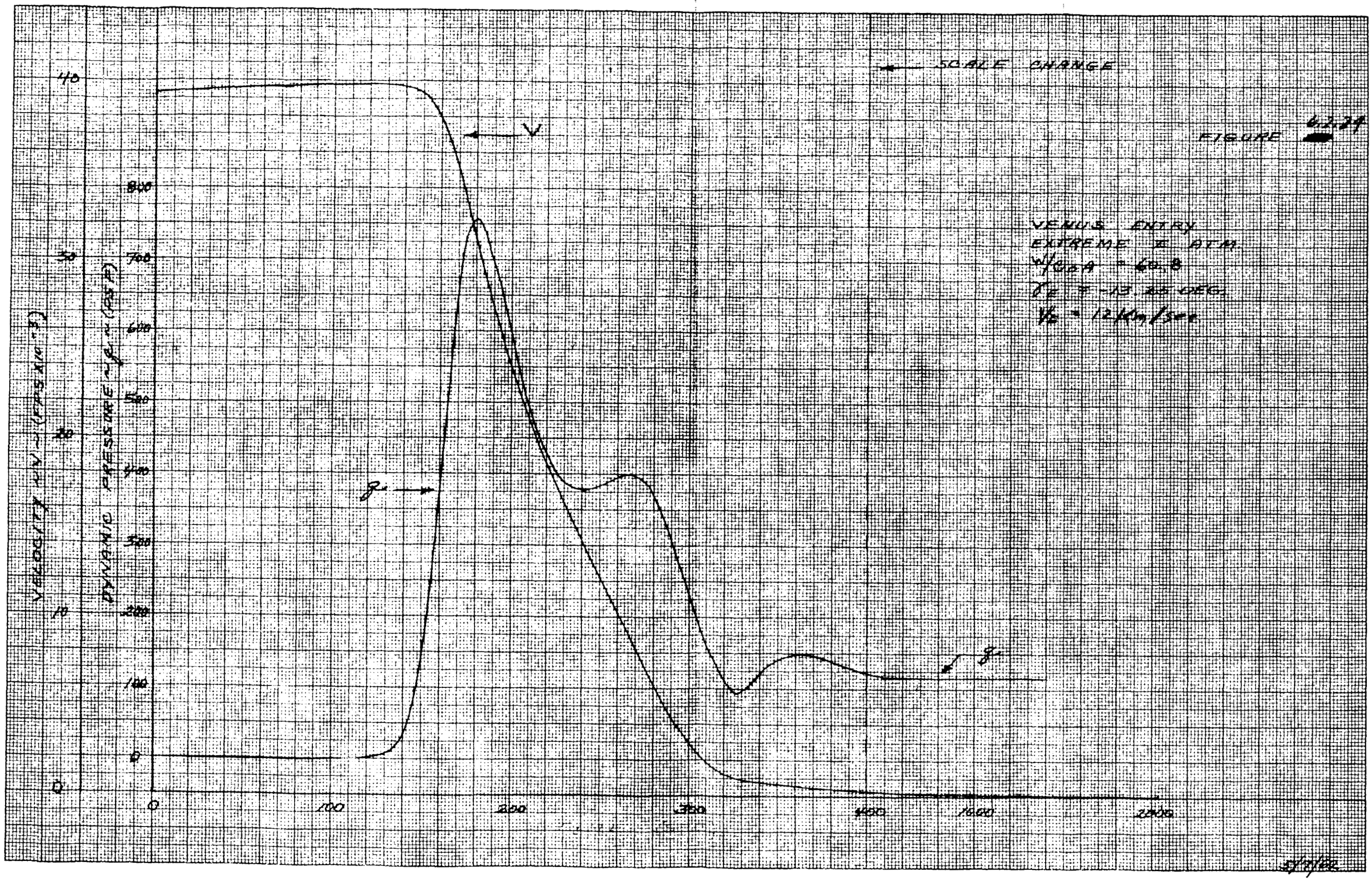

SCALE CHANGE
FIGURE 6.2.24
VENUS ENTRY
EXTREME Σ ATM.
W/CoA = 60.8
γE = -13.25 DEG.
VE = 12 Km/sec
VELOCITY ~ V ~ (FPS X 10^-3)
DYNAMIC PRESSURE ~ q ~ (PSF)
V
q
0
10
20
30
40
100
200
300
400
500
600
700
800
1000
2000
5/7/62

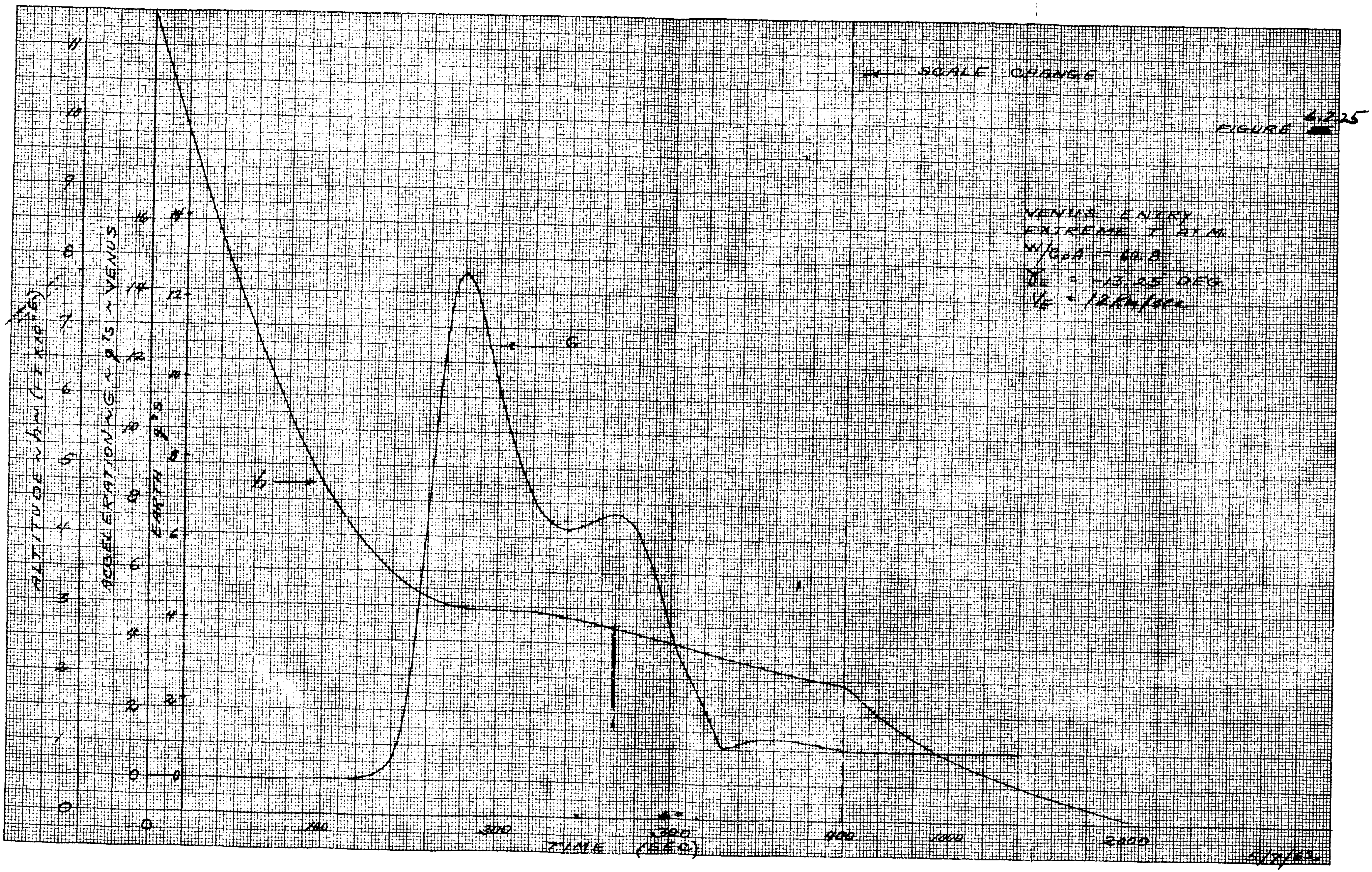
FIGURE 4.2.25
SCALE CHANGE
VENUS ENTRY
EXTREME I ATM.
W/CDA = 60.8
γE = -13.25 DEG.
VE = 12 Km/sec
G
h
ALTITUDE ~ h ~ (FT x 10^-5)
ACCELERATION ~ G ~ g's ~ VENUS
EARTH g's
TIME (SEC)
5/7/62

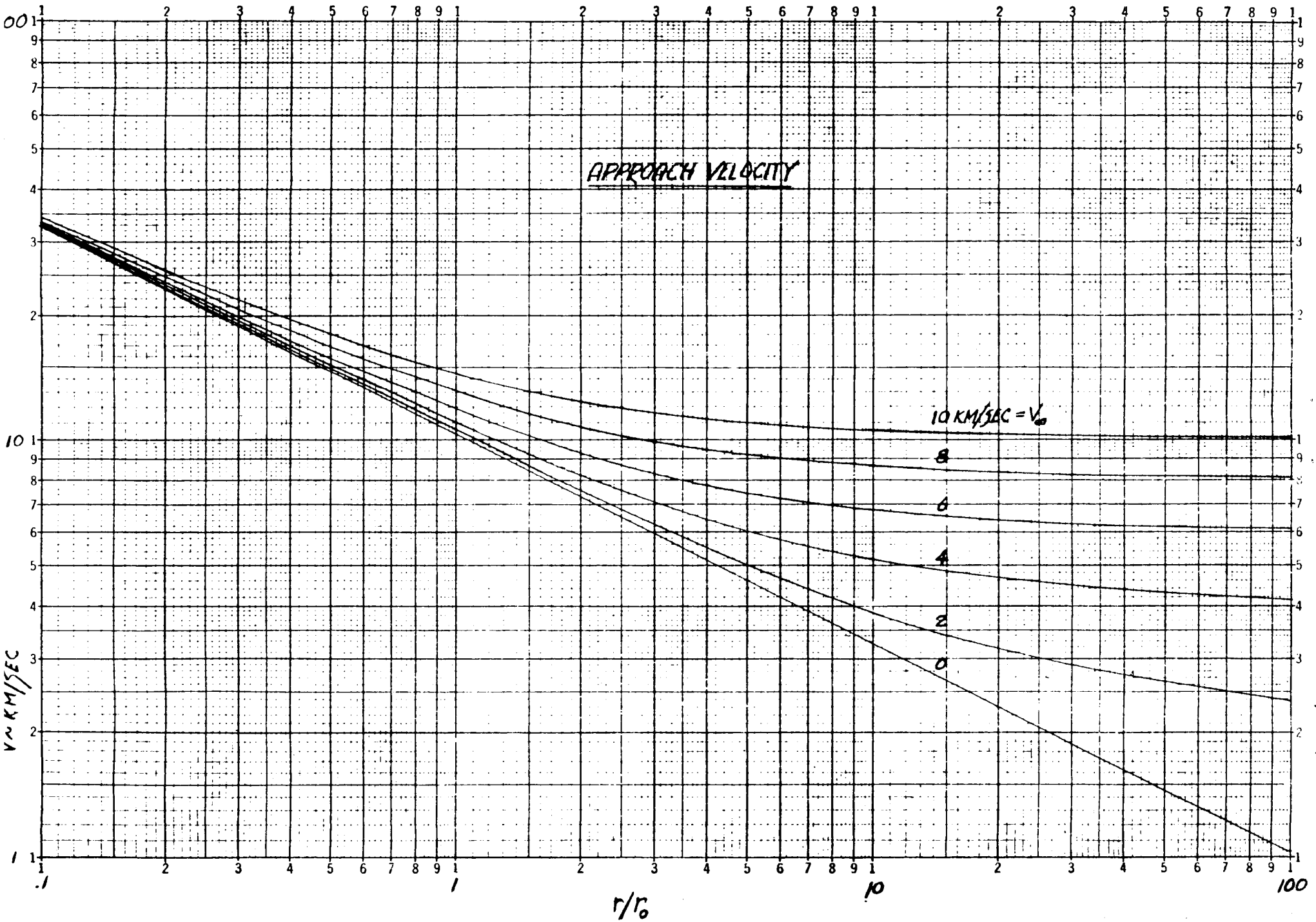
APPROACH VELOCITY
10 KM/SEC = V_∞
8
6
4
2
0
V ~ KM/SEC
r/r_0
.1
1
10
100

FIGURE 6.2.26

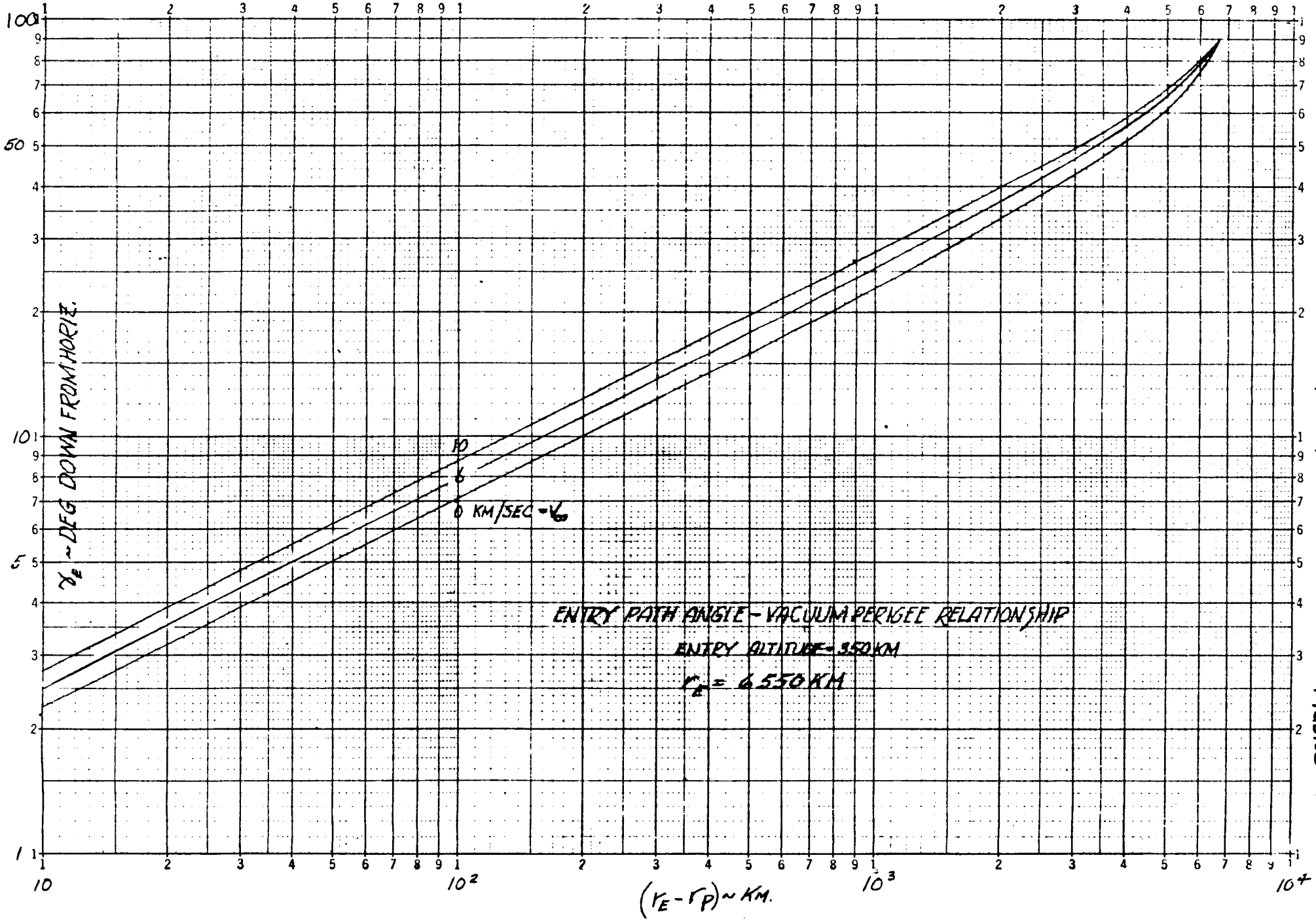
ENTRY PATH ANGLE - VACUUM PERIGEE RELATIONSHIP
ENTRY ALTITUDE - 350 KM
r_E = 6550 KM
10
6
0 KM/SEC = V_∞
γ_E ~ DEG DOWN FROM HORIZ.
$(r_E - r_P)$ ~ KM.
100
50
10
5
1
10
10^2
10^3
10^4

FIGURE 6.2.27

FIG 6.2.28

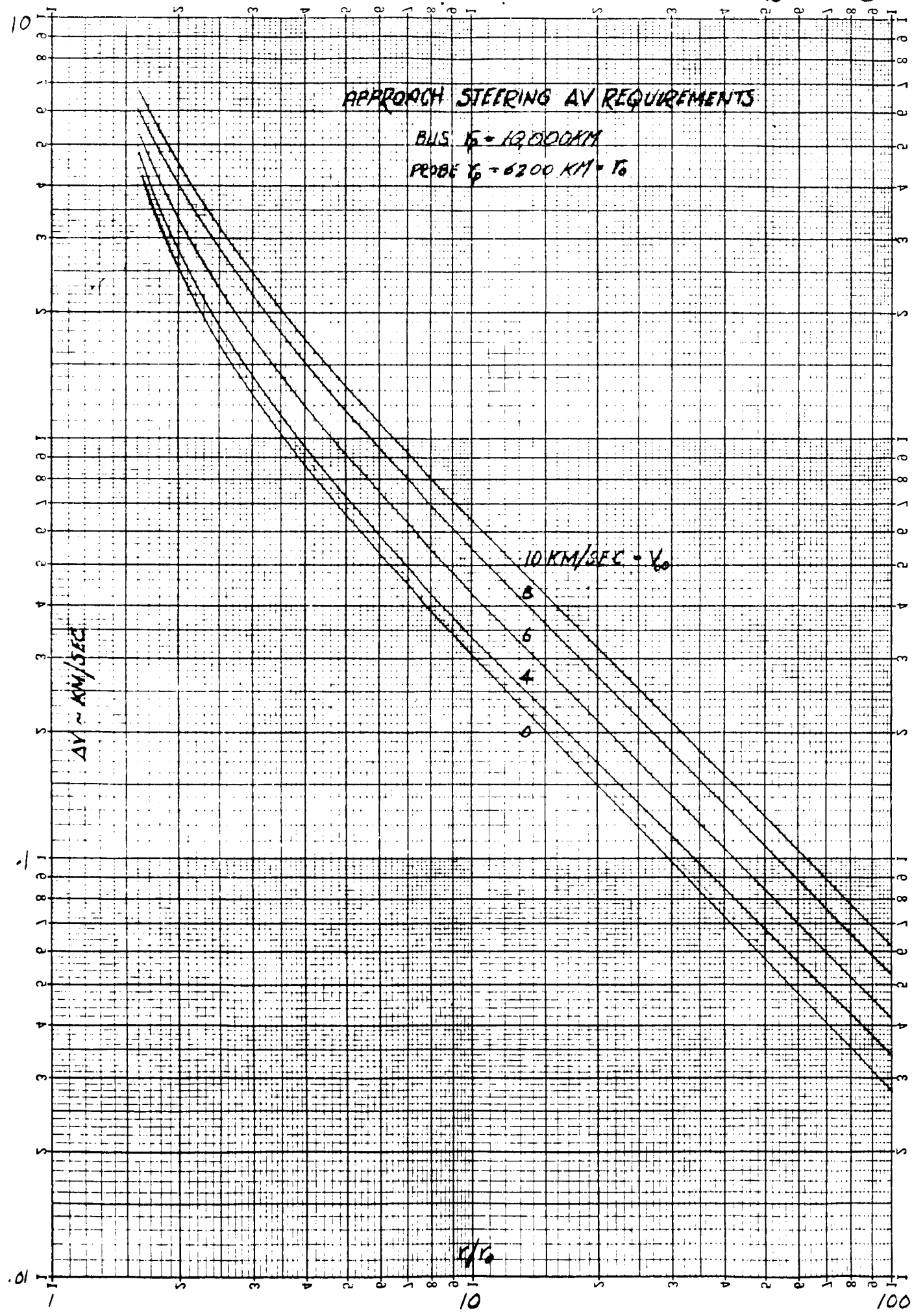
APPROACH STEERING ΔV REQUIREMENTS
BUS r_p = 10,000 KM
PROBE r_p = 6200 KM = r_0
10 KM/SEC = V_∞
8
6
4
2
ΔV ~ KM/SEC
r/r_0
10
.1
.01
1
10
100

FIGURE 6.2.29

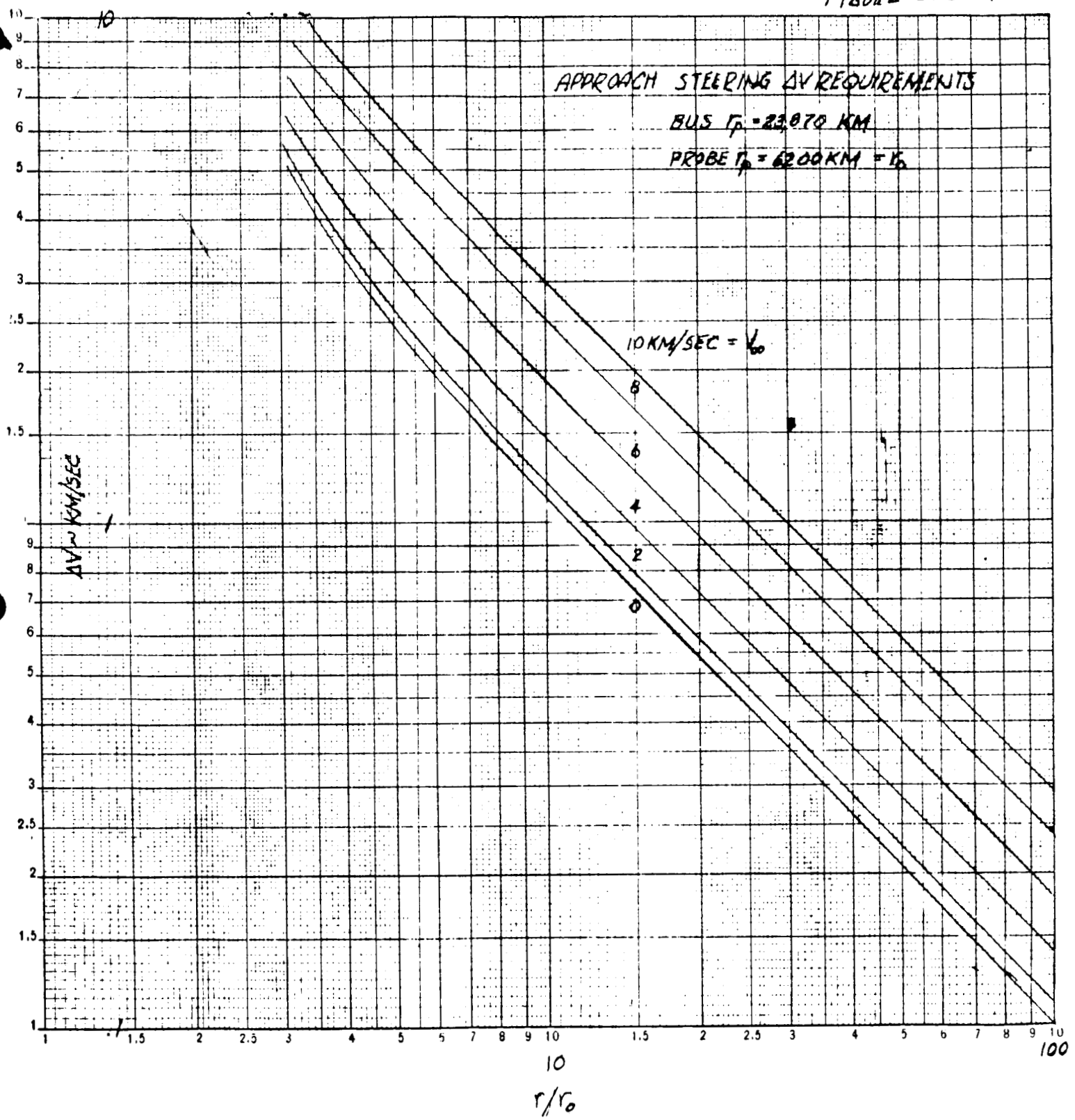
APPROACH STEERING ΔV REQUIREMENTS
BUS r_p = 23,870 KM
PROBE r_p = 6200 KM = r_0
10 KM/SEC = V_∞
8
6
4
2
0
ΔV ~ KM/SEC
r/r_0

FIGURE 6.2.30

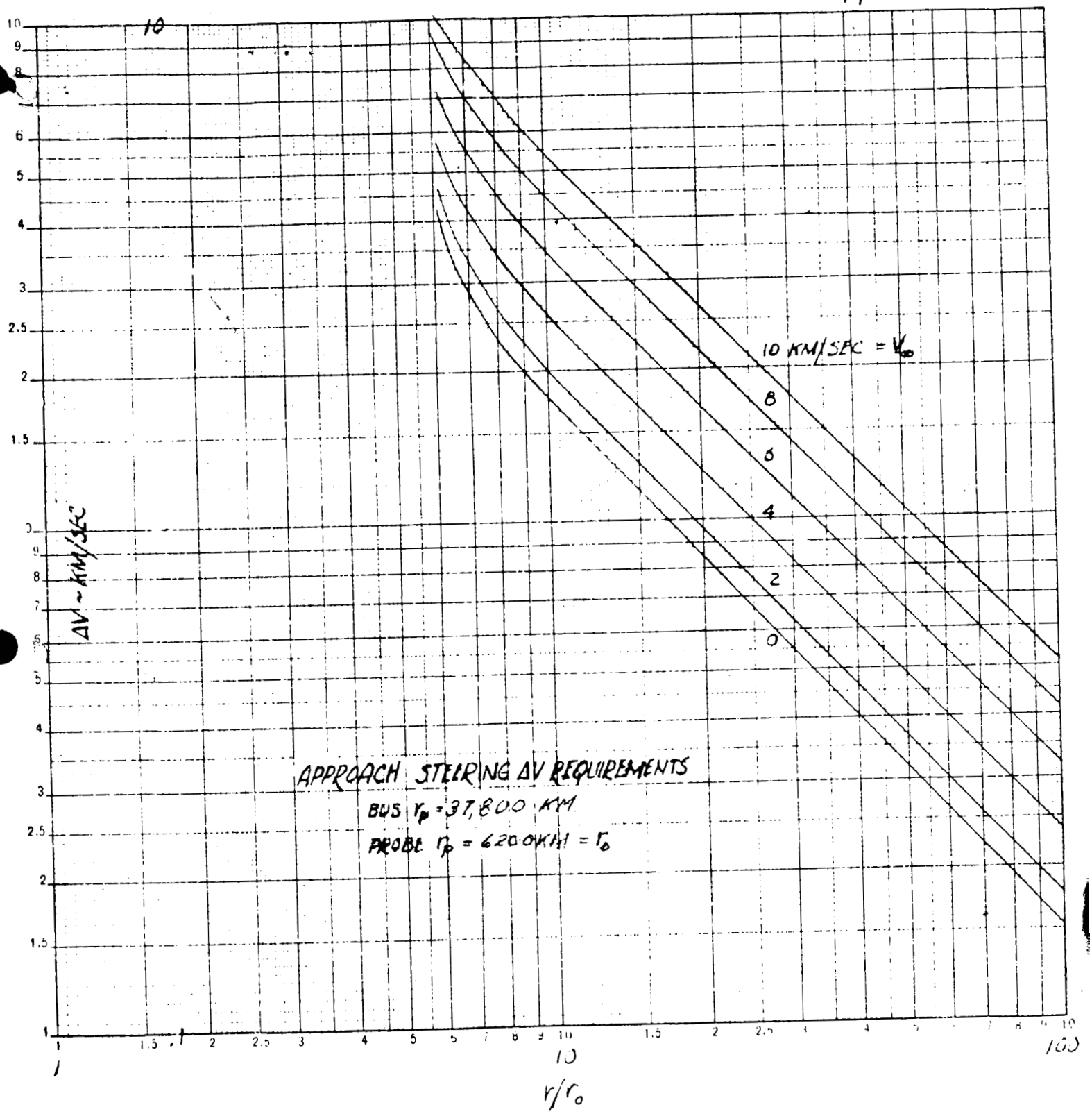
10 KM/SEC = V_∞
8
6
4
2
0
APPROACH STEERING ΔV REQUIREMENTS
BUS r_p = 37,800 KM
PROBE r_p = 6200 KM = r_0
ΔV ~ KM/SEC
r/r_0

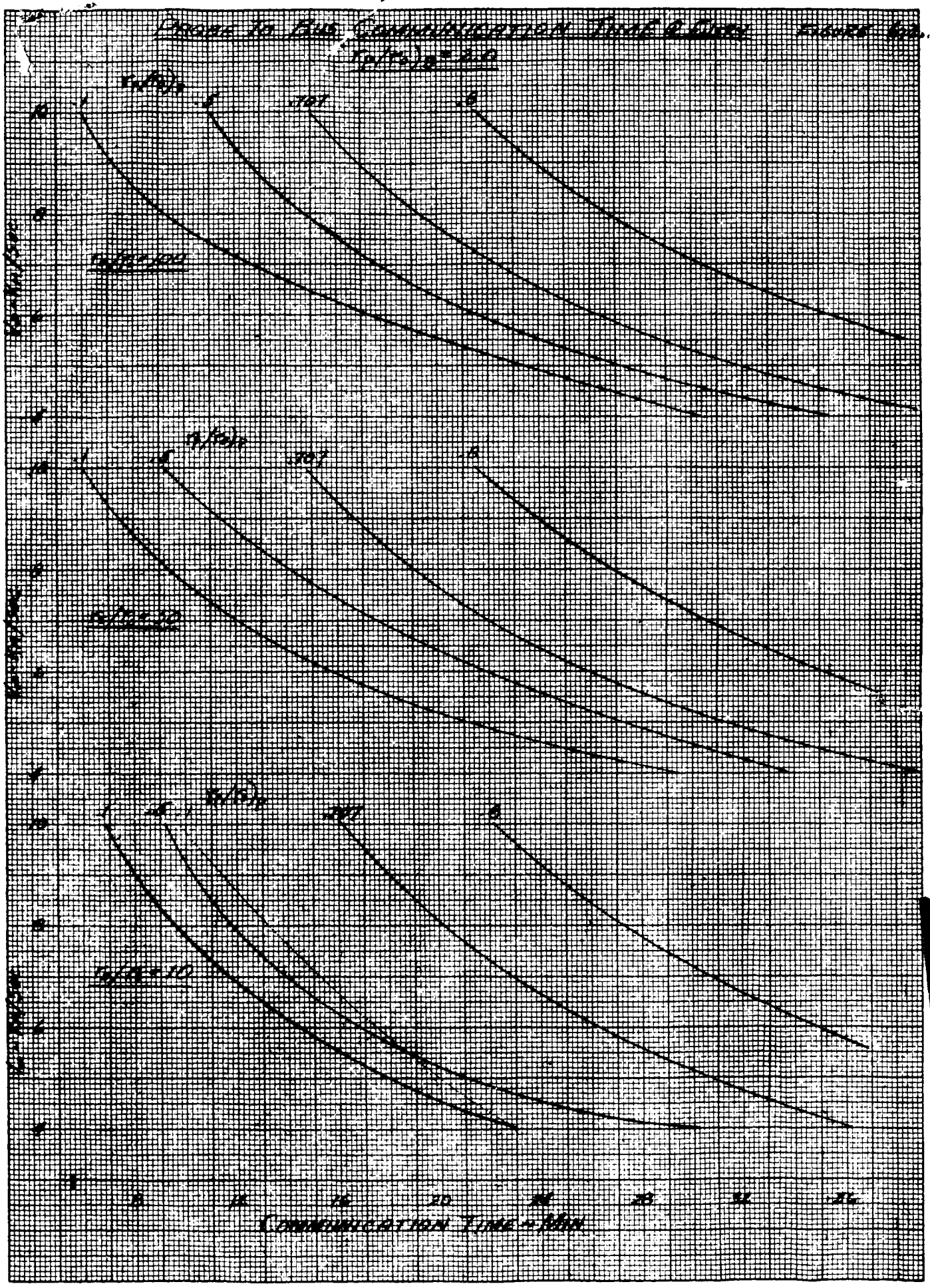

Probe To Bus Communication Time & Delay
Figure 6.31
$r_p/r_o)_B = 2.0$
$r_p/r_o)_B$
.1
.5
.707
.8
$r_p/r_o = 100$
$r_p/r_o = 50$
$r_p/r_o = 10$
10
8
6
4
8
12
16
20
24
28
32
36
Communication Time ~ Min

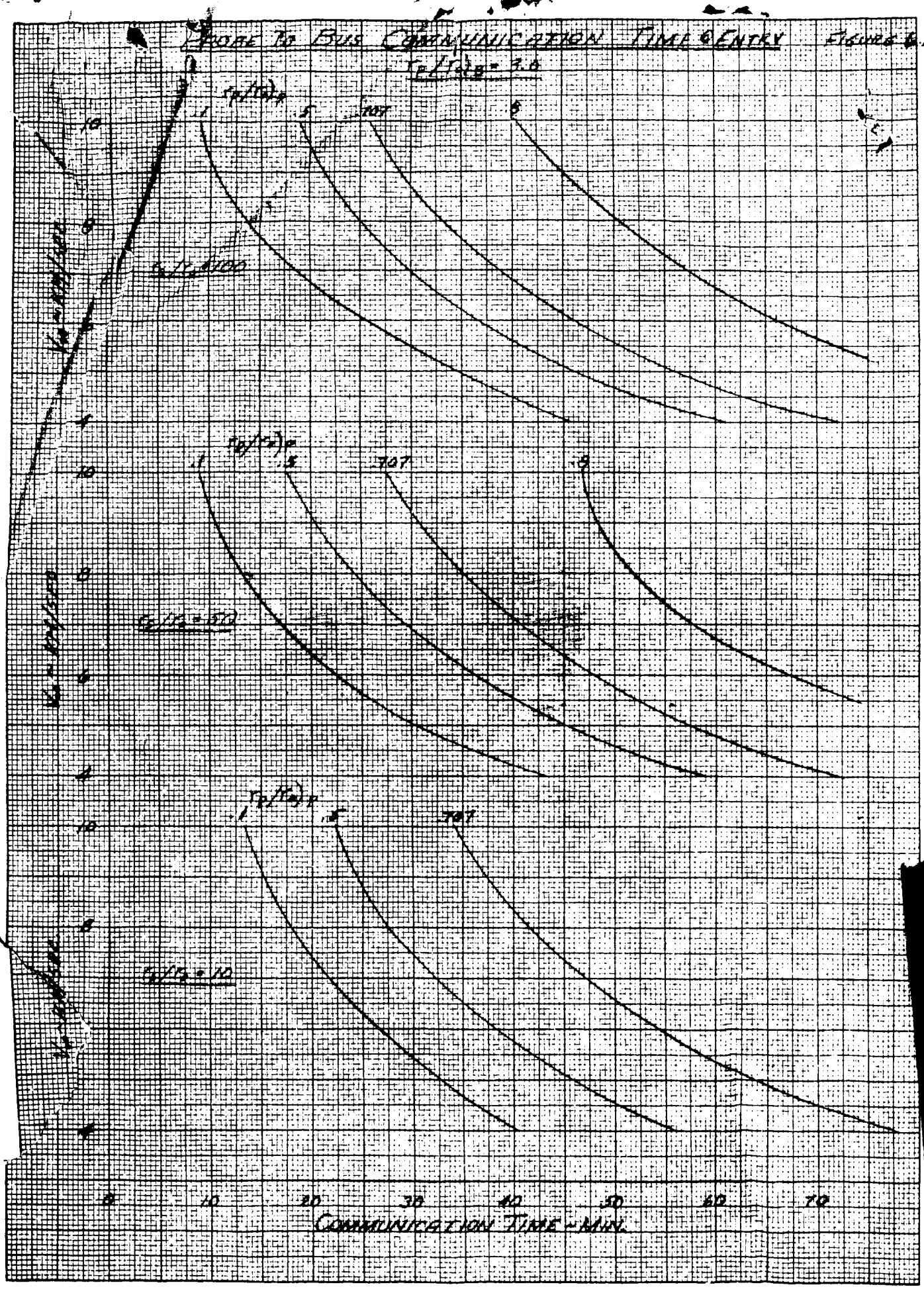
PROBE TO BUS COMMUNICATION TIME @ ENTRY
FIGURE 6
$r_p/r_a)_B = 3.0$
$r_p/r_a)_p$
.1
.5
.707
.8
$r_b/r_a = 100$
$r_b/r_a = 50$
$r_b/r_a = 10$
10
8
6
4
0
10
20
30
40
50
60
70
COMMUNICATION TIME ~ MIN.